



Reynolds, Paul M (2015) *From high-content to super-resolution investigation of cell behaviour on nanostructured surfaces*. PhD thesis.

<https://theses.gla.ac.uk/6490/>

Copyright and moral rights for this work are retained by the author

A copy can be downloaded for personal non-commercial research or study, without prior permission or charge

This work cannot be reproduced or quoted extensively from without first obtaining permission in writing from the author

The content must not be changed in any way or sold commercially in any format or medium without the formal permission of the author

When referring to this work, full bibliographic details including the author, title, awarding institution and date of the thesis must be given

Enlighten: Theses

<https://theses.gla.ac.uk/>  
[research-enlighten@glasgow.ac.uk](mailto:research-enlighten@glasgow.ac.uk)



**UNIVERSITY**  
*of*  
**GLASGOW**

From high-content to super-resolution investigation of cell  
behaviour on nanostructured surfaces

Paul M. Reynolds

Submitted in fulfilment of the requirements for the degree of Doctor of Philosophy

2015

## **Abstract**

The environment in which cells find themselves is a complex, three dimensional one which provides a variety of inputs and cues capable of controlling and guiding cell behaviour. These environmental signals take a fertilised egg through development to become an adult human being made up of trillions of cells. As such, the power of environmental cues to provide context and guidance to cell behaviour cannot be understated. Without attempting to directly mimic the *in vivo* environment, it has been shown that micro- and nanostructured surfaces can influence cell behaviour when we try and engineer biology *in vitro*. Identification and optimisation of powerful topographies is, however, tedious, and so this thesis provides techniques to expedite the discovery of new and potent surfaces to drive cell behaviour.

A new fabrication technique has been developed which allows for the fabrication of gradients of feature height at both the micro- and nanoscale. This involves the use of plasma polymer gradients as novel etch masks alongside existing lithographic techniques. After fabrication and mass replication by injection moulding, use of these surfaces as platforms for the high-content screening of cell response is demonstrated. These can be considered high-content due to both the range of surface structures on a single sample, and also the microscopy techniques used to investigate cell response. Distinct cell types were found to respond differently to topographical cues, exhibiting varying degrees of alignment, proliferation, and organisation in both mono- and co-culture systems.

A new cell culture device has also been developed and patented which ensures that screening experiments begin with an accurate and repeatable distribution of cells across the high content array. The impact of uneven cell seeding on studies involving stem cell differentiation was also investigated – showing the importance of improved control.

Finally, the interaction of cells with such nanostructured surfaces is investigated using new super-resolution microscopy techniques. New methods are presented for the correlation of multiple nanoscale imaging techniques to view cell-nanostructure interactions with unprecedented resolution. This reveals insights into the way in which the cellular substructure is being modulated by underlying nanotopography. Indeed, it paints a picture which is remarkably different to the structure observed under a standard widefield microscope over the past 10 years.

## Table of Contents

Abstract .....	2
Table of Contents .....	3
List of Tables.....	7
List of Figures .....	8
Glossary of Abbreviations .....	16
Output.....	17
Publications (4) .....	17
Conference Presentations (6) .....	17
Patents (1) .....	17
Acknowledgements .....	18
Author's Declaration.....	19
1 Introduction.....	20
1.1 Biomaterials & biomedical engineering.....	20
1.2 Background .....	20
1.3 Gradient and array platforms.....	22
1.4 Cell-surface interactions.....	24
1.5 Gradient fabrication.....	27
1.6 High-content screening formats .....	28
1.7 Aims and outcomes of the thesis .....	30
1.8 Structure of the thesis .....	31
2 Materials & methods.....	33
2.1 Micro- and nanofabrication .....	33
2.2 Injection moulding .....	34
2.2.1 Mass replication of polymeric substrates .....	35



2.3	Cell culture .....	36
2.4	Microscopy .....	37
2.4.1	Immunohistochemistry .....	38
2.4.2	Correlative microscopy .....	39
2.5	High-content image processing .....	39
2.5.1	Image processing example .....	41
2.5.2	Common settings, issues & solutions .....	43
3	Fabricating continuous gradients of feature depth.....	45
3.1	Introduction .....	46
3.1.1	Microgroove topographies.....	47
3.2	Methods .....	49
3.2.1	Photolithography .....	49
3.2.2	Injection moulding inlay fabrication .....	49
3.2.3	Cell culture .....	50
3.2.4	Data acquisition – large area imaging .....	50
3.2.5	Data acquisition - immunofluorescence .....	51
3.3	Plasma polymers for micro- and nanofabrication .....	51
3.3.1	Plasma polymer deposition .....	51
3.3.2	Plasma polymer gradients .....	53
3.3.3	Dry etch cycles .....	54
3.4	Continuous gradients of groove depth.....	55
3.5	Gradient amplification.....	58
3.6	Cellular response to continuous variation in groove depth and pitch .....	61
3.7	Cell alignment on a microgroove gradient .....	63
3.8	Conclusions .....	66
4	Label free segmentation of co-cultured cells on a nanotopographical gradient	67
4.1	Introduction .....	68

4.2	Methods .....	72
4.2.1	Electron beam lithography .....	72
4.2.2	Injection moulding inlay fabrication .....	73
4.2.3	Co-culture labelling .....	74
4.2.4	Data acquisition – immunofluorescence .....	74
4.3	Analysing morphometric data .....	76
4.4	Machine learning & data processing .....	79
4.5	Principal component analysis .....	87
4.6	Conclusions .....	93
5	Uniform cell seeder .....	96
5.1	Introduction .....	97
5.2	Methods .....	101
5.2.1	Device fabrication .....	101
5.2.2	Cell seeding .....	102
5.3	Cell seeding accuracy and its implications in vitro .....	103
5.4	Cell seeding timescales .....	108
5.5	Improving stem cell differentiation through homogeneous seeding .....	110
5.6	Conclusions .....	114
6	Imaging the nanoscale architecture of focal adhesions .....	116
6.1	Introduction .....	117
6.2	Methods .....	120
6.2.1	Data acquisition - super-resolution imaging .....	120
6.2.2	Secondary fixation for electron microscopy .....	122
6.3	Correlative light electron microscopy (CLEM) .....	124
6.4	Quantification of adhesion geometry on nanopatterns .....	130
6.5	Conclusions .....	137
7	Conclusion & discussion .....	139

Appendix A: immunohistochemistry protocol.....	141
Appendix B: plasma chamber operation protocol.....	142
Appendix C: PCA code.....	143
Appendix D: manual classification exercise.....	147
Appendix D: reagents.....	152
References.....	153

## List of Tables

TABLE 1.1 AN OVERVIEW OF FABRICATION METHODS FOR GRADIENTS OF SURFACE CHEMISTRY, TOPOGRAPHY AND MECHANICAL PROPERTIES. THIS THESIS FOCUSES ON THE FABRICATION AND IMPLEMENTATION OF TOPOGRAPHICAL SURFACE GRADIENTS, BUT VARIOUS ASPECTS OF EXPERIMENTAL PROCEDURE AND DATA ACQUISITION/ANALYSIS ARE APPLICABLE TO ALL GRADIENT FORMATS. ....	30
TABLE 2.1 STANDARD PARAMETERS FOR INJECTION MOULDING TWO MATERIALS USED IN THIS THESIS.....	35
TABLE 2.2 CELL TYPES USED THROUGHOUT THIS THESIS. *WORK USING SA121 CELLS WAS CONDUCTED BY A COLLABORATOR IN DENMARK (CELL CULTURE & IMAGING), WITH DATA ANALYSIS AND PRESENTATION FORMING PART OF THIS THESIS.....	36
TABLE 2.3 THE PROPERTIES OF INDIVIDUAL FLUORESCENT CHANNELS DETERMINE HOW THEY ARE PROCESSED.....	41
TABLE 2.4 OBJECTS ARE DETECTED BY SETTING AN INTENSITY THRESHOLD AFTER RESCALING IMAGES FROM 0 TO 1. POOR DETECTION CAN LEAD TO SPURIOUS MEASUREMENTS OF, FOR EXAMPLE, NUCLEAR SIZE/SHAPE AS SHOWN ABOVE. ....	44
TABLE 3.1 ETCH RATES AND CORRESPONDING SELECTIVITY VALUES FOR VARIOUS ETCH AND MATERIAL COMBINATIONS USED IN THIS THESIS. WHERE SUFFICIENT DATA WAS AVAILABLE SELECTIVITIES ARE PRESENTED AS AVERAGES OF AT LEAST THREE SAMPLES. IT SHOULD BE NOTED THAT ETCH PERFORMANCE IS INTRINSICALLY LINKED TO THE EQUIPMENT USED. THESE VALUES ARE SUBJECT TO DRIFT OVER TIME USING EQUIPMENT IN THE JWNC, AND PROVIDE ONLY AN INDICATION OF POTENTIAL BEHAVIOUR ON COMPARABLE SYSTEMS IN OTHER SETTINGS. ONE SHOULD ALWAYS CALIBRATE ETCH RATES AND MATERIAL SELECTIVITIES WHEN DEVELOPING/IMPLEMENTING A NEW PROCESS. ....	54
TABLE 4.1 CONFUSION MATRIX OF ML CLASSIFICATION SHOWING THREE CELL TYPES CLASSIFIED USING CPA. ....	84

## List of Figures

FIGURE 1.1 CELLS SENSE THEIR ENVIRONMENT THROUGH THREE MAIN ‘COLUMNS’ OF SENSING: CHEMICAL, MECHANICAL AND TOPOGRAPHICAL.....	22
FIGURE 1.2 A GRAPHICAL UNDERSTANDING OF THE LITERATURE. COLLATED DATA FROM 25 PAPERS WITH AT LEAST 50 CITATIONS WHICH USE STRUCTURED POLYMER MICROTOPOGRAPHIES[19]–[29] OR NANOTOPOGRAPHIES[30]–[43] TO DRIVE CELLULAR RESPONSE. PLOTTED ALONGSIDE THESE ARE GREEN AND PURPLE CROSSES, REPRESENTING THE RANGE OF TOPOGRAPHICAL FEATURES SINGLE GRADIENT SAMPLES USED IN THIS THESIS.....	23
FIGURE 1.3 CONTINUOUSLY VARIED SURFACE PARAMETERS MUST BE DISCRETISED FOR ANALYSIS, BOTH FOR LINEAR GRADIENTS (A) OR MULTIDIMENSIONAL/ORTHOGONAL GRADIENTS (B). THIS YIELDS EXTENSIVE MULTIVARIATE DATASETS WHICH CAN REVEAL THE SUBTLE CHANGES IN CELL RESPONSE TO VARIATION IN FEATURE PROPERTIES. THE SHEER COMPLEXITY OF THE DATASETS CAN ALSO BE A HINDRANCE, AS USERS MUST CHOOSE THE CORRECT WAY TO INTERPRET THE FULL DATASET. ....	26
FIGURE 1.4 POLYMER GRADIENT FABRICATION TECHNIQUES. ....	29
FIGURE 2.1 THE FABRICATION FLOW BEGINS WITH THE LITHOGRAPHIC DEFINITION OF A PATTERN ON A SILICON/QUARTZ SUBSTRATE. PATTERN TRANSFER BY REACTIVE ION ETCHING IS CARRIED OUT WITH SOFT (PMMA), HARD (NiCr) AND NOVEL (PPHEX) ETCH MASKS. AN INLAY FOR INJECTION MOULDING IS CREATED BY IMPRINTING THE PATTERNED MASTER SUBSTRATE INTO AN SU8 LAYER ON A POLYMERIC SUBSTRATE (CIRLEX™). THIS IS USED AS A DIE FOR MASS REPLICATION BY INJECTION MOULDING. ....	33
FIGURE 2.2 ILLUSTRATION OF AN INJECTION MOULDING MACHINE CONFIGURATION AND STANDARD OPERATION PROCESS. POLYMER BEADS ARE MELTED (1) AND THE POLYMER INJECTED TO FILL A CAVITY (2) WHICH IS PACKED AT HIGH PRESSURE AND ALLOWED TO COOL (3) BEFORE BEING OPENED AND THE PART EJECTED (4). IMAGE ADAPTED FROM[73]. ....	34
FIGURE 2.3 CELL RESPONSE TO NANOSTRUCTURED SURFACES WAS INTERROGATED OVER A RANGE OF LENGTH SCALES – REVEALING NOT ONLY THE BEHAVIOUR OF WHOLE CELL POPULATIONS, BUT ALSO CHANGES IN CELL MORPHOLOGY WITHIN SUCH POPULATIONS, AND ALSO THE STRUCTURE OF SUBCELLULAR COMPONENTS SUCH AS FOCAL ADHESIONS. ....	37
FIGURE 2.4 STRUCTURE OF EUKARYOTIC CELLS.....	40
FIGURE 2.5 AUTOMATED DETECTION OF CELLS IN FLUORESCENT MICROGRAPHS. CELL NUCLEUS AND BODY ARE DETECTED, AND OUTLINED IN WHITE. THIS ALLOWS FOR DETAILED MEASUREMENT OF CELL FEATURES AND SHAPE, INCLUDING THE INTENSITY OF PROTEIN STAINING WITHIN THE CELL AREA. ARROWS INDICATE INACCURATE DETECTION OF THE CELL PERIMETER. IN THIS CASE, THIN FILLOPODIAL PROTRUSIONS HAVE BEEN EXCLUDED FROM DETECTION AS PART OF THE CELL BODY DUE TO THE PROCESSING SETTINGS. ....	42
FIGURE 2.6 BOTH SUBCELLULAR STRUCTURES AND THE CELL BODY ITSELF CAN BE AUTOMATICALLY EXTRACTED FROM AN IMAGE BY THRESHOLDING.....	43
FIGURE 3.1 THERMAL IMPRINT PROCESS FOR TRANSFER OF MICROPATTERNS IN SILICON TO AN INLAY FOR REPLICATION BY INJECTION MOULDING.....	50
FIGURE 3.2 PLASMA POLYMERS ARE STRUCTURALLY DISTINCT FROM CONVENTIONAL POLYMERS. THE POLYMERISATION PROCESS CREATES A HIGHLY CROSS-LINKED POLYMER AS MONOMERS ARE DISSOCIATED IN THE PLASMA, CONDENSING ON THE SURFACE. WHEREAS CONVENTIONAL POLYMERS MAY POLYMERISE AS A REPEATABLE SEQUENCE, WITH SUBUNITS LINKING AT	

DESIGNATED SITES, PLASMA POLYMERS ARE CROSS LINKED BROADLY ACROSS MULTIPLE SITES AND VIA DISSOCIATED FRAGMENTS OF MONOMER.....	52
FIGURE 3.3 DEPOSITION OF PLASMA POLYMER FILMS UNDER A DIFFUSION MASKS CREATES A GRADIENT OF FILM THICKNESS WHICH CAN BE USED AS A SACRIFICIAL ETCH MASK. CONVENTIONAL UNIFORM ETCHING (LEFT) FORMS ONLY ONE DEPTH AT A TIME – MEANING MANY ROUNDS OF LITHOGRAPHY AND ETCHING ARE REQUIRED TO FABRICATE MULTIPLE DEPTHS ON A SINGLE SAMPLE. PLASMA POLYMER GRADIENTS (RIGHT) WHICH EXHIBIT A VARIATION IN THICKNESS ACROSS THE SAMPLE ARE SACRIFICIALLY ETCHED OVER TIME – RESULTING IN A VARIATION OF ETCH DEPTH. FILM THICKNESS IS REDUCED ALONG THE MASK LENGTH AS DIFFUSION OF MONOMER (RED) IS CONSTRICTED. ....	53
FIGURE 3.4 THE DEPOSITION OF PLASMA POLYMERISED HEXANE (PPHEX) UNDER A DIFFUSION MASK GIVES A GRADIENT OF THICKNESS ALONG THE PRE-DEFINED CHANNEL LENGTH. ....	55
FIGURE 3.5 SACRIFICIAL ETCHING OF THIS FILM TRANSFERS A GRADIENT OF DEPTH INTO THE SILICON SUBSTRATE. THE SILICON MASTER CAN THEN BE USED TO FABRICATE A POLYMER INLAY FOR REPLICATION OF THE PATTERN BY INJECTION MOULDING OF POLYCARBONATE. ....	56
FIGURE 3.6 SURFACE ROUGHNESS OF THE POLYMER REPLICAS WAS MEASURED BY AFM IN THE GROOVE BASE (A), WHICH ACTUALLY UNDERWENT THE DRY ETCHING PROCESS, AND ON TOP OF THE INTERMEDIATE RIDGES (B) WHICH WERE MASKED THROUGHOUT FABRICATION. THESE REGIONS HAD A RMS SURFACE ROUGHNESS OF 4.5 NM AND 1.3 NM RESPECTIVELY. NO SIGNIFICANT DETERIORATION IN EITHER LATERAL DEFINITION OR DEPTH OF THE PATTERN WAS OBSERVED ON INJECTION MOULDED POLYCARBONATE REPLICAS. ....	57
FIGURE 3.7 A) A GRAPHICAL REPRESENTATION OF THE DUAL TOPOGRAPHY GRADIENT ON AN INJECTION MOULDING INLAY – RIDGES INCREASE IN HEIGHT ACROSS THE SAMPLE, WHILST PITCH INCREASES ORTHOGONALLY. INJECTION MOULDING THEREFORE CREATES SAMPLES WITH THE COMPLIMENTARY GROOVE GRADIENT. B) INCREASE IN DEPTH ALONG THE LENGTH OF THE 5 $\mu\text{M}$ WIDE GROOVES CAN CLEARLY BE SEEN IN AN OPTICAL MICROGRAPH AS THE MICROPATTERN EMERGES FROM THE PLANAR SURFACE. ....	57
FIGURE 3.8 TANDEM ETCHING OF POLYMER GRADIENTS INTO THE SILICON SUBSTRATE ALLOWS FOR GRADIENT AMPLIFICATION TO MUCH STEEPER LATERAL HEIGHT CHANGES. HERE, THE SELECTIVITY OF ETCH A (4.5:1) AND ETCH B (11:1) COMBINE TO TRANSFER THE INITIAL POLYMER GRADIENT INTO THE SILICON SUBSTRATE WITH A SELECTIVITY WHICH IS EFFECTIVELY $4.5 \times 11 = \sim 50$ .....	58
FIGURE 3.9 OVERLAY OF SILICON DIOXIDE THICKNESS ON AN 8 MM X 8 MM ARRAY OF HEXAGONAL FEATURES WITH ORTHOGONALLY VARIED DIAMETER. THE WIDTH OF THE HEXAGONS INCREASES FROM 50 $\mu\text{M}$ TO 250 $\mu\text{M}$ WITH A CONSTANT FEATURE PITCH OF 300 $\mu\text{M}$ . INSERT: SEM MICROGRAPH OF LARGE HEXAGON PATTERN, AT THE DEEPEST POINT OF THE GRADIENT PITS ARE OVER 5 $\mu\text{M}$ DEEP. ....	59
FIGURE 3.10 THIN POLYMER FILMS ONLY 110 NM IN THICKNESS CAN BE AMPLIFIED INTO MICRON SCALE GRADIENTS IN SILICON SUBSTRATES. SELECTIVITIES FAR IN EXCESS OF THE 11:1 ACHIEVED HERE ARE POSSIBLE WITH SWITCHED ETCHES, IN WHICH CASE A LOG PLOT WOULD BE REQUIRED TO CONVEY THE SCALE OF AMPLIFICATION. ....	60
FIGURE 3.11 INTERFEROMETER TRACE SHOWING THE FINAL ETCH INTO SILICON THROUGH THE AMPLIFIED OXIDE MASK. ETCH STOP IS DETERMINED BY THE SECOND APEX OF THE SIGNAL TRACE AS THE OXIDE MASK IS DEPLETED. ....	61
FIGURE 3.12 THREE CELL TYPES (HTERT FIBROBLASTS, MDCK EPITHELIAL CELLS AND LE2 ENDOTHELIAL CELLS) WERE CULTURED ON THE DUAL MICROGRADIENT SURFACE, EXHIBITING DISTINCT MORPHOLOGIES AND GROWTH CHARACTERISTICS DEPENDING	

ON GROOVE PITCH AND DEPTH (A-I). HEATMAPS IN THE RIGHTMOST COLUMN INDICATE THAT AVERAGE DENSITY ACROSS THE FULL GRADIENT PLATFORM HAD LOCALISED HOTSPOTS OF MDCK AND LE2 GROWTH, WITH A MORE EVEN DISTRIBUTION OF HTERTS. REPRESENTATIVE IMAGES (A-I) ARE TAKEN FROM THE LOCATIONS INDICATED ON HEATMAPS. .	62
FIGURE 3.13 CELLULAR ALIGNMENT ON THE DUAL GRADIENT TOPOGRAPHY AS A FRACTION OF THE TOTAL NUMBER OF CELLS. A) A HEATMAP OF FIBROBLAST ALIGNMENT AS A FUNCTION OF GROOVE PITCH AND DEPTH, WITH PITCH INCREASING VERTICALLY AND DEPTH INCREASING HORIZONTALLY. B) ENDOTHELIAL CELL ALIGNMENT. CORRESPONDING CROSS SECTIONS OF THE HEATMAP DATA ARE PLOTTED (C&D) SHOWING THE ALIGNMENT AS GROOVE DEPTH INCREASES FOR THREE CHOSEN GROOVE PITCH VALUES WITH INSET IMAGES SHOWING REPRESENTATIVE MORPHOLOGY AT DEPTHS OF 100 NM, 550 NM AND 950 NM. ....	65
FIGURE 4.1 CHALLENGES ASSOCIATED WITH MANUAL SEGMENTATION OF CO-CULTURES ARISE FROM THE DIVERSITY OF PHENOTYPES ON DISPLAY ACROSS A SINGLE CELL TYPE. ON A FLAT SURFACE, FIBROBLASTS A & E CAN DISPLAY DRASTICALLY DIFFERENT MORPHOLOGIES. ENDOTHELIAL CELLS B, C & D ALSO DISPLAY A BROAD VARIATION IN APPEARANCE. IN THIS INSTANCE, ONLY THE DIFFERENCE IN THE STRUCTURE OF UROPODIA (ARROWS) INDICATES THAT D & E ARE DIFFERENT CELL TYPES. MANUAL CLASSIFICATION OF LARGE NUMBERS OF IMAGES CONTAINING MANY CELLS IS THEREFORE BOTH TIME CONSUMING AND PRONE TO A LEVEL OF SUBJECTIVE ERROR. ....	69
FIGURE 4.2 REGULAR ARRAYS OF NANOPILLARS, WITH A PITCH OF 300 NM, PILLAR HEIGHT OF 100 NM AND PILLAR DIAMETER OF 100 NM DRIVE TWO DISTINCT BEHAVIOURS IN FIBROBLAST AND ENDOTHELIAL CELLS. SUBSTRATES WERE FABRICATED BY EMBOSSING PCL FILMS TO CREATE PATTERNED AND FLAT AREAS ON A SUBSTRATE. SEPARATE CULTURE OF FIBROBLAST AND ENDOTHELIAL CELLS SHOWED THAT THE NANOPILLARS ARRAY REPELLED FIBROBLASTS, WHEREAS ENDOTHELIAL CELLS EXHIBITED ENHANCED PROLIFERATION. FIGURE ADAPTED FROM CSADEROVA ET AL. 2010. ....	70
FIGURE 4.3 DEPTH PROFILE OF QUARTZ MASTER, INJECTION MOULDING INLAY REPLICA AND THE FINAL INJECTION MOULDED PART IN POLYSTYRENE, ACCOMPANIED BY SELECTED AFM SCANS OF FEATURES AT THE SHALLOW, A, MEDIUM, B, AND TALL, C, REGION OF THE SAMPLE. TOP RIGHT: REPRESENTATIVE SEM IMAGE OF NANOPILLARS WITH A HEIGHT OF 140 NM. BOTTOM RIGHT: HISTOGRAM OF HEIGHT DATA TAKEN FROM AFM IMAGE SHOWING TWO PEAKS, WHICH WERE USED TO DETERMINE PILLAR HEIGHT ACROSS AFM IMAGES. ....	71
FIGURE 4.4 FABRICATION PROCESS FOR NANOPIT AND NANOPILLAR ARRAYS .....	72
FIGURE 4.5 FABRICATING INLAYS FOR INJECTION MOULDING. AFTER FABRICATION OF MICRO- OR NANOSTRUCTURES ON QUARTZ SUBSTRATES, THE PATTERN IS TRANSFERRED INTO AN SU-8 LAYER ON A CIRLEX™ SUBSTRATE BY UV-IMPRINT (1-3). ....	73
FIGURE 4.6 SCHEMATIC OF SCANNING STRATEGY ACROSS THE NANOPILLAR GRADIENT. EACH 18 IMAGE SCAN CONSISTED OF 4 IMAGES ON THE FLAT REGION ADJACENT TO THE SHORT PILLAR REGION, FOLLOWED BY 10 CONTIGUOUS IMAGES ACROSS THE RISING PILLAR GRADIENT, AND A FURTHER 4 IMAGES ON THE FLAT AREA ADJACENT TO THE TALL NANOPILLARS REGION. ....	75
FIGURE 4.8 SCATTERMATRIX OF THE FULL CO-CULTURE DATASET, INCLUDING GROUPING BY LOCATION ON THE GRADIENT SAMPLE. FIBROBLASTS (RINGS) AND ENDOTHELIAL CELLS (CIRCLES) HAVE BEEN COLOUR CODED BASED ON THEIR SUBSTRATE LOCATION. A DISTINCTION IS MADE BETWEEN THE FLAT SURFACE ADJACENT TO TALL PILLARS AND THE FLAT SURFACE ADJACENT TO SHORT PILLARS. 6 MEASUREMENTS ARE PLOTTED AGAINST ONE ANOTHER: INTENSITY OF CELLTRACKER DYE, CELL AREA, INTEGRATED EDGE INTENSITY (SUM OF PIXELS AROUND THE CELL EDGE), VARIANCE OF THE CELL CYTOSKELETON INTENSITY, AND CELL COMPACTNESS (A MEASURE OF CELL SHAPE AND IRREGULARITY). DIAGONAL SHOWS HISTOGRAMS OF THE TOTAL POPULATION (BOTH CELL TYPES). ....	78

FIGURE 4.9 PROCESSING FLOW FOR LABEL FREE SEGMENTATION OF CO-CULTURED CELLS. THE MORPHOMETRIC PROFILE OF CELLS (B) CAN BE USED TO DETERMINE CELL TYPE. WHEN COMPARED TO TRACKING CELL TYPE WITH A DIRECT PROBE (C) THIS IS APPROXIMATELY 84% ACCURATE, WITH SOME MIS-CLASSIFICATIONS (D). .....	80
FIGURE 4.10 COMPARISON OF VARIOUS SEGMENTATION STRATEGIES FOR ANALYSING A CO-CULTURE OF ENDOTHELIAL AND FIBROBLAST CELLS. ACCURACY OF AUTOMATED CLASSIFICATION BASED ON TRACKER PROBE INTENSITY IS GIVEN AS A PERCENTAGE OF CELLS IN MONOCULTURE WHICH WERE ABOVE A SET THRESHOLD OF TRACKER INTENSITY. ALL OTHER HIT RATES ARE GIVEN AS A PERCENTAGE RELATIVE TO TRACKER CLASSIFICATION OF CO-CULTURED CELLS.....	82
FIGURE 4.11 CLASSIFICATION OF CO-CULTURES BY EYE IS INEFFECTIVE DUE TO THE BROAD RANGE OF PHENOTYPES ON SHOW. PARTICIPANTS WITH A BACKGROUND IN BIOLOGY, WHO ARE MORE EXPERIENCED IN INTERPRETING FLUORESCENT IMAGES, HAD A LOWER AVERAGE ACCURACY THAN THOSE WITHOUT ANY BACKGROUND IN BIOLOGY. ....	83
FIGURE 4.12 RESPONSE OF FIBROBLAST (HTERT-BJ1) AND ENDOTHELIAL (LE2) CELLS IN CO-CULTURE TO A GRADIENT OF NANOPILLAR HEIGHT IS SHOWN. THE RATIO OF ENDOTHELIAL / FIBROBLAST CELLS AFTER 96H CULTURE WAS CALCULATED BY (A) DIRECT LABELLING OF THE SUB-POPULATIONS WITH CELLTRACKER PROBES AND (B) APPLYING MACHINE LEARNING TO CELL MORPHOLOGY AND NUCLEUS DATA TO PREDICT CELL TYPE – GREYSCALE BACKGROUND GRADIENT REPRESENTS INCREASING PILLAR HEIGHT FROM LEFT TO RIGHT WITH DASHED LINE INDICATING THE NANOPILLAR-FLAT BOUNDARY. STATISTICALLY, EACH DATA POINT WAS COMPARED TO THE ‘BASELINE’ FLAT REGION, * $p < 0.01$ , ** $p < 0.001$ . IMAGES C, D, E SHOW CELLULAR RESPONSE AT VARIOUS POINTS ACROSS THE NANOGRAIDENT SAMPLE, F. FROM THIS ANALYSIS, IT APPEARS THAT NANOPILLAR HEIGHT IN EXCESS OF APPROXIMATELY 75 NM IS SUFFICIENT TO INDUCE A STATISTICALLY SIGNIFICANT CHANGE IN THE RATIO OF ENDOTHELIAL / FIBROBLAST CELL, HOWEVER AS PILLAR HEIGHT INCREASES THE AVERAGE NUMBER OF CELLS PER IMAGE FELL. ....	85
FIGURE 4.13 NANOPILLAR ARRAY WITH A GRADIENT OF FEATURE HEIGHT FROM LEFT TO RIGHT. NANOPILLARS EFFECTIVELY DRIVE SEPARATION OF TWO CELL TYPES, WITH ENDOTHELIAL CELLS REMAINING AND PROLIFERATING ON THE NANOPILLAR ARRAY, WHILST FIBROBLAST CELLS HAVE MIGRATED AWAY TO THE FLAT REGION ADJACENT TO THE ARRAY. CHARACTERISTIC ENDOTHELIAL CELL MORPHOLOGY IS VISIBLE ON THE STRUCTURED REGION AND ALSO ON THE FLAT SURFACE, WHEREAS THE WELL SPREAD FIBROBLAST MORPHOLOGY IS ONLY VISIBLE ON THE FLAT AREA.....	86
FIGURE 4.14 COLOUR CODED LOADING PLOT OF THE DISTRIBUTION OF DIFFERENT MEASUREMENT CLASSES FOR THE FIRST TWO PRINCIPAL COMPONENTS. THESE TWO COMPONENTS DEFINE OVER 50% OF THE TOTAL VARIANCE IN THE DATASET, WHICH IS COMPOSED OF 137 MEASUREMENTS PER CELL – WHICH COULD BE COLLECTIVELY REFERRED TO AS THE CELL ‘CYTOPROFILE’. .....	89
FIGURE 4.15 VARIANCE EXPLAINED BY THE FIRST 10 PRINCIPAL COMPONENTS OF FIBROBLAST AND ENDOTHELIAL CELLS ON A NANOPILLAR GRADIENT. ....	90
FIGURE 4.16 PCA SCATTER PLOT FOR FIBROBLAST AND ENDOTHELIAL CELL PHENOTYPE ON NANOPILLAR GRADIENT ARRAY WITH GRADIENT SPATIAL RESOLUTION OF 450 $\mu\text{M}$ . ....	91
FIGURE 4.17 ENDOTHELIAL CELLS ON THE NANOPILLAR GRADIENT ARRAY SEPARATE INTO THREE DISTINCT CLUSTERS AFTER PCA – INDICATING A CHANGE IN PHENOTYPE WHICH IS LINKED TO NANOPILLAR HEIGHT. DATAPOINTS ARE CIRCLED TO HIGHLIGHT THEIR SEPARATION, THIS DELINEATION DOES NOT REPRESENT ANY STATISTICAL ANALYSIS OF THEIR PROXIMITY. ....	92



FIGURE 4.18 FIBROBLAST CELL MORPHOLOGY APPEARS TO GROUP INTO DISTINCT REGIONS DEPENDING ON CELL LOCATION WITH RESPECT TO NEARBY PILLAR HEIGHT. DATAPPOINTS ARE CIRCLED TO HIGHLIGHT THEIR SEPARATION, THIS DELINEATION DOES NOT REPRESENT ANY STATISTICAL ANALYSIS OF THEIR PROXIMITY. ....	93
FIGURE 4.19 GRADIENT PLATFORMS OFFER A DRASTIC INCREASE IN THE YIELD FROM A SINGLE EXPERIMENT. MULTIPLE SAMPLES ARE REQUIRED IN CONVENTIONAL EXPERIMENTS, LEFT, EACH WITH A UNIQUE SURFACE PROPERTY. COMBINING THIS VARIATION ONTO A SINGLE SAMPLE, RIGHT, SIMPLIFIES EXPERIMENTS. FURTHER PROGRESS IN AUTOMATED DETECTION OF CELL TYPE ALSO ALLOWS CO-CULTURES ON A SINGLE SAMPLE. ....	94
FIGURE 5.1 THE PROBLEM OF UNEVEN CELL SEEDING. PATTERN ARRAYS ARE SEEDED WITH VARIED CONCENTRATIONS OF CELLS. .	98
FIGURE 5.2 CELL SEEDING METHODS CAN BE DIVIDED INTO THREE CATEGORIES; PIPETTING OF A SINGLE DROPLET OF CELL SUSPENSION ONTO THE SURFACE (A), FILLING THE CULTURE VESSEL WITH MEDIA AND PIPETTING A CONCENTRATED CELL SUSPENSION INTO THE FLUID (B), AND THE METHOD PRESENTED HERE – A RIGID SURFACE PLACED 1MM ABOVE THE SURFACE WHICH CONFINES THE CELL SEEDING VOLUME IN A DEFINED VOLUME ACROSS THE FULL SAMPLE (C). MOVEMENT TO THE INCUBATOR FOR CULTURE (D) REPRESENTS A CRITICAL STEP, WHEREBY REDISTRIBUTION OF UNATTACHED CELLS DUE TO FLOW WITHIN THE WELL CAUSES UNEVEN DISTRIBUTION, GENERALLY IN THE CENTRE OF THE WELL DUE TO CENTRIFUGAL FLOW. FINAL ANALYSIS OF RESULTS (E) IS THEREFORE AFFECTED BY THIS UNEVEN DISTRIBUTION IN THE PLATE – LEADING TO INCREASED EXPERIMENTAL ERROR. ....	98
FIGURE 5.3 LOCAL CELL DENSITIES INFLUENCE CELL BEHAVIOUR THROUGH CELL-CELL COMMUNICATION - BOTH CHEMICAL AND MECHANICAL. ONE MAY ENVISION THREE TERMINAL CELL DIFFERENTIATION STATES (GREEN/PINK/BLUE) ARISING FROM THREE DIFFERENT SEEDING DENSITIES ACROSS A SINGLE WELL. ANY FURTHER STUDY OF CELL RESPONSE TO A NOVEL BIOMATERIAL OR STRUCTURED SURFACE THEN BECOMES A STUDY OF A MIXED POPULATION, UNBEKNOWNST TO THE USER. ....	100
FIGURE 5.4 INJECTION MOULDED UCS DEVICES. THREE FEET HOLD THE DEVICE 1 MM ABOVE THE SURFACE TO BE SEEDED (YELLOW ARROWS) WHILST AN INLET ALLOWS FOR THE INJECTION OF CELL SUSPENSION (RED ARROWS) .....	101
FIGURE 5.5 UCS DEVICES WERE MACHINED FROM POLYCARBONATE FOR USE IN 12-WELL PLATES.....	101
FIGURE 5.6 THE UNIFORM CELL SEEDER IS FILLED BY INJECTING CELL SUSPENSION THROUGH A HOLE IN THE LID. IT SITS ON THE SURFACE WITH SPACER FEET CREATING A FLUID SHAPING VOLUME WHICH IS A DEFINED HEIGHT ACROSS THE SAMPLE - THEREFORE HOMOGENISING CELL DENSITY. ....	102
FIGURE 5.7 COMMON SAMPLE SEEDING METHODOLOGIES DISTRIBUTE CELLS ACROSS INJECTION MOULDED SAMPLES IN A HETEROGENEOUS MANNER WHICH IS UNDESIRABLE. CONTROLLED SEEDING USING THE UCS DEVICE RESULTS IN A DRASTIC IMPROVEMENT IN THE UNIFORMITY OF CELL DISTRIBUTION ON THE SUBSTRATE – AS EVIDENCED BY THE LACK OF CELL DENSITY ‘HOT SPOTS’ IN SUMMED IMAGES OF 10 SAMPLES (RIGHTMOST IMAGES). ....	103
FIGURE 5.8 THE ‘QUALITY’ OF CELL SEEDING ON A SURFACE CAN BE QUANTIFIED IN TERMS OF THE TOTAL NUMBER OF CELLS, THEIR DISTRIBUTION ACROSS THE SURFACE, AND THE INTER-CELL SPACING. EQUIDISTANT CELLS ACROSS A MILLIMETRE SCALE CULTURE VESSEL IS DEEMED TO REPRESENT ‘IDEAL’ SEEDING, WHEREBY THERE ARE NO LARGE SCALE CHANGES IN CELL DISTRIBUTION DERIVED FROM VARIATION FROM EXPERIMENT TO EXPERIMENT (I.E. HOW QUICKLY WAS THE DISH MOVED, WAS IT ACCIDENTALLY KNOCKED). ....	104
FIGURE 5.9 CELLS CAN BE MORE ACCURATELY SEEDED WITH THE UCS DEVICE WHEN COMPARED TO STANDARD SEEDING WITHOUT IN OPEN WELLS. A NARROWER DISTRIBUTION OF LOCAL CELL DENSITY VALUES IS EVIDENT FOR ALL SEEDING DENSITIES WHEN	

CELLS ARE SEEDED USING THE UCS (DASHED LINES). STANDARD SEEDING METHODS YIELD A BROAD DISTRIBUTION ACROSS THE FULL CULTURE SPACE (SOLID LINES).....	105
FIGURE 5.10 IMPROVEMENTS IN CELL SEEDING PERFORMANCE ARE QUANTIFIABLE IN TERMS OF THE CELL DENSITY ACROSS A FULL CULTURE VESSEL AND ALSO IN TERMS OF THE DISTANCE TO EACH CELL'S NEAREST NEIGHBOUR. AS A RATIO OF TARGET SEEDING VERSUS ACTUAL SEEDING, THE UCS IS MORE ACCURATE COMPARED TO DROPLET SEEDING AND OPEN SEEDING. BARS SHOW THE STANDARD DEVIATION. DATA FROM OVER 500,000 CELLS, $p < 0.005$ STUDENT'S T-TEST.....	106
FIGURE 5.11 USE OF THE UCS DEVICE LEADS TO A MARKED IMPROVEMENT IN THE UNIFORMITY OF CELL SEEDING. SEEDING UNIFORMITY IS SHOWN AS A FUNCTION OF LOCAL CELL POPULATIONS - EACH CELL IS COLOURED BASED ON THE NUMBER OF NEIGHBOURS WITHIN A 150 $\mu\text{M}$ RADIUS - THE MORE CONSISTENT THE COLOURING THE MORE EVEN THE SEEDING. ....	107
FIGURE 5.12 MICROSCOPY SETUP FOR IMAGING THE SETTLE TIME OF CELLS ONTO A FLAT SURFACE. ILLUMINATION FROM THE SIDE IS COUPLED OUT INTO THE OBJECTIVE WHEN CELLS SETTLE TO WITHIN A FEW HUNDRED NANOMETRES OF THE GLASS PLATE. LIGHT (ARROWS) IS SUPPLIED BY LEDs FROM THE SIDE OF THE PLATE. ....	108
FIGURE 5.13 AFTER INITIAL SEEDING, IT TAKES APPROXIMATELY 5 MINUTES FOR THE MAJORITY OF CELLS TO SETTLE TO THE SURFACE WHEN SEEDING IS PERFORMED USING A 1 MM HIGH UCS. TOP: SETTLEMENT OF CELLS ONTO A SURFACE OVER 10 MINUTES. AN IMPROVISED MICROSCOPE SETUP WAS USED TO ILLUMINATE ONLY CELLS WHICH WERE TOUCHING THE SURFACE; BOTTOM IMAGES SHOW THE SETTLEMENT OVER TIME. ....	109
FIGURE 5.14 HES CELLS SEEDED WITH THE UCS DEVICE AT A CONCENTRATION OF 100K CELLS PER WELL AFTER INITIAL DIFFERENTIATION TO THE DEFINITIVE ENDODERM USING A PROPRIETARY PROTOCOL DEVELOPED BY NOVO NORDISK.....	111
FIGURE 5.15 MONTAGES OF 21MM DIAMETER WELLS, SEEDED AT VARIOUS DENSITIES BOTH WITH AND WITHOUT THE UCS DEVICE. CELLS WERE FIXED AND STAINED FOR Nkx6.1, WHICH INDICATES COMMITMENT TO THE PANCREATIC ENDODERM (CELLS WERE RE-SEEDED AFTER DIFFERENTIATION TO THE DEFINITIVE ENDODERM). CENTRAL AGGREGATION OF CELLS WHEN SEEDED WITHOUT THE UCS APPEARS TO YIELD MORE POSITIVE CELLS AT LOWER DENSITIES, AND ALSO SHOWS AN ARTEFACT IN THE CENTRE OF THE WELL AT HIGHER DENSITIES. ....	112
FIGURE 5.16 CLUSTER SIZE AFTER DIFFERENTIATION USING OPEN SEEDING (WITHOUT THE UCS) AND THE UCS DEVICE TO CONTROL CELL SEEDING. FULL WELL MONTAGES (TOP) SHOW THE INHOMOGENEOUS DISTRIBUTION OF Nkx6.1 POSITIVE CELLS AT LOW SEEDING DENSITIES, WHICH IS LESS PRONOUNCED AT HIGHER DENSITIES. SEEDING ARTEFACTS ARE VISIBLE IN THE WELL CENTRE FOR BOTH SEEDING METHODS. HISTOGRAMS OF Nkx6.1 POSITIVE COLONY SIZE (BOTTOM) SHOW A DRASTIC REDUCTION IN DIFFERENTIATION EFFICIENCY USING THE UCS, WHEREAS BOTH SEEDING METHODS ARE COMPARABLE FOR HIGHER SEEDING DENSITIES. ....	113
FIGURE 6.1 STANDARD RESOLUTION FLUORESCENT MICROGRAPH OF A CELL IN WHICH THE FOCAL ADHESION PROTEIN PAXILLIN HAS BEEN LABELLED. A SUPER-RESOLUTION RECONSTRUCTION OF A SMALL REGION OF INTEREST IS OUTLINED IN YELLOW. PROCESSING THIS HIGHER RESOLUTION AREA TOOK APPROXIMATELY 5 DAYS ON A HIGH PERFORMANCE CLUSTER COMPUTING SYSTEM (COLUMBIA UNIVERSITY, NYC).....	118
FIGURE 6.2 ADHESION, TENSION AND PHENOTYPE. FIGURE ADAPTED FROM TSIMBOURI ET AL. FOCAL ADHESIONS ARE LONGER ON DISORDERED NANOPIT ARRAYS AS COMPARED TO FLAT AND ORDERED SURFACES. THIS CORRESPONDS TO HIGHER LEVELS OF P-MYOSIN EXPRESSION, WHICH IS INDICATIVE OF GREATER INTRACELLULAR TENSION. CELLS ON ORDERED AND DISORDERED SURFACES ALSO SHOW INVERTED PROFILES FOR MARKERS OF OESTROGENIC DIFFERENTIATION (BOTH RUNX2 AND PRUNX2	

ON NSQ SURFACE) AND MARKERS OF STEM CELL QUIESCENCE (STRO1 ON SQ SURFACE). THIS POINTS TO A CHANGE IN THE MECHANICAL SENSING OF A SURFACE, WHICH IS DEPENDENT ON PATTERN GEOMETRY.....	119
FIGURE 6.3 THREEB SUPER-RESOLUTION MICROSCOPY. A) INTEGRATION OF 200 FRAME DATASET. B) DATASET BLEACHING PROFILE OVER TIME. C) ITERATIVE PROCESS CAN BEGIN WITH ONE OF TWO INITIAL DISTRIBUTIONS, BOTH CONVERGING ON APPROXIMATELY EQUAL IMAGES. D) WHERE ROIS ARE TOO SMALL AND FLUOROPHORES OVERLAPPING ARTEFACTS CAN OCCUR. E) INTEGRATION OF 200 FRAME DATASET, F) THREEB RECONSTRUCTION OF HIGHLIGHTED ROI. ....	121
FIGURE 6.4 SECONDARY FIXATION BEFORE SEM IS ESSENTIAL FOR CORRELATIVE MICROSCOPY STUDIES. CONTRAST IS POOR WHEN SAMPLES ARE DEHYDRATED DIRECTLY AFTER FLUORESCENT MICROSCOPY (A-C). D) SECONDARY FIXATION WITH GLUTERALDEHYDE DRASTICALLY IMPROVES CONTRAST, REVEALING CELLULAR INTERACTIONS WITH SURFACE FEATURES DOWN TO NANOMETRE RESOLUTION. ....	123
FIGURE 6.5 CELLS WERE CULTURED ON SUBSTRATE WHICH COMBINED STRIPES OF ORDERED AND DISORDERED NANOPITS. BOTH PATTERNS ARE COMPOSED OF NANODOTS WHICH ARE 100 NM WIDE, 100NM DEEP PITS WITH A NOMINAL PITCH OF 300 NM. THE ORDERED SQUARE ARRAY (SQ) HAS A CONSTANT CENTRE-CENTRE PITCH OF 300NM. IN THE DISORDERED 'NEAR SQUARE' (NSQ) EACH INDIVIDUAL PIT IS OFFSET BY A RANDOM AMOUNT WITHIN A RANGE OF +/- 50 NM IN BOTH THE X AND Y DIRECTIONS. THESE TWO PATTERNS ARE HIGHLIGHTED IN GREEN BOXES ABOVE. OTHER SPACINGS WERE ALSO INCLUDED, WITH A TOTAL OF 47 COMBINATIONS OF SYMMETRIES AND STRIPE WIDTHS. ....	125
FIGURE 6.6 LOW MAGNIFICATION SEM OF MOUSE EMBRYONIC FIBROBLAST (MEF) CELL ON A NANOPITTED POLYCARBONATE SURFACE AS DESCRIBED ABOVE. OVERLAID ONTO THE SEM IN GREEN IS A WIDEFIELD FLUORESCENCE IMAGE OF THE SAME CELL, IMMUNOLABELLED WITH PAXILLIN. ....	126
FIGURE 6.7 SUPER-RESOLUTION RECONSTRUCTION OF AREA OF INTEREST. FOCAL ADHESIONS ARE BROADER AT THE PROXIMAL SIDE, AND APPEAR TO CONCENTRATE AT THE DISTAL SIDE. ....	128
FIGURE 6.8 CORRELATED SUPER-RESOLUTION IMAGE OF PAXILLIN AND SEM OF CELL ON NANOSTRUCTURED SURFACE. NARROW FOCAL ADHESIONS NAVIGATE BETWEEN NANOPITS, PROPAGATING AT ANGLES WHERE OBSTRUCTIONS ARE MINIMISED, WITH BENDS AND KINKS IN STRUCTURE TO WORK AROUND NANOFEATURES. ALTERNATING ORDERED AND DISORDERED PATTERNS APPEAR TO FORCE ADHESIONS TO DIVERT MORE STRONGLY FROM A LINEAR PATH. WHITE ARROWS INDICATE A TRANSITION FROM DISORDER TO ORDER ACCOMPANIED BY A PRONOUNCED BEND IN THE FA BEFORE CONTINUING TOWARDS THE CENTRE OF THE CELL. ....	128
FIGURE 6.9 HIGH MAGNIFICATION SEM IMAGES OF FILLOPODIAL EXTENSIONS ON NANOPIT ARRAYS. HERE, IT IS EVIDENT THAT CELLULAR PROTRUSIONS 'NAVIGATE' BETWEEN NANOPITS, EXTENDING THROUGH THE FLAT REGION BETWEEN FEATURES. ....	129
FIGURE 6.10 FOCAL ADHESION ORIENTATION ON NANOPIT ARRAYS. ADHESIONS EXTEND IN BETWEEN NANOPITS AT APPROXIMATELY 45°. HERE, A REGULAR ARRAY WITH PITCH OF 300 NM HAS BEEN OVERLAID ONTO A SUPER-RESOLUTION RECONSTRUCTION OF PAXILLIN LABELLED FOCAL ADHESION COMPLEX. AS THE NANOSTRUCTURES CANNOT BE OBSERVED IN BRIGHTFIELD OR FLUORESCENCE, THERE IS NO MEANS OF ALIGNING THE GRID TO THE TRUE UNDERLYING STRUCTURE. ....	130
FIGURE 6.11 LINE SCAN ACROSS SUPER-RESOLUTION RECONSTRUCTION OF FOCAL ADHESIONS ON DISORDERED NANOPIT ARRAY. ADHESION FORMATION IS QUANTISED SPATIALLY INTO THE REGIONS BETWEEN NANOPITS. WHAT APPEARS TO BE A SINGLE ADHESION (A) IS REVEALED TO BE TWO SEPARATE STRUCTURES WITH A PITCH OF APPROXIMATELY 300 NM .....	132

- FIGURE 6.12 POSSIBLE AVENUES OF FA PROPAGATION FROM A CENTRAL POINT IN A SQUARE NANOPIT ARRAY (100 NM DIAMETER PITS, 300 NM PITCH). BLUE ARROWS REPRESENT PROPAGATION ROUTES. RED DOTS REPRESENT PITS WHICH BLOCK/INTERFERE WITH THOSE ROUTES. GREEN DOTS IN (B) ARE RANDOMLY DISPLACED IN SUCH A MANNER AS TO ALLOW THE ROUTE OF PROPAGATION TO CONTINUE WHILST RED DOTS ARE DISPLACED BUT STILL BLOCK THE FA PATH. HERE, WE CAN SEE HOW DISPLACEMENTS IN THE PATTERN MAY ALLOW FOR LARGER FAS VERSUS ON HIGHLY ORDERED PATTERNS..132
- FIGURE 6.13 FOCAL ADHESIONS WERE QUANTIFIED BY GENERATING A MANUAL OVERLAY ON FLUORESCENT MICROGRAPHS CAPTURED AT 40X. ORIGINAL IMAGES (LEFT) WERE LOADED IN IMAGEJ AND AN OVERLAY CREATED (RIGHT) WHICH WAS THEN ANALYSED.....133
- FIGURE 6.14 THE GEOMETRICAL ARRANGEMENT OF NANOPIT ARRAYS DIRECTLY INFLUENCES THE SIZE OF FOCAL ADHESIONS. DIFFERENCES IN ADHESION LENGTH ARE STATISTICALLY SIGNIFICANT BETWEEN SURFACES ( $p < 0.001$  BY ONE WAY ANOVA). BARS SHOW SEM. ....133
- FIGURE 6.15 FOCAL ADHESIONS ORIENTATE TO THE UNDERLYING NANOTOPOGRAPHY. ORIENTATION TO THE HORIZONTAL AXIS WAS MEASURED FOR AT LEAST 500 MEF ADHESIONS ON EACH SURFACE TYPE STAINED FOR PAXILLIN. THESE WERE CLASSIFIED INTO 5° BINS FROM 0° TO 180°. DIFFERENCES IN ADHESION ORIENTATION ARE STATISTICALLY SIGNIFICANT BETWEEN SURFACES ( $p < 0.001$  BY ONE WAY ANOVA). ....134
- FIGURE 6.16 CLASSIFICATION OF FA ORIENTATION AT STANDARD MAGNIFICATIONS (A) IS PRONE TO ERROR. UPON CLOSER INSPECTION (B-D) WHAT APPEARS TO BE A VERTICAL ADHESION IS COMPOSED OF SHORT SUB-MICRON SECTIONS WHICH INTERSECT AT 60° ANGLES(E&F). THIS FITS THE PROPOSED MODEL OF ADHESIONS PROPAGATING BETWEEN PILLARS/PITS (G&H). SUPER-RESOLUTION IMAGING CONFIRMS THE NANOSCOPIC STRUCTURE – AGAIN REINFORCING THAT ADHESIONS ARE BUILT IN THE FREE SPACE BETWEEN PITS.....136

## Glossary of Abbreviations

AFM	atomic force microscope
ASM	angular second moment
BME	$\beta$ -mercaptoethanol
CP	CellProfiler
CPA	CellProfiler analyst
DNA	Deoxyribose Nucleic Acid
EBL	electron beam lithography
FACS	fluorescence activated cell sorting
FA	focal adhesion
ICP	inductively coupled plasma
JWNC	James Watt Nanofabrication Centre
ML	Machine Learning
NiCr	Nickel-Chromium (60%-40% alloy)
PCA	Principal Component Analysis
Phold	holding pressure
PMMA	poly(methyl methacrylate)
RIE	Reactive Ion Etching
SEM	Standard Error of the Mean
SEM	scanning electron microscope
TPFS	Trichloro(1H,1H,2H,2H-perfluorooctyl)silane
UCS	Uniform Cell Seeder

## Output

### Publications (4)

Tsimbouri PM, Gadegaard N, Burgess KV, White K, **Reynolds PM**, Herzyk P, Oreffo RC, & Dalby MJ. Nanotopographical effects on mesenchymal stem cell morphology and phenotype. *Journal of Cellular Biochemistry*, September 2013; DOI: 10.1002/jcb.24673 [Citations:13]

**Reynolds PM**, Pedersen RH, Stormonth-Darling JM, Dalby MJ, Reihle MO, Gadegaard N. Label free segmentation of co-cultured cells on a nanotopographical gradient. *Nano Letters*, February 2013; DOI:10.1021/nl304097p. [Citations:9]

Tsimbouri PM, McMurray RJ, Burgess KV, Alakpa EV, **Reynolds PM**, Kingham E, Oreffo RC, Gadegaard N & Dalby MJ. Using nanotopography and metabolomics to identify biochemical effectors of multipotency. *ACS Nano*. October 2012; DOI: 10.1021/nn304046m [Citations:9]

**Reynolds PM**, Pedersen RH, Reihle MO, Gadegaard N. A Dual Gradient Assay for the Parametric Analysis of Cell-Surface Interactions. *Small*, June 2012. DOI:10.1002/sml.201200235 [Citations:8]

### Conference Presentations (6)

**Reynolds PM**, Pedersen RH, Stormonth-Darling JM, Dalby MJ, Reihle MO, Gadegaard N. Co-culture Separation and Assembly by Nanotopographical Persuasion of Cells. *Society For Biomaterials 2013*, Boston (oral)

**Reynolds PM**, Pedersen RH, Stormonth-Darling J, Gadegaard N. Development of a dual step etch process for fabrication of enhanced depth range microgradients. *Micro and Nano Engineering 2012*, Toulouse (poster)

Pedersen RH, **Reynolds PM**, Stormonth-Darling J, Dalby M, Reihle MO, Gadegaard N. Nanostructured topographical gradient patterns for cell-surface interaction studies. *Micro and Nano Engineering 2012*, Toulouse (poster)

**Reynolds PM**, Pedersen RH, Reihle MO, Gadegaard N. Parametric analysis of cell surface interactions. *EPSRC Inter-DTC Symposium 2012*, Warwick (oral)

**Reynolds PM**, Pedersen RH, Reihle MO, Gadegaard N. Fabrication of 3D cell screening topographies using plasma polymerised gradients as a secondary etch mask. *Micro and Nano Engineering 2011*, Berlin (poster)

**Reynolds PM**, Pedersen RH, Gadegaard N. Fabrication of 3D cell screening topographies using plasma polymerised gradients as a secondary etch mask. *PGBiomed 2011*, Glasgow (oral)

### Patents (1)

**Reynolds PM**, Riehle MO, Gadegaard N. Cell seeding method and device. May 2014. WO 2014064449 A1.

## Acknowledgements

Thanks to Nikolaj for first inspiring me and then persuading me to pursue research after my undergraduate degree (and for *not* hiring me at the first time of asking). It's been a great experience thanks to the engaging work, enthusiasm for doing things, and the freedom to meander from the straight path. Also, thanks to Mathis for all the help, advice, interesting discussions, and endless flow of ideas over the years. I've gone from having no understanding of cell culture to publishing papers, fermenting beer, and baking sourdough.

My thanks also extend to the rest of the research group, past and present. Rasmus, Johnny and Affar took me in as a youngster with daft hair and showed by example how to get things done in research. Neven provided perspective and sanity in the occasional madness, and I'm grateful for all the chats and advice along the way. Alex, Andy, Alistair, Maranda, Anwer, and I am sure there is someone I have forgotten. I am extremely grateful to the technical staff at both the JWNC and CCE - both centres deliver excellent support and make it that much easier to get great work done.

Thanks to my parents, my sisters and my family for all the love and support. To my Dad for calling my teenage bluff and letting me follow my 'dream' and go to college and study music after school. Perhaps more importantly, for making sure I had a deferred place at university beforehand.

Time spent in New York over the course of this PhD was a fantastic bonus, and my thanks go out to Nikolaj for helping me secure considerable funding from both the Principal's Early Career Mobility Fund and the School of Engineering. Thanks to Mike for graciously hosting me at Columbia; both he and the whole Sheetz lab made me feel at home in the big apple (Ana, James, Haguy, Shuaimin, Edward, Tomas, Luis). Special thanks go to Jared and Soha for putting me up both times I visited NY and teaching me how to tip 30% with a smile...Thanks to the Legion of Doom for the good times had by all, and for telling me to just shut up and write my thesis.

Finally, thanks to Jillian for everything through the years; for your love, support and patience. Your cookery skills saved me from a life of oven pizzas after long days, and your belief in me was just as important in sustaining me. Without you to come home to this would have surely been a terrible experience.

## **Author's Declaration**

I declare that all the work presented in this thesis has been carried out by me, unless otherwise acknowledged or referred to.

Paul M. Reynolds

October 2014



# 1 Introduction

## 1.1 Biomaterials & biomedical engineering

Our understanding of materials and their interactions with biological systems has developed rapidly over the past few decades. In the modern era of healthcare, the first biomaterials were simply inert upon implantation – often with a rudimentary structural role. These were followed by second generation biomaterials which were not only inert, but also biodegradable to alleviate the requirement for revision surgeries for removal. Current developments in the third generation of biomaterials are focused on biologically active materials, which elicit a specific response from the host[1]–[3]. The inherent complexity of biological systems, which operate through diverse pathways with multiple redundancies built in, means that it is extremely challenging to develop an interface which behaves in a specified manner – or rather, drives the biological system to an optimal response. This is complicated still further by variation from person to person – our bodies can be as diverse as our personalities in how they react to medical intervention. From the early implant devices which were crudely designed and implemented, tissue engineering has grown since the 1960s into a diverse field, pushing forward our understanding of how the biology and engineering must intersect and work in synergy together. In step with developments in the field itself, micro- and nanofabrication techniques developed initially for the semiconductor industry have found near ubiquitous use in biomedical engineering laboratories[4][5]. We now find ourselves in a dynamic research landscape where new fabrication techniques are being developed and old ones re-appropriated to answer both practical and fundamental questions in biology.

## 1.2 Background

Biological systems interact with artificial polymeric materials in a complex, multi-stage and iterative process of sensing and response[6]. The biological response at the cellular level to polymeric substrates has been studied at great length. However, this is often done on individual samples with a uniform coating of a given chemistry/topography. This results in experiments which are limited only to samples that the investigator can imagine – leaving potentially interesting samples or sample combinations hidden from use.

Subtle variations in surface properties can have a drastic impact on cell response, and therefore a considered and careful approach must be employed in surface design and fabrication. Following the example set by combinatorial chemistry and high-throughput screening applied to drug discovery by the pharmaceutical industry in the 1990s,[7] researchers are increasingly turning to similar methodologies in biomaterial design [8]–[15]. This involves creating high-content samples for exploring the full sample space, usually taking the form of a highly multiplexed array platform, or a continuous variation of a single material property as a gradient. Creating such dense sample formats presents a series of unique challenges in both their fabrication and implementation. In the case of surface modification for biomedical applications, platforms must be created which offer broad variations in surface properties, and they must also be designed in such a way as to allow meaningful interpretation of often complex responses.

Gradients seem to offer the ideal solution in terms of manufacture and sample variation. Gradients may be fabricated in 2D or 3D, however whilst 3D studies are generally considered to be more representative of the *in vivo* architecture of most biological systems, they present problems in terms of fabrication, data acquisition, and data analysis. For this reason, studies investigating cellular response to engineered surface cues are predominantly carried out in 2D *in vitro* systems. The use of semiconductor fabrication techniques, which have consistently increased in resolution since their inception[5] has allowed 2D surface patterning at length scales which now approach that of single molecules, and surpassed that of the single cell many years ago[16]. Chemical, mechanical and topographical features of a polymeric surface have all been shown to be capable of independently affecting cell behaviour and response to an engineered surface[6]. Gradients of each surface property can be fabricated independently or orthogonally to one another to create multiplexed parameter variations on a single substrate, **Figure 1.1**. Chemical gradients may range from a simple change in surface energy, to surface modification with proteins, functional molecules or peptides. Mechanical gradients are a modulation of a mechanical property such as the Young's modulus of a substrate but may also encompass a change in the mechanical link between cell and surface – such as the tethering strength of adhesive ligands[17]. Topographical gradients present a variation of surface structure, which have been shown to be a powerful manipulator of biological response. Figure 1.1 D-F depicts how gradients of surface properties may be combined into linear (D)

orthogonal (E) or radial gradients (F) which provide a means of comparing the interplay between two material factors in a biological response.

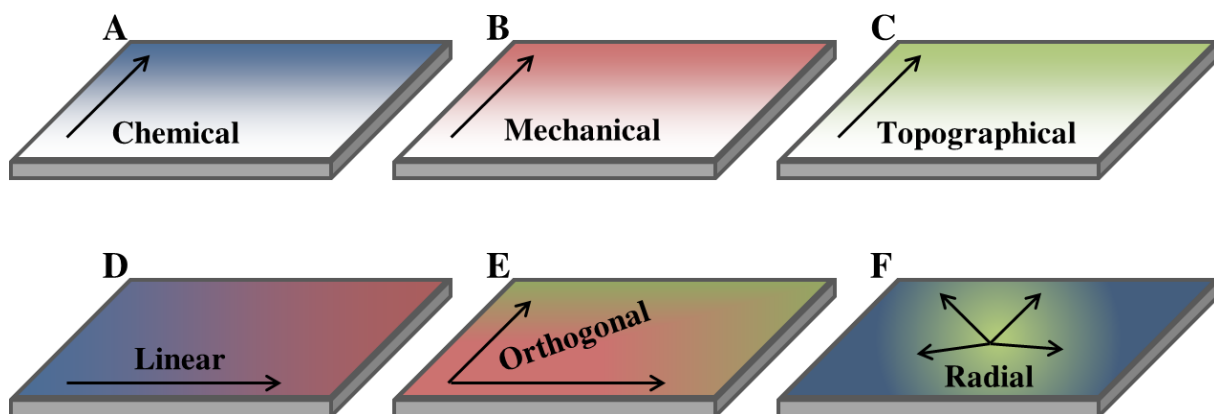


**Figure 1.1 Cells sense their environment through three main ‘columns’ of sensing: chemical, mechanical and topographical.**

Ease of fabrication, data analysis and interpretation makes the use of linear gradients most favourable. Single properties may be varied in a single direction, *Figure 1.1 A-C*, or multiple may be varied in opposite directions to create a bi-directional linear gradient, *Figure 1.1 D*. Orthogonal variation of two parameters serves to create as many possible combinations of two surface parameters as possible. Radial gradients have surface properties which change continuously from a central point outwards, and are most often used when fabrication makes use of diffusion based processes from a single point source[9], [18]. These gradients are least favourable due to the difficulties associated with mapping cell response to corresponding surface properties.

### 1.3 Gradient and array platforms

The distinction between gradient and array formats as high-content screening (HCS) methods is an important one. A gradient is a continuous variation of a feature, such as structural dimension or surface chemistry. This feature changes ‘continuously’ from one value to another, however its resolution is essentially defined by its nature – a gradient of chemistry may only change spatially in so much as its molecular structure allows. Arrays, however, are discrete variations in a surface parameter, separated or congruent on a single sample. These areas may be completely isolated from one another, or may exist on a single substrate and used in an open environment. Essentially, then, based on the property in

question, an array might have a fine enough resolution so as to offer a working resolution which is comparable with a continuous gradient.

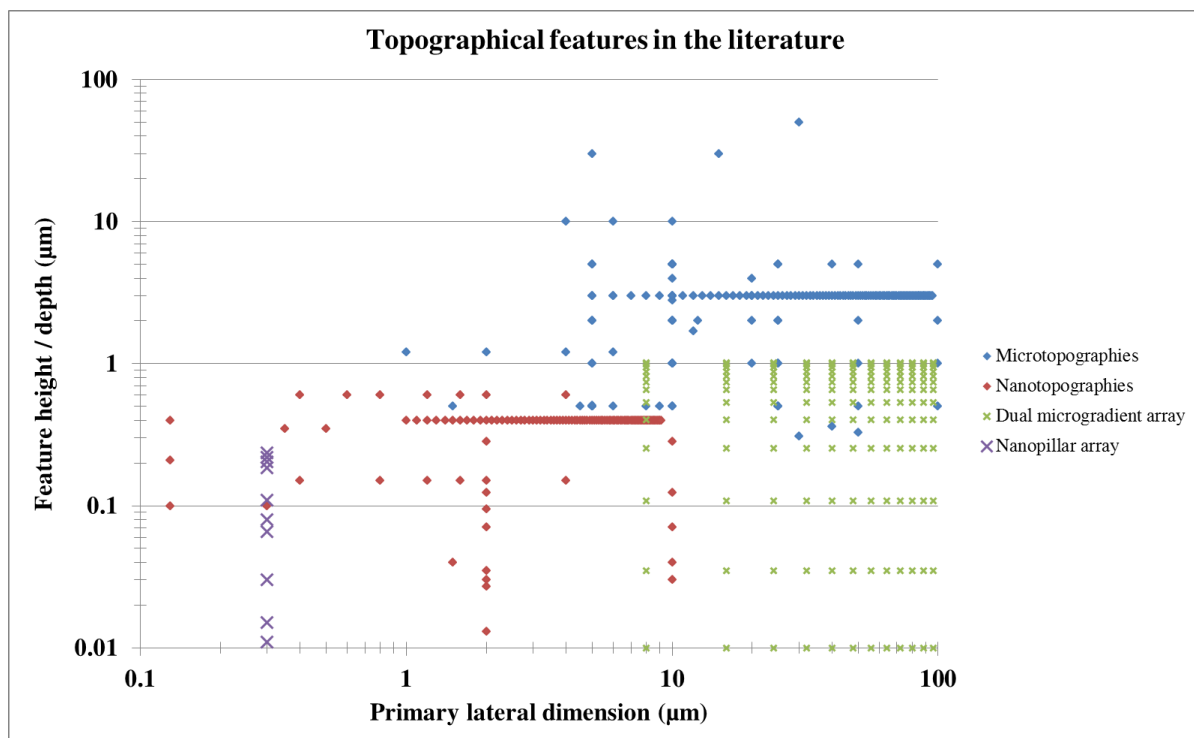


**Figure 1.2 A graphical understanding of the literature. Collated data from 25 papers with at least 50 citations which use structured polymer microtopographies[19]–[29] or nanotopographies[30]–[43] to drive cellular response. Plotted alongside these are green and purple crosses, representing the range of topographical features single gradient samples used in this thesis.**

The graphical comparison of the literature presented in Figure 1.2 focuses only on structures produced by common semiconductor fabrication techniques, so as to simplify data comparison – as each study was conducted with certain feature dimensions in terms of feature height and lateral dimensions. Similar means of comparisons may prove useful in the comparison of, for example, biomaterial polymer chain length, surface energy, or mechanical properties. In this case, each paper is generally represented by one or two single points due to the limitations of fabricating individual, homogeneous samples. Alongside these data points, publications resulting from this thesis (nanopillar array[44] and dual microgradient array[45]) which seeks to more fully explore the sample space by using gradients of topographical features. Continuous variation of nanopillar height was used to investigate the differential response of fibroblast and endothelial cells to the surface, blue[44]. This is described in **Chapter 4** of this thesis. Furthermore, the use of

dual topographical gradients – variation of microgroove depth, with orthogonally varied microgroove pitch – was demonstrated, green[45]. This is described in **Chapter 3** of this thesis. This demonstrates the ability of gradient platforms to more fully cover the sample space, rather than limiting results to a small subset of individually fabricated samples.

The key difference in understanding their use and implementation is that cells or molecules are free to move along or adsorb across a gradient platform, with cell motility yielding further information about how they interact with the surface. In an array platform, this is not possible – as cells or biomolecules interact with sample conditions which are isolated from each other, or at least separated spatially. There are benefits to each of these methods, and the impact of gradient or array formats should be carefully considered. Whether a continuous gradient or a microarray platform should be used must be taken into consideration, with *Hook et al* suggesting that gradients are most useful in optimisation of surface properties, whereas microarray platforms are preferable in the discovery of new cell-material interactions[10]. Nonetheless, gradients represent a significant improvement on discrete material tests for screening the relative change in properties such as adsorption of nanoparticles or proteins, and cell behaviour itself.

The continuous nature of gradients can present a problem in experimental design, in that artefacts such as cell migration along the gradient and cell-cell communication across it are a unique part of the biological response. Some groups choose to instead prioritise the use of microarray platforms as these provide distinct variations in material properties and are therefore produce data which is easier to interpret. These difficulties are offset by advantages such as a lower cell number and culture media usage, reduced biological variation between conditions and reduced sample material usage – these are significant advantages when working with rare or problematic biological specimens/materials.

## 1.4 Cell-surface interactions

Polymer surfaces can broadly be divided into three groups, in based on their mode of action, *Figure 1.1*. They may provide topographical cues via their micro- and nanoscale architecture. Surfaces may also provide chemical cues which may comprise biomolecules directly tethered to the surface, or a tuned wettability which modulates protein adsorption.

Finally, their mechanical properties such as stiffness and rigidity can direct biological activity. This section will present a series of emerging fabrication techniques which allow the creation of high-content gradient platforms for all three classifications, including combinations of the three.

Preparing and characterising individual samples with different properties is a time consuming and costly approach to finding polymer materials which are fit for purpose. Including multiple conditions on a single sample, in the form of either arrays or continuous gradients, can greatly expedite the characterisation of biological response to it. High-content libraries of topographical motifs have been demonstrated as powerful tools for the discovery of optimal surface topographies, with a single 2 cm × 2 cm chip containing 2176 distinct geometric patterns generated algorithmically by combining three primitive shapes, fabricated by photolithography, and applied to the analysis of human mesenchymal stromal cells to these geometric combinations[46]. *Simon and Gibson* compiled an excellent review on combinatorial approaches to biomaterial design including both array and gradient formats[8]. Numerous other review articles are available for further reading[9]–[15]. Genzer et al present a compilation of 24 innovative gradient fabrication methodologies, covering a broad range of functionalization methods for both polymeric and inorganic substrates.[9] Inorganic substrates such as silicon are often used as a substrate, which is functionalised with bioactive molecules. Whilst incompatible with direct applications in biological systems, the use of such substrates enables the screening of biological response to a variation in functionalization, which may then be translated onto compatible bulk materials[47]. In fact, the use of thin film polymer coatings alleviates the need for bulk materials to be fully compatible with prospective applications.

Besides discussing the three cues listed above, one must also address how such gradient substrates are evaluated. Commonly they are simply discretised and analysed in a similar fashion to arrayed samples or platforms. In this respect, the use of gradients may seem counterproductive, if high resolution variations in surface parameters are simply reduced to single instances of a parameter, *Figure 1.3*. The strength of parameter gradients lies in the fact that a spatially discretised gradient may include surface parameters which may not have been included in a spatially discretised array. In addition, fabrication of a wide range of surface parameters in a single process may be faster and more reliable than fabrication of individual samples.

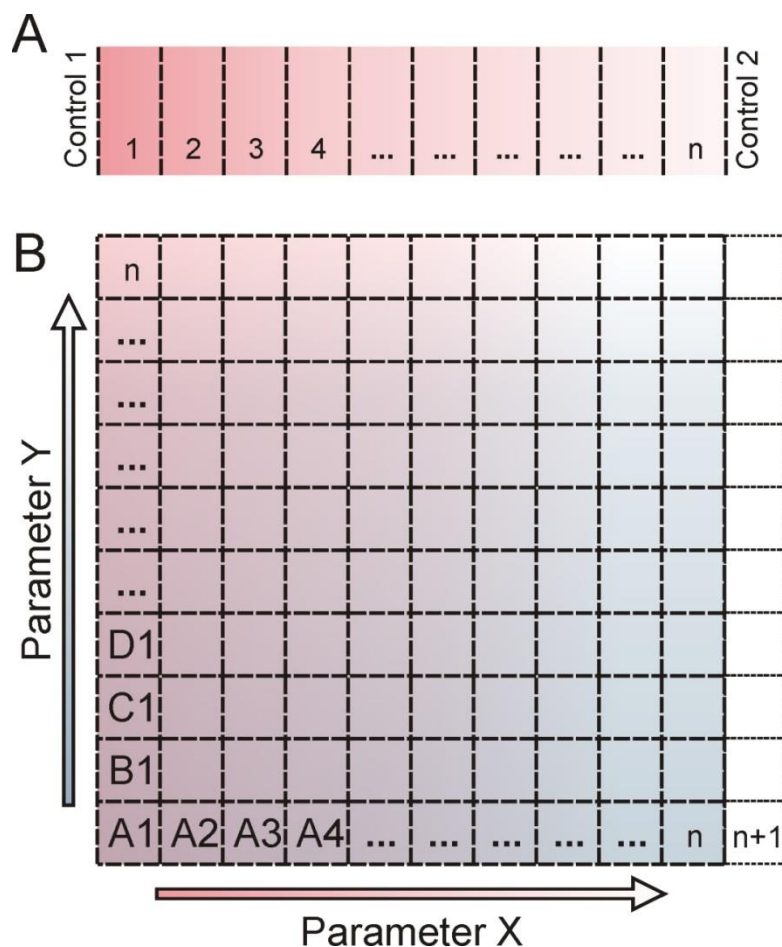


**Figure 1.3** Continuously varied surface parameters must be discretised for analysis, both for linear gradients (A) or multidimensional/orthogonal gradients (B). This yields extensive multivariate datasets which can reveal the subtle changes in cell response to variation in feature properties. The sheer complexity of the datasets can also be a hindrance, as users must choose the correct way to interpret the full dataset.

Cell culture studies have a theoretical maximum resolution of the spread of a single cell along the gradient axis. Whilst modern scanning stage microscopes and automated image analysis software makes this possible, the most common approach in the literature is to divide linear or two dimensional gradients into subunits of size  $L/n$ , where  $L$  is the total gradient length and  $n$  is the number of subunits[23]. This yields an inherent variation in a single subunit, which is often presented as a uniform value in the literature, masking underlying variation in surface properties and therefore cell response. A square imaging array, captured with a camera which has a rectangular field of view will also be disproportionately loaded in each datapoint with variation in one axis versus the other. Both linear gradients, Figure 1.3 A, and multi-dimensional gradients, Figure 1.3 B, must be divided into subunits for image analysis.

Despite increasing resolution of surface characterisation techniques allowing a finer determination of the variation of a given property along a gradient, the literature does little to address the methodologies used to segment biological results on gradients. The default spatial unit of measurement is frequently found to simply be the width of an image frame, for example images captured at 10x magnification are commonly 800  $\mu\text{m}$  – 1000  $\mu\text{m}$  in width. These images become individual datapoints, when in reality they contain an intrinsic variation across them, depending on the spatial rate of change of the underlying gradient. This results in a quantisation of the gradient in a semi-arbitrary fashion, and is particularly inflexible to tolerances in the imaging method. For example, using a motorised stage to capture congruent images across a linear or two dimensional gradient relies strongly on accurately aligning the substrate and ensuring uniformity in imaging locations across samples.

The location of controls in investigations making use of gradient surfaces also merits some consideration. A surface gradient may occupy a given sample space, with blank control regions surrounding it. Our work on gradients of nanopillar height has shown differences in cell phenotype on flat regions which are adjacent to tall nanopillars versus short nanopillars[44]. Local migratory behaviours and cell-cell interactions influence cell response at these adjacent regions, as can be seen in **Chapter 4** as an increase in cell number adjacent to one end of a linear gradient. Such effects, most prominent when comparing flat regions to a section of the gradient, must be considered as also having an influence on the patterned regions themselves. This can lead to situations whereupon scale up of a region of the gradient, after identifying it as driving a positive cellular response, a homogeneous sample covered in the same pattern does not elicit the same response. This inherent tendency for cross talk between cells on gradient platforms must be considered when interpreting results. Expansion of individual gradient points into larger homogeneous areas may not produce the same biological response, perhaps indicating that the complex gradient environment has a strong effect on the experiment.

## 1.5 Gradient fabrication

Fabrication of micro- and nanoscale topographies for biomedical engineering borrows a host of techniques from the semiconductor industry; however the materials used differ starkly. Patterns are often realised in silicon, making use of these semiconductor



processes, before transfer into biocompatible or biodegradable polymers. This has two benefits – cell interactions with engineered surfaces are analysed in materials which are more likely to be used in the body, and also many samples can be fabricated from a single high value master. Micro- and nanofabrication is an expensive pursuit, and so creating a single master from which many more substrates can be imprinted or thermoformed is vitally important. Not only has biomedical engineering made keen use of sub millimetre fabrication techniques, but biomedical engineering has also driven the development of new fabrication methods to answer biological questions, offering new insights for micro- and nanofabrication as a whole.

In most cases, uniformity and homogeneity represent the gold standard in sample fabrication. Variability between experimental materials is recognised as a source of irreproducible results, slowing and distorting studies of cell-material interactions. As a result, there has been a vast deal of effort invested in ensuring that sample fabrication schemes are consistent and reproducible. This has meant that until relatively recently, there was little work available on the controlled fabrication of non-uniform gradient substrates. There has, however, been a recent increase in the reporting of new methods for the fabrication of gradient surfaces – encompassing chemical, topographical and mechanical modifications of a range of materials[10], [48], [49]. Such samples are viable alternative to groups of individual samples as they can provide a more complete variation in a property, such as hydrophobicity. Conducting a full experiment on a single sample also reduces problems associated with biological variability between large numbers of samples.

## **1.6 High-content screening formats**

Fabrication of samples with a single surface structure or chemistry makes optimisation of these features a laborious process. Borrowing from techniques used in the pharmaceutical industry in high-throughput screening of drug compounds, there is a growing interest in creating surfaces with a high number of different parameters on a single sample, either through arraying or the use of continuous gradients. This section will describe the current state of the art, and the new fabrication methods which have been developed to address these questions.

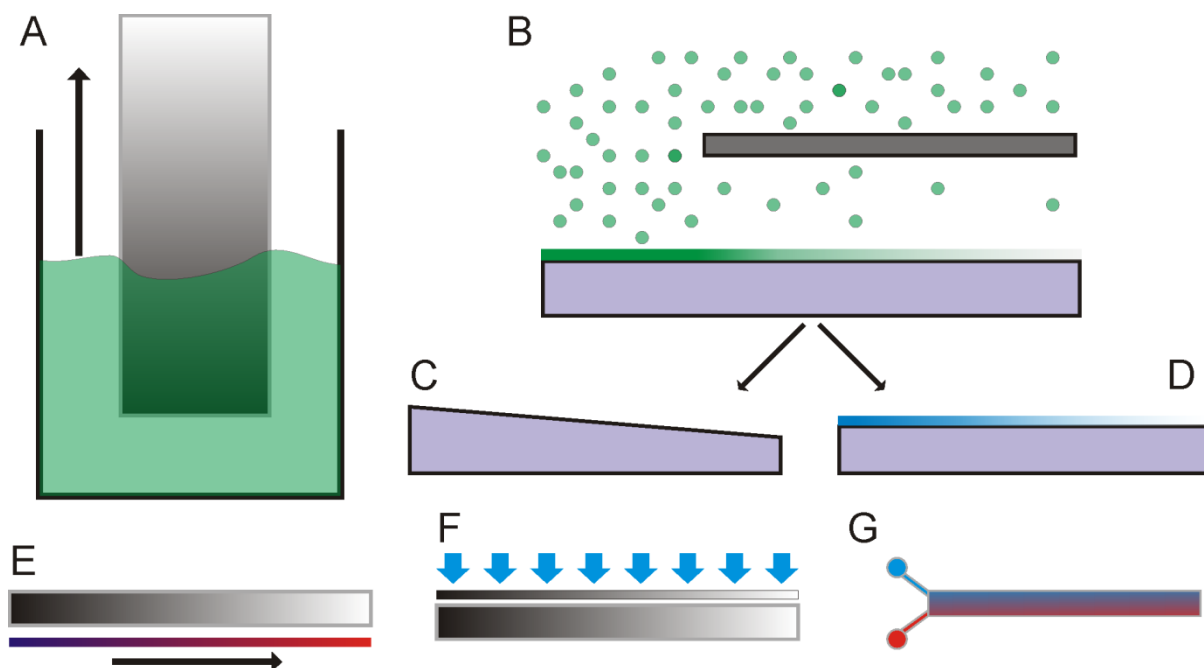


**Figure 1.4 Polymer gradient fabrication techniques.**

Figure 1.4 shows a range of gradient fabrication methodologies. A: sample immersion and removal from a solution of monomer, solvent or etchant – creating a gradient based on retraction rate. B: plasma polymerisation excited by RF glow discharge under a diffusion mask, yielding a decrease in monomer concentration into the channel which translates into a variation in deposited film thickness or chemical composition. Plasma polymer gradients may be used in their deposited state, B, as wettability gradients[50], [51], or they may be used as sacrificial masks in a dry etching process to transfer a gradient of etch depth into a substrate, C[44], [45]. Monomers with reactive groups such as carboxyl[52] or amine groups may be functionalised after deposition with biomolecules such as proteins or short chain peptides[53], D. E: polymer microspheres annealed on a temperature gradient have a continuously varying crystallinity across the sample[54]–[56]. F: greyscale lithography or localised UV irradiation can be used to deliver a gradient of light across a photoactive substrate[47], [57]. G: microfluidic mixing devices allow precise mixing of monomer solutions or suspensions of biomolecules into gradients on a surface[58]–[62].

Polymer gradients may be classified in terms of properties such as their mode of interaction with a biological system, their dimensionality, and their range (either steep or shallow). An overview of fabrication methods are presented below in Table 1.1.

	<b>Fabrication Method</b>	<b>Gradient Type</b>	<b>Length Scale</b>	<b>Speed</b>	<b>Ref</b>
<b>Chemical</b>	Plasma polymerisation under a diffusion mask	Wettability / surface functionalisation	Up to 20 mm	Moderate	[52], [63]–[66]
	Microfluidic mixing of component solutions	Surface functionalization	10 $\mu$ m to 1 mm	Slow	[58]–[62]
	Substrate movement through a vessel	Wettability / surface functionalisation	Up to 10 mm	Fast	[67]–[69]
<b>Topographical</b>	Direct write lithography	Micro- or nano	Up to 10 mm	Slow	[23]
	Grey scale lithography	Micropatterning	Up to 10 mm	Fast	[47], [57]
	Annealing on a temperature gradient	Surface roughness / feature depth	Up to 10 mm	Moderate	[55], [70]
	Plasma polymer thickness gradient, used as sacrificial etch masks	Feature depth	Up to 10 mm	Moderate	[44], [45]
<b>Mechanical</b>	Curing under UV or thermal gradients, multi-layer lithography	Elastic Modulus	Up to 10 mm	Moderate	[71], [72]
	Microfluidic mixing	Elastic Modulus	10 $\mu$ m to 1 mm	Slow	[58]

**Table 1.1 An overview of fabrication methods for gradients of surface chemistry, topography and mechanical properties. This thesis focuses on the fabrication and implementation of topographical surface gradients, but various aspects of experimental procedure and data acquisition/analysis are applicable to all gradient formats.**

## **1.7 Aims and outcomes of the thesis**

The concept of investigating biological response to engineered surfaces has been reviewed in this chapter. Considerations of experimental design, substrate fabrication, cell culture, data acquisition and data analysis/processing will be explored throughout the remainder of this thesis. This body of work offers new approaches for biomedical engineering going forward, in fabrication, microscopy and data analysis/interpretation.

The aims of this thesis are as follows:

- Develop new fabrication methodologies to open up the dimension of feature height/depth for analysis by gradient screening on gradient platforms. New semiconductor fabrication processes are required, which are characterised and repeatably demonstrated.
- In the application of surface gradients as screening platforms, experimental procedures will be standardised to ensure repeatability across experiments, users and labs. Development of new cell seeding apparatus will allow reproducibly uniform seeding across gradient/array platforms as well as for seeding of cell populations which are sensitive to local density variations.
- Use high-content imaging to develop new ways to interpret biological datasets acquired on surface gradients. Making use of modern scanning stage microscopes and open source image analysis suites this thesis will demonstrate new avenues in analysing biological response to topographical cues. These methods will have potential application in numerous other cell based studies. Furthermore, this thesis will move towards single cell resolution in gradient screening studies, with discussion on the practicalities and feasibility of such an aim.
- Finally, emerging super-resolution microscopy techniques such are used to delve deeper into the relationship between the cell and topographical cues.

## 1.8 Structure of the thesis

This thesis is arranged as a series of experimental chapters, detailing four key pieces of work conducted over the past three years, not necessarily presented in chronological order. It was common to develop new understanding and analysis skills as time passed, allowing me to re-visit old datasets and find new insight. This is particularly so in the case of **Chapter 4**, in which I returned to a published dataset to apply new multivariate analysis methods.

Each experimental chapter begins with a grey factsheet, detailing the key findings, scope of the experimental work and contributions which made it possible. This is followed by an overview/introduction to the problem at hand, and a discussion of specific methods employed in solving it. Results are then presented, and are finally followed by discussion of their meaning and prospective relevance to the field as a whole.

**Chapter 2** describes the materials and methods which were used over the course of the project, including theoretical explanations where appropriate and considerable process development has been done as part of the project. **Chapters 3 & 4** describe work which was published over the course of the project in *Small*[45] and *Nano Letters*[44] respectively. These chapters describe two key results which were not previously reported – firstly the fabrication of continuous gradients of feature depth/height on injection moulded polymer samples. Secondly, the use of machine learning for label free segmentation of co-cultured cells is shown. Both of these chapters demonstrate an increase in the potential yield of a single experiment – allowing multiple cell types and a range of surface properties to be investigated on a single sample, including enhanced information such as the interplay between two cell types as well as their individual response.

**Chapter 5** details the invention of a new device for use in cell culture studies, addressing a fundamental problem which stems from variability between users. The concept of the device is described, along with design considerations for usability and experimental proof of efficacy. Subsequently, the effect of improved seeding density on the differentiation of stem cells is investigated. The final experimental Chapter utilises emerging microscopy techniques to further investigate the behaviour of cells on engineered substrates.

Finally, **Chapter 7** draws conclusions and outlook, assessing the work completed and its likely impact on the wider research community – along with a critical appraisal of any omissions or shortcomings in the work including suggestions for future work.

## 2 Materials & methods

This chapter describes the core methodologies which have been used throughout the thesis. Further methods developed for, or specific to, the experimental work will be included in **Chapters 3-6**.

### 2.1 Micro- and nanofabrication

Micro- and nanofabrication techniques employed by the semiconductor industry have found prolific use in biomedical engineering, and are now near ubiquitous in some form or another in labs across the world[5], [16]. The ability to fabricate structures on the same length scale as biological systems allows us to directly interface with and manipulate them. There are, however, specific challenges to be addressed in the way fabrication techniques are deployed. As compared to semiconductor research, i.e. fabricating a small number of novel transistor designs followed by testing of electrical characteristics, fabrication for biomedical studies requires large sample areas and sample volumes. Furthermore, biocompatible polymeric materials are preferred over silicon, meaning that micro- and nanopatterns must be transferred from silicon to polymer for application.

The basic fabrication paradigm employed in this thesis was:

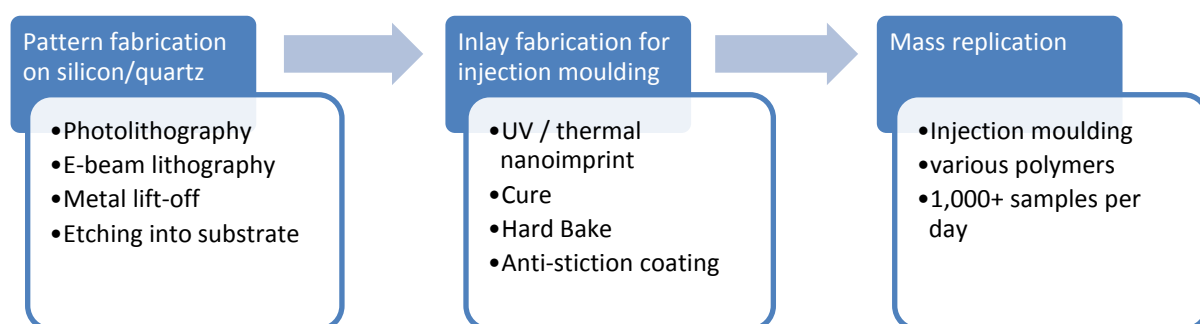


**Figure 2.1** The fabrication flow begins with the lithographic definition of a pattern on a silicon/quartz substrate. Pattern transfer by reactive ion etching is carried out with soft (PMMA), hard (NiCr) and novel (ppHex) etch masks. An inlay for injection moulding is created by imprinting the patterned master substrate into an SU8 layer on a polymeric substrate (Cirlex™). This is used as a die for mass replication by injection moulding.

All substrates were initially prepared by the same process, with the standard size used being a 25 mm x 25 mm piece. Silicon substrates (*PI-KEM, UK*) were cleaved from 4-inch wafers using a wafer scribe tool. Quartz substrates (*Newcastle Optical, UK*) were purchased pre-cut. Substrates were thoroughly cleaned by 5 min stepwise sonication in Opticlear, acetone, methanol and isopropanol before blow drying with nitrogen. A dehydration bake at 180°C for 2 h minimum ensured the surface was free from moisture before further processing.

More detailed information on the micro- and nanofabrication processes used to create high-content screening surfaces is presented in **Chapters 3 &4** respectively.

## 2.2 Injection moulding

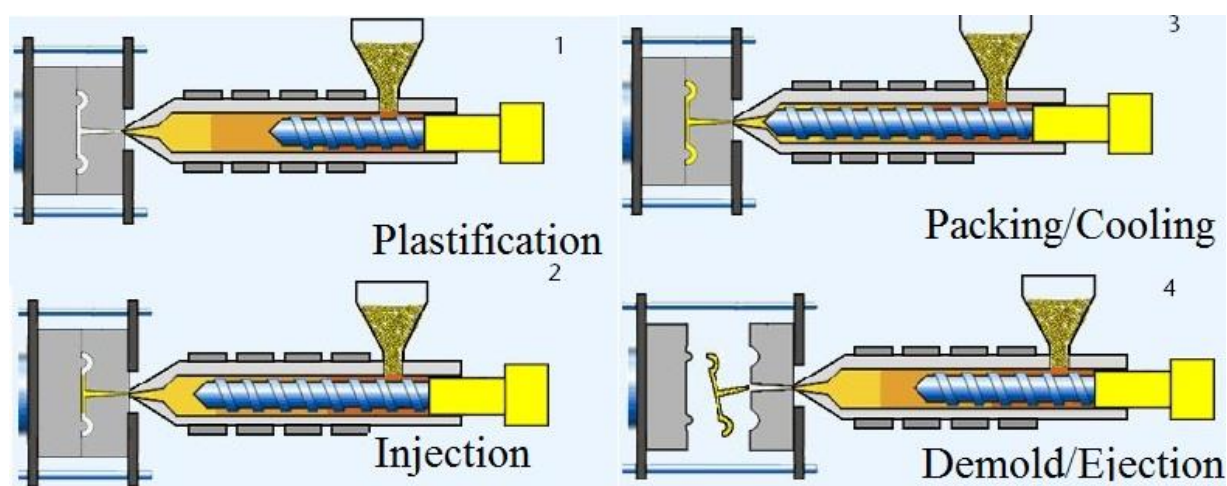


**Figure 2.2** Illustration of an injection moulding machine configuration and standard operation process. Polymer beads are melted (1) and the polymer injected to fill a cavity (2) which is packed at high pressure and allowed to cool (3) before being opened and the part ejected (4). Image adapted from[73].

High volume fabrication of plastic parts by injection moulding has transformed the design and manufacture of plastic commodity parts. Its ability to replicate surface structure down to the nanometre level in biocompatible polymers makes it an ideal process for biomedical engineering. Micro- and nanopatterned substrates described in this thesis were fabricated in polycarbonate by injection moulding. Whilst the injection moulding process is most commonly associated with mass replication of identical parts, i.e. optical media, methods have been developed to allow for prototyping of a multitude of patterned surfaces[74]. Optical media are produced using a nickel shim insert, allowing a single tool

to produce a variety of parts with a similar shape but differing surface structure. Nickel shims can be readily created from semiconductor substrate materials such as silicon, for both injection moulding and nanoimprint applications.

Whilst there are numerous types of injection moulding machines, Figure 2.2, their operation follows a broadly similar process as follows. Plastic pellets are placed in the hopper, falling through a cooled feed throat into a heated barrel. A linearly actuated screw turns, pushing the pellets along the screw. These pellets melt from a combination of barrel heating and shear heating of the material as the screw tapers towards the nozzle. The injection chamber at the head of the screw then fills with molten polymer which is well above its glass transition temperature and therefore readily flowable. The tool is clamped shut, sealing the cavity, and the screw is pushed forward by either by hydraulic or electrical actuation. The cavity is filled, and the screw is drawn back to fill the injection chamber with another polymer shot. After a period of cooling, the mould is opened, and ejector pins move forward to release the part. These are retracted, and the process is repeated until the production target is met.

<b>Material</b>	<b>Melt (°C) Nozzle/z1/z2/z3</b>	<b>Tool (°C)</b>	<b>Injection speed (cm<sup>3</sup>s<sup>-1</sup>)</b>	<b>Holding pressure (bar)</b>	<b>Cooling time (s)</b>
<b>Polycarbonate OD2015</b>	280/270/260/250	80	50	1000	5
<b>Polystyrene Total 1810</b>	260/250/240/230	40-60	50	1000	5

**Table 2.1 Standard parameters for injection moulding two materials used in this thesis**

### **2.2.1 Mass replication of polymeric substrates**

Micro- and nanopatterned samples were replicated in polycarbonate (Makrolon OD2015) by injection moulding (Victory 28, Engel GmbH). The polymer pellets were dried for three hours under vacuum at 110°C prior to use, and processed with a melt temp of 280°C and a tool temp of 80°C. To date over 1,000 samples of both the micro- and nanopattern gradients, discussed in **Chapters 3 & 4** of this thesis respectively, have been moulded with no visible evidence of inlay degradation. It should be noted that in the work of Dr John Stormonth-Darling creating more challenging nanostructures there was a build-up of polymer in the inlay which was removed periodically in acetone.[75]



## 2.3 Cell culture

Multiple cell culture systems were used over the course of this PhD, including 6 cell types in monoculture on patterned surfaces, as well as co-cultures. Immortalised cell lines were preferred to primary cultures due to their availability and relative ease of use in preliminary screening studies.

Cell Type	Description	Media	Studies/usage
<b>hTERT-BJ1</b>	Human fibroblast cell line	DMEM	Response to nanopillar gradient Response to microgroove gradient Uniform cell seeding
<b>LE2</b>	Murine lung capillary endothelial cell line	HAMS	Nanopillar gradient Microgroove gradient Uniform cell seeding
<b>MDCK</b>	Canine epithelial cell line	DMEM	Response to microgroove gradient
<b>MG63</b>	Human Osteosarcoma cell line	DMEM	Machine learning control
<b>MEF</b>	Mouse embryonic fibroblast cell line	DMEM	Super-resolution microscopy
<b>SA121*</b>	Human embryonic stem cells (hES)	DEF-CS™ 500	Uniform cell seeding

**Table 2.2 Cell types used throughout this thesis. \*Work using SA121 cells was conducted by a collaborator in Denmark (cell culture & imaging), with data analysis and presentation forming part of this thesis.**

Cell lines were obtained from existing low passage stocks within the Centre for Cell Engineering, University of Glasgow, and from the Sheetz Lab, Columbia University. Cell lines were cultured up to passage 25 before being discarded and fresh aliquots revived. Studies carried out in collaboration with Camilla Rasmussen, a PhD student and collaborator from Denmark, were done with commercially acquired human embryonic stem cells which were differentiated towards the pancreatic endoderm by a proprietary protocol (*Novo Nordisk & DTU, Denmark*).

Cells were seeded onto injection moulded parts using uniform cell seeder (UCS) devices and allowed to settle in the flow hood for 10 min to prevent fluid movement redistributing cells over the topography. The UCS device and its operation is described in detail in **Chapter 5**. Culture vessels were then moved to the incubator to allow full attachment of cells to the surface. After 1 hour, 4 ml of fresh media was added to each well and the UCS removed. Substrates were incubated at 37°C in 5% CO<sub>2</sub> atmosphere. Media was changed after 24 h, and every 48 h thereafter until the termination of experiments. Media formulations are included in the appendices.

## 2.4 Microscopy

A variety of microscopy techniques ranging in resolution and complexity were used in this thesis to screen cellular response to micro- and nanostructured surfaces. Over the course of the project, the resolution at which cell-surface interactions were investigated was improved from initial experiments using flatbed scanners which were crudely capable of detecting a single cell, to emerging super-resolution microscopy techniques with resolution approaching the single molecule level.

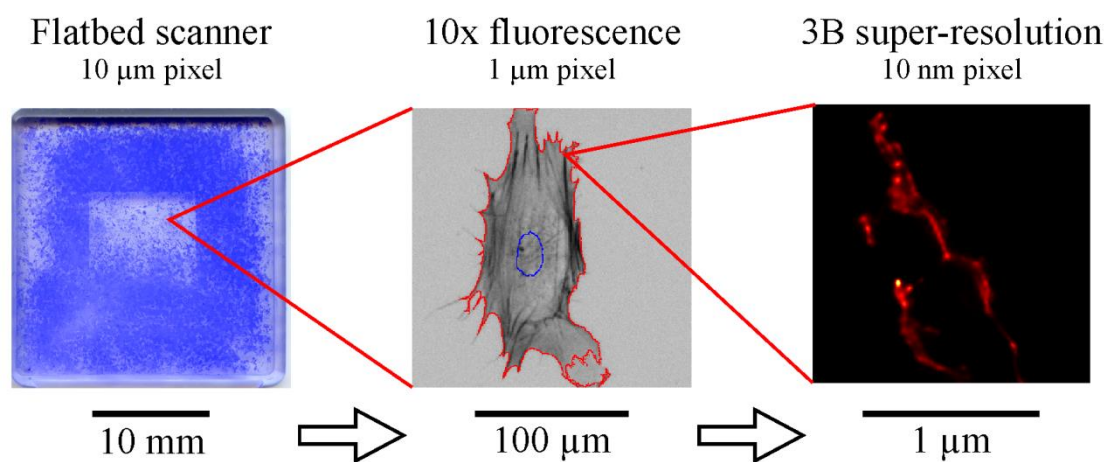


**Figure 2.3** Cell response to nanostructured surfaces was interrogated over a range of length scales – revealing not only the behaviour of whole cell populations, but also changes in cell morphology within such populations, and also the structure of subcellular components such as focal adhesions.

To interrogate the cellular response to micro- and nanotopographies produced in this PhD, advanced microscopy techniques were used rather than biochemical analysis. Microscopy is the method of choice as it allows correlation of individual cell phenotype

with the underlying micro- or nanotopography. In the case of surface gradients, a motorised stage was used to capture large areas of the samples. Emerging super-resolution microscopy techniques were also employed to image cellular interactions with nanotopographies – with resolution approaching the single molecular level and showing a heterogeneity of cell response to nanostructured surfaces at the sub-micron level.

### 2.4.1 Immunohistochemistry

After culture, samples were washed twice in 1x PBS followed by fixation in 4% paraformaldehyde at 37°C for 10 min. After fixation they were rinsed once more in 1x PBS. Cells were permeabilized with a 0.1% Triton-X 100™ solution for 10 min at 4°C and blocked in 1% bovine serum for a further 1 h at 4°C to reduce non-specific binding. Substrates were then incubated with primary antibodies (i.e. goat anti paxillin diluted 1:500) overnight at 4°C. Substrates were washed three times with 1% Tween-20 on shaker set to slow swirl for 5 min, followed by incubation at 4°C with a secondary antibody (i.e. Alexa-488 anti-goat diluted 1:500) and a cytoskeletal marker (i.e. rhodamine-phalloidin diluted 1:1000). Substrates were washed three more times, and mounted by inverting onto suitably sized #0 coverslips using a mounting media containing DAPI to further stain nuclear DNA.

The full staining protocol is included as an appendix. All immunohistochemistry was carried out using the ‘staining buffer’ described in the appendix, with special thanks to Dr Thomas Iskratch (*Columbia University, New York*) for the formulation. Reagents were obtained from *Sigma Aldrich*, primary antibodies obtained from *Abcam*, and fluorescent probes from *Life Technologies*.

This immunostaining protocol was found to be effective for the majority of labelling experiments conducted over the course of this PhD. The actin cytoskeleton was labelled using both rhodamine-phalloidin and also alexa-488 conjugated phalloidin. Antibodies for focal adhesion component proteins such as vinculin (*Invitrogen*: 700062) and paxillin (*Invitrogen*: 44-1022G) were also used successfully with this protocol. Immunostaining of another focal adhesion protein of interest, talin proved more difficult, with multiple experiments failing despite variation of fixation and staining parameters including methanol fixation. Successful staining has been reported in the literature[76],

however it is often noted that immunolabelling of talin can be difficult, with even gentle fixation cross linking focal adhesion plaques and preventing antibody binding to the target epitope. Failure to develop a working protocol within the time available undoubtedly left some interesting avenues of investigation unchecked.

## 2.4.2 Correlative microscopy

Registration of fluorescent images and SEM micrographs was carried out by adding fiducial markers to the sample after fixation at a density of  $5 \times 10^6 \text{ cm}^{-2}$ . This gave approximately 10-15 fiducial markers within the  $20 \mu\text{m} \times 20 \mu\text{m}$  field of view of the imaging microscope. TetraSpeck microspheres (*Life Technologies*: T-7279) with a diameter of  $0.1 \mu\text{m}$  were incubated at room temperature on the sample, readily adsorbing to both the polymer surface and also the cell membrane. This adsorption appeared to be strong enough to withstand sample processing for both immunofluorescent and SEM imaging. Some beads were visibly lost between imaging modes, however sufficient beads remained to allow for image registration. Other methods are reported in the literature, such as the use of gold nanoparticles to register images[77] or fiducial free methods, transforming images into sparse representation models for registration[78].

## 2.5 High-content image processing

Automated image analysis software has been used extensively throughout this PhD to measure and quantify cell response and distribution on micro- and nanostructured surfaces. New methods have been developed which make use of multivariate datasets which describe cell morphology on micro- and nanostructured surfaces.

Starting with a dataset comprising three channel images of, for example, the nucleus, cytoskeleton and a protein/marker of interest, the location and shape of individual cells can be determined by stepwise detection. There is a reason this combination of images works so well, and it is to do with the levels of contrast available in defining the structures of interest which are being measured against the background. With a robust method of distinguishing a cell and its components from both the background and neighbouring cells, a multitude of characteristics of the cell can be measured. Microscopy data contains a wealth of information which is rarely exploited in full by researchers –

choosing to collect qualitative data, when in fact a rich multivariate dataset can be generated in a relatively similar timeframe.

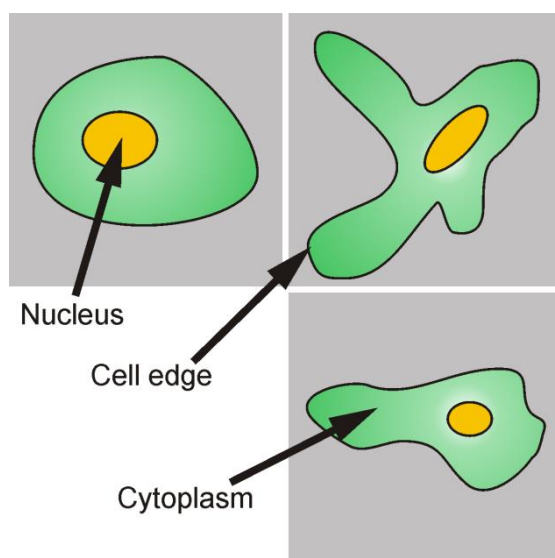


**Figure 2.4 Structure of eukaryotic cells**

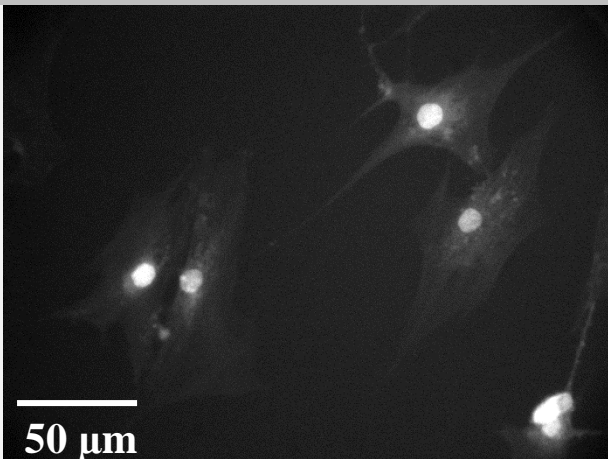
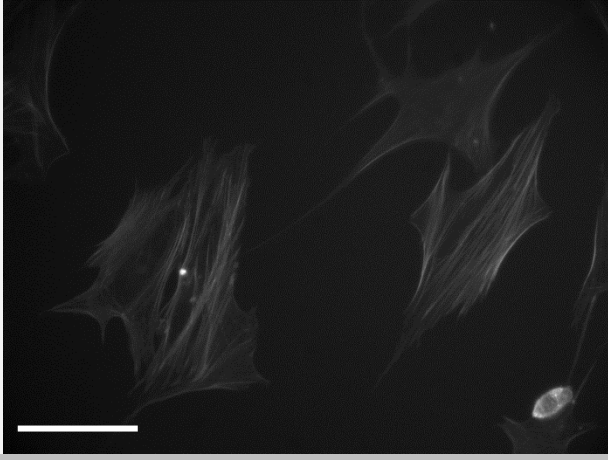
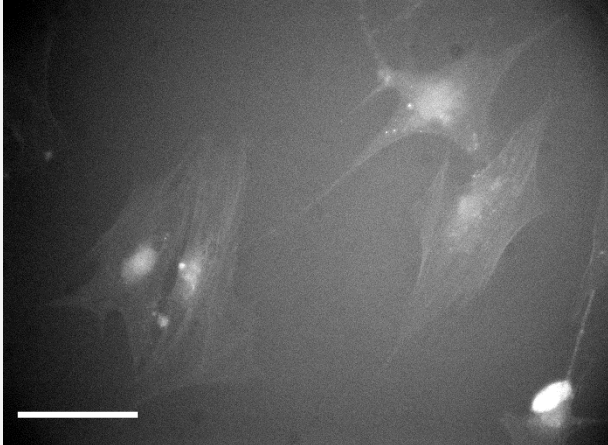
The biology of eukaryotic cells fortuitously lends itself to the detection of individual cells in microscopy data. The various subcellular compartments provide distinct objects within the cell which stand out clearly from the background, i.e. nuclei which can be easily labelled by staining of nuclear DNA. These compartments can be labelled and then detected – essentially providing a coordinate within each individual cell. It is then simply a case of expanding this starting object outwards to detect the edge of the cell by thresholding

another image, in which a cellular structure which covers the majority of the cell is stained. The actin network of the cell cytoskeleton is an ideal candidate, as it extends almost completely to the cell edge. After detection of the full cell body measurements can be made that describe both the structure of these cellular components and also the presence of various protein markers within the cell in terms of fluorescent intensity.

The CellProfiler software package allows the sequential execution of these steps, automatically pairing image sets together, detecting objects, making measurements and exporting data. Whilst the CellProfiler development team has created a versatile package which can be used to extract meaningful data from even poor quality images, every effort should be taken to capture high quality microscopy data. Confocal microscopy and TIRF systems provide excellent images with very little background interference – making detection of cell and object edges a relatively simple task. If only standard wide field immunofluorescence techniques are available, then every care should be taken to correctly calibrate and setup the microscope. This means alignment of the light source to provide a flat field illumination, minimising parasitic background light and contaminant particles on the sample (which often autofluoresce and interfere with measurements), and also maintaining consistent exposure and gain levels on the image capture device to limit noise in the images.

### 2.5.1 Image processing example

In this example, a long term culture of hMSCs on polymer substrates has culminated in their fixation and staining for a protein of interest, CD271, which is indicative of stem cell phenotype. This data was reported in a journal article[79].

	<p style="text-align: center;"><b>DNA</b> <i>Nucleus</i></p> <p>This stain brightly illuminates the cell nucleus, providing an easy to threshold point within each cell.</p> <p>This image shows a high level of background illumination, however the nuclei can still be detected against this with ease</p>
	<p style="text-align: center;"><b>F-Actin</b> <i>Cytoskeleton</i></p> <p>This stain gives broad definition to the cell, whilst also providing useful information on the structure of the cytoskeleton.</p> <p>Excellent signal to noise ratio against the background makes this image simple to threshold.</p>
	<p style="text-align: center;"><b>CD271</b> <i>Protein of Interest</i></p> <p>Various intercellular proteins may be labelled, and their prevalence in a sample quantified in terms of fluorescent intensity.</p> <p>The low signal strength in this image makes standalone quantification near impossible.</p>

**Table 2.3** The properties of individual fluorescent channels determine how they are processed

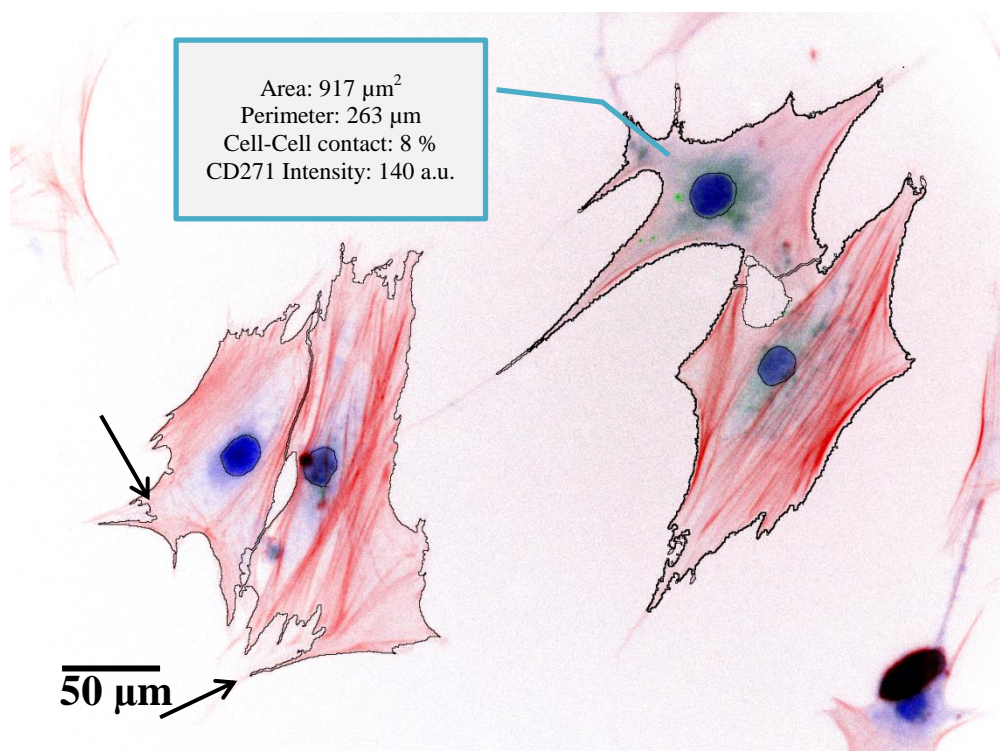


**Figure 2.5 Automated detection of cells in fluorescent micrographs. Cell nucleus and body are detected, and outlined in white. This allows for detailed measurement of cell features and shape, including the intensity of protein staining within the cell area. Arrows indicate inaccurate detection of the cell perimeter. In this case, thin filopodial protrusions have been excluded from detection as part of the cell body due to the processing settings.**

After detection of both nuclei and the cell body, outlines can be drawn to assist with calibration and confirmation of appropriate detection. It is evident that this is a powerful software tool. Nuclei have been successfully identified despite a challenging source image, and the location of the nucleus has subsequently been used as a seed point to detect the cell body using the cytoskeletal image. This enables remarkably accurate dividing lines to be drawn between objects, if the program modules are properly configured to recognise the motifs present when cells meet, and also to cope with the cell edge in instances where there is no distinct change in intensity.

Creating a pipeline which can successfully handle the different types of thresholding requirement, even within a single image, is vitally important in maximising the data generating potential of CellProfiler. The faint levels of CD271 staining in this image set are measured as a function of pixel intensity within the cell. This creates data which is immediately more relevant when compared to global image averages, as it can be used to define protein expression per cell, and to remove user bias introduced during



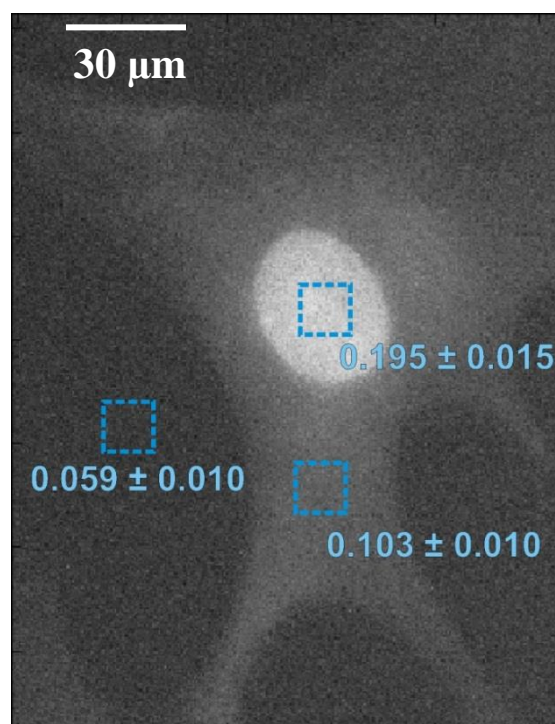
microscopy. In terms of the efficacy of automated detection and measurement, the thin filopodial protrusions which have not been detected are a missed opportunity (Figure 2.5, arrows). The frequency, size and direction of such protrusions may be an integral part of the phenotype of a given cell type under a given experimental condition.

The question of user bias is an important one. It undoubtedly manifests itself in any microscopy study where image acquisition is not automated, as the user is faced with the choice of how to frame cells within an image. As such, studies based solely on microscopy should be viewed with a critical eye, and perhaps considered as ‘studies of the good looking cells’ rather than as being representative of the full picture.

### 2.5.2 Common settings, issues & solutions

Images are segmented by thresholding based on pixel intensity values – i.e. a crude value is taken, and all pixels with a higher intensity are classified as within an object, and all pixels below the threshold are classified as outside it.

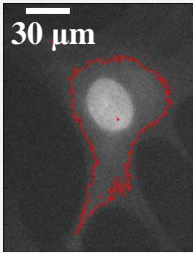
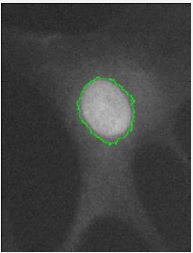
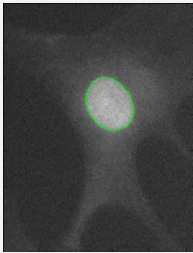
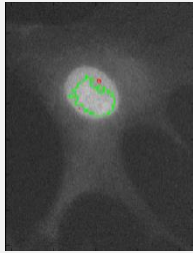
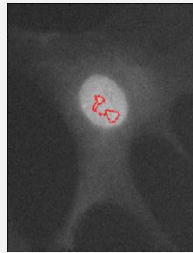
Figure 2.5 shows an image of a cell which has been stained for nuclear DNA, and imaged using a fluorescent microscope. We can see the higher intensity of the nucleus, along with the background intensity of the cell and the image background itself. These regions of the image have distinct intensity values, as shown by computing the average intensity of three areas of interest around the cell. When this image is thresholded, based on the average intensity in the nucleus being 0.195, and the surrounding cellular background having an average intensity of 0.103 – a threshold value between these two should allow detection of the nuclear structure.



**Figure 2.6 Both subcellular structures and the cell body itself can be automatically extracted from an image by thresholding.**



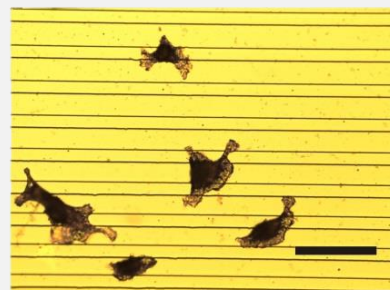
Table 2.4 shows the impact of the thresholding value on detection of subcellular objects, and gives an indication of how to determine whether the chosen threshold is being calculated as too lenient, or too strict. A lenient threshold is characterised by the inclusion of excess area around the object in a jagged pattern, as nearby pixels with a high intensity are mistakenly included in the object. A strict threshold results in an underestimation of the object perimeter, outlining regions of marginally higher intensity within the target object itself.

Very Lenient	Lenient	Correct	Strict	Very Strict
				
Threshold 0.100	Threshold 0.125	Threshold 0.150	Threshold 0.188	Threshold 0.200
Correction Factor 0.8	Correction Factor 1	Correction Factor 1.2	Correction Factor 1.5	Correction Factor 1.6

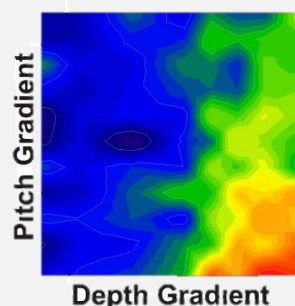
**Table 2.4** Objects are detected by setting an intensity threshold after rescaling images from 0 to 1. Poor detection can lead to spurious measurements of, for example, nuclear size/shape as shown above.

### 3 Fabricating continuous gradients of feature depth

**Background:** Discovery of new structured surfaces for biomedical applications is often constrained by the inability to fabricate arrays or gradients of feature depth on a single sample. Analysing cell response at a single depth leaves potential targets unexplored. There is a need to expand the number of topographical motifs on a single sample to speed up discovery and characterisation.



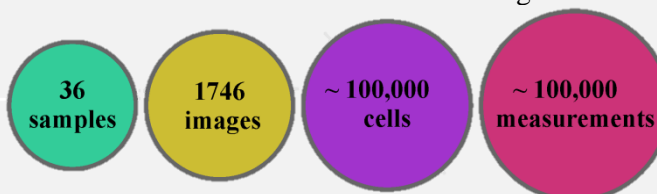
**Results:** Plasma polymer films are deposited and etched as a unique method of fabricating continuous gradients of feature depth. Both deposition and etching processes are optimised, with **continuous gradients from flat up to a depth of 5  $\mu\text{m}$**  demonstrated with a process capable of ranges over 100  $\mu\text{m}$ . A polymeric microgrooved substrate with **orthogonal variation of pitch and depth is created**, presenting a wide variation of groove dimensions on a single substrate. Groove pitch ranges from 5  $\mu\text{m}$  to 100  $\mu\text{m}$ , whilst groove depth progresses from flat to 1  $\mu\text{m}$ . Fibroblast alignment increased rapidly for groove depths over 500 nm, and was highest when these grooves were closer together. Endothelial cells did not align unless constrained by grooves on either side, but appeared to proliferate rapidly in a ‘sweet spot’ of depth and pitch to form a confluent layer.



**Conclusions:** The depth and pitch of microgrooves has a distinct effect on the behaviour of different cell types. Combinations of depth and height were identified which could either drive fibroblast alignment or increase endothelial/epithelial growth into a confluent monolayer. The conditions required for fibroblast alignment were distinct to those required for endothelial cell alignment – suggesting different mechanisms are at play.

#### Experiments:

Length scale: microtopographies  
 Cell type: human fibroblast (hTERT-BJ1), rat endothelial (LE2), canine epithelial (MDCK)  
 Analysis: flatbed scanner & 10x immunofluorescence images



#### Output:

This work was published in *Small* [45].

### 3.1 Introduction

Lithographic techniques developed for the semiconductor industry are the subject of painstaking development to minimise non-uniformity across many thousands of wafers. This limits the tools which are available for the creation of surfaces to explore the full parameter space when investigating cell response to structured surfaces. Creating many individual samples, each with a separate topography, simplifies fabrication but complicates biological experiments. For example, in the creation of microgrooved substrates to study the alignment of fibroblast cells, which depth should be chosen? It is relatively simple to create many different lateral groove dimensions on a single sample though direct write lithography, but there is no such fabrication route for variation in groove depth whilst retaining the lateral resolution.[80]–[82]

Exploration of the final dimension has been approached by creating a variation in feature depth by annealing nanoimprinted structures on a temperature gradient[83], however such techniques require a trade-off in spatial resolution as features are rounded off due to surface tension. Screening cellular response to a continuous change in a surface parameter, i.e. a gradient, allows the full sample space between two values to be explored in what is effectively a parametric sweep. Gradients of surface roughness,[84] chemistry,[85] ligand density[47] and wettability[66] have all been demonstrated in the search for optimal surface parameters, and can often be fabricated in a single deposition step.[64], [86] Spatial density can be increased still further by the positioning of two gradients of distinct surface features orthogonally to one another, presenting a two dimensional variation in surface properties, such as a variation in chemistry across a substrate with grooves of varying pitch.[21] Cell adhesion and orientation can then be evaluated across the whole sample, creating heat maps which describe the interplay and individual influence of two surface parameters on cellular response.

Despite the documented effect of feature depth on cellular response,[27], [87], [88] there have been few reports of the application of a continuous gradient of depth in the optimisation of surface parameters.[83] To that end, a new fabrication technique was developed which enables the creation of continuous gradients of depth by sacrificial etching a plasma polymerised hexane (ppHex) film. This work was done with a great deal of help from Dr Rasmus H Pedersen, who was responsible for building the plasma

polymerisation apparatus before the beginning on this project. Plasma polymerisation of organic monomer species[89] allows the deposition of conformal thin films on pre-structured topographies by RF excitation of gas phase molecules. A diffusion mask can be placed above the substrate, depositing a polymer film with a variation in thickness under the mask,[64] providing a simple alternative to previously demonstrated techniques which make use of mechanical substrate manipulation to deposit plasma polymer gradients.[47] The high level of cross-linking and conformal nature of these films make them ideal for use as a sacrificial mask in a reactive ion etching (RIE) process, transferring the film thickness gradient into a truly analogue variation in groove depth across a silicon substrate.

Etching through a plasma polymerised gradient film deposited over a predefined hard etch mask sacrifices none of the nanometre scale resolution which is available through modern lithography techniques in the generation of a depth/height gradient.

### 3.1.1 Microgroove topographies

Micro- and nanogrooved surfaces have been investigated at great length in the literature. Constriction of cell morphology to a single axis drives alignment, which has numerous functional applications. Various tissues exhibit *in vivo* alignment of cells to form the tissue superstructure, with such macroscale organisation conferring functional properties such as tensile strength to human tissues such as tendons and also playing a vital role in muscle movement. As a result, there is a strong focus in the literature on creating tissue engineering constructs which confer such structural organisation on cells for *in vivo* use [80], [90]–[92]. The binary nature of previous studies (i.e. screening a single subset of discrete topographies at a time), is not the fault of the imagination of researchers, but rather the limitations of fabrication methodologies available to them. As structuring surfaces at the micro- and nanoscale to create highly ordered grooved substrates depends chiefly on semiconductor fabrication processes, there are avenues of exploration which are not yet available as industry demands homogeneous fabrication processed rather than the development of processes for heterogeneous sample fabrication.

Chiefly, one must consider that whilst surface structure is limited to a single face of a surface, it is by no means simply two dimensional. The depth/height of topographical motifs fabricated on a structure must be considered to be equally as important as the first

two. However, whilst direct write lithography techniques make it straightforward (if time consuming) to fabricate a wide range of surface features on a single sample in the first two dimensions, there is no simple means of fabricating a range of dimensions in the third. Semiconductor fabrication processes are painstakingly designed with uniformity in height of paramount concern across full wafer areas – there has been little development in fabricating a range of feature heights alongside one another.

If we are to fabricate truly inclusive screening platforms to optimise surface features for a given application, new methods for the fabrication of gradients/arrays of feature depth are required. Some progress has been made in the fabrication of discrete arrays encompassing multiple values of feature height by combining a series of lithography and etching steps – producing 16 discrete values of feature height in only 5 etch steps [93]. This method, however, is still limited in producing discrete height values and eschewing the possible feature dimensions in-between. To that end, the fabrication of screening platforms in this thesis has made use of plasma polymer gradients to produce truly continuous variation in feature height/depth. This ensures that the full parameter space between two height values may be explored on a single surface.

## 3.2 Methods

### 3.2.1 Photolithography

A microgroove pattern consisting of 5  $\mu\text{m}$  ridges with increasing pitch across a 10 mm area was defined by photolithography. A primer (*Chestech MS Primer (HMDS)*) was applied to substrates before spinning photoresist to aid adhesion. Primer was spun for 30 s at 4000 rpm, followed immediately by spin coating photoresist for 30 s at 4000 rpm and a soft bake at 90°C for 30 min. Using S1818 photoresist this gives a 1.8  $\mu\text{m}$  film. A chrome mask, defining a grating gradient pattern of 5  $\mu\text{m}$  lines of increasing pitch was used to pattern the resist in a Karl Suss MA6 mask aligner for 4.8s. The pattern was developed for 75 s in a 50:50 mixture of Microposit developer : water. The hard etch mask was deposited by evaporation of 50 nm Nickel:Chromium alloy (NiCr), and subsequent lift off in an acetone soak for at least 2 h at 50°C, followed by a brief sonication, IPA rinse and blow dry in nitrogen.

### 3.2.2 Injection moulding inlay fabrication

Polymer inlays were created for mass replication of micro- and nanotopographies by injection moulding, Figure 3.1. Firstly, fluorination of the silicon stamp to prevent sticking is performed by vapour deposition of Trichloro(1H,1H,2H,2H-perfluorooctyl)silane (TPFS) as described previously by the group[74]. A Cirlex™ piece coated with 30  $\mu\text{m}$  of SU8 3050 by a standard spin recipe was placed on top and the two sandwiched together at 95°C for 15 min, imprinting the inverse pattern into the SU8. The imprinted stack was cooled to 45°C and separated with a razor blade before curing of the SU8 by UV flood exposure for 1 min using the MA6 mask aligner and post exposure bake at 95°C for 10 min. After imprinting, Cirlex™ inlays were hard baked at 190°C for two hours to fully harden the SU-8 layer.[75]

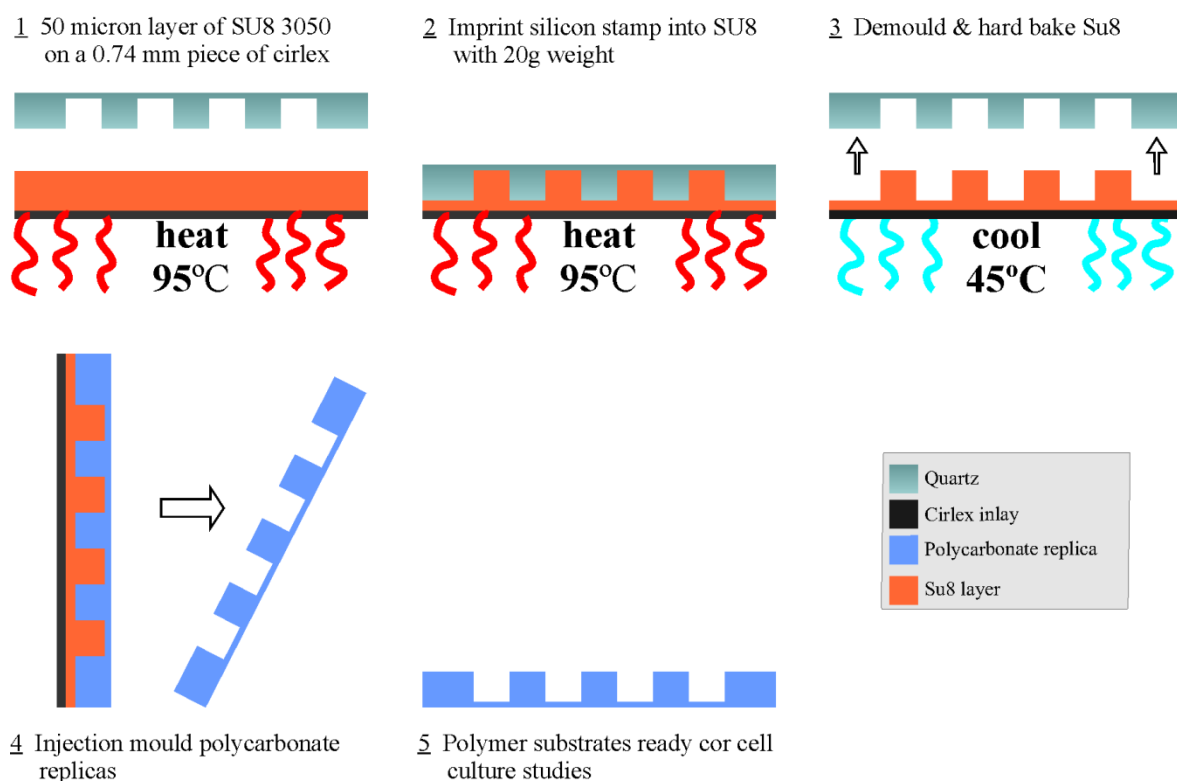


**Figure 3.1 Thermal imprint process for transfer of micropatterns in silicon to an inlay for replication by injection moulding.**

### 3.2.3 Cell culture

Cells were seeded on the dual gradient topographies at a density of 4,000 cells  $\text{cm}^{-2}$  using the uniform cell seeder device described in **Chapter 5** to ensure that the initial distribution of cells across the surface was homogeneous. This allowed for samples to simply be fixed after 72h and the final distribution of cells analysed. Cells were cultured in appropriate media as described in the relevant section of **Chapter 2**.

### 3.2.4 Data acquisition – large area imaging

Initial analysis of gradient substrates took a global approach, using a flatbed scanner to capture images of fixed samples after staining with Coomassie blue. Coomassie blue is a triphenylmethane dye which is used extensively in biochemistry to stain proteins. When applied to fixed cell cultures it labels intra- and extracellular proteins blue, yielding a high contrast with the background. It is most commonly used to study the relative distribution of cells on a surface after a period of culture, and is therefore ideal for use in

gradient screening experiments. Cells were fixed in 10% formaldehyde/PBS at 37°C for 30 min, and stained with 0.5% Coomassie blue for 5 min before thorough washing in ultra-pure water. After allowing the samples to dry at room temperature, the surface was imaged on a flatbed scanner, at a resolution of 6400dpi. Images were imported into ImageJ, and the *HeatMap from Stack* plugin was used to generate heat maps of cellular coverage over 6 samples. Selected optical images of Coomassie stained cells were also captured using a Leica INM20 microscope operating in Nomarski mode using a 50x objective.

### **3.2.5 Data acquisition - immunofluorescence**

Immunofluorescence images were captured using an Olympus CX41 upright microscope equipped with a Prior motorised stage operated with ImagePro+ (Media Cybernetics, Marlow, UK) scanning 96 images across the pattern in an 8x12 grid with a 10x objective. A process flow was created in CellProfiler image analysis software[94] which calculated cell coverage and alignment to the groove axis (+/- 15 degrees) using images of DAPI stained nuclei and phalloidin stained actin. Statistical analysis of cellular alignment was performed using the Minitab software package, performing a student's t test on the triplicate data sets for each cell type with significant results having  $p < 0.1$ .

## **3.3 Plasma polymers for micro- and nanofabrication**

### **3.3.1 Plasma polymer deposition**

Plasma polymerisation, facilitated by radio frequency glow discharge, allows the deposition of highly tuneable polymer films onto a variety of substrates[89]. In a seminal text on the topic, *Yasuda et al* described in great detail a host of parameters which can be used to control the nature of such depositions. Further work in the literature over the past 30 years has built upon these findings, exploring new and innovative techniques. Pressure, temperature, excitation power, frequency, duty cycle, monomer flow rate, chamber geometry, electrode positioning and monomer type all affect the deposition rate and composition of films[95].

Low molecular weight monomers can be introduced into a low pressure reaction chamber, where various electrode configurations can be used to create a glow discharge



plasma. The plasma is initiated by the acceleration of free electrons, which are present in any gaseous medium, by a high power RF field applied across the chamber. These electrodes can be external or internal, and capacitive or inductive in nature. Accelerated electrons collide with monomer molecules, donating energy and causing fragmentation or chain scission. These molecules become energised, emitting further electrons and protons, along with photons which give the plasma its characteristic glow. These electrons go on to collide with further molecules, initiating a cascade reaction until the plasma saturates, which is a function of monomer availability and the RF excitation. Excited monomer ions recombine to form a polymer which is decidedly different in nature to conventional polymers, Figure 3.2. Due to the high concentration of excited molecules present during the polymerisation process, there is a high degree of cross linking. This leads to polymer deposits which are highly stable and pinhole free. The conformal nature of these coatings allows complex surface topographies to be reliably coated.

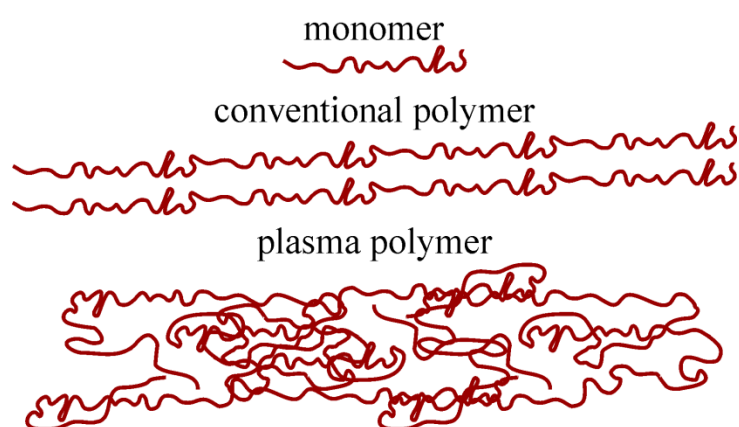


**Figure 3.2 Plasma polymers are structurally distinct from conventional polymers. The polymerisation process creates a highly cross-linked polymer as monomers are dissociated in the plasma, condensing on the surface. Whereas conventional polymers may polymerise as a repeatable sequence, with subunits linking at designated sites, plasma polymers are cross linked broadly across multiple sites and via dissociated fragments of monomer.**

### 3.3.2 Plasma polymer gradients

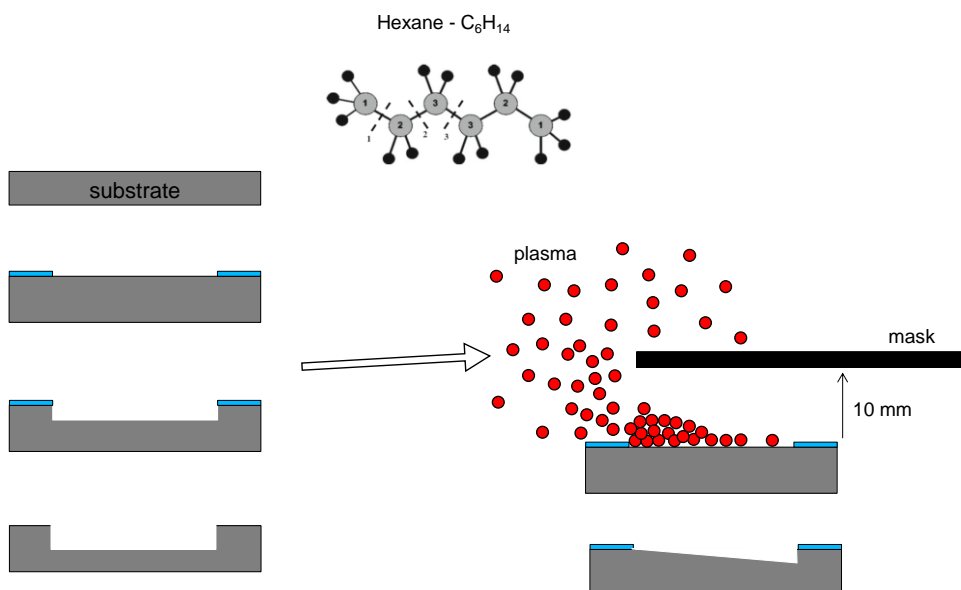


**Figure 3.3** Deposition of plasma polymer films under a diffusion masks creates a gradient of film thickness which can be used as a sacrificial etch mask. Conventional uniform etching (left) forms only one depth at a time – meaning many rounds of lithography and etching are required to fabricate multiple depths on a single sample. Plasma polymer gradients (right) which exhibit a variation in thickness across the sample are sacrificially etched over time – resulting in a variation of etch depth. Film thickness is reduced along the mask length as diffusion of monomer (red) is constricted.

Plasma polymerised hexane (ppHex) films were deposited at 0.4 mbar in a custom built borosilicate T-shaped chamber, as a secondary (and sacrificial) etch mask on top of the primary etch mask. The plasma was ignited by capacitively coupled band electrodes driven by a 13.56 MHz RF generator, supplying 100 W peak power pulsed at 50ms on time- and 950ms off time[96]–[98]. The excitation waveform was optimised for deposition rate, maximising the thickness of ppHex films which could be deposited in a single polymerisation run. A gradient of film thickness was achieved by placing a 10 mm high polymer mask over the substrate (Figure 3.3), resulting in a diffusion controlled ingress of ppHex into the channel, and therefore a variation in film thickness along its length.[97], [99]. Modified plasma deposition rates in close proximity to the physical mask (the plasma sheath[100]) result in differences in film thickness which are not defined by the channel geometry. To mitigate for this, a mask was used which was 20 mm wide, i.e. twice as large as the patterned region, with the mask placed offset from the pattern start by 2 mm to

account for the plasma sheath. This yielded a plasma polymer gradient which varied in a single direction along the microgradient pattern.

Instructions detailing the operation of the plasma chamber used during this work are included in the appendix. Initially written by Dr Rasmus H Pedersen, and subsequently modified by myself to include new instructions & features. Further details of the ppHex deposition process have been published elsewhere [45], [64], [101]

### 3.3.3 Dry etch cycles

The sacrificial ppHex mask was etched in a standard RIE process ( $\text{SF}_6/\text{C}_4\text{F}_8$ ), transferring the gradient of film thickness into the silicon substrate, with a selectivity of approximately 1.8:1. As a result, a ppHex film which was 120 nm thick could be used to etch approximately 210 nm into the silicon substrate. Care was taken to terminate the etch before the secondary ppHex mask was completely removed. Successive cycles of ppHex deposition and RIE created a gradient of depth from sub 5 nm to over 1  $\mu\text{m}$ .

<b>Mask</b>	<b>Substrate</b>	<b>Etch Gas</b>	<b>Etch Rate (nm/min)</b>	<b>Selectivity</b>
<b>ppHex</b>	Si	$\text{SF}_6 / \text{C}_4\text{F}_8$	800	$1.8 \pm 0.26$
<b>ppHex</b>	SiO <sub>2</sub>	$\text{CHF}_3 / \text{Ar}$	35	$8.42 \pm 0.91$
<b>SiO<sub>2</sub></b>	Si	$\text{SF}_6 / \text{C}_4\text{F}_8$	800	$10.80 \pm 0.13$
<b>ppHA</b>	Si	$\text{SF}_6 / \text{C}_4\text{F}_8$	800	$2.33 \pm 0.12$
<b>ppHA</b>	SiO <sub>2</sub>	$\text{CHF}_3 / \text{Ar}$	35	$3.71 \pm 0.09$
<b>PMMA</b>	Si	$\text{SF}_6 / \text{C}_4\text{F}_8$	800	~1.5:1
<b>S1818</b>	Si	$\text{SF}_6 / \text{C}_4\text{F}_8$	800	~1.7:1
<b>NiCr</b>	Si	$\text{SF}_6 / \text{C}_4\text{F}_8$	800	>100:1
<b>NiCr</b>	Quartz	$\text{CHF}_3 / \text{Ar}$	35	~10:1

**Table 3.1 Etch rates and corresponding selectivity values for various etch and material combinations used in this thesis. Where sufficient data was available selectivities are presented as averages of at least three samples. It should be noted that etch performance is intrinsically linked to the equipment used. These values are subject to drift over time using equipment in the JWNC, and provide only an indication of potential behaviour on comparable systems in other settings. One should always calibrate etch rates and material selectivities when developing/implementing a new process.**

### 3.4 Continuous gradients of groove depth

A primary etch mask defining the lateral pitch gradient was created by photolithography followed by lift-off of NiCr as a hard etch mask. Deposition of ppHex under a 10 mm high diffusion mask created a thin film which was 120 nm thick at the mouth of the mask, with thickness decreasing along the length of the channels[100]. Diffusion of the monomer into the channel results in a decrease in concentration as it is depleted by the plasma polymerisation reaction. The measured film thickness along the gradient span fits a power law, Figure 3.4, confirming that it is diffusion of monomer species into the channel which defines the gradient slope. Sacrificial etching of the ppHex film transferred a gradient of depth into the silicon substrate, Figure 3.5. Selectivity of the ppHex film was observed to be approximately 1.8:1 against silicon in a non-switched SF<sub>6</sub> : C<sub>4</sub>F<sub>8</sub> inductively coupled plasma (ICP) process, allowing grooves which were 210 nm deep to be etched from a 120 nm ppHex film. Remarkably, this selectivity measures favourably in comparison to PMMA (1.5:1) and S1818 resist (1.7:1). In order to create grooves which were over 1 μm deep, the process of ppHex deposition, followed by etching, was repeated five times as it was not possible to deposit a film with sufficient thickness to withstand the etch to that depth. Simply layering multiple ppHex films before etching resulted in a poor quality etch. It is assumed that the film composition, in terms of oxygen/carbon, ratio is modified by exposure to atmospheric conditions,[102], [103] which may result in spatial variations in selectivity and a poor quality etch.

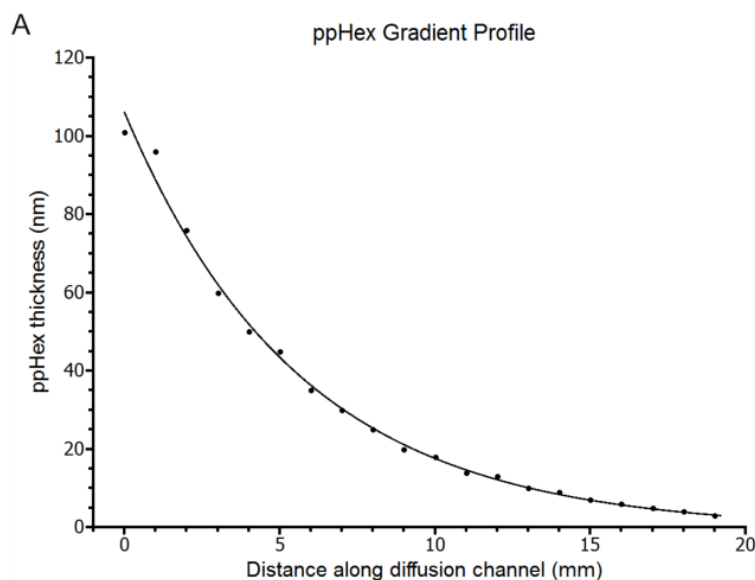


**Figure 3.4** The deposition of plasma polymerised hexane (ppHex) under a diffusion mask gives a gradient of thickness along the pre-defined channel length.

This requirement for repeated cycles of ppHex deposition followed by silicon etching introduced some variation in the silicon gradient profile, which was measured by making a scratch in films deposited on silicon pieces followed by thickness measurement by surface profilometer (Dektak 6M, Veeco, USA). Re-aligning the diffusion mask on the sample by hand resulted in sequential gradients which did not fully overlap, giving the somewhat erratic profile in silicon as seen in Figure 3.5 despite the repeatably smooth ppHex gradients shown in Figure 3.4.

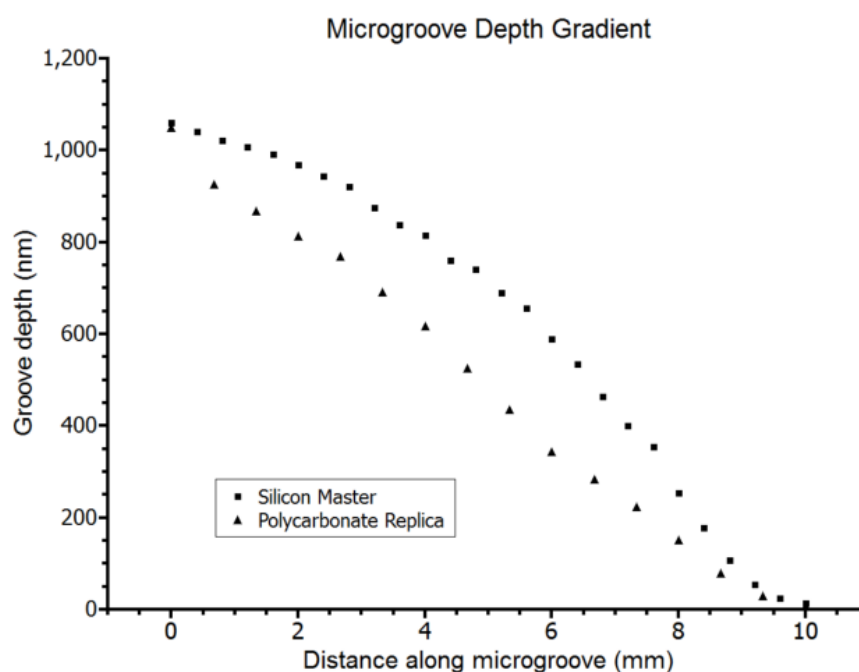


**Figure 3.5 Sacrificial etching of this film transfers a gradient of depth into the silicon substrate. The silicon master can then be used to fabricate a polymer inlay for replication of the pattern by injection moulding of polycarbonate.**

Atomic force microscope (AFM) scans of the replica surface in the etched region (in groove) and the masked region (on ridge) showed an RMS roughness of 4.5 nm and 1.3 nm, respectively, Figure 3.6, indicating that the etching process caused a degree of surface roughness. The in groove roughness of 4.5nm was deemed to be acceptable, however one should bear in mind that surface roughness can also impact upon cell response and has been investigated using gradient platforms in the literature[55]. A gradient of groove depth in a polymer substrate spanning two orders of magnitude was successfully fabricated by this process, with a shallow groove depth of less than 10 nm confirmed by AFM, increasing along the 10 mm length of the grooves to a depth of 1055 nm. The gradient of

depth is visible under an optical microscope as a gradual definition of the pattern from left to right in Figure 3.7 B.

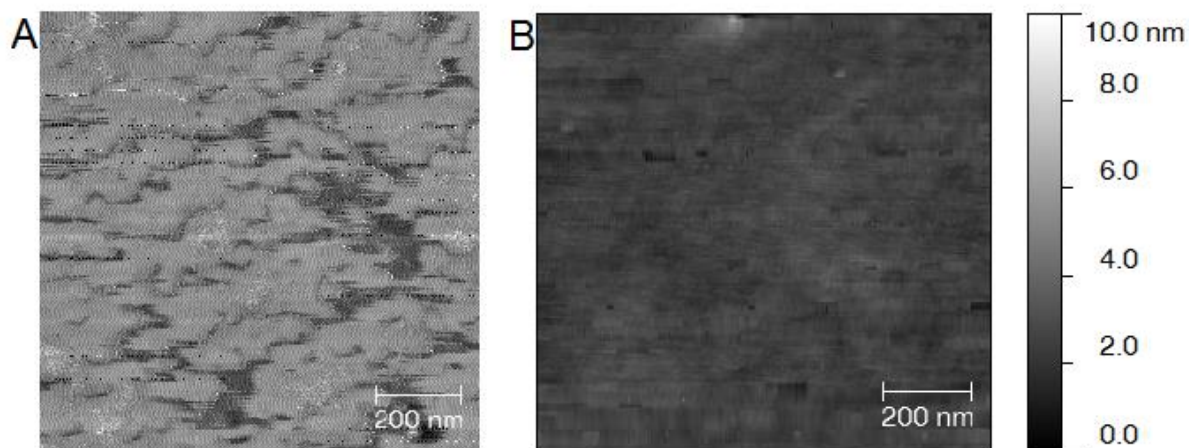


**Figure 3.6** Surface roughness of the polymer replicas was measured by AFM in the groove base (A), which actually underwent the dry etching process, and on top of the intermediate ridges (B) which were masked throughout fabrication. These regions had a RMS surface roughness of 4.5 nm and 1.3 nm respectively. No significant deterioration in either lateral definition or depth of the pattern was observed on injection moulded polycarbonate replicas.

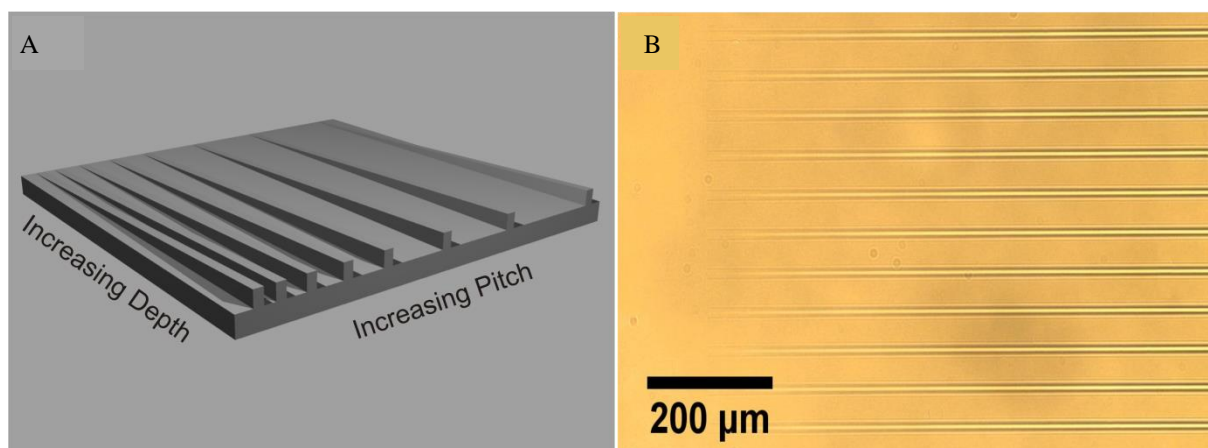


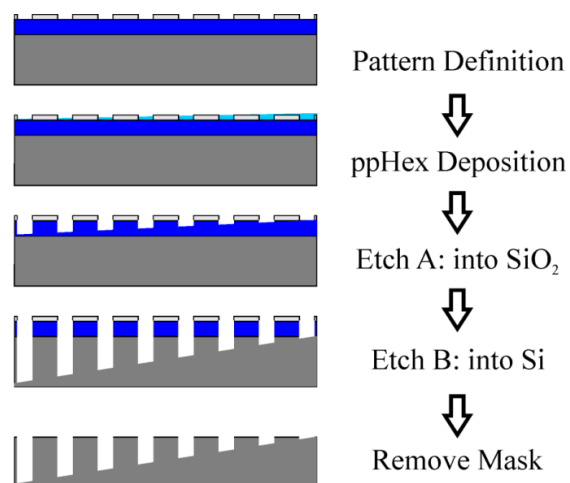
**Figure 3.7** A) A graphical representation of the dual topography gradient on an injection moulding inlay – ridges increase in height across the sample, whilst pitch increases orthogonally. Injection moulding therefore creates samples with the complimentary groove gradient. B) Increase in depth along the length of the 5 μm wide grooves can clearly be seen in an optical micrograph as the micropattern emerges from the planar surface.

### 3.5 Gradient amplification

Deposition of a film thickness gradient, followed by etching into a silicon substrate allows for the fabrication of depth gradients up to 1  $\mu\text{m}$ . This process is limited by the selectivity of ppHex against the silicon substrate which is approximately 1.8:1 in a non-switched etch. To etch a gradient reaching 1  $\mu\text{m}$  depth a polymer film of 250 nm is therefore required – which is a challenging target thickness using the equipment to hand[96]. Specifically, using the plasma polymerisation apparatus available (vacuum chamber with copper band electrodes, 13.56 MHz excitation frequency, 50W power) , this is considered to be a ‘thick’ film, and is only achievable by sequential depositions of approximately 50 nm in thickness, which results in undesired variations in film thickness and composition.

Rather than etching the silicon substrate directly, transferring the polymer gradient into an intermediate layer on the substrate allows for the ‘amplification’ of ppHex gradients into much steeper gradients in the silicon substrate.

**Figure 3.8 Tandem etching of polymer gradients into the silicon substrate allows for gradient amplification to much steeper lateral height changes. Here, the selectivity of etch A (4.5:1) and etch B (11:1) combine to transfer the initial polymer gradient into the silicon substrate with a selectivity which is effectively  $4.5 \times 11 = \sim 50$ .**



The relative difference in etch selectivity of etch A and etch B as shown in Figure 3.8 results in a ‘amplification’ of the total thickness gradient. The relatively poor etch performance of ppHex against silicon is circumvented by etching via an intermediate layer with more favourable performance against both materials. This results in a 110 nm ppHex film masking a 500 nm oxide layer at the thickest section, whilst this is completely etched



at the thin end at which there is little or no ppHex. This newly created gradient of oxide thickness which spans from 500 nm down to nothing can then be used to mask a silicon etch to depths of 5  $\mu\text{m}$  using a non-switched etch with selectivity of approximately 10:1, or much deeper using a switched RIE etch, which can etch with selectivities of 100:1 or higher. This paves the way for the creation of gradients which span over 100  $\mu\text{m}$  in depth.

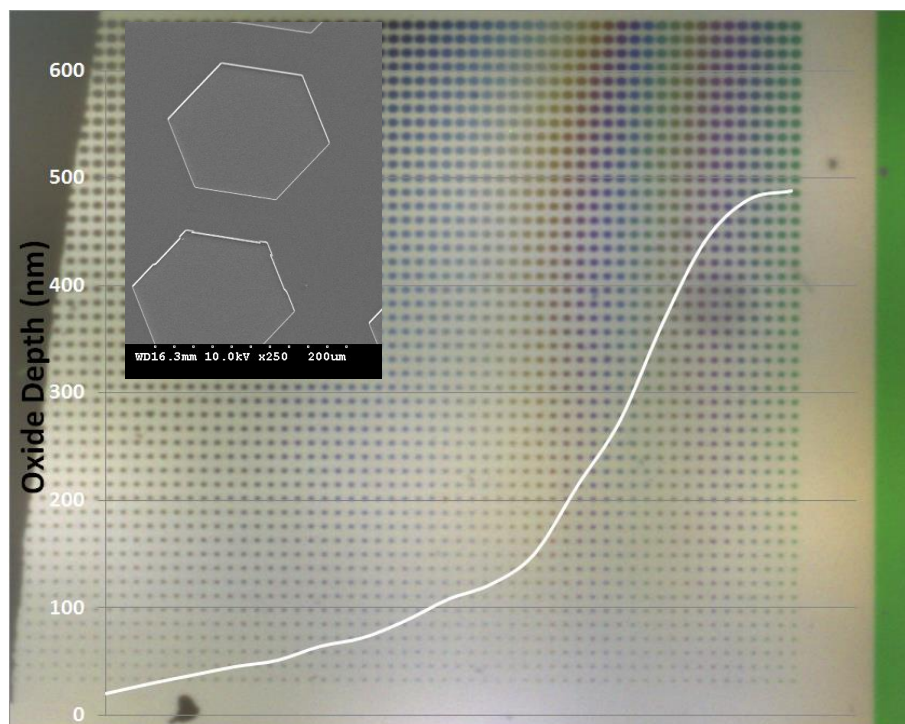


**Figure 3.9** Overlay of silicon dioxide thickness on an 8 mm x 8 mm array of hexagonal features with orthogonally varied diameter. The width of the hexagons increases from 50  $\mu\text{m}$  to 250  $\mu\text{m}$  with a constant feature pitch of 300  $\mu\text{m}$ . Insert: SEM micrograph of large hexagon pattern, at the deepest point of the gradient pits are over 5  $\mu\text{m}$  deep.

This was demonstrated by the fabrication of an orthogonal array of hexagonal microstructures. An array with hexagon diameter ranging from 50  $\mu\text{m}$  to 250  $\mu\text{m}$  and feature depth ranging from 750 nm to 5  $\mu\text{m}$ . This screening array was used to study the response of human osteoprogenitor cells when cultured within angular structures, the results of which are not presented here.



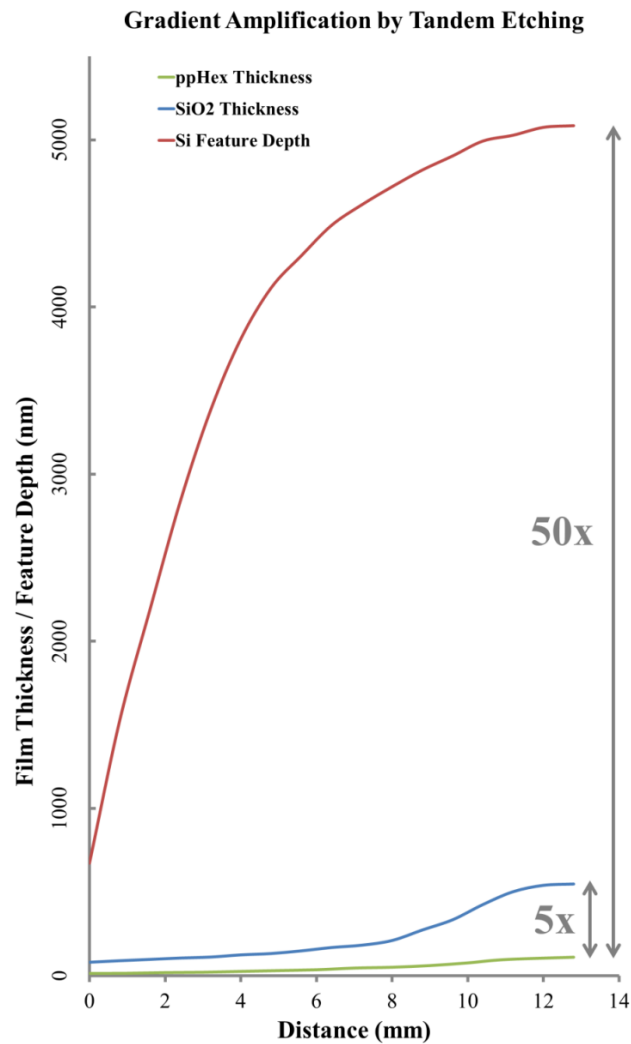


**Figure 3.10** Thin polymer films only 110 nm in thickness can be amplified into micron scale gradients in silicon substrates. Selectivities far in excess of the 11:1 achieved here are possible with switched etches, in which case a log plot would be required to convey the scale of amplification.

It should be noted that over etching into the SiO<sub>2</sub> film created a gradient which does not start from very shallow or flat features, but rather the final gradient begins at approximately 750 nm depth and extends to over 5  $\mu\text{m}$  deep, Figure 3.10. This obscures a potentially vital part of the depth range. Continuous gradients such as those fabricated by etching of plasma polymer gradient films may not be suitable for discrete topographical structure such as these, with individual diameters of, for example, 200  $\mu\text{m}$ . The rate of change of feature height of 5  $\mu\text{m}$  over an 8 mm pattern leaves individual features which have an internal difference of 200 nm in height. This aspect of the fabrication process could be used to create structures with asymmetric height/depth profiles. It does, however, mean that fabrication of height gradients in this manner is more suited to either continuous

structures such as gratings, or discrete structures whose scale is orders of magnitude smaller than the gradient span – i.e. nanopillars with a sub-micrometre pitch.

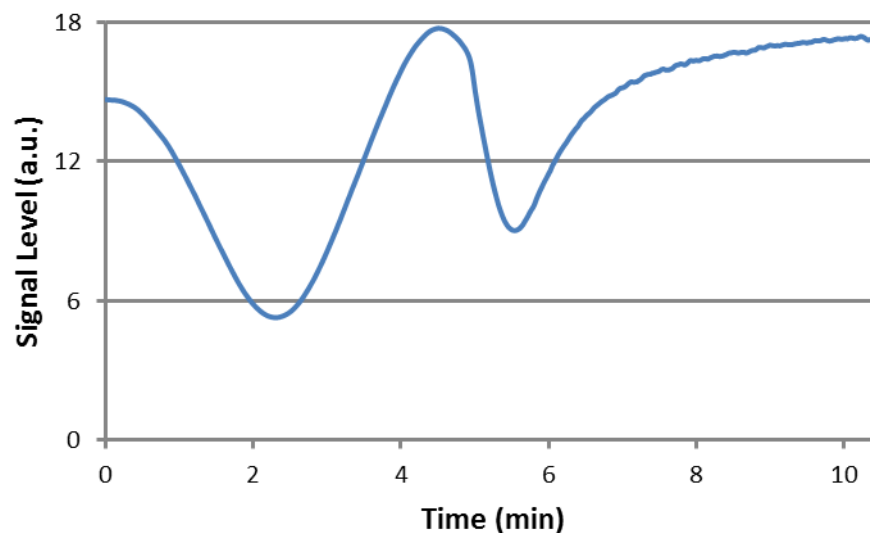


**Figure 3.11 Interferometer trace showing the final etch into silicon through the amplified oxide mask. Etch stop is determined by the second apex of the signal trace as the oxide mask is depleted.**

### **3.6 Cellular response to continuous variation in groove depth and pitch**

The speed at which implantable biomaterials are incorporated into biological systems, and indeed the manner of the biological response in terms of the type and quality of tissue produced is of key interest. Three cell types arising from different tissues were chosen and cultured on this dual topographical gradient, with the localisation of certain responses indicating the combination of groove pitch and depth which is capable of driving targeted behaviour from interfacing biological systems. Rapid analysis was performed by staining substrates after 72 hours culture with Coomassie blue, and imaging the full 10 mm x 10 mm pattern using a high resolution flatbed scanner.

The manner in which cells are seeded on high-content assays is of paramount importance if cellular distribution is to be taken as a true response to topographical motifs, chiefly to avoid confusing artefacts of inhomogeneous seeding with areas of enhanced or inhibited proliferation, differential adhesion or significant cell motility. An even

distribution of the cell suspension across the assay topography ensured that the number of cells seeded was consistent across the substrate, using the UCS device described in **Chapter 5**. Variability in initial cellular attachment and compatibility with polycarbonate substrata may also be excluded as all cell types showed a high degree of adhesion after 1 hour. Other high-content and high-throughput systems presented in the literature have alluded to the requirement for seeding uniformity[46].

Clear differences were observed in the response of fibroblast type cells when compared to epithelial and endothelial. Heat maps were created which show the coverage of cells across the full gradient topography after 72h culture, Figure 3.12. Hot spots were observed for epithelial and endothelial type cells, whilst no discernible region of enhanced coverage could be seen in fibroblast cells. Analysis of cell orientation, however, showed that hot spots of alignment did indeed exist for fibroblasts, Figure 3.13, which was not observed for the other cell types.

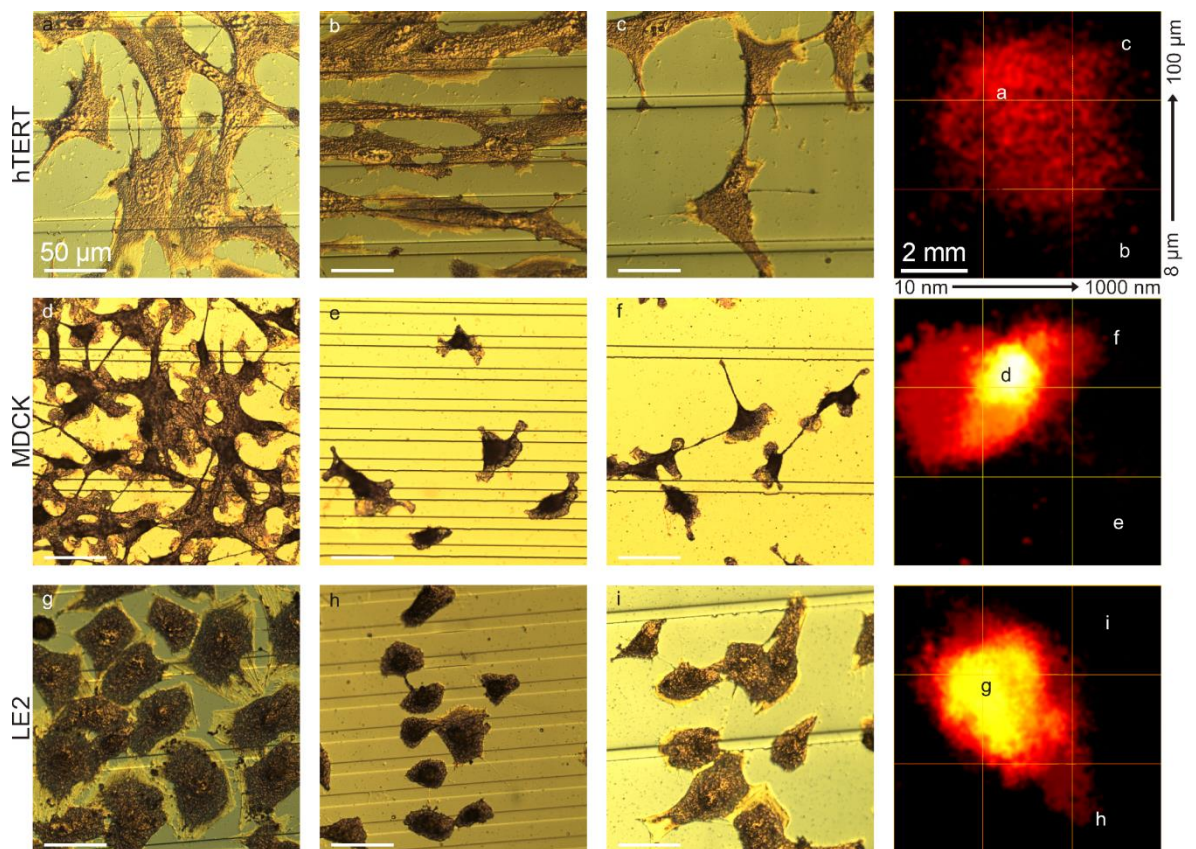


**Figure 3.12** Three cell types (hTERT fibroblasts, MDCK epithelial cells and LE2 endothelial cells) were cultured on the dual microgradient surface, exhibiting distinct morphologies and growth characteristics depending on groove pitch and depth (a-i). Heatmaps in the

**rightmost column indicate that average density across the full gradient platform had localised hotspots of MDCK and LE2 growth, with a more even distribution of hTERTs. Representative images (a-i) are taken from the locations indicated on heatmaps.**

Presenting continuous variation of two surface parameters allows not only the optimal property for a given feature to be extrapolated, but also the interplay between two parameters and its effect on cellular response can be examined in greater depth. It is clear, based on Figure 3.12, that a specific combination of feature pitch and depth is required in order to stimulate the fastest response towards a conformal epithelial/endothelial cell sheet. Whilst a groove with pitch in the 70  $\mu\text{m}$  range is effective where the corresponding groove depth is between 400 and 600 nm, deeper or shallower grooves of the same pitch do not elicit the same preferential response. These results suggest that excessive groove depth may present an obstacle which the cell cannot negotiate, preventing cells crossing grooves to form a cell sheet. On the other hand, grooves which are too shallow provide no guidance to cell orientation, failing to cluster attached cells together and encourage an increase in signalling and tissue formation. Therefore the hot spot is thought to represent an ideal combination of groove pitch and groove depth, bringing cells close together to form characteristic ‘cobblestone’ sheets without depriving them of sufficient surface area to proliferate freely.

### **3.7 Cell alignment on a microgroove gradient**

Further substrates were seeded and cultured, followed by immunostaining for F-actin and DNA, to allow investigation of their morphological response in more detail, Figure 3.13. The orientation and maturation of focal adhesions have been demonstrated as a key factor in cellular interaction with planar substrate.[104] Whilst the total surface area presented to the cell has been suggested as a driving factor in cellular response to nanostructured topographies, i.e. pillars and pits,[36] it is likely that a different mechanism governs response to microstructured grooves – i.e. not all topographical stimuli are created equal. It was observed that depths as shallow as 50 nm induce fibroblast alignment to the groove axis. This is in keeping with previously reported data which suggested a structure height of only 20 nm was enough to impact upon the development of focal adhesions, whilst lower depths are considered too shallow to impact significantly on cellular response.[105] In regions where the spacing between grooves is narrow this leads to

extension of the cell into a polarised morphology; an ideal response in the formation of strong connective tissue and muscle.

A microscope fitted with a scanning stage was used to collect data from dual gradient assays in a multi-well plate format, for subsequent processing in CellProfiler. It is essential that high density assays such as this are coupled with high-content imaging techniques in order to fully utilise the vast quantity of data they provide from a single sample. Heat maps were created detailing cellular response across the dual gradient topography in terms of orientation. The expectation being that epithelial/endothelial cell sheets would show no specific orientation whilst fibroblast/myoblast cells would show areas of increased polarisation in line with previous studies performed on grooved substrata. Figure 3.13 shows fibroblast cells were readily polarised as groove depth increases, and that the narrowest groove pitch provided the highest level of orientation to the groove direction. An ellipse was defined around the cell's actin network, and the angle of the ellipse major axis compared to the groove direction. Where this angle was within  $\pm 15$  degrees the cell was considered to have aligned to the microtopography. Alignment of fibroblasts and other cells associated with connective tissue is seen as a gold standard for applications in the targeted repair of strong, functional tissue[90], [92], [106]. When compared to the random alignment of cells on non-structured regions of the sample, grooves with a depth in excess of 500 nm, and a pitch below 50  $\mu\text{m}$  show a marked increase in alignment. Figure 3.13 C&D show the standard deviation of cellular orientation across the sample topography – indicating that the response observed here is statistically significant across both groove depth and pitch.

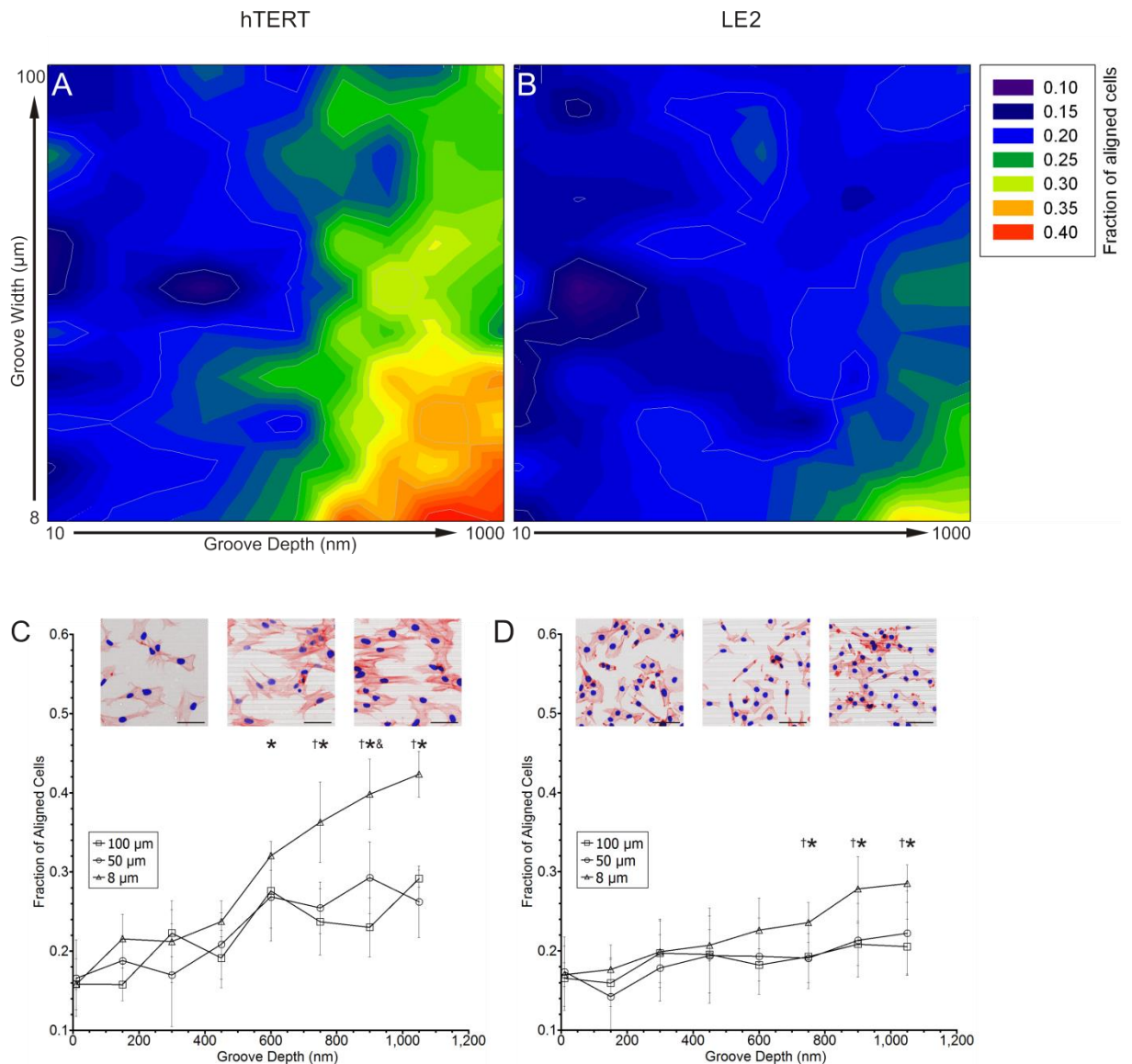


**Figure 3.13 Cellular alignment on the dual gradient topography as a fraction of the total number of cells. A) a heatmap of fibroblast alignment as a function of groove pitch and depth, with pitch increasing vertically and depth increasing horizontally. B) endothelial cell alignment. Corresponding cross sections of the heat map data are plotted (C&D) showing the alignment as groove depth increases for three chosen groove pitch values with inset images showing representative morphology at depths of 100 nm, 550 nm and 950 nm. Statistically significant increases in cellular alignment ( $p < 0.1$ ) are indicated for 8  $\mu\text{m}$  versus 5  $\mu\text{m}$  ( $\dagger$ ), 8  $\mu\text{m}$  vs 100  $\mu\text{m}$  (\*), and 50  $\mu\text{m}$  vs 100  $\mu\text{m}$  (&),  $n=6$ .**

Alignment of cells to the groove axis differs drastically for each cell type. Whilst fibroblasts appear to require only an interface, i.e. alignment to deep grooves which are much wider than individual cells, endothelial alignment is only increased in locations where the cell is fully confined by grooves – with contact guidance[27], [107] forcing the cell to conform to the narrow space available. Increased ratios of aligned cells after a given groove depth at all

**groove pitches for fibroblast cells indicate a necessary threshold of groove depth to drive alignment, but that only a single interface is required.**

### **3.8 Conclusions**

Fabrication and application of a simple assay format has been demonstrated, allowing the high-content analysis of cellular response to continuous variation of groove pitch and depth. Specific regions of the sample prompted a cellular response which was selective, based on the cell type screened – highlighting the variation in cellular behaviour and the power of microtopographies in guiding these responses. Similar cell lines - MDCK and LE2 - displayed a common response to varied groove depths and pitch, whilst a fibroblast cell line showed a drastic difference in response, also indicating optimal surface properties existed within the parameter space. Such cell specific responses to the same topography highlight the need for varied solutions to biomaterial interface problems where multiple cell types are present, and the potential to guide complex biological systems with relatively simple topographical cues.

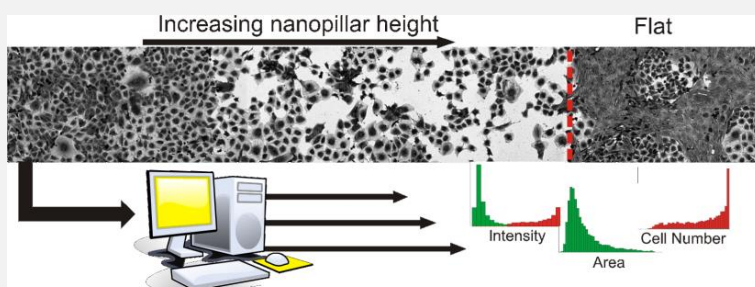
Cellular response was analysed for 88 different combinations of groove pitch and depth on a single sample, and quantified in terms of cellular alignment to the microgroove axis along with cell density after 72h culture. Mass replication of the dual gradient assay readily allows its application to further studies, and the investigation of a host of other effects and cellular responses induced by variation of the depth and pitch and microgrooves. These disposable polycarbonate parts offer a low cost, efficient, and information rich method to further our understanding of the relationships between cell behaviour and multiple surface properties.

Beyond direct etching into substrates through plasma polymer sacrificial etch masks, a tandem etching process has also been demonstrated which is capable of amplifying a gradient of film thickness 50 fold into a silicon substrate. This novel fabrication method makes use of the selective etching of first an intermediate oxide layer before transfer into the silicon substrate, making the fabrication of micron range depth gradients for future studies relatively simple. The 0 – 1000 nm gradient of groove depth demonstrated here could also have been fabricated in only two etch steps, rather than the 5 cycles of ppHex deposition and etching that were required using a direct etch process.



## 4 Label free segmentation of co-cultured cells on a nanotopographical gradient

**Background:** Cell response to micro- and nanofabricated surfaces for biomedical applications is often screened using monocultures, however there are very few monocultures *in vivo*. New methods are required to facilitate more representative *in vitro* studies.

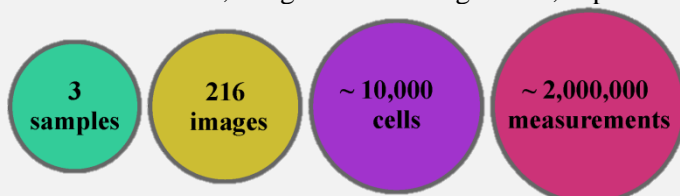


**Results:** Label free analysis was demonstrated of **two cell types in co-culture** on nanopillar gradient surfaces. Using this technique, the two cell types could be distinguished from fluorescence microscopy data captured as linear arrays along the nanopillar height gradient. This removed any need for cell type specific labelling, with a demonstrated segmentation **accuracy of 84%**. Culture on nanopillars induced a spatial re-organisation of the two cell types which appears to be driven by the surface structure. Results correlate with earlier work which was carried out on a different polymer – indicating that the effect is not material specific. The open source software used for automated measurement and classification of cells provided a rich dataset of almost 200 metrics per cell, approaching single cell resolution on a gradient topography spanning 9 mm. Further analysis of this large dataset by principal component analysis revealed that nanopillar arrays modify different aspects of **fibroblast and endothelial morphology**. This goes some way to explaining their differing response to the same surface.

**Conclusions:** Co-cultures can be accurately segmented into their constituent cell types using a machine learning approach based on cell morphology. Fibroblast and endothelial cell behaviour is directly regulated by nanopillar height, exhibiting a varied response as pillar height increases.

### Experimental:

Length scale: nanometres (100 nm diameter pillars, height ranging from < 5 nm to 150 nm)  
 Cell type: human fibroblast (hTERT-BJ1), rat endothelial (LE2)  
 Analysis: 10x immunofluorescence images with single cell resolution  
 Dataset: 3 channel fluorescence, image scan across gradient, triplicate samples



### Output:

This work was published in *Nano Letters* [44].



## 4.1 Introduction

Systematic studies of nanotopography and cell response have typically been limited to single cell types and a small set of topographical variations. This chapter demonstrates a radical expansion of experimental throughput using automated detection, measurement and classification of co-cultured cells on a nanopillar array where feature height changes continuously from planar to 250 nm over 9mm. Individual cells are identified and characterized by more than 200 descriptors, which are used to construct a set of rules for label free segmentation into individual cell types. Using this approach, label free segmentation with 84% confidence is demonstrated across large image datasets, allowing the suggestion of optimized surface parameters for nanostructuring of implant devices such as vascular stents.

Functional tissue rarely exists as a homogeneous population of cells[108], [109]. With this in mind, it is of critical importance that when screening novel biomedical materials[110], topographies[46] and drug targets[7] *in vitro*, researchers have the ability to utilize heterogeneous populations of cells and so develop real biological context[111], [112]. Cell type specific antibody staining, for example using cluster of differentiation (CD) markers, or pre-loading of tracker dyes into subpopulations, is the standard means of segmenting co-cultures at the image analysis stage. This, however, wastes a full fluorescent channel which might be better used to co-stain for other cellular responses such as metabolomic activity[113] and stem cell differentiation[35]. Manual segmentation by visual inspection is possible to an extent,

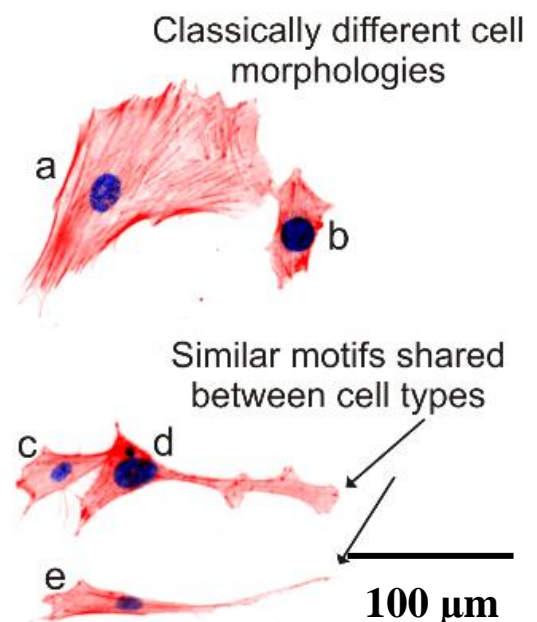
Figure 4.1, although as datasets increase in size this becomes a significant limitation to experimental throughput and the bias of the individual undertaking the analysis becomes increasingly problematic.

Rapid micrograph analysis and machine learning techniques are now accessible with relative ease thanks to the open source CellProfiler[115] and CellProfiler Analyst[116] software suites respectively, with other tools also available[117], [118]. These methods of automated image analysis can generate large multivariate datasets from microscopy data, whereas previous analyses were predominantly subjective. Such datasets have been demonstrated in training a machine learning algorithm to detect 15

morphological changes in RNA interference screens[119]. This method can be applied to the label free segmentation of co-cultures, allowing more detailed analysis of *in vitro* models of *in vivo* systems – moving forward from narrow studies using cultures of single cell types.

Developing methods to allow for the simple analysis of co-cultures and beyond will greatly increase the yield from a single experiment, whilst also providing a more biologically relevant picture of cell response. When coupled with arrayed surface features[22], [46], [120], or continuous gradients in which features are varied over a millimetre or centimetre scale[47], [84], a truer picture of the interplay between cell type and surface structure is created. This chapter presents a novel method for fabrication and mass replication of substrates with a continuous gradient of feature height, in this case nanopillars. On this nanopillar gradient topography, Figure 4.3, a new technique is demonstrated for the rapid and efficient segmentation of diverse cell populations without the need for extra labelling steps, by processing cell morphology and cytoskeletal structure with machine learning algorithms. The relative response, morphological characteristics, and abundance of each cell type may then be related to the underlying topography at that point, and this insight applied to the design of future tissue engineering constructs such as cardiovascular stents[121].

**Figure 4.1 Challenges associated with manual segmentation of co-cultures arise from the diversity of phenotypes on display across a single cell type. On a flat surface, fibroblasts a & e can display drastically different morphologies. Endothelial cells b, c & d also display a broad variation in appearance. In this instance, only the difference in the structure of uropodia (arrows) indicates that d & e are different cell types. Manual classification of large numbers of images containing many cells is therefore both time consuming and prone to a level of subjective error.**



Regular arrays of nanoscale pillars have previously been used to influence the adhesion, proliferation and differentiation of a range of cell types [35], [122]. It has been shown previously that regular nanopillar arrays can have a cell selective influence on different cell types, Figure 4.2. Arrays of 110 nm tall pillars were shown to enhance endothelial attachment and proliferation, whilst inhibiting fibroblast proliferation, when cultured separately on polycaprolactone (PCL) [36]. It is known that the depth or height of patterns have significant influence on cell adhesion [123], and thus producing a sample with a continuous variation in height over a long distance (1 cm or more) will allow for rapid investigation of optimal parameters for substrate driven cell separation. In addition, a simple and effective method of co-culture analysis allows the effect of nanotopographical stimulation on the two cell types to be confirmed in a more realistic representation of the *in vivo* environment.

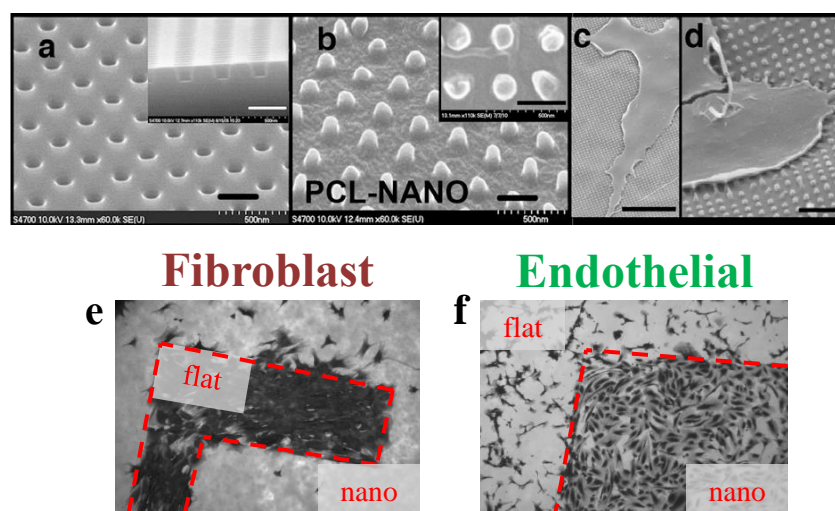


**Figure 4.2** Regular arrays of nanopillars, with a pitch of 300 nm, pillar height of 100 nm and pillar diameter of 100 nm drive two distinct behaviours in fibroblast and endothelial cells. Substrates were fabricated by embossing PCL films to create patterned and flat areas on a substrate. Separate culture of fibroblast and endothelial cells showed that the nanopillar array repelled fibroblasts, whereas endothelial cells exhibited enhanced proliferation. Figure adapted from Csaderova et al. 2010.

A smooth gradient of nanopillar height was realised by sacrificial etching of plasma polymerized hexane (ppHex) gradient, as described in **Chapter 3**. In this case, rather than initially transferring a micropattern onto silicon, a pattern of nanodots was defined on quartz as a replica of the previous work by *Csaderova et al* in 2009. The nanopattern defined in aluminium, and the superimposed gradient defined in ppHex, were transferred to the substrate using a standard RIE processes for quartz:  $\text{CHF}_3/\text{Ar}$  (Oxford Instruments 80+

RIE)). The etch was timed to stop shortly after all the plasma polymer material had been etched. Multiple etch runs were carried out, which resulted in some heterogeneity in the pillar height gradient, as can be seen in Figure 4.3.

Nanostructured samples were created in high volume with high fidelity to the original master by injection moulding of polystyrene (PS)[74], [124]–[126]. The gradient of nanopillars height was further enhanced during the injection moulding process due to stretching of the nanopillars structures as the part is ejected from the mould. The characteristics of this stretching effect are reported in more detail by *Pedersen et al*, using the nanopillars gradient as a tool to quantify the level of stretching under various processing conditions[99].

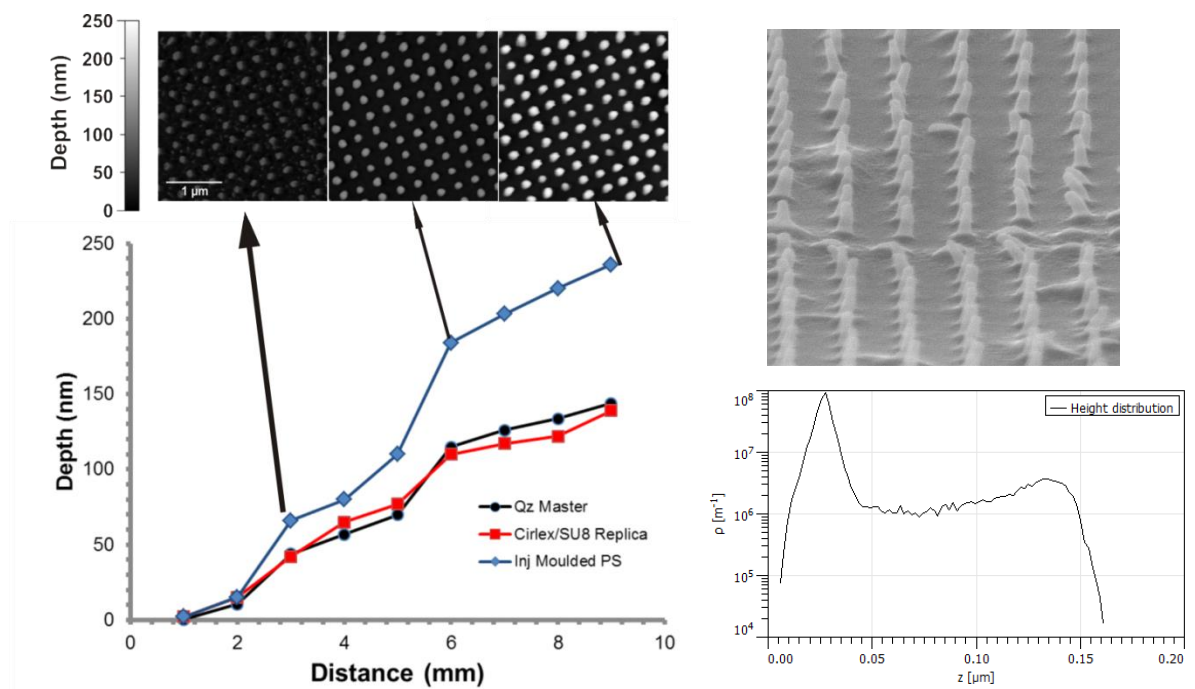


**Figure 4.3** Depth profile of quartz master, injection moulding inlay replica and the final injection moulded part in polystyrene, accompanied by selected AFM scans of features at the shallow, a, medium, b, and tall, c, region of the sample. Top right: representative SEM image of nanopillars with a height of 140 nm. Bottom right: histogram of height data taken from AFM image showing two peaks, which were used to determine pillar height across AFM images.

## 4.2 Methods

### 4.2.1 Electron beam lithography

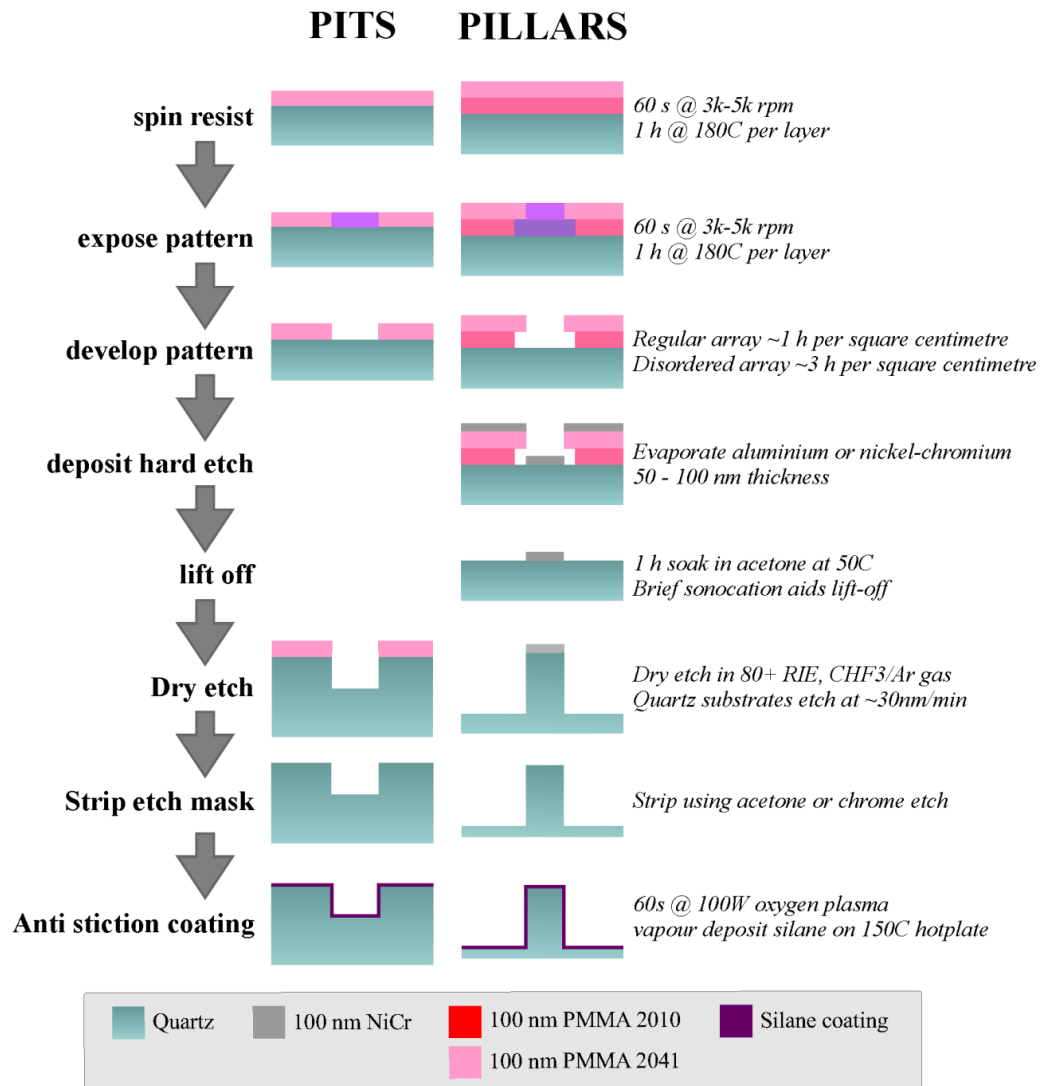


**Figure 4.4 Fabrication process for nanopit and nanopillar arrays**

Poly(methyl methacrylate) (PMMA) resist was used for all electron beam lithography (EBL), at various thicknesses from 100 nm to over 500 nm to create features from 50 nm to 2  $\mu$ m in size. The most commonly fabricated structures were nanopits and nanopillars with diameters around 100 nm, on quartz substrates. The fabrication of both these pattern types is similar, as detailed in Figure 4.4. Nanopit samples were fabricated by direct etching of a single PMMA mask layer into quartz, which was later removed in acetone. Nanopillars used a hard etch mask, which was realised by evaporation through

holes in a resist bi-layer. A lower molecular weight PMMA layer under the patterning layer is overexposed compared to the patterning layer. This creates an undercut profile, meaning that after evaporation of the hard metal etch mask the solvent used to remove the resist layer can readily access it without evaporated metal forming a barrier. The gradient of nanopillar height used in this chapter was fabricated by Dr Rasmus Pedersen.

#### 4.2.2 Injection moulding inlay fabrication

Polymer inlays were created for mass replication of micro- and nanotopographies by injection moulding. After fluorination of the quartz stamp to prevent sticking, a Cirlex™ piece coated with 30 µm of SU8 3050 by a standard spin recipe was placed on top and the two sandwiched together at 95°C for 15 min, imprinting the inverse pattern into the SU8. In the case of transparent quartz substrates, a 3W UV LED emitting at 365 nm was used to cure the SU-8 resist by exposure for 2 min and a post exposure bake at 95°C for 10 min. After imprinting, Cirlex™ inlays were hard baked at 190°C for two hours to fully harden the SU-8 resist.

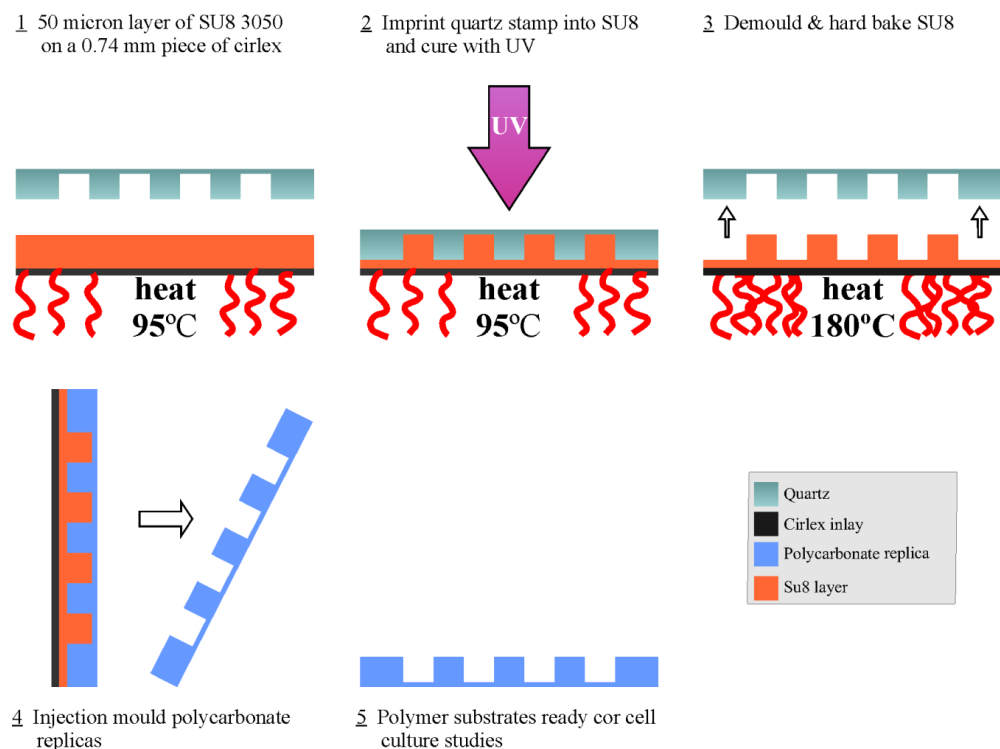


**Figure 4.5** Fabricating inlays for injection moulding. After fabrication of micro- or nanostructures on quartz substrates, the pattern is transferred into an SU-8 layer on a Cirlex™ substrate by UV-imprint (1-3).

### 4.2.3 Co-culture labelling

Before combining the two cell populations, the endothelial cells were incubated in suspension with 5  $\mu\text{M}$  green CellTracker<sup>TM</sup> dye (Molecular Probes, UK) added to the media for 30 min at 37°C as per manufacturers specifications. The suspended cells were washed by spinning down and resuspension in media three times to ensure complete removal of excess tracker dye from the cell suspension which may have been taken up by fibroblast upon mixing. This membrane permeable non-fluorescent dye is taken up by the cells and cleaved by common cellular processes, becoming a cell-impermeable fluorescent tracker. The intensity of endothelial tracker dye reduced with proliferation and there was some uptake of tracker dye by fibroblasts, presumably due to membrane-membrane contact and blebbing during mitosis and cell locomotion[127]. Across the full dataset the mean intensity of tracker dye was 5 times higher in LE2 cells versus hTERT cells after 96 hours, allowing a robust determination of cell type with minimal false positives. Positive controls conducted as monocultures which were then combined after the same time period confirmed that the dye remained 97% accurate in labelling the endothelial cells after 96 hours. As fixation using a formaldehyde crosslinking agent works by forming a methylene bridge between reactive groups which are commonly nitrogen based, the CellTracker dye within the endothelial cells was retained after fixation. The intracellular reactions which transform the glutathione-reactive dye into a cell impermeable fluorescent molecule include the addition of functional groups which react with aldehyde fixatives, meaning that the fluorescent probes are bound upon fixation.

### 4.2.4 Data acquisition – immunofluorescence

After seeding, the cells were allowed to settle and attach before being moved to an incubator set at 37°C in a 5% CO<sub>2</sub> atmosphere. Fresh media was added to culture dishes daily, and total culture time was 96 h. After this culture period, cells were fixed in 10% (w/v) formaldehyde solution at 37°C for 10 min, followed by permeabilization at room temperature for 5 min and nonspecific blocking in 1% (w/v) PBS/BSA for 10 min. F-actin fibers and DNA were stained using phalloidin-rhodamine (Life Technologies) and Vectashield DAPI mounting fluid respectively.

Images of the cultured samples were acquired as a linear scan of 18 contiguous locations across the gradient topography – 4 on the flat substrate, 10 across the pillar gradient and a further 4 on the flat substrate, Figure 4.6. Three fluorescent channels were automatically captured for processing using an Olympus CX41 upright microscope equipped with a Prior motorized stage and 10X objective, camera acquisition and stage were operated by ImageProPlus (Media Cybernetics, UK). A total of 216 locations were captured, comprising 12 linear scans across 3 substrates, as described in Figure 4.6. These Images were analysed using CellProfiler to detect individual cells using the DNA and cytoskeleton stain. The intensity of CellTracker staining was also measured to act as a positive control classification of the full dataset into fibroblast and endothelial cells – against which to compare machine learning classification based on the nucleus and cytoskeleton alone.

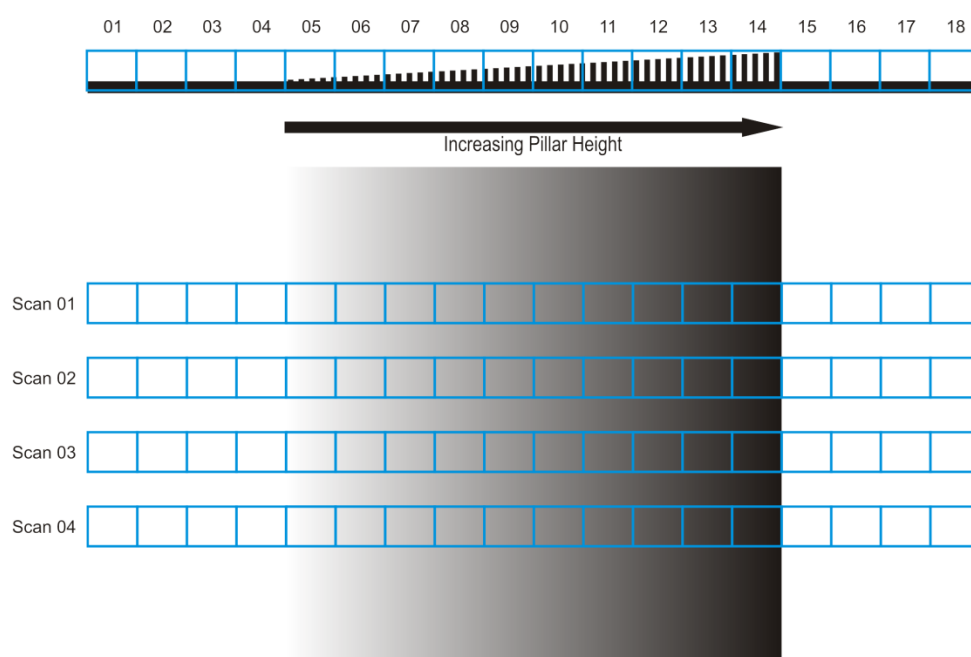


**Figure 4.6 Schematic of scanning strategy across the nanopillar gradient. Each 18 image scan consisted of 4 images on the flat region adjacent to the short pillar region, followed by 10 contiguous images across the rising pillar gradient, and a further 4 images on the flat area adjacent to the tall nanopillars region.**

Processing of the full dataset took approximately 2 hours on an Intel® Core™ i7 2600 CPU @ 2.4 GHz with 16Gb DDR2 RAM using a custom CellProfiler image processing pipeline. In total, over 10,000 individual cells were detected across the 216 image dataset, measuring 137 distinct attributes of each cell comprising information on cell



size, shape, cytoskeletal texture, intensity and location relative to other cells. The data was then transferred into CellProfiler Analyst, which provides a simple to use classifier tool, discerning the difference between the two cell types based solely on ‘cytoprofile’ measurements. Initially, data was quantised into discrete measurements of individual images, which had a frame width of 900  $\mu\text{m}$ , giving 10 datapoints across the 9 mm gradient. After image processing, a centroid value for each detected cell allowed absolute cell location on the pattern to be determined, increasing resolution to 20 points after binning data into 450  $\mu\text{m}$  sections.

### 4.3 Analysing morphometric data

Automated measurement and quantification of microscopy data has developed at a rapid pace over the past decade thanks to the availability of improved digital cameras, automated microscopes and stages, and more generally thanks to the increase in computing power available to laboratories in standard desktop machines. Researchers who previously found themselves scoring histology slides by eye can now acquire and process huge image datasets in a single day. Interpretation of these often complex multivariate datasets can present a challenge, as users either cycle through measurements to find ‘favourable’ metrics of cell response to a surface, or become overwhelmed by the sheer quantity. Techniques and strategies for visualisation of multivariate data have been presented and documented in the literature – and often require a departure from common graphing methods as multivariate datasets with over three dimensions are incompatible[128]. Geometric projection techniques such as parallel coordinate systems, treillis displays, hyperboxes and scatterplot matrixes all allow trends and correlations to materialise for visual presentation of data. Icon based schemes such as Chernoff faces and radar/star plots can be used to encode classes of measurement within a larger structure – with trends appearing as changes in shape. Pixel based systems are also useful, wherein each variable is assigned to a pixel within a larger area. These are particularly amenable to data acquired from pixel type experimental systems such as arrays of surface properties.

Figure 4.7 shows a scatterplot matrix extracted from a co-culture of fibroblast and endothelial cells on a nanotopographical gradient. 18 images were acquired across the gradient, containing both fibroblast cells and also endothelial cells which had been pre-

labelled with a CellTracker dye to allow for determination of cell type and therefore relative response and abundance across the gradient.

This plot shows average per-image values for 6 different measurements in triplicate images across the gradient. Images of fixed samples were processed using CellProfiler to detect cell shape and measure intensity of the cytoskeleton and tracker dye. Stark trends are apparent, some of which are expected and some of which can be used to interpret the response of these two cell types. Firstly, the intensity of the tracker dye is distinct enough to allow for classification into cell type based on this value alone, as described in section 4.2.3. The average cell area of the two cell types is spread with no apparent distinction between the two, despite the classic morphologies shown in Figure 4.1, implying that endothelial cells should be comparatively smaller than fibroblasts. As the underlying nanotopography can impact on cell area, this may explain the lack of distinction as the substrate is influencing cell area.

The angular second moment (ASM) is a measure of local uniformity within a specified window – 10 pixels by 10 pixels in this case. Low values of ASM indicate that there are prominent textural features in the object, such as sharply contrasting bands of actin. This results in a clear grouping of fibroblast and endothelial cell values in Figure 4.7 as the well spread fibroblast phenotype with defined actin cytoskeleton is drastically different from the endothelial morphology. Variance – which is a measure of the grey tone variance of the actin channel, also shows a higher value for the more distinct fibroblast cytoskeleton. The difference in morphology is also borne out in the measure of cell compactness, which is the variance of the radial distance of a cell from the centroid divided by the area – i.e. how regular is the cell shape. Well spread fibroblasts have numerous angular protrusions, as seen in Figure 4.1, leading to higher values of compactness.

The data can be segmented still further to delineate the underlying topography at each datapoint, revealing changes in cell morphology as a function of nanopillar height, and adding clear trends to the data:

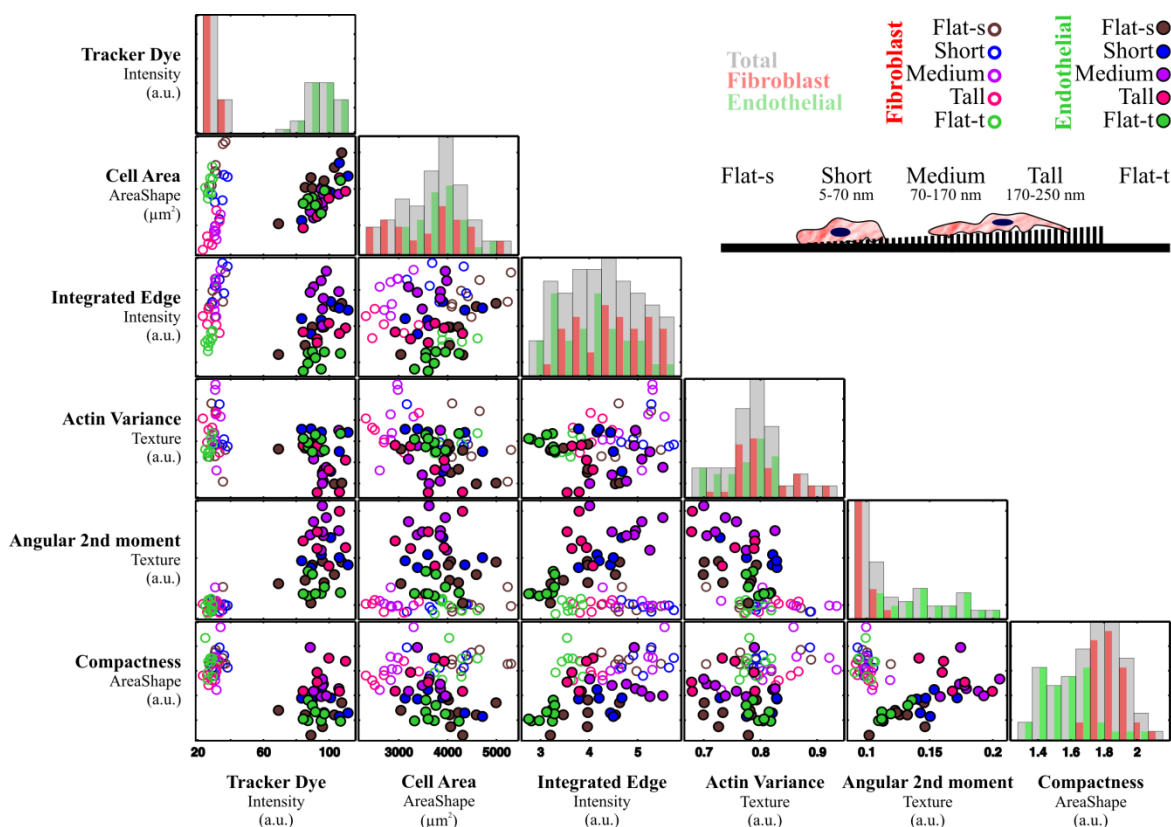


**Figure 4.7** Scattermatrix of the full co-culture dataset, including grouping by location on the gradient sample. Fibroblasts (rings) and Endothelial cells (circles) have been colour coded based on their substrate location. A distinction is made between the flat surface adjacent to tall pillars and the flat surface adjacent to short pillars. 6 measurements are plotted against one another: intensity of CellTracker dye, cell area, integrated edge intensity (sum of pixels around the cell edge), variance of the cell cytoskeleton intensity, and cell compactness (a measure of cell shape and irregularity). Diagonal shows histograms of the total population (both cell types) in grey, along with individual distributions for each cell type.

In Figure 4.7, the nanopillar gradient substrate was divided into five sections – short (5-70 nm), medium (70-170 nm) and tall (170-250 nm) pillars, as well as two flat regions adjacent to either the tall or short region of the pillar array. It would be possible to increase the number of bins to 20, 30 or even 40; however the ability to represent such a large number of data points on a single plot limits the quantisation of the gradient data.

Explaining the apparent uniformity of cell area seen in the total population histograms (grey bars), when the plot is segmented into pillar height and the histogram is divided into cell type as above, we see that there are in fact two peaks for fibroblast area. The lower peak is composed of fibroblasts on medium and tall pillars, indicating a strong substrate driven effect on fibroblast morphology which forces them into an atypical phenotype. Endothelial cell area, on the other hand, appears to have a single peak across all pillar heights.

#### **4.4 Machine learning & data processing**

Machine learning based classification of cell types within the co-culture applied to screening cell response across the high-content nanopillar gradient topography, ranging from a planar surface to a regular array of 250 nm high pillars. Having shown previously that regular nanopillar arrays can exert a cell specific effect on proliferation and adhesion [36], this gradient topography was devised as a means of finding the ‘optimal’ pillar height for enhanced endothelial response in a co-culture environment under substrate driven cell separation.

Using the CellProfiler Analyst classifier tool, 400 randomly selected cells were sorted by visual inspection of tracker dye intensity as fibroblasts or endothelia. Images of both cell types in mono-culture were also used to similar effect. This training set was used to generate a set of rules for segmentation of the images using the tracker probe information. The rules created by the machine learning algorithm focused on a threshold intensity of the tracker dye within the detected cell shape, as was anticipated, to determine cell type. The full dataset was classified using these rules, with 20 random images selected (approx. 800 cells) and inspected with no visible mis-classifications, Figure 4.8c. To determine the experimental error which may be induced by poor retention of the tracker dye, monocultures were processed under the same conditions. An accuracy of 97% after 96h culture indicated minimal levels of mis-classification due to poor dye uptake by the endothelial cells or poor retention due to loss of cytoplasm/blebbing.

Using the Bayesian classifier provided by cell profiler analyst, the dataset of fluorescent images containing two cell types across the nanopillar gradient was segmented into two groups – one for cells classified as endothelial and one for cells classified as

fibroblast. Comparing the intensity of tracker dye with the cell structure based classification indicated that approximately 84% of cells were correctly classified. The misclassification of 16% of cells may be a result of atypical phenotypes being displayed by either cell type, such as cells which were undergoing mitosis, had very recently divided, or were migrating at the point of fixation. Cells located in close proximity to one another or on top of each other also present a source of error for automated analysis.

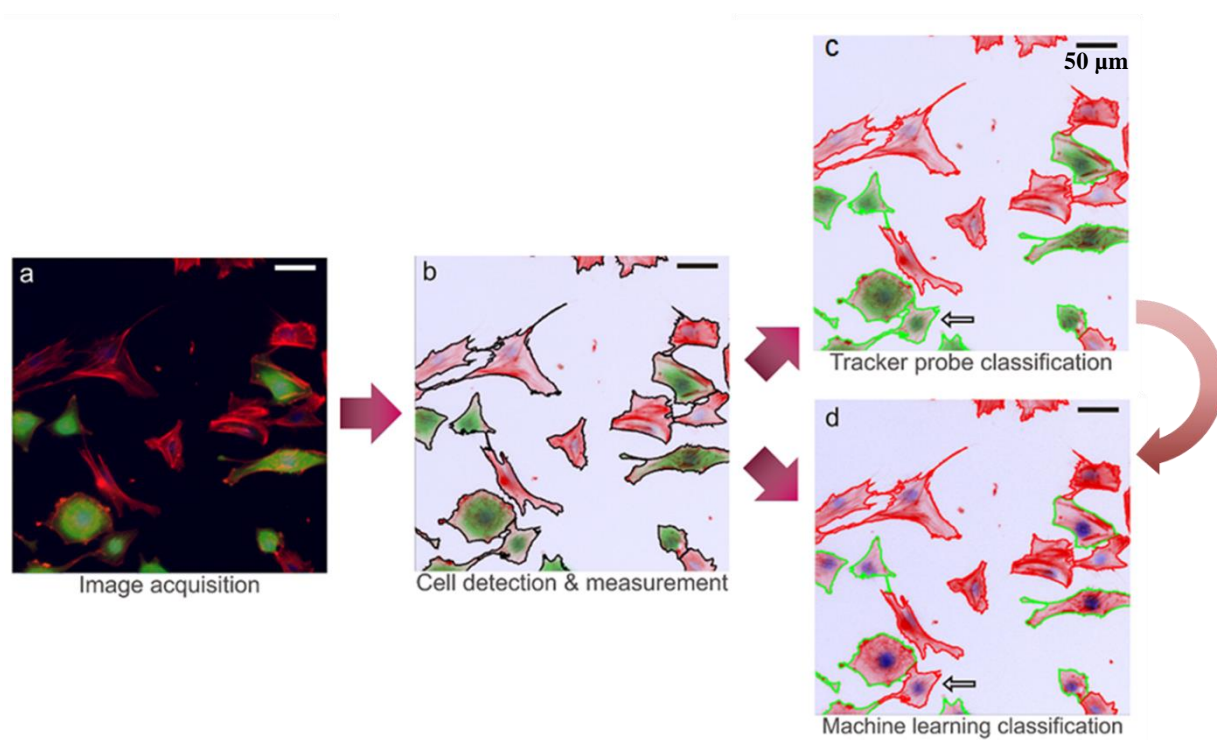


**Figure 4.8 Processing flow for label free segmentation of co-cultured cells. The morphometric profile of cells (b) can be used to determine cell type. When compared to tracking cell type with a direct probe (c) this is approximately 84% accurate, with some misclassifications (d).**

In Figure 4.8 (a) 3 channel images are acquired after staining for DNA (DAPI-blue), the actin cytoskeleton (rhodamine phalloidin – red) and a tracking dye preloaded into one cell type (CellTracker – green). (b) the CellProfiler software suite performs automated counting and detection of cells in each image (thousands can be run as a batch operation). Cells touching the image periphery are excluded as the data for the full cell has not been acquired. After detection, the cells are measured for up to 500 morphological traits. These include structural metrics such as area/perimeter/shape – as well as textural and intensity measurements of the cytoskeletal stain and also any tertiary protein staining

or tracker dyes. This generates a dataset containing millions of datapoints which can be used to segment the cells into categories for each cell type by a simple measurement of tracker dye intensity (c) or without the tracker dye by using the full cytoprofile in a machine learning driven classifier (d). Arrows in (c) and (d) indicate misclassification of cells where the less robust machine learning classification is used.

Figure 4.9a shows immunofluorescence images are captured of co-cultured cells on nanopillar substrates; nuclear DNA (DAPI, blue) and cytoskeleton (phalloidin-rhodamine, red) are labelled with fluorescent markers. Before the cultures were combined, one cell type (LE2 endothelial) was loaded with a CellTracker dye (FITC, green). The CellProfiler software suite is used to batch process 216 image sets, measuring 200 distinct attributes of 10,237 individual cells. The CellProfiler Analyst classifier can then be used to classify each cell as belonging to either the endothelial class or the fibroblast class. Using the tracker probe intensity to segment images into endothelial (green outline) and fibroblast (red outline) yields an accuracy of 97%, as shown in Figure 4.9c.

This generates a set of 50 rules to classify cells based morphology (i.e. aspect ratio, area, perimeter, nucleus size) and also the organization of the cytoskeleton (i.e. radial distribution of actin intensity, actin texture). Visual observation of the cells did indeed indicate, that size and cytoskeletal organization are valid methods of distinguishing between the two, and a human may draw on these factors. However, when human classification is compared to rules generated by a machine learning algorithm it is clearly impractical for a human to consider 50 rules when classifying each cell; reinforcing the power of this new methodology.

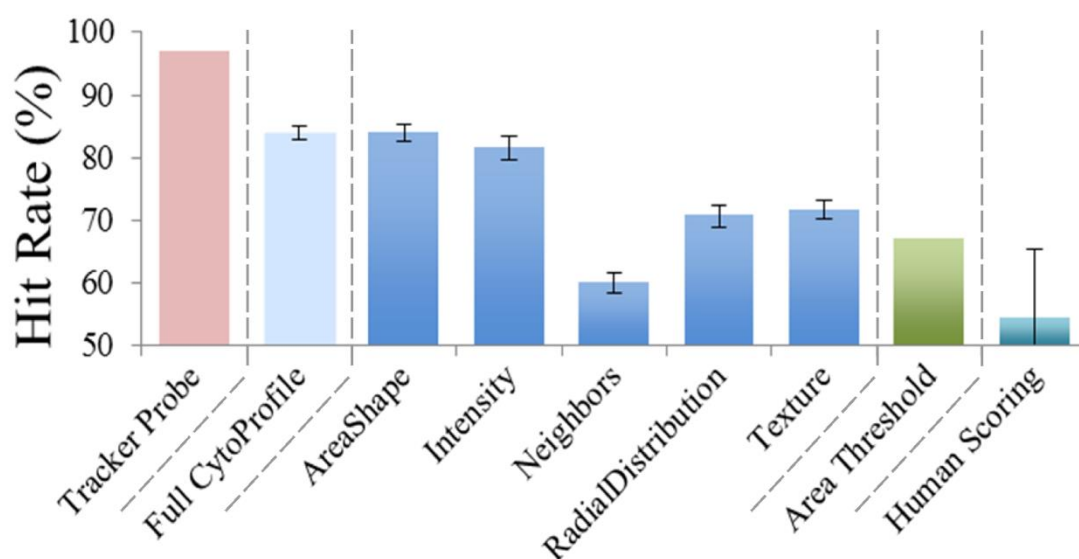


**Figure 4.9 Comparison of various segmentation strategies for analysing a co-culture of endothelial and fibroblast cells. Accuracy of automated classification based on tracker probe intensity is given as a percentage of cells in monoculture which were above a set threshold of tracker intensity. All other hit rates are given as a percentage relative to tracker classification of co-cultured cells.**

An accuracy of 83.9% can be achieved using only the cytoskeleton stain, i.e. shape, staining intensity, texture, radial distribution and cell neighbours. e) changing the feature sets available to the machine learning algorithm in creating classification rules has an impact on accuracy – offering insight into the dominant features which enable correct classification. A simple filter which divides the co-culture by a cell area threshold is less than 70% accurate, due to the heterogeneity of cell size in the dataset.

The rules of the classifier themselves indicate the relative weight of each measurement value in determining the classification of an unknown cell. Statistically, using hundreds of measurements of multiple types (i.e. area, shape, intensity, texture) was no more reliable in classifying cells than using only data from certain measurement classes, Figure 4.9. Classification based on the full scope of over 300 measurements is no more effective than using only metrics of cell area or cytoskeletal staining intensity. Other measurement classes such as the number of neighbours, radial distribution of cytoskeletal staining and cytoskeletal texture are approximately as effective as simply applying a threshold to the distribution of cell area values at approximately 65% accuracy. This is not to say that there is no discriminative data contained in each of these measurement classes.

It is more likely that the training set employed in this experiment did not encompass the true variation in phenotype of both the fibroblast and endothelial cells. Furthermore, it is also possible that the true variation in phenotype could not be adequately encompassed within only 50 classifier rules. Any manner of classification based on automated measurement is more effective than human classification, which was no better than random in a group of 10 researchers.

To better determine the accuracy of human classification of co-culture datasets, two interactive 'classification' exercises were performed with a group of researchers with various backgrounds, Figure 4.11. After a brief training period in which images of typical phenotypes were presented, participants were shown a series of randomly selected images from a co-culture dataset and asked to label each cell as either fibroblast or endothelial. In a group of 10 researchers, of which half considered themselves to be trained biologists, the scoring across the pool was no better than random. This reinforces the need for automated segmentation of co-culture datasets without the introduction of bias from users. The full image set which was used to assess human scoring is included in the appendix.

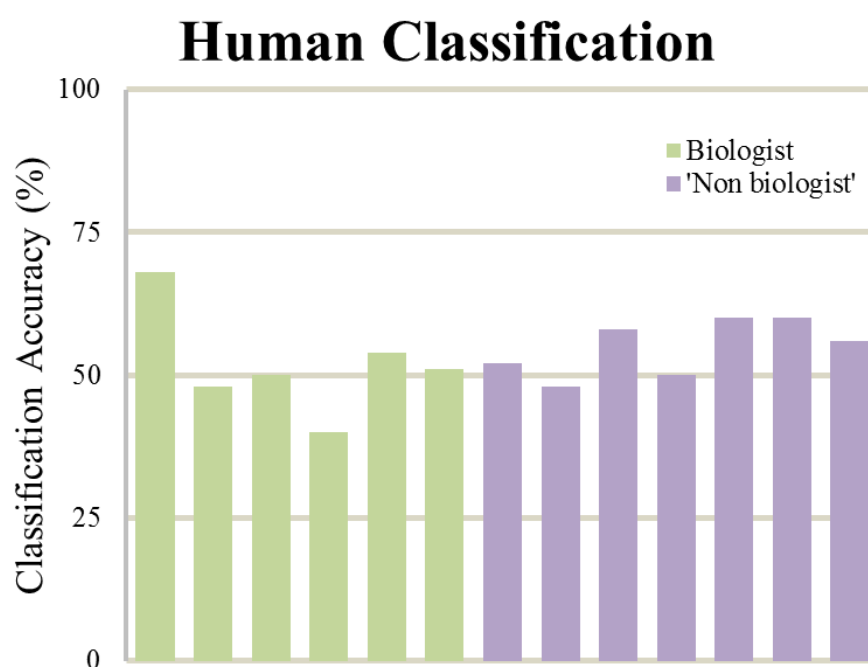


**Figure 4.10 Classification of co-cultures by eye is ineffective due to the broad range of phenotypes on show. Participants with a background in biology, who are more experienced in interpreting fluorescent images, had a lower average accuracy than those without any background in biology.**



A confusion matrix, outlining the ability of automated co-culture segmentation to distinguish between two and three cell types, is shown in Table 4.1. The higher rate of error in fibroblast classification may be attributed to the inherent difficulty in cell detection from image based screens – their tendency to interact by climbing on top of other cells can lead to spurious detection of cell boundaries. Endothelial cells, however, tend not to grow above a monolayer and to form a ‘cobblestone’ layer which is more readily segmented into individual cells. A third cell type was introduced with minimal mis-classification.

		Machine Learning Classification				Hit Rate
		Total Cells	Fibroblast (hTERT)	Endothelial (LE2)	Osteosarcoma (MG63)	
Actual Cell Type	Fibroblast (hTERT)	5972	5362	610	-	89.7 %
	Endothelial (LE2)	4265	1043	3222	-	75.5 %
	Osteosarcoma (MG63)	468	4	23	441	94.2 %

**Table 4.1 Confusion matrix of ML classification showing three cell types classified using CPA.**

After initial seeding of the two cell types at an even density across the nanotopographical gradient, the ratio of endothelial to fibroblast cells varied over time as a function of the underlying and local topographical motifs. Cells were fixed after 96 h culture, resulting in a final distribution of cells which was a combination of proliferation and migration – which have both been shown to be influenced by nanotopographical stimulation. The number of fibroblasts was found to fall steadily with increasing nanopillar height, whilst there was a moderate increase in the abundance of endothelial cells with increasing pillar height – although endothelial cell numbers also fell away at extreme pillar heights.

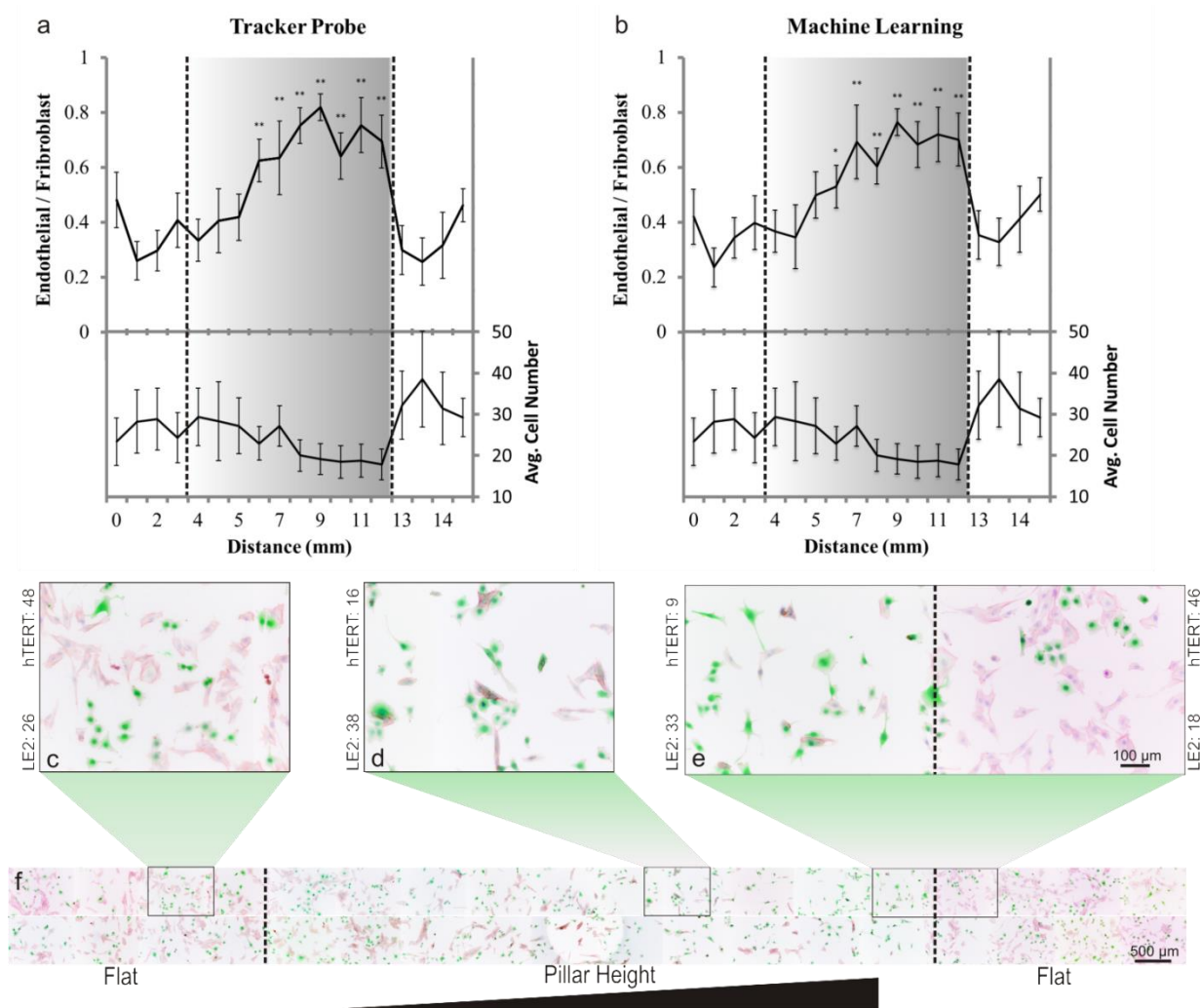


**Figure 4.11** Response of fibroblast (hTERT-BJ1) and endothelial (LE2) cells in co-culture to a gradient of nanopillar height is shown. The ratio of endothelial / fibroblast cells after 96h culture was calculated by (a) direct labelling of the sub-populations with CellTracker probes and (b) applying machine learning to cell morphology and nucleus data to predict cell type – greyscale background gradient represents increasing pillar height from left to right with dashed line indicating the nanopillar-flat boundary. Statistically, each data point was compared to the ‘baseline’ flat region, \* $p < 0.01$ , \*\* $p < 0.001$ . Images c, d, e show cellular response at various points across the nanogradient sample, f. From this analysis, it appears that nanopillar height in excess of approximately 75 nm is sufficient to induce a statistically significant change in the ratio of endothelial / fibroblast cell, however as pillar height increases the average number of cells per image fell.

The average major axis length of endothelial and fibroblast cells was 54.9 μm and 72.8 μm respectively, giving a nominal local gradient in pillar height of 1.53 nm and 2.02 nm across the 9 mm surface gradient. This did not appear to be locally steep enough to drive any directed cell migration. A steeper local gradient of pillar height may have led to

directed migration (i.e. polarisation) from tall to short, however there was no statistical variation in cell orientation which may have indicated directed migration on this topography.

Comparison of the ratio of endothelial to fibroblast cells as pillar height increases suggests that there is a height at which the cell selective response of the topography is ‘switched on’ and a statistically significant change in the ratio is observed. At the same time, a reduction in the total cell number is also observed as pillar height increases which is not exclusive to the fibroblast population, Figure 4.11a,b. This apparent repellent effect of tall nanopillars on both endothelial and fibroblast cells leads to a conclusion that to maximize cell number with the lowest possible ratio of endothelial / fibroblast cells, a pillar height of approximately 75 nm is recommended. This is a promising result, which may be practically applied to the design of cell culture dishes to reduce fibroblast contamination in primary endothelial cultures, and to attempt to prevent restenosis of cardiovascular stents, where the potential of the nanotopography to expedite *in situ* endothelialization may offer considerable benefits in terms of implant success.

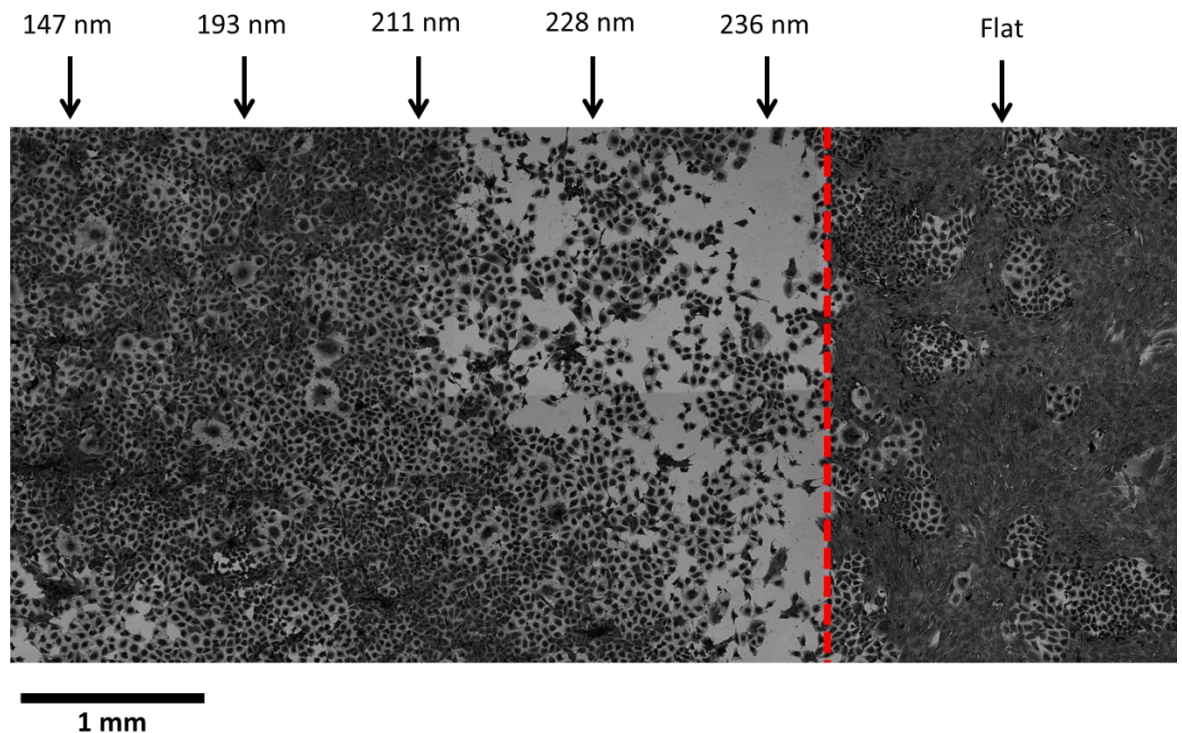


**Figure 4.12 Nanopillar array with a gradient of feature height from left to right. Nanopillars effectively drive separation of two cell types, with endothelial cells remaining and proliferating on the nanopillar array, whilst fibroblast cells have migrated away to the flat**

**region adjacent to the array. Characteristic endothelial cell morphology is visible on the structured region and also on the flat surface, whereas the well spread fibroblast morphology is only visible on the flat area.**

In the data set of 10,237 cells, 1,653 cells were miss-classified. This amounts to a success rate of 83.9% in the classification of co-cultures by machine learning algorithm, which may be open to improvement through further optimization. Analysis of cell response to the variation in nanopillar height by fluorescent tracker, Figure 4.11a, or machine learning, Figure 4.11a, yield the same interpretation of the data in terms of optimal pillar height – indicating that automatic cell type segmentation of co-culture images by machine learning is a viable alternative to fluorescent tracking or antibody staining. Applying this simple and rapid co-culture segmentation technique to gradient and arrayed surface features or chemistries can allow the screening of potential solutions in a context which is closer to the target in vivo system. Large area reorganisation of the two cell populations into superstructures is possible through patterning of nanopillar arrays, and applications may make use of multiple pillar heights to tune response, Figure 4.12.

## **4.5 Principal component analysis**

Automated detection and measurement of cells cultured on structured surfaces was initially approached as a means of quantifying a single feature, i.e. alignment to the microgroove gradient detailed in **Chapter 3**. Moving on from there, this chapter has demonstrated the use automated detection to measure the morphological profile of cells. The volume of information which is produced by CellProfiler analysis of fluorescent datasets requires a new way of extrapolating the true changes in cell morphology rather than the standard approach of looking at a single feature – i.e. area, perimeter, orientation, and others. This requires the implementation of data analysis techniques such as principal component analysis (PCA) to fully understand the source of variance in the dataset, which may be compounded across many features. The CPA classifier is trained by the user, who selects cells of each type by visual inspection and classifies them accordingly. A sufficiently large training set of approximately 200 examples per phenotype is required to generate a robust set of rules that are capable of accurately classifying unknown cells into either group. There is, therefore, an element of intrinsic bias introduced if pure training sets are not available.

PCA is a multivariate analysis technique which reduces the dimensionality of large datasets, and so is well suited to the analysis and interpretation of the large measurement datasets produced by processing immunofluorescence images with CellProfiler. With over 200 measurements recorded for each cell, and thousands of cells per measurement/experimental condition. The variation in the dataset is reduced into principal components which describe as much of the true variance of the dataset in as few variables as possible. The dataset, containing measurements in a broad range of units with differing levels of variance, must be standardised to prepare it for PCA. Each variable in the data matrix was divided by the standard deviation of that variable across the dataset – thus centring the data around zero and allowing PCA to find the correlation between measurements (Appendix C).

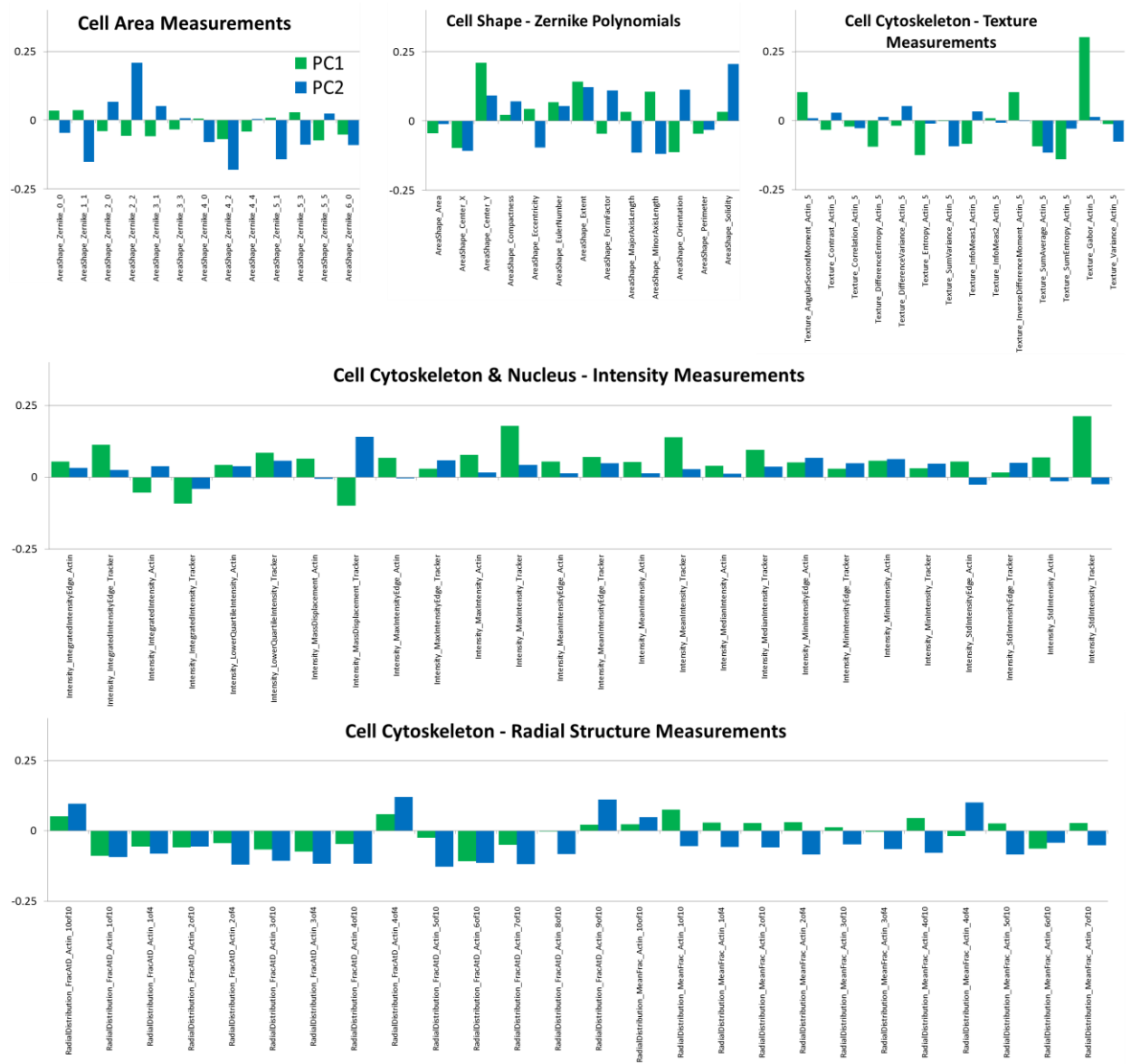


**Figure 4.13** Loading plots showing the relative impact of different measurement classes on the first two principal components. These two components define over 50% of the total variance in the dataset, which is composed of 137 measurements per cell – collectively referred to as the cell ‘cytoprofile’. Here, measurements are displayed in subgroups relating to their type, i.e. measurements of intensity, texture, shape, distribution and area.

Loading plots show the relationship between variables in the multivariate dataset and the subspace variables – i.e. the principal components. Figure 4.13 plots the relationship of the 137 variables per cell which were used to perform principal component analysis. These are coloured by groupings based on the measurement class, using custom MATLAB® code to generate the plot. The first two principal components, which define over 60% of the variance of the dataset in this case (see Figure 4.14) are a combination of

these 137 measurements, with the relative weight of a single measurement on a given component defined by the vector length and location in the loading plot. Grouping of measurement types in regions of the plot is apparent, with intensity measurements grouped in the upper left quadrant, and radial distribution measurements grouped in the lower left. These are measurements of the cytoskeletal intensity and distribution within the cell, and so indicate that the impact of nanopillar substrates has a direct effect on the organisation of both fibroblast and endothelial cell structure.

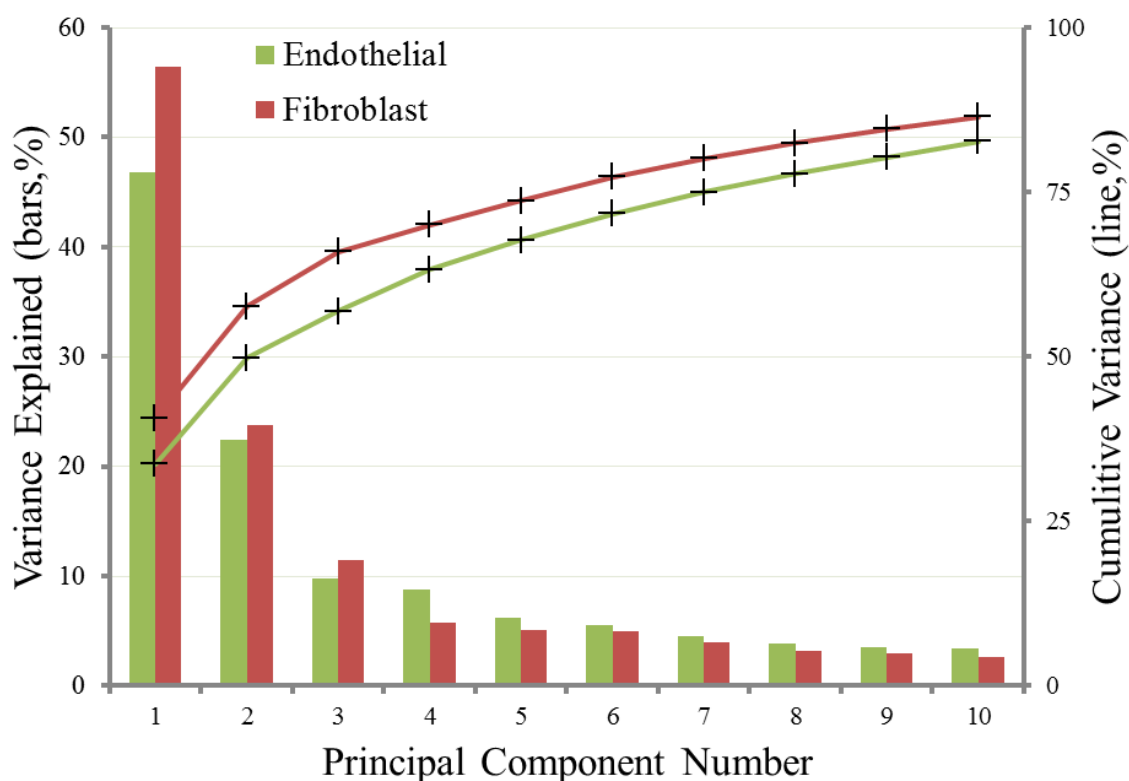


**Figure 4.14** Variance explained by the first 10 principal components of fibroblast and endothelial cells on a nanopillar gradient.

PCA was performed on this segmented dataset in MATLAB®. The code used has been included in an appendix to this thesis. A total of 137 measurements were included, with both cell types extracted from the co-culture dataset using the intensity of tracker dye to segment the dataset (97% accurate). 80% of the total variance in the dataset was explained by the first 10 principal components, with the endothelial subset proving to be less dimensional as it was more readily explained in fewer components, as seen in Figure 4.14 above. The first two principal components accounted for 50% and 58% of the variance seen in fibroblast and endothelial populations respectively.



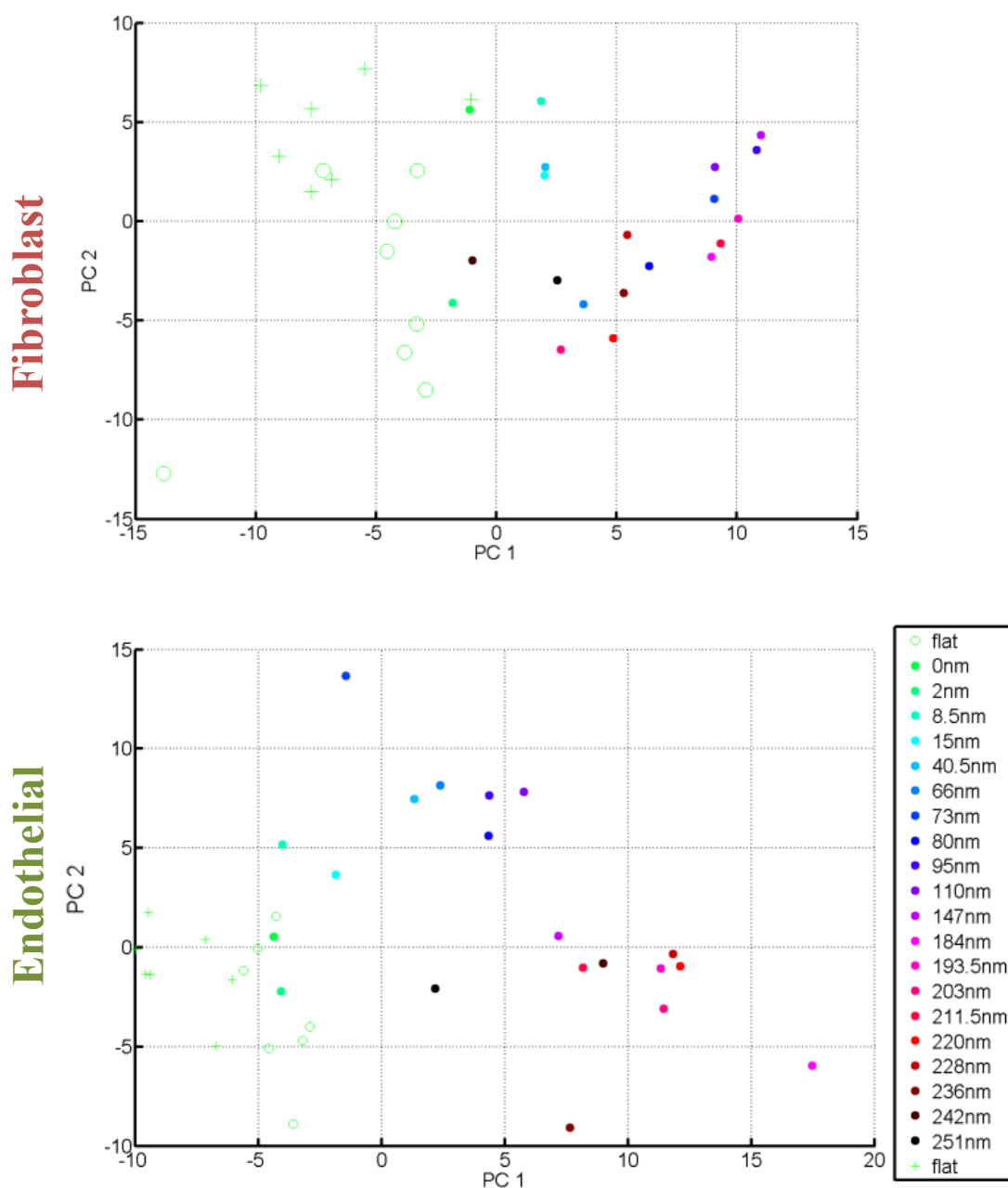


**Figure 4.15 PCA scatter plot for fibroblast and endothelial cell phenotype on nanopillar gradient array with gradient spatial resolution of  $450\ \mu\text{m}$ .**

Figure 4.15 shows the fibroblast and endothelial cell morphologies, as described by the first two principal components of the dataset. Datapoints have been colour coded to correspond to the underlying topography, with each point being a  $450\ \mu\text{m}$  wide section of the sample. The most striking aspect of Figure 4.15 is the separation of fibroblast datapoints which define cells on the flat regions on either side of the gradient array. Data from the flat region nearest the short end of the pillar gradient (+) differs starkly from data acquired on the flat region adjacent to the tall end of the pillar gradient ( $\circ$ ). This is a



surprising result, as one might expect the morphology of cells on the same surface to be equal. In fact, as nanopillar height increases from short to tall (green-blue-red-black) similar pillar heights are clustered together. Endothelial cells do not show any distinction between flat regions depending on the height of adjacent pillars, with the data instead clustering in three broad categories of flat, short and tall pillars:

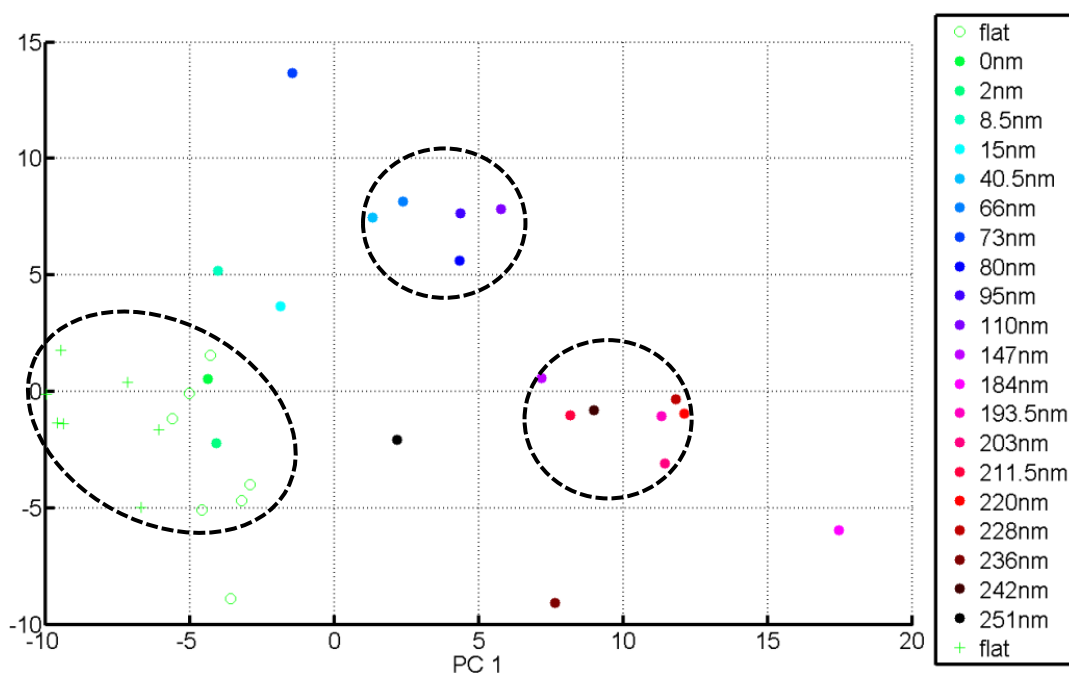


**Figure 4.16 Endothelial cells on the nanopillar gradient array separate into three distinct clusters after PCA – indicating a change in phenotype which is linked to nanopillar height. Datapoints are circled to highlight their separation, this delineation does not represent any statistical analysis of their proximity.**

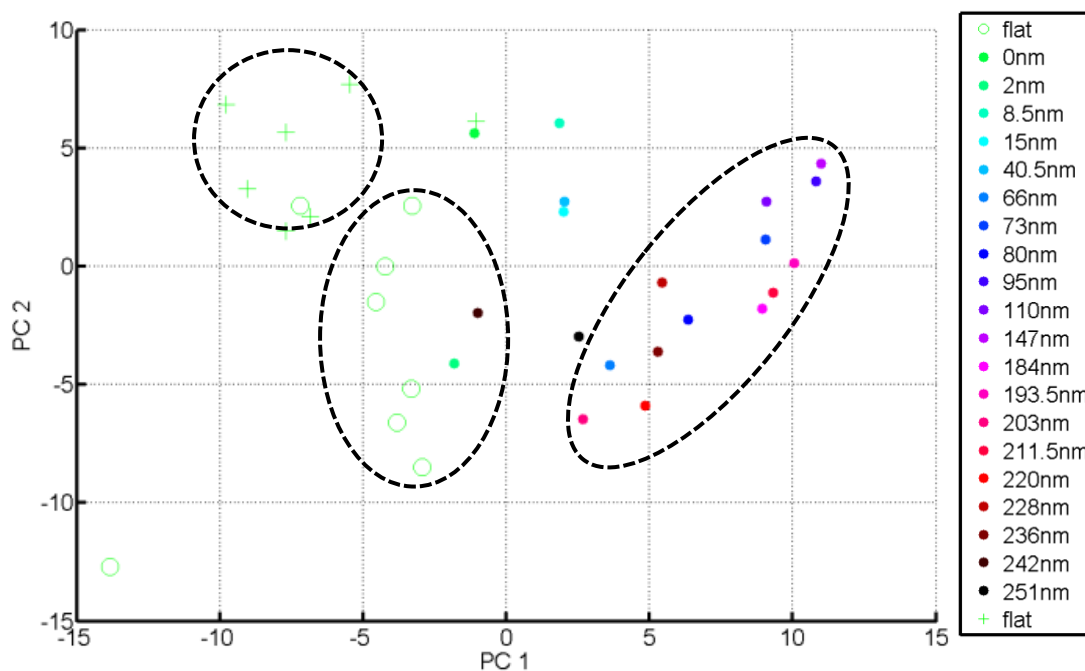


**Figure 4.17 Fibroblast cell morphology appears to group into distinct regions depending on cell location with respect to nearby pillar height. Datapoints are circled to highlight their separation, this delineation does not represent any statistical analysis of their proximity.**

In Figures 4.17-4.18, the resolution of analysis has been increased, making use of the same dataset presented in Figure 4.7. Absolute cell locations on the gradient were calculated, allowing cells to be segmented into a range of 20 bins along the length of the nanopillar gradient. These bins were evenly spaced in 450  $\mu\text{m}$  increments along the 9 mm height gradient, and each bin was correlated with a nanopillar height acquired by AFM. Division of the dataset into still smaller bins is possible, however 20 were deemed appropriate to limit the complexity of visualisation. Using 450  $\mu\text{m}$  bins gives a nominal gradient of pillar height within each datapoint of 12.5 nm.

## 4.6 Conclusions

Building on previous work using nanopillar arrays in PCL substrates, this work combined both cell types in a single experiment – yielding results which correlate with the previously reported data. Using a new platform of nanopillar gradient arrays, the further development of high-content screening methods reported here results in a drastic improvement in experimental throughput on a single sample. Rather than screening two cell types on multiple samples with different topographical features, a single experiment

can now capture the response of multiple cell types across the full range of nanopillar heights from flat to over 250 nm, Figure 4.18. The key benefit is that the gradient array platform is fabricated by a single etch step, whereas masters for fabricating a range of individual samples would each require separate etch cycles for each desired depth. In this case, nanopillar heights between chosen values would have been excluded from the sample set, whereas with a continuous gradient the full sample space can be explored. Further to this, co-cultures were used instead of separate monocultures – better reflecting the applications of engineered surfaces in which multiple cell types are present and all must be ‘guided’ towards a desired response. The use of machine learning techniques to segment these two cell types on a single sample has added potential benefits as it removes the need to use a fluorescent channel to label each cell type individually. This allows for more information to be garnered from a single sample, by also labelling for a protein of interest or cellular structure.

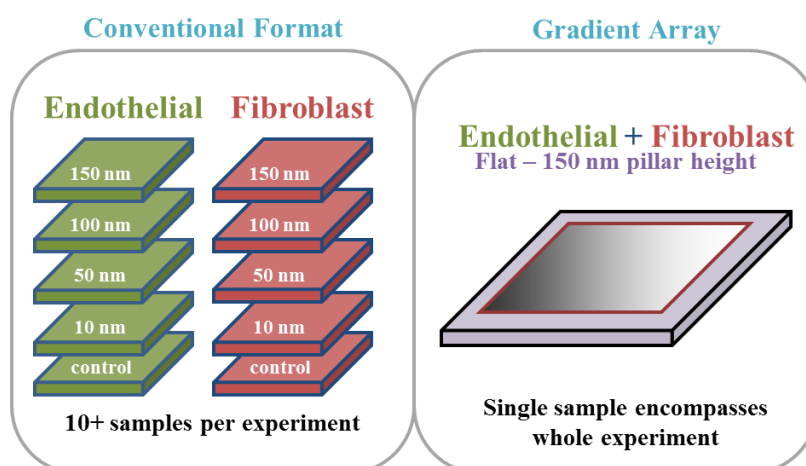


**Figure 4.18 Gradient platforms offer a drastic increase in the yield from a single experiment. Multiple samples are required in conventional experiments, left, each with a unique surface property. Combining this variation onto a single sample, right, simplifies experiments. Further progress in automated detection of cell type also allows co-cultures on a single sample.**

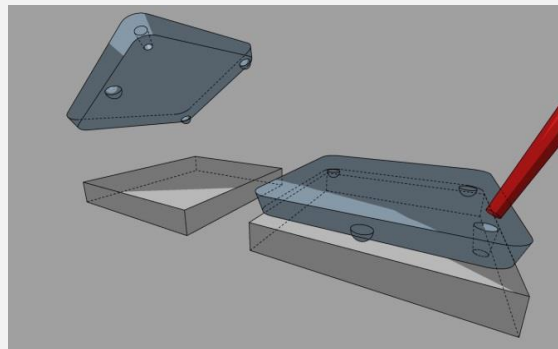
An accuracy of >84% was demonstrated using a new label free segmentation technique of co-cultures, which leaves room for improvement when compared to cell type specific labelling.

Lateral resolution on the gradient was considered, in terms of the analysis method and also the data processing involved. Full sample imaging on a flatbed scanner showed the global density of cells, whilst tiled brightfield images improved resolution and allowed for quantitative investigation of relative cell densities of two cell types. The main dataset was acquired as immunofluorescent images of the cell nucleus, cytoskeleton, and a CellTracker dye. After initial analysis on a per-image basis, in which the frame size was approximately 0.9 mm across, the lateral resolution was improved by dissecting images into two halves of 450  $\mu\text{m}$  each. This yielded more detail in the difference in cell response across the gradient. Automated cell detection and measurement makes it possible to continue this improvement in resolution to single cells, relating a given cell phenotype to its underlying nanopillar height and this may provide still more information on the changing phenotype across the nanopillar gradient array.

This stepwise increase in resolution appears to show that biological systems are acutely sensitive to variations in the topographical substratum on which they find themselves – from the broad system down to the single cell. Chapter 6 looks at this idea in greater detail, investigating whether subcellular structures can sense and adjust themselves in response to changes in topography within a single cell.

## 5 Uniform cell seeder

**Background:** Cell seeding on tissue culture plastic or patterned substrates is done by hand – often giving an irregular spread of cells across the culture area due to a lack of control of the seeding space and volume. High-content screening arrays and gradients demand that cells are evenly distributed to yield reliable results. A device was designed and tested to address the issue of inhomogeneous cell seeding in cell culture studies on 2D screening platforms.

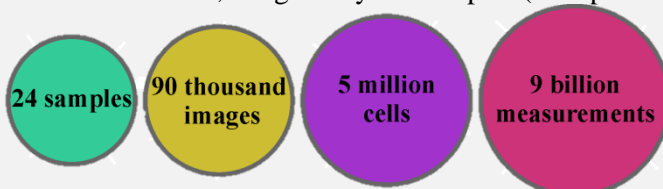


**Results:** Custom tooling was fabricated by CNC milling of aluminium to create uniform cell seeder devices by injection moulding. This fabrication route is ideal for this type of disposable labwear. Seeding cells at various densities on both patterned and blank injection moulded substrates, along with 12- and 6-well plates showed a drastic improvement in seeding uniformity across the culture area.

**Conclusion:** Standard seeding methods introduce experimental errors through variation in local cell density. The device fabricated here effectively standardises the seeding process – removing a source of experimental error and improving repeatability between experiments, users, and labs. Cell coverage and response on gradient topographies could be interpreted properly thanks to even distribution at the point of seeding. Furthermore, the impact of variation in local cell density on stem cell differentiation was demonstrated – showing that within individual wells of a multiwell plate there were disparities in marker expression which could be homogenised using the uniform cell seeder. This shows that the device has applications in broader cell culture use, and is not limited in its applications to high-content screening platforms.

### Experimental:

Length scale: millimetre scale cell culture vessels  
 Cell type: rat endothelial (LE2), human embryonic stem cells (hES)  
 Analysis: 10x immunofluorescence image arrays  
 Dataset: 3 fluorescence channels, image arrays of samples (well plates/injection moulded)



### Output:

An international patent on the technology was filed in May 2014. A paper presenting this work is currently in preparation. All work in collaboration with Camilla Holzmann Rasmussen, PhD student at Novo Nordisk and the Technical University, Denmark.

## 5.1 Introduction

Biological experiments involving cell culture, from biomaterial testing [1], [110], [129], [130] to drug discovery[7], [131] often begin with cells being seeded onto a flat substrate to form a two-dimensional culture. This is the foundation on which the experiment as a whole is built, and is therefore arguably one of the most critical steps. Common practice for this crucial step often varies between disciplines, laboratory's, individual researchers, and even from day to day. Suggested protocols exist, however these recommended methods by no means eliminate user dependence [132]. Such user dependence can in turn introduce huge variability to the results and mean others struggle to reproduce the work. There is a growing concern in the scientific community regarding the reproducibility of high profile work[133][134], and as such a method for the standardisation and deskilling of a key part of cell culture studies is of critical importance. This compliments published methods for statistical analysis and data presentation, towards a more consistent experimental process across cell biology studies. The manner in which almost all researchers seed cells onto a flat surface can be roughly categorised into two methods. Either a droplet of fluid is placed on the substrate, and the vessel back filled with culture media after a period of attachment, or the substrate is immersed in culture media, with a concentrated cell suspension then pipetted over the substrate in as even a manner as possible. The literature also suffers from the confusion of listing cell seeding densities in either  $\text{ml}^{-1}$  or  $\text{cm}^{-2}$ .

Uneven seeding arises using these methods due to three factors – the macro scale turbulent flow of cell seeding suspension as it is added to the well, disturbing the cell suspension as plates are moved to the incubator, and also to a lesser extent the meniscus which forms around the wall of the culture plate. The impact of the meniscus becomes more prominent as the culture vessel becomes smaller, i.e. 96 well plates.

The problems associated with uneven cell seeding are aparent in the volume of forum posts (e.g. at researchgate.net) from students looking for help in improving their seeding, after struggling with experimental variability. Studies investigating the otimal means of cell seeding have sought to identify the source of uneven cell distribution[135]. The direct impact of cell seeding practices on the behaviour of osteogenic cells on titanium fibre meshes has also been demonstrated[132], so there is a clear need for improvement.

Cell seeding approaching a ‘perfect’ distribution has been demonstrated using microfluidic channels in which the cell suspension is delivered to the surface under laminar flow conditions (i.e. no turbulence)[136], however outwith the context of microfluidic studies there remains a need to improve the efficiency of cell seeding. Whilst broader investigations into the impact of cell seeding have attempted to resolve the issues, the proposed solution was still a cumbersome microchannel approach, which is incompatible with large area culture and time consuming to implement[137].

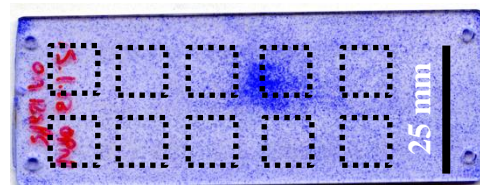


**Figure 5.1** The problem of uneven cell seeding. Pattern arrays are seeded with varied concentrations of cells.

The injection moulded slide shown in [Figure 5.1](#) has an array of nanopatterns across the surface in a 5 x 2 configuration of squares. Cells were seeded using standard seeding techniques by a post-doc with no affiliation to this project. The deficiencies in this seeding method are evident, with a central aggregation of cells and sparse coverage in outer regions. Cells were allowed to attach in the flow hood for 30 min before the slides were moved to the incubator. After 6h the cells were fixed in PFA and stained with Coomassie blue. It is clear that seeding array slides in this manner leaves experimental results prone to error and misinterpretation.

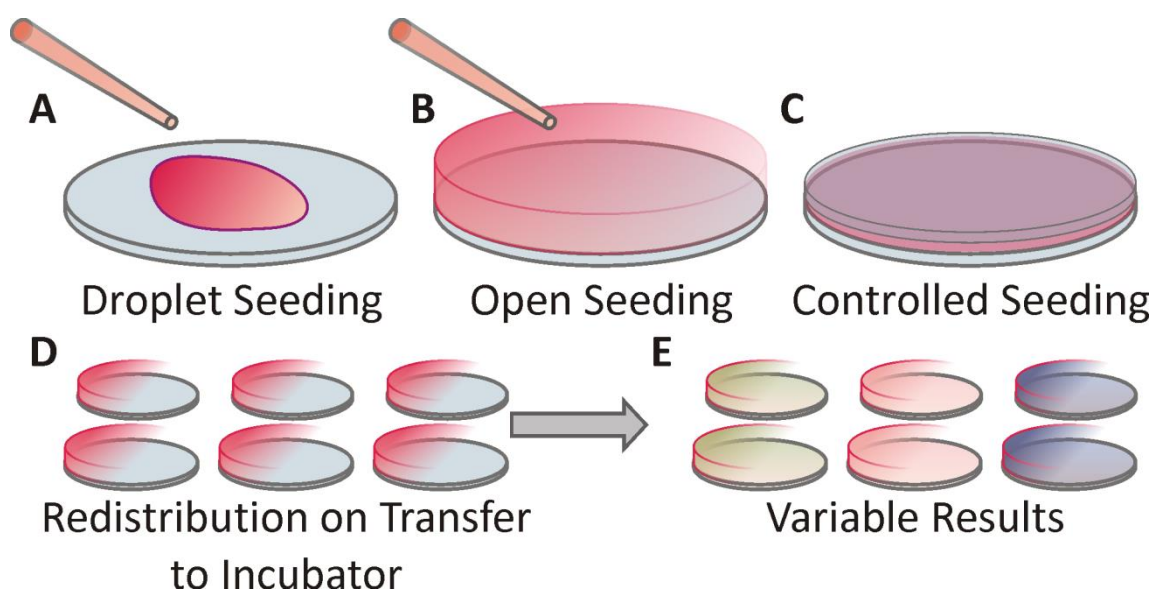


**Figure 5.2** Cell seeding methods can be divided into three categories; pipetting of a single droplet of cell suspension onto the surface (A), filling the culture vessel with media and

**pipetting a concentrated cell suspension into the fluid (B), and the method presented here – a rigid surface placed 1mm above the surface which confines the cell seeding volume in a defined volume across the full sample (C). Movement to the incubator for culture (D) represents a critical step, whereby redistribution of unattached cells due to flow within the well causes uneven distribution, generally in the centre of the well due to centrifugal flow. Final analysis of results (E) is therefore affected by this uneven distribution in the plate – leading to increased experimental error.**

Comparison of three common seeding techniques has shown a widespread variation in homogeneity, both between methods and also between users. Seeding cells as a sessile drop onto surfaces results in a much higher density in the centre of the drop compared with the periphery. Essentially, the distribution conforms to the shape of the cell suspension media at the time of seeding, Figure 5.2. To that end, the device presented here uses capillary force to hold the cell suspension 1 mm above the substrate across the whole substrate area.

An uneven initial seeding will create local cell densities across a well or an assay, Figure 5.2. Several studies have shown that the cell density affects cellular behaviour due to cell-cell communication, cell shape and mechanical coupling between cells and the extracellular matrix[138]–[140]. The commitment and differentiation of stem cells is, in particular, highly regulated by cell density [141]. One study showed that the initial seeding density of human embryonic stem cells plays a crucial role for germ layer speciation and affects the later commitment towards pancreatic progenitors[142]. Therefore, it is evident that cell culture studies must be built on a foundation of even seeding density across the full sample space. Issues with uneven seeding also arise in the case of array and screening platforms, whereby a disparity in cell density may introduce noise and variability – leaving the assays open to errors [139], [141]–[143]. Moreover, uneven seeding can skew results when conducting biomolecular assays across an entire well, Figure 5.3. Testing cell response to drug targets, hypoxic conditions or temperature variation in a culture vessel with uneven cell distribution yields a result which is a combination of the experimental stimulus and an average of cell response in various microenvironments caused by uneven seeding.



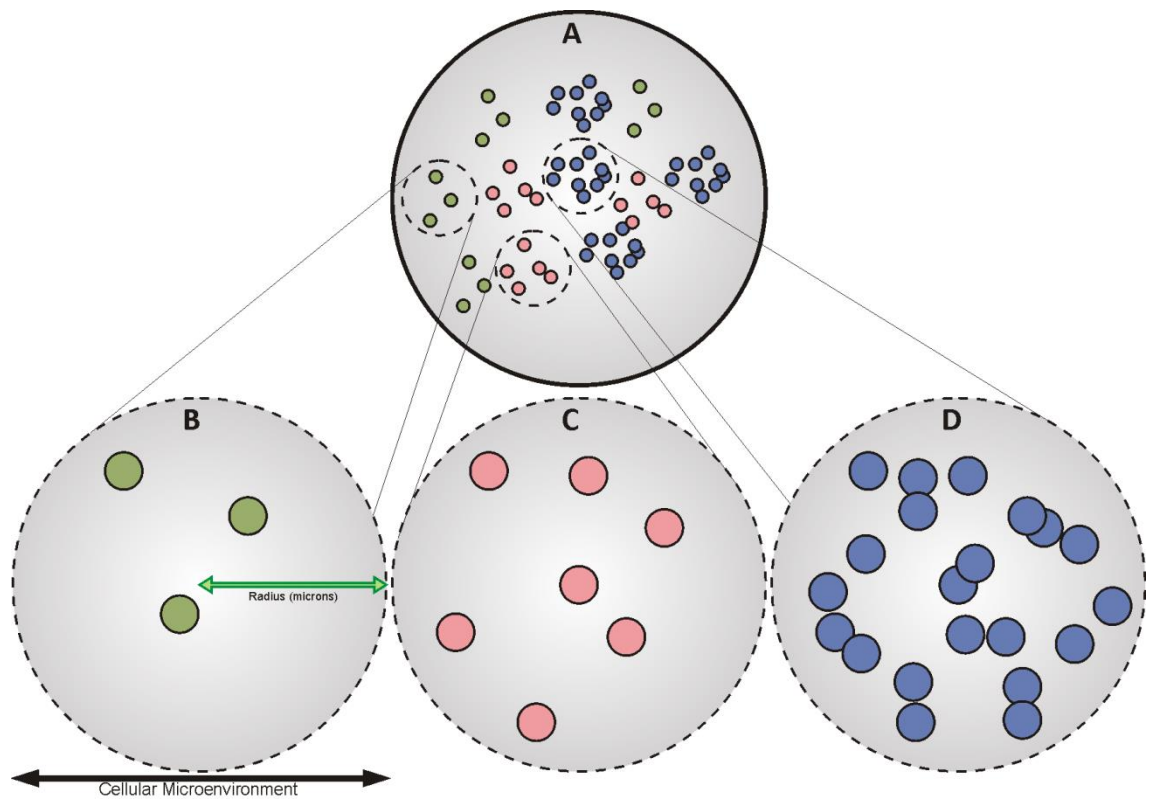


**Figure 5.3 Local cell densities influence cell behaviour through cell-cell communication - both chemical and mechanical. One may envision three terminal cell differentiation states (green/pink/blue) arising from three different seeding densities across a single well. Any further study of cell response to a novel biomaterial or structured surface then becomes a study of a mixed population, unbeknownst to the user.**

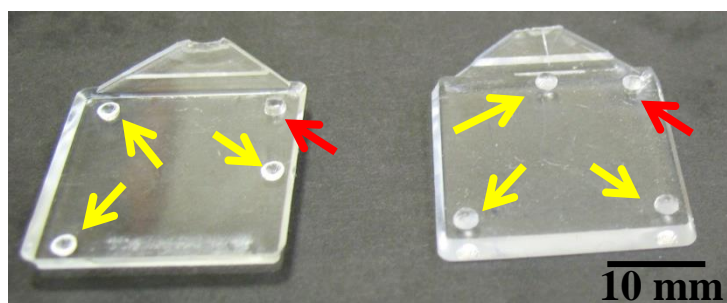
Frequently, studies investigate the control of cell behaviour by modulating small microenvironments[144], [145]. This seeding technique which allows the precise homogeneous control of the cell microenvironment across millimetre length scales – yielding improvements in attachment efficiency, differentiation potential and final experimental outcomes. Local density has been shown to influence the lineage commitment of various stem cell types, for example three distinct seeding densities may exist in a single well due to uneven seeding distribution, Figure 5.3. *Lu et al* reported a divergence in lineage commitment which was dependent on density[138].

## 5.2 Methods

### 5.2.1 Device fabrication

The uniform cell seeder (UCS) required fabrication at an entirely different length scale as compared to the work of **Chapters 3 & 4**. It was evident that the UCS could be a simple piece of disposable labware, and therefore a mass fabrication route was used to make the device available to as many collaborators as possible. Injection moulding of thousands of UCS devices for distribution alongside injection moulded micro- and nanopatterns was seen as a means of improving experimental consistency across users and labs alongside other benefits of homogeneous cell seeding. A custom inlay was milled from aluminium on a CNC machine, however the tooling design and operation is not covered in this thesis.

**Figure 5.4** Injection moulded UCS devices. Three feet hold the device 1 mm above the surface to be seeded (yellow arrows) whilst an inlet allows for the injection of cell suspension (red arrows)



UCS devices were injection moulded in polycarbonate, as a square of plastic with three feet which create a constant 1 mm gap between the surface and the UCS, Figure 5.4. An injection hole was included to allow cell suspension to be added. Studies in 12-well plates required a circular seeder geometry which could not be injection moulded using the tooling available. A set of 12 seeders were individually machined from a 3mm polycarbonate sheet. Spacers of 0.5 mm width which held the device 1 mm above the well surface were included around the circumference of the device, Figure 5.5.

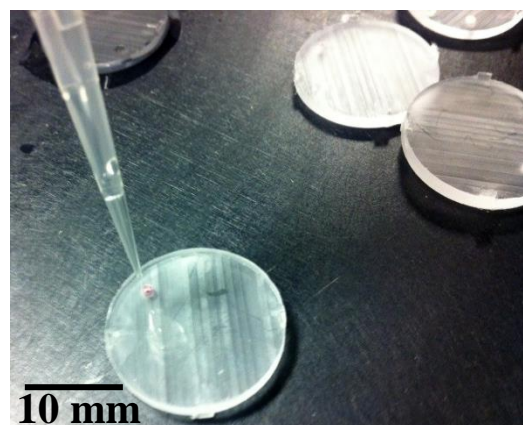


**Figure 5.5** UCS devices were machined from polycarbonate for use in 12-well plates.

### 5.2.2 Cell seeding

Human fibroblast cells (hTERT-BJ1) were suspended in DMEM media at a concentration of  $50 \times 10^4$  cells per ml. Cells were seeded onto planar tissue culture surfaces at three different seeding densities by three methods;

- I. Droplet seeding, whereby a concentrated droplet of cell suspension is placed in the centre of the well. The cells were allowed to attach at room temperature for 1 – 2 hours before the well was backfilled with media. [Figure 5.2A]
- II. Open seeding, whereby the well was filled with 2ml of culture media, and a concentrated cell suspension pipetted into the media. [Figure 5.2B]
- III. Controlled seeding, by placing a UCS device in the well, and filling the fluid cavity with cell suspension through a filling hole. [Figure 5.2C]

Substrates were left stationary for 10 min, before being moved to an incubator for a further 50 min. They were then fixed using 4% paraformaldehyde at 37C for 10 min, and stained with Coomassie blue for 5 mins before washing 3 times in 1X PBS. Inspection revealed that in this timeframe, cells had been given enough time to attach to the surface without fully spreading or beginning to migrate. Fixing at this time point gives a realistic snapshot of cell distribution on the surface after seeding. Array images were acquired using an Olympus CX41 upright microscope equipped with a Prior motorized stage and 10x objective. Automated scanning and acquisition across the surface was driven by ImageProPlus (Media Cybernetics, UK) to capture a contiguous array of at least 5 separate samples for all cell seeding methods outlined above. These images were analysed using the CellProfiler software suite (Broad Institute, Harvard, USA) to automatically detect and count cells in each frame.



**Figure 5.6** The uniform cell seeder is filled by injecting cell suspension through a hole in the lid. It sits on the surface with spacer feet creating a fluid shaping volume which is a defined height across the sample - therefore homogenising cell density.



### 5.3 Cell seeding accuracy and its implications in vitro

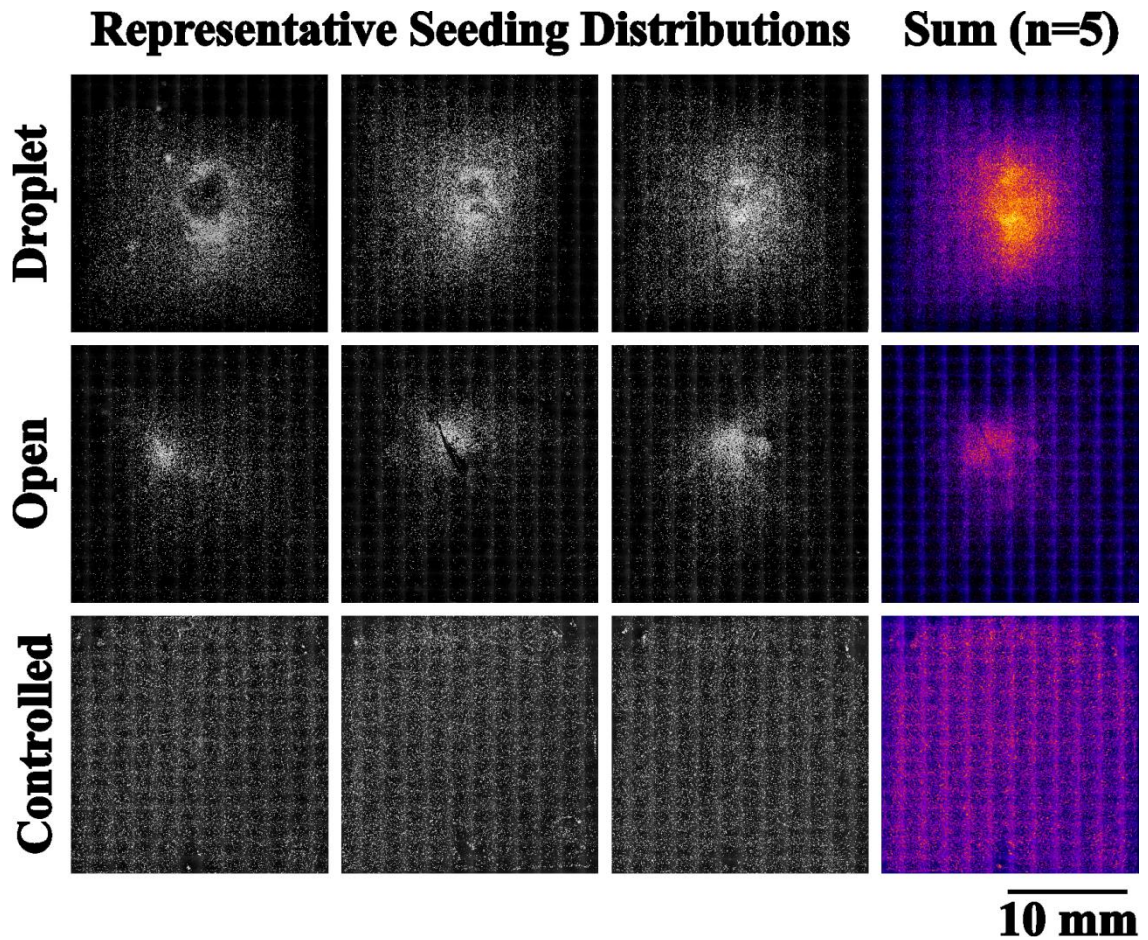
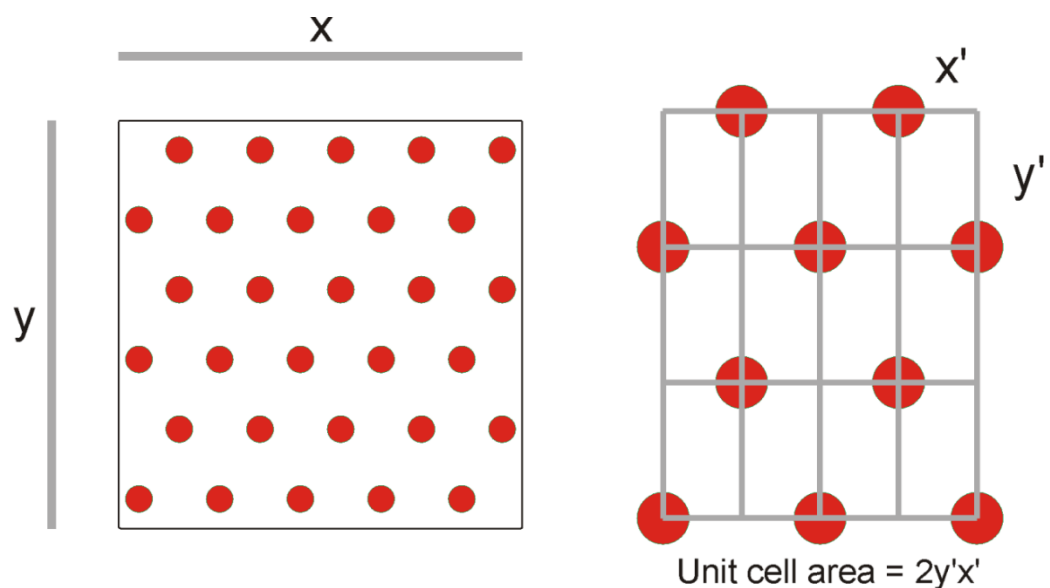


Figure 5.7 Common sample seeding methodologies distribute cells across injection moulded samples in a heterogeneous manner which is undesirable. Controlled seeding using the UCS device results in a drastic improvement in the uniformity of cell distribution on the substrate – as evidenced by the lack of cell density ‘hot spots’ in summed images of 10 samples (rightmost images).

Figure 5.7 shows the variation in cell density which results from the seeding methods outlined in Figure 5.2. Droplet seeding creates a dome of fluid which is higher in the centre than at the edges – as cells settle out of suspension the greater volume in the centre results in a greater concentration in the centre. In the case of the three samples shown above, a single sample has both sparsely populated and fully confluent regions within 6 h of seeding. Similarly, using the open seeding method does not distribute cells evenly. In this case, where the substrate is submerged in culture media and a concentrated seeding suspension is pipetted onto it, the location of droplets influences density across the

substrate. Not only are their confluent and sparse regions on a single sample, but the target seeding concentration is missed as cells settle in the culture vessel rather than on the sample.

Qualitative analysis of cell seeding was carried out to identify problems with the current methods used in virtually all cell seeding studies. In order to compare samples and methods, a model for 'perfect' cell seeding is proposed as one in which cells are equidistant in the 2D space as they settle onto the surface and attach, Figure 5.8.



**Figure 5.8** The 'quality' of cell seeding on a surface can be quantified in terms of the total number of cells, their distribution across the surface, and the inter-cell spacing. Equidistant cells across a millimetre scale culture vessel is deemed to represent 'ideal' seeding, whereby there are no large scale changes in cell distribution derived from variation from experiment to experiment (i.e. how quickly was the dish moved, was it accidentally knocked).

The accuracy of a given cell seeding technique was defined in terms of the consistency of the local microenvironment across a 12 well plate (20 mm diameter, 3.14cm<sup>2</sup>). Defining this as the number of cells within a radius of 150 μm, large image arrays were captured across multiple wells and culture conditions to understand the seeding distribution resulting from each method. Controlled seeding carried out using the UCS provided more consistent seeding in terms of the local microenvironment surrounding each cell – with a significant reduction in the standard deviation of local cell numbers.

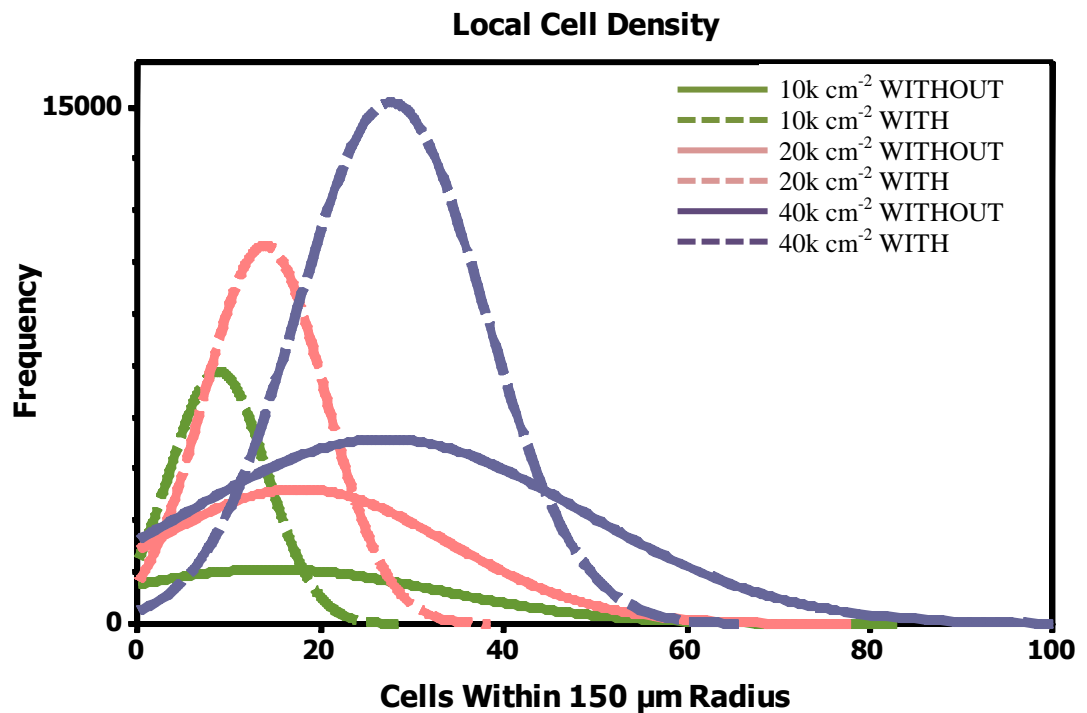
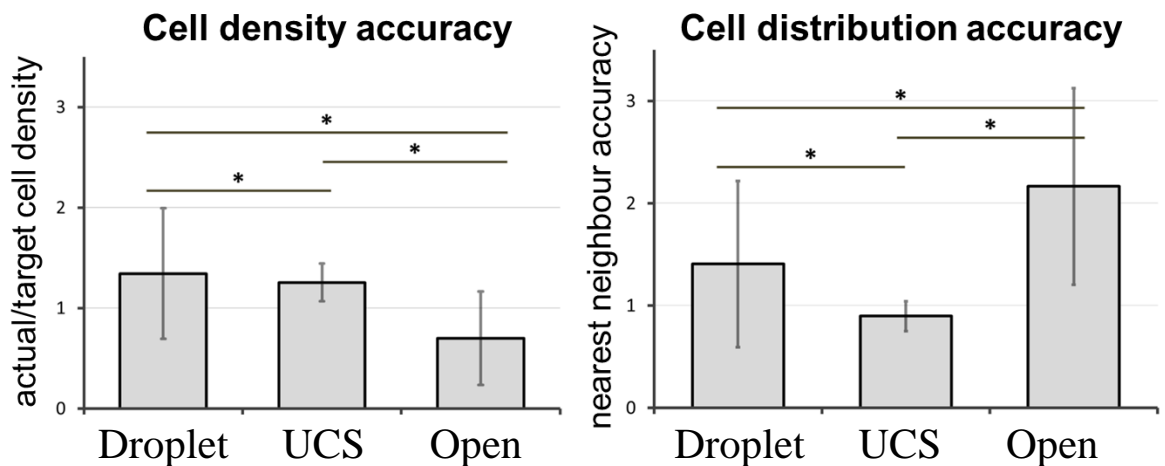


Figure 5.9 Cells can be more accurately seeded with the UCS device when compared to standard seeding without in open wells. A narrower distribution of local cell density values is evident for all seeding densities when cells are seeded using the UCS (dashed lines). Standard seeding methods yield a broad distribution across the full culture space (solid lines).

Other metrics of cell seeding accuracy may be considered, such as the nearest neighbour to a given cell, and the number of neighbours within an area. The dataset consisted of over 500,000 cells seeded using the three methods outlined. The number of cells within a 150 μm radius of each cell is shown for three seeding densities in Figure 5.9, seeded both with and without the UCS device. It is clear that sharper peaks for dashed lines (in which the UCS was used) indicate that across the cell culture area, it was more likely for a given cell to have a consistent number of other cells in its local microenvironment. Using the UCS, a consistently spaced cell culture can be seeded onto the material/array/surface of interest – meaning experiments are more reproducible and may be more reliably compared. Seeding which matched the ideal model presented in Figure 5.8 would be a sharp peak, as all cells find themselves surrounded by an equal number of neighbours in their local microenvironment.



**Figure 5.10** Improvements in cell seeding performance are quantifiable in terms of the cell density across a full culture vessel and also in terms of the distance to each cell's nearest neighbour. As a ratio of target seeding versus actual seeding, the UCS is more accurate compared to droplet seeding and open seeding. Bars show the standard deviation. Data from over 500,000 cells,  $p < 0.005$  student's t-test.

Normalising cell density data allows comparison of seeding which is independent of the quantity of cells being seeded – therefore allowing a general comparison of existing techniques to the UCS device. Figure 5.10 compares three methods of seeding on injection moulded samples, which are 21 mm x 21 mm polycarbonate squares. These were seeded with cells in a 6-well plate using either the UCS device, a sessile droplet of concentrated cell suspension, or by immersing the sample in media and pipetting a cell suspension over it. Both the actual cell density per image and also the nearest cell neighbour are plotted as a ratio of actual to target. In both metrics, the UCS yields a reduction in standard deviation, and resulting seeding is close to the target value. Open seeding, in which the sample is submerged in media before seeding, has the least cells which actually adhere – and these can often be found in the bottom of the well after the experiment is over. When working with rare/valuable populations of genetically modified cells or primary explants, the UCS offers the ability to accurately seed cells in the desired location with minimal wastage to the culture vessel.

The UCS therefore addresses a fundamental issue with gradient and array platforms. It homogenises cell density across the surface, which is of vital importance if the surface contains its own variation in surface properties. These screening platforms can only be reliably used with even seeding, and the UCS enables that.



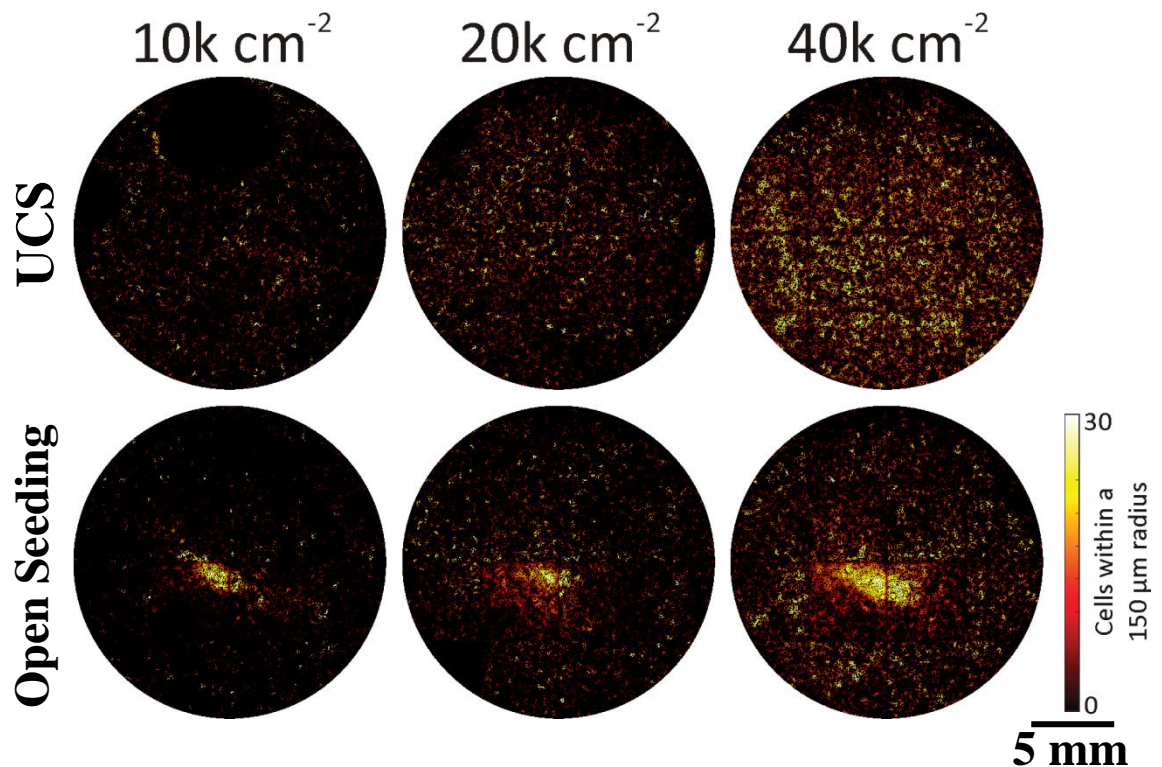


**Figure 5.11** Use of the UCS device leads to a marked improvement in the uniformity of cell seeding. Seeding uniformity is shown as a function of local cell populations - each cell is coloured based on the number of neighbours within a  $150\ \mu\text{m}$  radius – the more consistent the colouring the more even the seeding.

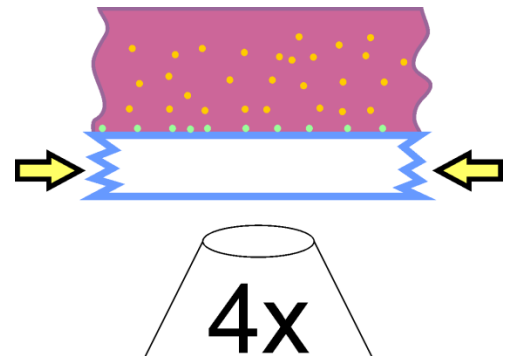
The UCS device addresses the problems of homogeneous cell seeding by confining the seeding suspension above the substrate - yielding a consistent fluid volume and therefore a more consistent cell density from edge to edge. To ensure that the inhomogeneous seeding artefacts were not the result of a single person's poor technique, at least 5 other users have been enlisted who all report improved cell seeding distribution. Figure 5.11 shows human embryonic stem cells, seeded in a 6-well plate by a collaborator in Denmark (Camilla Rasmussen, *Novo Nordisk & DTU, Denmark*). Montage images were captured of the full well after staining the cells for nuclear DNA, and processed using CellProfiler to measure the local density as a function of cell count within  $150\ \mu\text{m}$  radius of each individual cell. This demonstrates control of the cell microenvironment across a millimetre scale culture vessel by using the UCS device.



## 5.4 Cell seeding timescales

The methods for seeding cells on patterned surfaces generally involve a period in which the cells are allowed to ‘settle’ on the lab bench before the culture vessel is moved to the incubator. This is done to minimise fluid flow which may re-distribute cells in an uneven manner, either in a central clump or around the outsides of the vessel. A microscope was equipped with a modified illumination setup to show cells as they approach the surface – similar to interference reflection microscopy. A 10 mm thick glass plate was illuminated from the side with white LEDs, Figure 5.12. As cells settle to the surface they couple light out perpendicularly and into the objective. This revealed that after only 5 minutes the majority of cells are settled on the surface, Figure 5.13. Using the UCS device removes any need to allow this settlement to take place in the cell culture hood. After filling the device with fluid the samples can be transferred immediately to the incubator.

**Figure 5.12 Microscopy setup for imaging the settle time of cells onto a flat surface. Illumination from the side is coupled out into the objective when cells settle to within a few hundred nanometres of the glass plate. Light (arrows) is supplied by LEDs from the side of the plate.**



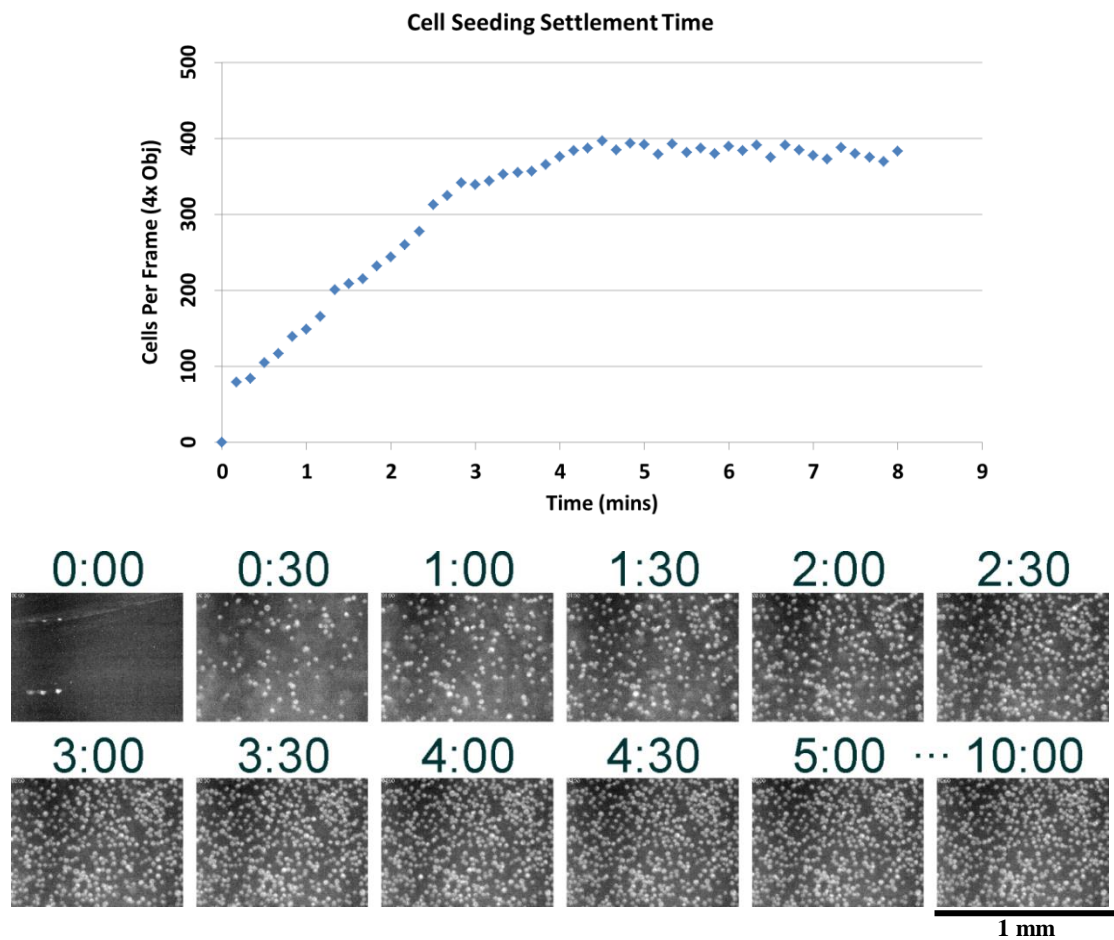


**Figure 5.13** After initial seeding, it takes approximately 5 minutes for the majority of cells to settle to the surface when seeding is performed using a 1 mm high UCS. Top: settlement of cells onto a surface over 10 minutes. An improvised microscope setup was used to illuminate only cells which were touching the surface; bottom images show the settlement over time.

As the UCS device holds the cell suspension fluid in place over the surface, moving the sample after seeding results in little or no fluid flow and therefore little or no redistribution of cells. This is the case as long as the sample container is kept flat, with surface tension maintaining a well-defined fluid volume above the sample. Taking into account that the settlement of cells from solution appears to reach a steady state after only 5 minutes, it is recommended that substrates require no longer than 10 minutes stationary time in the flow hood after seeding. Some user protocols involve leaving seeded substrates/arrays/scaffolds out at room temperature for up to an hour to allow for initial attachment. Bearing the data presented in Figure 5.13 in mind, this can be reduced to 10 min using the UCS with no redistribution.

## 5.5 Improving stem cell differentiation through homogeneous seeding

Whilst the UCS was designed to address the problem of uneven seeding across array and gradient substrates, there are also profound implications for the *in vitro* culture of cell types which are sensitive to local density[141]–[143], [146]. Reports in the literature indicate that local cell density in the microenvironment plays a critical in differentiation behaviour. Therefore, the insights into the quality of standard seeding techniques presented here indicate that researchers are introducing variations in cell density within multiwell plates as standard practice. In the case of hES cells used to generate insulin producing cells for implantation in the treatment of type I diabetes, the literature indicates that the production of pancreatic progenitor cells expressing the marker PDX.1 is density dependent[147]. In collaboration with Camilla Rasmussen, (*Novo Nordisk & DTU, Denmark*) hES cells were differentiated towards the definitive endoderm using a patented protocol from Novo Nordisk, then replated at various densities both with and without the UCS device.

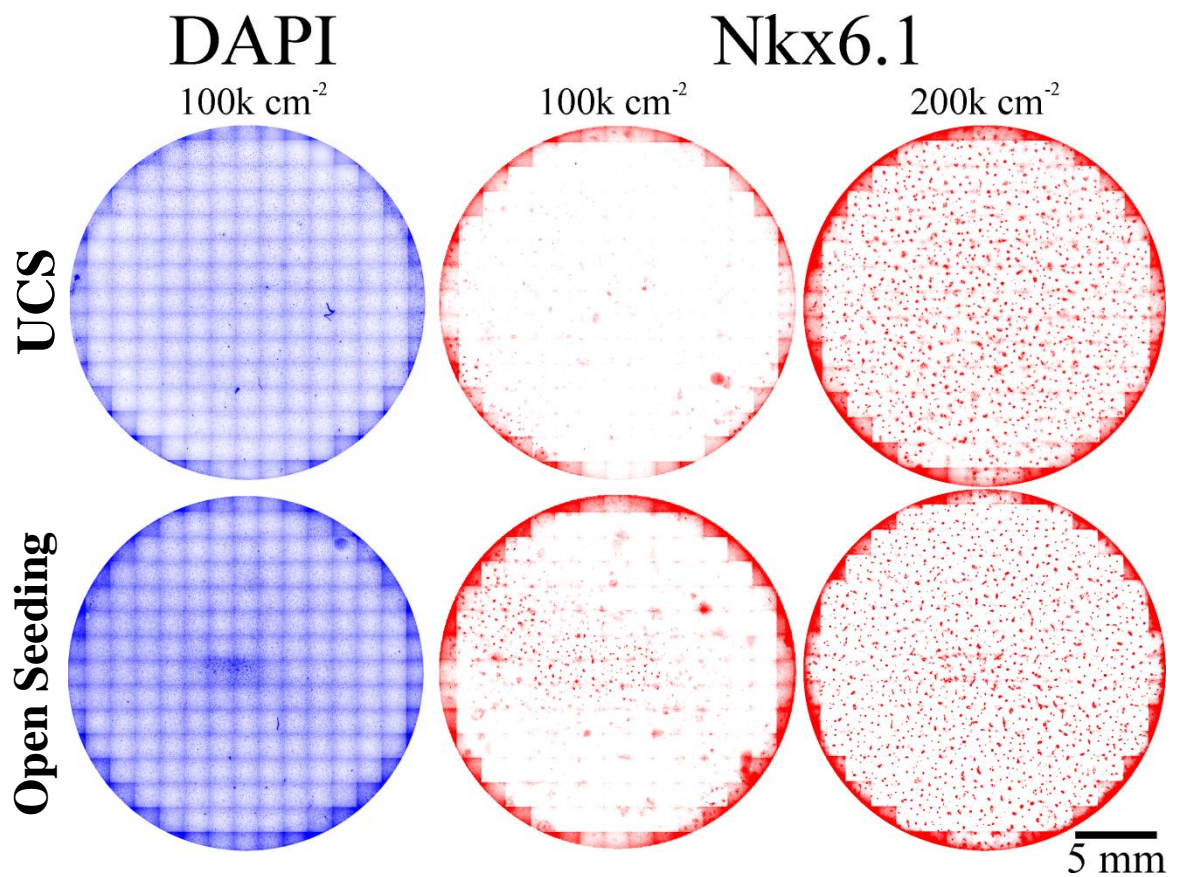


**Figure 5.14** hES cells seeded with the UCS device at a concentration of 100k cells per well after initial differentiation to the definitive endoderm using a proprietary protocol developed by Novo Nordisk.

Example montages of cell coverage using standard open seeding and the UCS are shown in Figure 5.14. Total cell coverage directly after seeding is shown by the DAPI channel, which demonstrates the inherent problem of uneven distribution using standard open seeding methods. Fixation and staining for Nkx6.1, a marker for differentiation to the target state of the pancreatic endoderm, demonstrates that discrepancies in seeding uniformity manifest themselves as discrepancies in differentiation efficiency.

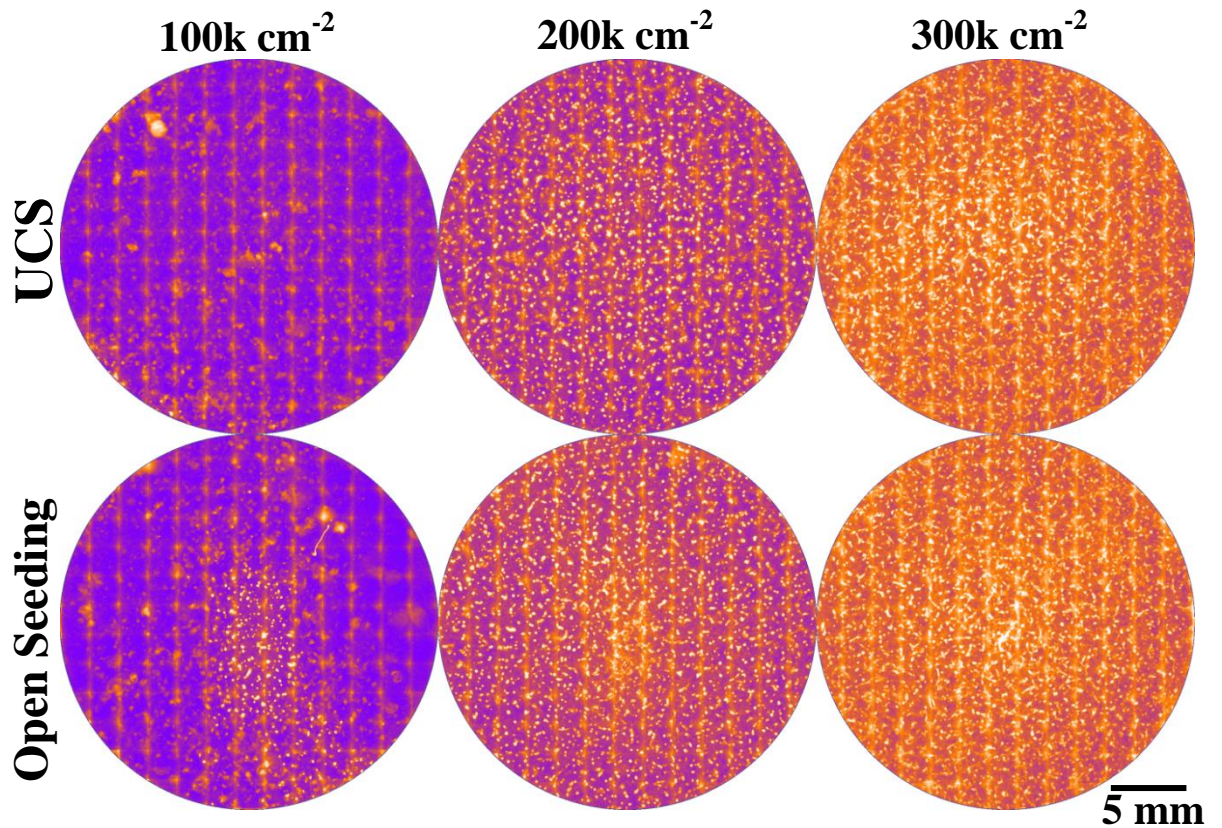
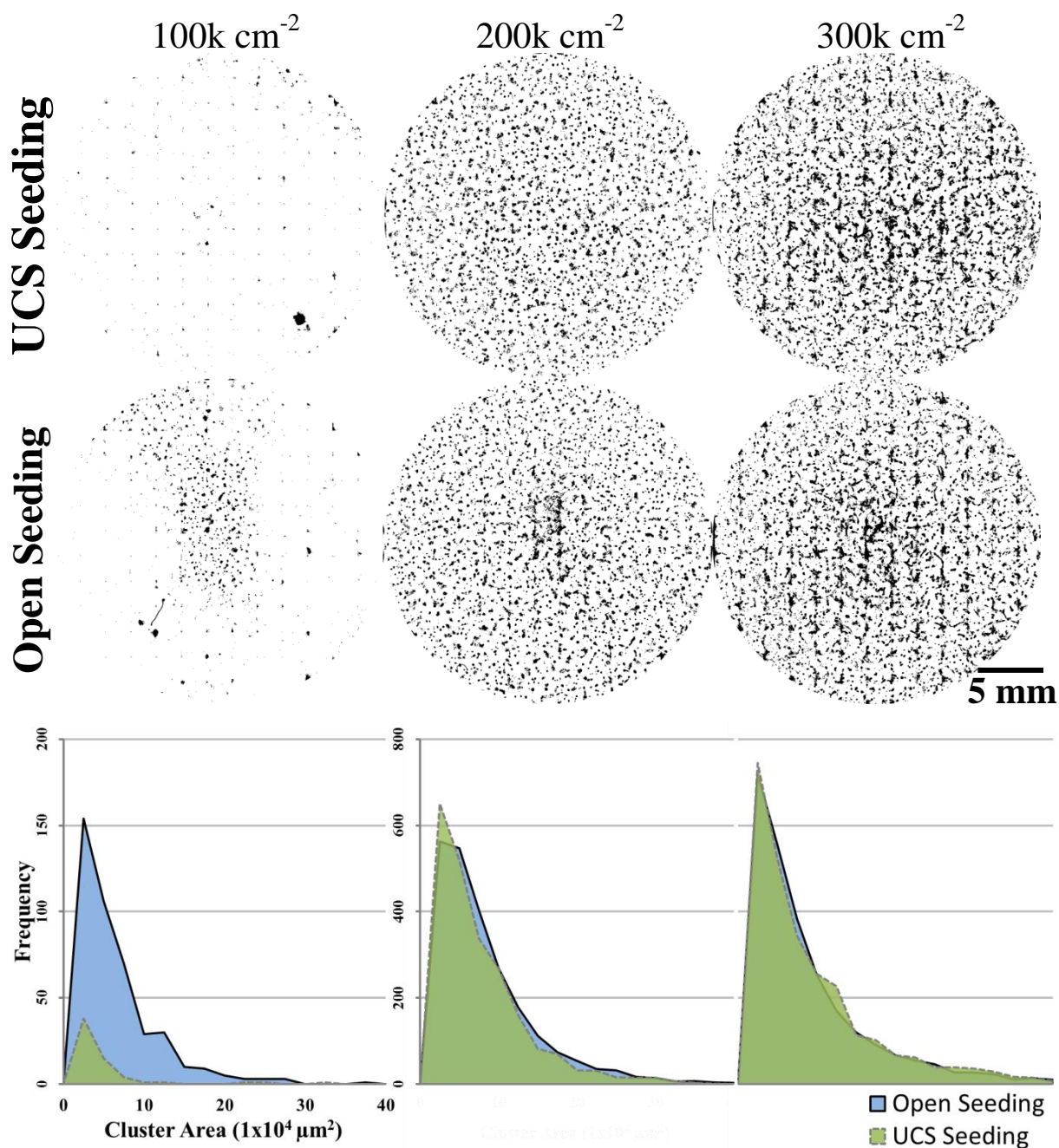


Figure 5.15 Montages of 21mm diameter wells, seeded at various densities both with and without the UCS device. Cells were fixed and stained for Nkx6.1, which indicates commitment to the pancreatic endoderm (cells were re-seeded after differentiation to the definitive endoderm). Central aggregation of cells when seeded without the UCS appears to yield more positive cells at lower densities, and also shows an artefact in the centre of the well at higher densities.





**Figure 5.16** Cluster size after differentiation using open seeding (without the UCS) and the UCS device to control cell seeding. Full well montages (top) show the inhomogeneous distribution of Nkx6.1 positive cells at low seeding densities, which is less pronounced at higher densities. Seeding artefacts are visible in the well centre for both seeding methods. Histograms of Nkx6.1 positive colony size (bottom) show a drastic reduction in differentiation efficiency using the UCS, whereas both seeding methods are comparable for higher seeding densities.

Experiments conducted with collaborators in Denmark indicate that in the case of their system, involving the differentiation of hES cells to beta cells for implantation in the treatment of diabetes, the UCS device has an effect on cell differentiation efficiency[142]. Using the UCS to homogenise cell distribution at low densities inhibits differentiation,

with less cells appearing positive for the marker Nkx6.1. This marries well with the opinion of the literature that there is a minimum cell density required for differentiation of these cell types[147]. In fact, the inhomogeneous seeding achieved by standard methods may in fact mask issues with cell seeding density – providing local areas of high density which produce at least some differentiated cells. In instances where, after initial differentiation, positive cells are automatically separated by fluorescence activated cell sorting (FACS), or other cell sorting methods, the yield may be sufficient to enable the studies at hand. This result, however, suggests that after optimisation of seeding density, a vast improvement in differentiation efficiency could be achieved simply by even distribution of cells across the culture area.

## 5.6 Conclusions

Cell seeding density plays a critical role in the outcome of cell culture experiments. Standard seeding methods in large culture vessels (12 & 6 well plates, culture flasks etc) do not provide a homogeneous distribution of cells on the culture surface. This results in local variations in cell density which affects the global outcome of an experiment – hampering accuracy and subsequent reproducibility. A simple methodology by which the uniformity of cell seeding across large culture areas can be drastically improved has been developed. By containing the cell seeding suspension in a defined space above the culture substrate, local fluctuations in cell density are minimised. Seeding efficiency, as defined by the homogeneity of intercellular spacing, was improved by a factor of 10. It is, of course, not entirely surprising that changes in cell density affect the behaviour of stem cells as they differentiate. It is, however, alarming to see the discrepancy in differentiation profiles within individual wells even across a single experiment. The UCS device represents an improvement on existing laboratory practices which is simple to implement, and based on the work presented in this chapter may have a profound impact on the reproducibility of certain cell culture studies.

The UCS described in this chapter addresses a fundamental problem in the use of high-content screening studies (i.e. array and gradient platforms) by ensuring that upon seeding, cells are distributed across the sample in a homogeneous manner. This allows us to ‘trust’ that changes in cell density and behaviour are the result of surface driven effects, rather than spurious seeding artefacts.

A quantifiable improvement in the quality of cell seeding has been demonstrated, effectively homogenising seeding protocols across users, experiments and samples. The variation in seeded cell density on injection moulded array samples, and also in multiwell plates, has been demonstrated as flawed in multiple users work. Reducing the standard deviation of local cell density by a factor of almost 5 on injection moulded samples allows for increased confidence in experimental results. This has led to a direct improvement in the reliability of studies on gradient substrates fabricated in this thesis, and represents a potentially valuable tool for other high-content screening systems moving forward.

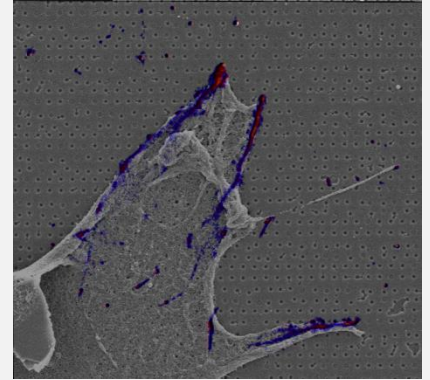
Furthermore, experiments were undertaken in collaboration with Novo Nordisk, Denmark, to elucidate the possible effect of cell seeding uniformity on their work with the differentiation of human embryonic stem cells to beta cells for the treatment of diabetes. Initial results indicate that the differentiation profile within 12-well plates depends on the seeding method. Variation in density across the surface of the well leads to a variation in positive differentiation of hES cells. Work is ongoing to confirm the quantitative change in differentiation yield using standard seeding approaches and the UCS.



## 6 Imaging the nanoscale architecture of focal adhesions

### Background:

Extensive work since the 1980's has demonstrated cell behaviour on patterned substrates, including this thesis, without necessarily understanding how topography drives cell behaviour. Nanopitted arrays are one of the most interesting substrates – appearing to drive the differentiation of mesenchymal stem cells with subtle variation in geometry. This chapter employs new microscopy techniques to provide a more detailed look at just how cells interact with precisely ordered and disordered nanostructures.



### Results:

Correlative microscopy was used to combine super-resolution microscopy with scanning electron microscopy – revealing changes in focal adhesion structure which were dependent on the underlying surface topography. New methods were developed for sample processing: preparation for immunofluorescence microscopy followed by further preparation for electron microscopy, along with the challenge of registration of images from two microscopes on a single image. It was revealed for the first time that cells build their focal adhesions around and in-between nanopit arrays, leading to a change in structure within single adhesions. A correlation between adhesion orientation and the symmetry of the topographies further reinforced this.

### Conclusions:

Focal adhesions have heterogeneous nanoscale architecture within the complex which is clearly guided by the symmetry and order of underlying nanopit topography. These changes in adhesion architecture are assumed to modulate the cellular mechanosensing of the surface properties – explaining why mesenchymal stem cells respond as though they are on a stiff/soft substrate when cultured on different nanopatterns.

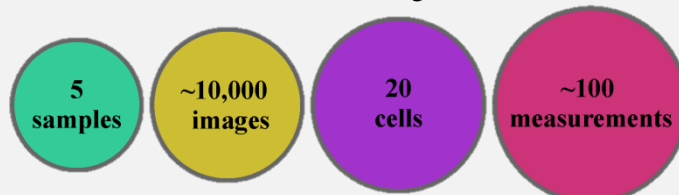
### Experimental

Length scale: nanometres (100 nm features, <30 nm resolution)

Cell type: mouse embryonic fibroblast (MEF)

Analysis: 200x immunofluorescence images

Dataset: Correlative fluorescence and SEM of single cells – 5 substrate topographies



### Output:

Further work is required to correlate the nanoscale architecture of focal adhesions to cellular mechanosensing. If a direct link can be found, a high impact publication is likely.

## 6.1 Introduction

Whilst it has been demonstrated that nanotopographical cues embedded in a surface can have a profound effect on cell response, the mechanisms by which these cues are translated into the presentation of a given phenotype are largely unknown [6], [148]–[150]. This thesis has already demonstrated that groove depth in the submicron range has a threshold of action, and also that a simple nanotopographical surface array can have a powerful and profoundly different impact on different cell types.

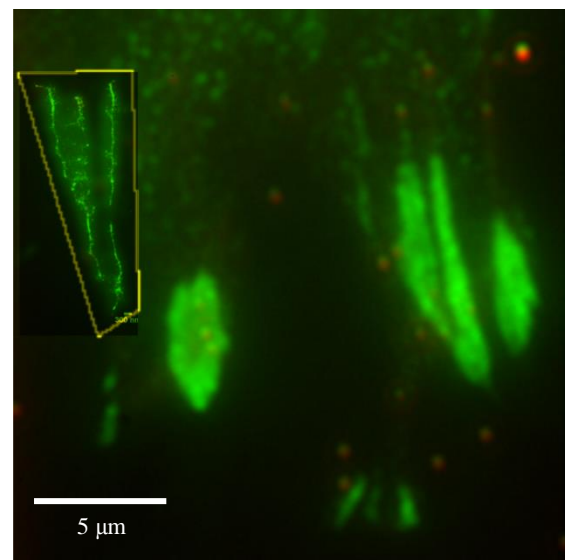
The key issues standing in the way of developing a deeper understanding of these cell-surface interactions are imposed by both the complexity of biological systems, and also the limitations of microscopy techniques available to researchers. Many of the intricate cellular activities which are thought to modulate the cell-substrate interface exist at length scales unresolvable using light microscopy. The so called Abbe limit [151] defines the smallest resolvable distance,  $d$ , at a given wavelength,  $\lambda$ , as being  $d = \lambda/2.8$  for optics with a high numerical aperture (NA) of 1.4. This was refined some years later by Lord Rayleigh to  $d = 0.16\lambda/NA$  [152]. The Rayleigh criterion states that two point sources are resolvable if the peak of one diffraction pattern is as far away as the first minimum in the airy pattern created by the diffraction in optical system. In practice, this gives a diffraction limited resolution of 200 nm using an ideally configured optical microscopy system. Techniques making use of methods other than light such as scanning electron microscopy (SEM) offer improved resolution, but are incompatible with the analysis of live biological samples.

There is a constant push in the biological sciences to increase resolution and delve deeper into the inner workings of the body. Since Hooke first described cells in 1665 new tools and techniques have been developed to understand the constituent parts which work together to give us the human body as we know it. From that first rudimentary microscope, 350 years of progress have given us exquisitely high NA objectives and cooled EMCCD cameras capable of high frame rate acquisition with low noise levels and high sensitivity.

In recent years, the Abbe limit itself has been comprehensively broken – or rather, circumvented, by a wave of new super-resolution microscopy techniques capable of resolving features only tens of nanometres apart. These techniques can be divided into two

categories – those which use structured illumination to restrict the sample area which receives excitation light, and those which rely on the stochastic behaviour of fluorescent molecules to subsequently extrapolate and model the probable position of individual molecules within an image. This new wave of techniques is described in depth in the literature[153]–[155], and has already offered ground-breaking insight into the nanoscopic behaviour of cells[156] as they interface with surfaces *in vitro*. The ingenuity of leading researchers in the field shows no sign of abatement, with new microscopy techniques capable of increasing spatiotemporal resolution being reported every few years [157].

**Figure 6.1 Standard resolution fluorescent micrograph of a cell in which the focal adhesion protein paxillin has been labelled. A super-resolution reconstruction of a small region of interest is outlined in yellow. Processing this higher resolution area took approximately 5 days on a high performance cluster computing system (Columbia University, NYC).**



Whilst exhibiting a different morphology *in vitro* as compared to *in vivo*, focal adhesion complexes have been shown to be involved in the modification of cell behaviour in response to a topographical surface cues[158]. These complexes are the focal point of cell-surface contact, and are met by dense actin bundles through which inter cellular tension is generated[77]. An understanding of how nanotopographical stimulation affects cellular response might lead to the ability to target surfaces towards certain behaviours – such as the formation of bone[35] or the maintenance of a stem cell phenotype[38].

Standard microscopy techniques which are diffraction limited do not necessarily lend themselves to the observation of important cellular mechanisms – and are particularly unsuited to observing structural changes in cell apparatus as a result of nanopatterned substrates. For example, what appears to be a wide adhesion which is 2 μm across may actually be only 0.5 μm wide, or composed of many smaller subunits rather than existing as one large complex. Super-resolution techniques have already been shown to bring a new

understanding of focal adhesion architecture on patterned substrates. Rather than topographical patterning, chemical patterning of fibronectin was used to investigate the resolution of focal adhesions[159]. Constricting the available area of ECM protein, and therefore limiting the number of integrin binding sites, forced adhesions to conform to the nanoscale patterns – with the vinculin pair distance (i.e. the centre-centre spacing between vinculin molecules) correlating with pattern dimensions. These patterns are on the same length scale as the nanopit arrays which show a modulation of MSC focal adhesions, and ultimately differentiation. Results from previous publications in Figure 6.2 demonstrate that modifying the structure at the nanoscale allows the modification of a cells focal adhesion composition, which translates into modified mechanosensing of the surface – driving cell behaviour.

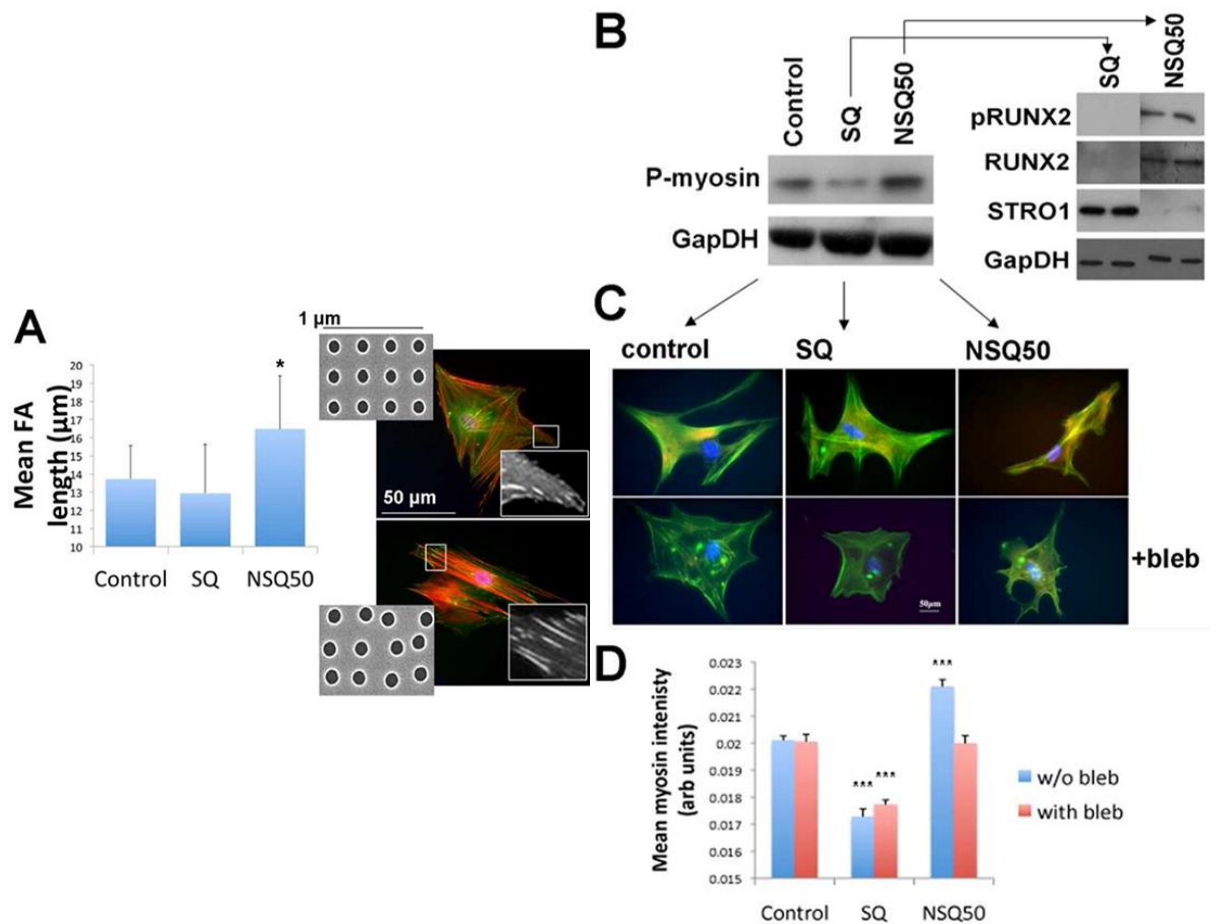


**Figure 6.2 Adhesion, tension and phenotype.** Figure adapted from Tsimbouri et al. Focal adhesions are longer on disordered nanopit arrays as compared to flat and ordered surfaces. This corresponds to higher levels of p-mycosin expression, which is indicative of greater intracellular tension. Cells on ordered and disordered surfaces also show inverted profiles for markers of oestrogenic differentiation (both RUNX2 and pRUNX2 on NSQ surface) and markers of stem cell quiescence (STRO1 on SQ surface). This points to a change in the mechanical sensing of a surface, which is dependent on pattern geometry.

## 6.2 Methods

To investigate the impact of nanopit array geometry on cell adhesion, new array substrates were fabricated. Combinations of disordered and ordered dots with various periods were fabricated by electron beam lithography (EBL), followed by replication in polycarbonate by injection moulding. Lithography was carried out using the methods outlined in 4.2.1 and 4.2.2.

### 6.2.1 Data acquisition - super-resolution imaging

Super-resolution imaging of focal adhesions on nanopatterned surfaces was carried out using a stochastic reconstruction technique called 3B[155], [160]. This technique has been used to demonstrate spatial resolution approaching 10 nm on a conventional microscope using a high sensitivity camera, making it ideal for investigating the interaction and organisational response of cellular structures such as FAs to nanoscale surface features.

3B is a localisation microscopy analysis method which creates reconstructions of fluorophores point locations from sequential image datasets. Fluorescent molecules do not emit a steady stream of light, rather they emit photons sequentially as energy is absorbed and emitted. 3B provides a route to super-resolved microscopy avoiding the high equipment costs commonly associated with high resolution microscopy. Bespoke microscope configurations and light sources are required for techniques such as Stimulated emission depletion (STED), saturated structured illumination (SSIM), photoactivated localization microscopy (PALM), and stochastic optical reconstruction microscopy (STORM)[153], [161], [162].

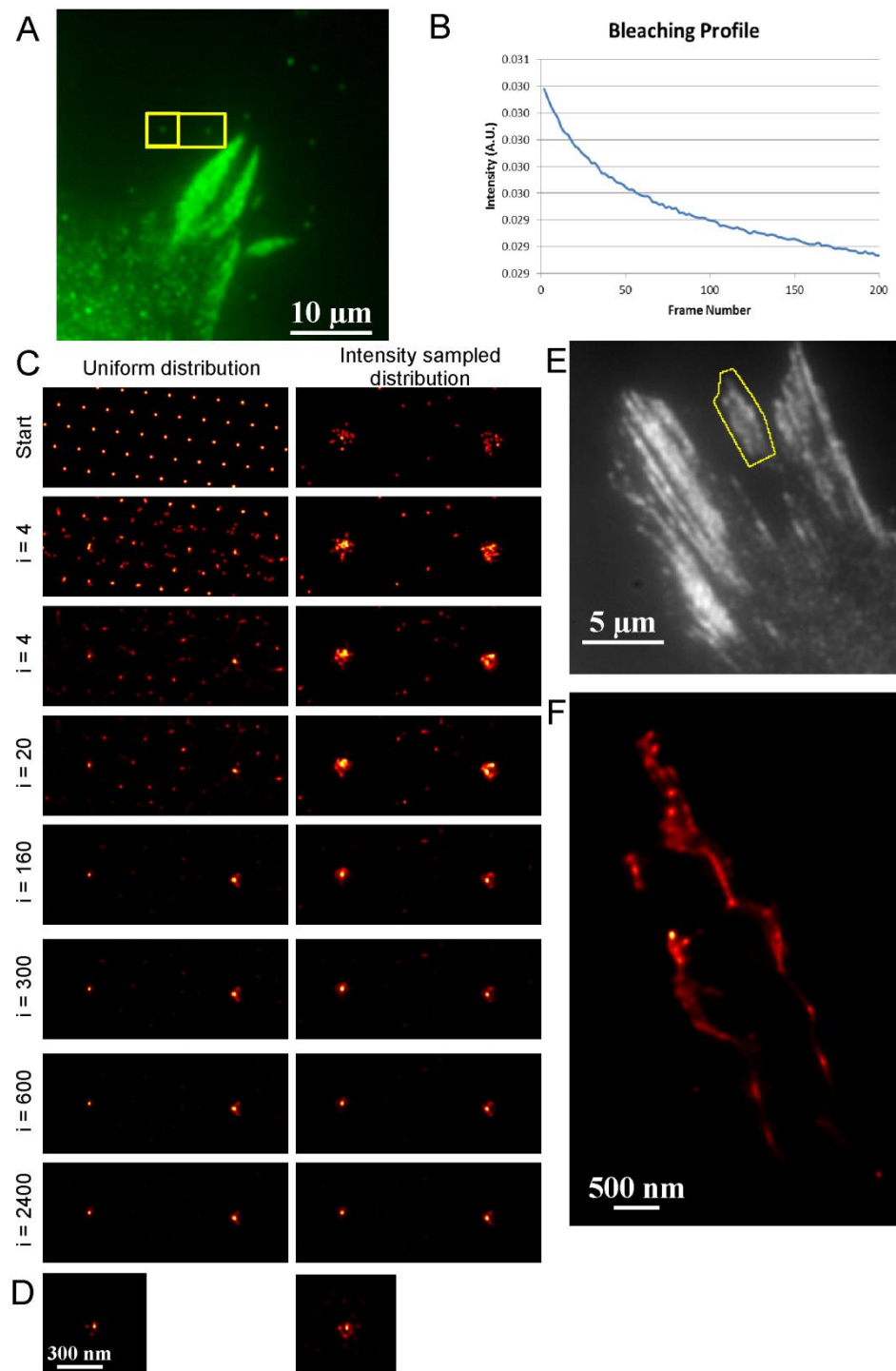


**Figure 6.3** ThreeB super-resolution microscopy. **A)** integration of 200 frame dataset. **B)** dataset bleaching profile over time. **C)** iterative process can begin with one of two initial distributions, both converging on approximately equal images. **D)** where ROIs are too small and fluorophores overlapping artefacts can occur. **E)** integration of 200 frame dataset, **F)** ThreeB reconstruction of highlighted ROI.

ThreeB imaging uses a time series of, e.g. 200 images, to estimate the location of individual fluorescent molecules based on intermittent stochastic bleaching and blinking events. It allows the reconstruction of images with sub diffraction resolution on a standard fluorescent microscope. The key requirement is that the camera used for acquisition be capable of frame rates which are on the same order as the intermittent blinking and bleaching of the fluorophores. Common CCD cameras are not currently sensitive enough at the required frame rates; nominal frame rates of 50 Hz are required. Cooled EMCCD cameras, and the new generation of sCMOS[163] cameras must be coupled with high NA objectives to produce sensitive imaging with small pixel sizes. Image reconstruction takes 100+ hours for a 2  $\mu\text{m}$  x 2  $\mu\text{m}$  square on a high spec desktop computer, meaning that access to high power computing facilities is essential for post processing of acquired data.

Figure 6.3 C outlines the iterative process by which the ThreeB algorithm estimates the location of individual fluorophores within a fluorescent time series. The intermittent bleaching and blinking of individual sources within the diffraction limit is used to predict their centroid, offering resolution well below the classical 'limit' for an optical microscope.

## 6.2.2 Secondary fixation for electron microscopy

The fixation process used for immunofluorescence microscopy is deliberately 'light' so as to minimise cross-linking of proteins of interest. Aggressive cross linking by any fixative obscures epitope targets onto which the antibodies used to label cell structures bind. In fact, some target proteins are incompatible with fixation by formaldehyde and require the use of dehydrating alcohol fixations. Rather than cross linking, fixation in alcohol causes the coagulation and precipitation of protein structures with no cross linking, however carbohydrates and lipids are not fixed. Formaldehyde fixation reacts primarily with proteins, forming a methylene bridge (-CH<sub>2</sub>-) between reactive atoms (primarily nitrogen). Molecules such as carbohydrates, nucleic acids and lipids are thought to be encapsulated in the cross linked mesh as formaldehyde binds proteins together. For microscopy techniques which use electron beams under high vacuum conditions, such as SEM, a higher level of cross linking is required. The reasons for this are twofold: imaging under high vacuum is only possible with dehydrated samples and contrast is improved through the increased density after harsh fixation.



For correlative microscopy studies on injection moulded plastic samples, cells were initially fixed for immunolabeling in 4% formaldehyde at room temperature for 5 min. This allowed for staining of focal adhesion complexes and the actin cytoskeleton with primary antibodies against FA proteins and a fluorescently conjugated phalloidin molecule respectively. Cells were mounted in a solution containing 10mM  $\beta$ -mercaptoethanol (BME), a reducing agent which induces bleaching and blinking of fluorophores. Modern fluorophores such as the Alexa series (life technologies) are so robust that they bleach too slowly for the ThreeB super-resolution technique and are so stable that they offer very little information in the way of blinking events.

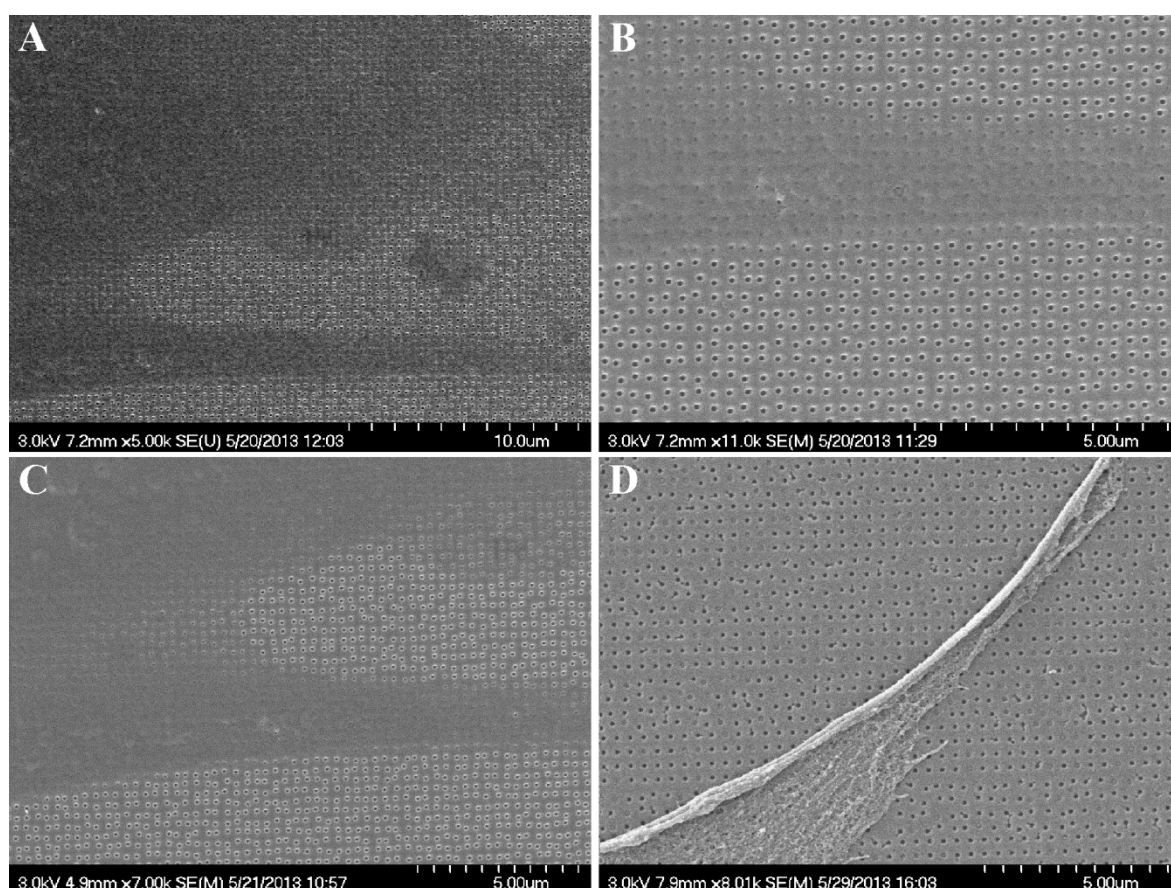


**Figure 6.4 Secondary fixation before SEM is essential for correlative microscopy studies. Contrast is poor when samples are dehydrated directly after fluorescent microscopy (A-C). D) Secondary fixation with gluteraldehyde drastically improves contrast, revealing cellular interactions with surface features down to nanometre resolution.**

The key to stochastic super-resolution techniques is that individual bleaching and blinking events occur in fluorophores which are separated by distances below the diffraction limit. If both fluorophores were to emit a constant stream of photons in sync



with each other they would be impossible to distinguish. However, as fluorophores undergo bleaching and blinking events and effectively turn on and off, analysis of sequential image frames can reveal their location.

### **6.3 Correlative light electron microscopy (CLEM)**

Here, ThreeB super-resolution imaging[155] has been combined with SEM on substrates designed to investigate the impact of nanoscale features on cell response. Correlative microscopy combining these two imaging modes has already been used to reveal new structural of specific proteins in their cellular context[164]–[166]. It has been shown previously that nanoscale pits arranged with differing order and geometry can induce osteogenic differentiation[35] or retention of stem cell phenotype[38] in human mesenchymal stem cells (hMSC). The mechanism by which this happens remains unknown, however the prevailing consensus is that the structured substrate influences the cells mechanical interpretation of the surface. Experiments using hMSC cells in which  $\beta 1$  integrins were blocked and subsequently recovered showed that changes in the metabolic profile of cells were effectively switched on and off as integrins were masked,

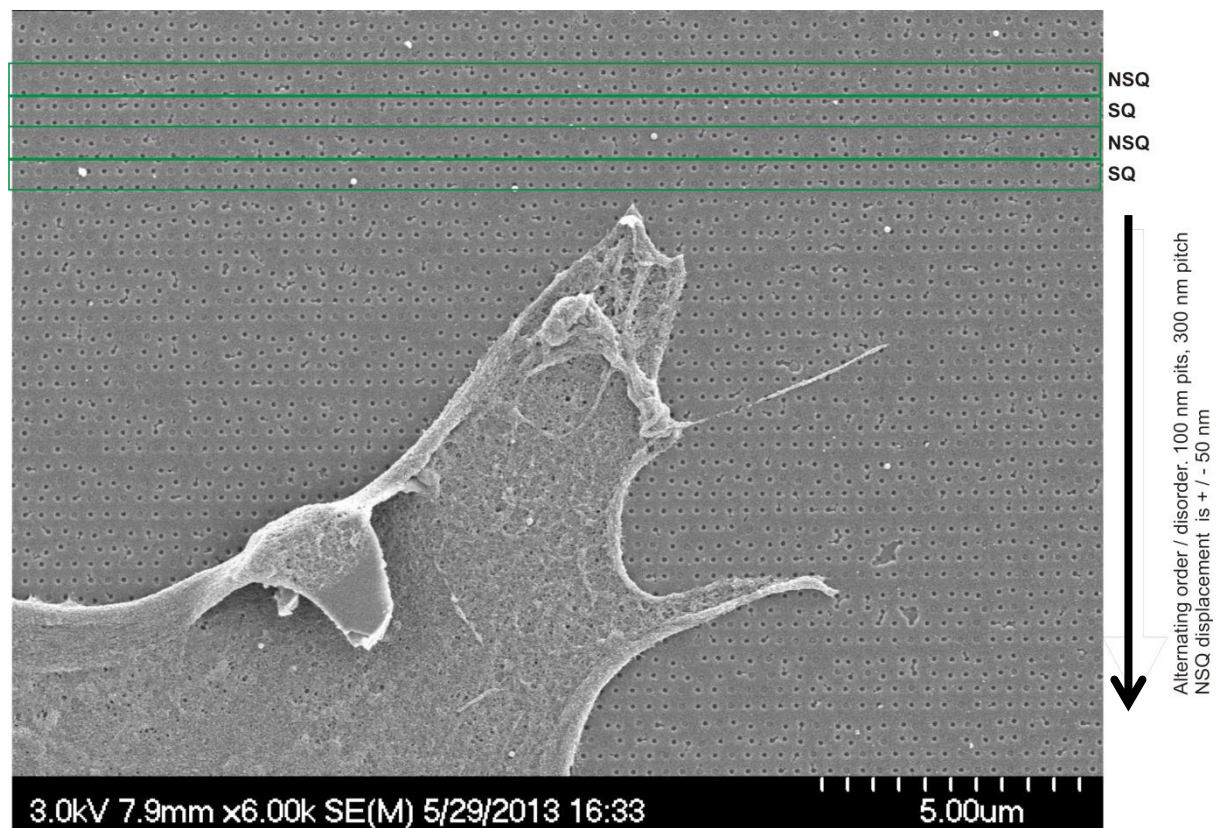


**Figure 6.5** Cells were cultured on substrate which combined stripes of ordered and disordered nanodots. Both patterns are composed of nanodots which are 100 nm wide, 100nm deep pits with a nominal pitch of 300 nm. The ordered square array (SQ) has a constant centre-centre pitch of 300nm. In the disordered ‘Near Square’ (NSQ) each individual pit is offset by a random amount within a range of +/- 50 nm in both the x and y directions. These two patterns are highlighted in green boxes above. Other spacings were also included, with a total of 47 combinations of symmetries and stripe widths.

Figure 6.5 shows disordered and ordered dots arranged in 600nm wide horizontal stripes across the substrate. This gives interspersed regions of order and disorder in the substrate, to determine the impact of subtle changes in nanoscale symmetry and disorder on focal adhesion (FA) structure locally within a single adhesion.

Having previously shown that these surfaces modulate FA length and area [79], there may be two possible types of interaction between the FA and the nanodots:

- i. ECM proteins accumulate within the nanodots, providing sites for integrin binding and leading to nucleation of FAs from these pits

- ii. The difference in height between the pit and the surface cannot be bridged by developing FAs, and sufficient protein cannot be recruited to fill the pits. This presents an obstacle which forces the FA to develop in an asymmetrical manner.

Previous work reporting that FAs are composed of a 40 nm thick ‘core’ of plaque proteins suggests that the nanofeatures of 100 nm depth are sufficient to prevent propagation of adhesions across them.

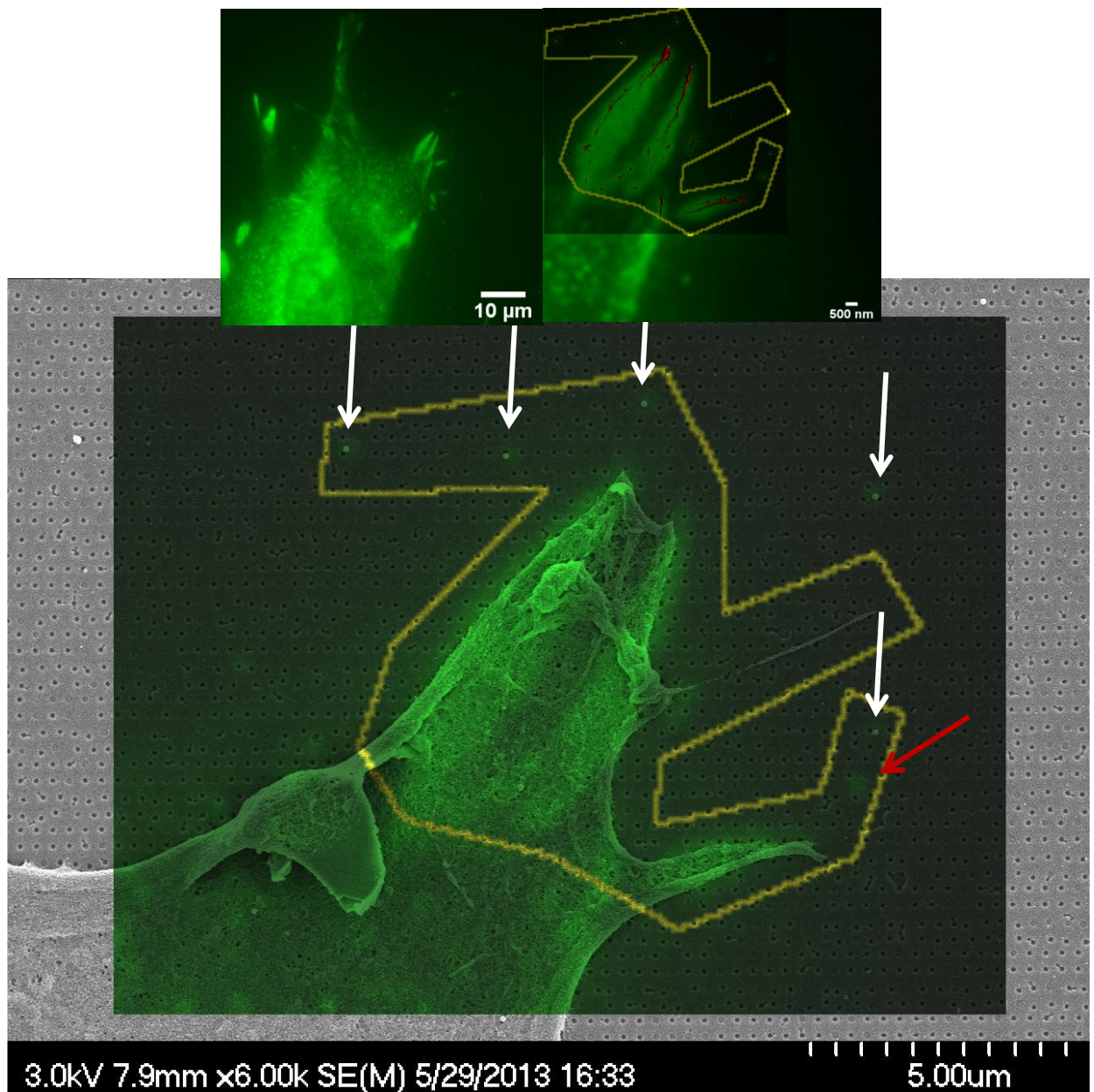


Figure 6.6 Low magnification SEM of Mouse Embryonic Fibroblast (MEF) cell on a nanopitted polycarbonate surface as described above. Overlaid onto the SEM in green is a widefield fluorescence image of the same cell, immunolabelled with paxillin.

The fluorescent overlay in Figure 6.6 was captured with a 100x objective as a time series of 200 images, each with an exposure time of 20 ms (4 seconds total acquisition time) – the image stack was averaged before alignment by hand on the SEM micrograph. The yellow outline denotes the area in which a ThreeB reconstruction was performed, which generates a super-resolution image based on the bleaching and blinking of fluorophores over the 200 frames sequence. 100nm polystyrene beads were added to the sample after fixation to act as fiducial markers, allowing correlation of the two images. These can be seen as small white spheres on the SEM image, and as a larger green blur on the fluorescent image – indicated by white arrows. The red arrow indicates a fiducial marker which appears to have been washed away during sample preparation for SEM imaging – this is concerning in that it shows the fiducial markers are not immobilised in place, rather adsorbed to the surface.

The sample is fixed in formaldehyde for fluorescence microscopy following a standard protocol and imaged wet in buffer solution (containing a reducing agent to induce further blinking in the fluorophore). It is then re-fixed in gluteraldehyde before dehydration in an alcohol gradient and finally dried in a critical point drier. A 5nm layer of gold-palladium is sputter coated before SEM imaging. A minimum of three fiducials are required to reliably calculate image scale, rotation and tilt differences when combining both fluorescent and SEM images. However, due to the apparent propensity of the markers used here to become dislodged during processing, it is suggested that at least 5-10 are used in order to detect any displaced fiducials and discard them accordingly. Functionalised fiducials (e.g. with a protein) could be used in the hope that the gluteraldehyde fixation step adheres them to the surface.

In order to investigate the interaction of the focal adhesion structures with nanopatterned surfaces, it is essential to have a combined surface and cell image – i.e. SEM and fluorescent micrograph overlay.



**Figure 6.7** Super-resolution reconstruction of area of interest. Focal adhesions are broader at the proximal side, and appear to concentrate at the distal side.

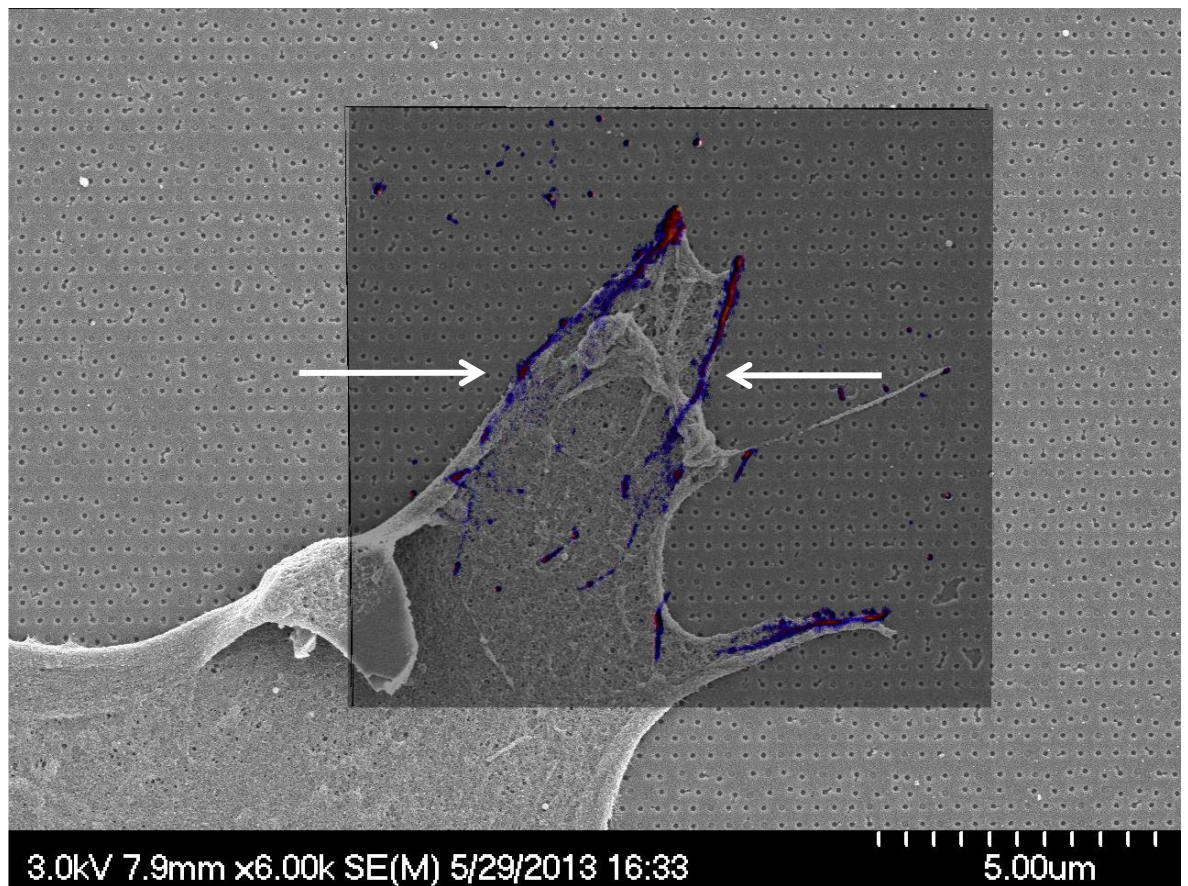
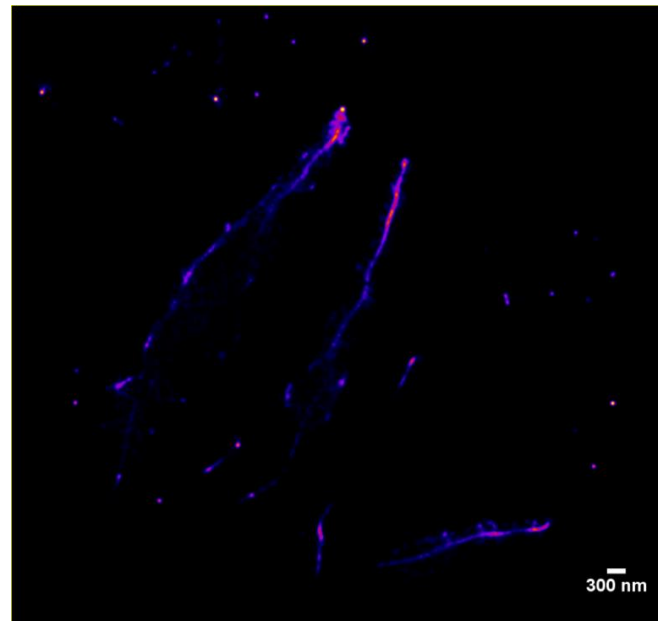


**Figure 6.8** Correlated super-resolution image of paxillin and SEM of cell on nanostructured surface. Narrow focal adhesions navigate between nanopits, propagating at angles where obstructions are minimised, with bends and kinks in structure to work around nanofeatures. Alternating ordered and disordered patterns appear to force adhesions to divert more strongly from a linear path. White arrows indicate a transition from disorder to order accompanied by a pronounced bend in the FA before continuing towards the centre of the cell.

Whilst generally straight and appearing to lie in between nanopits, the focal adhesion can be seen to ‘kink’ in disordered regions where the symmetry of the square array is disrupted (white arrows). Otherwise, it proceeds along the angles of symmetry within the array. It appears that, rather than the pits providing a nucleation site in which proteins accumulate, they restrict and constrain FA growth into the flat regions of the sample.

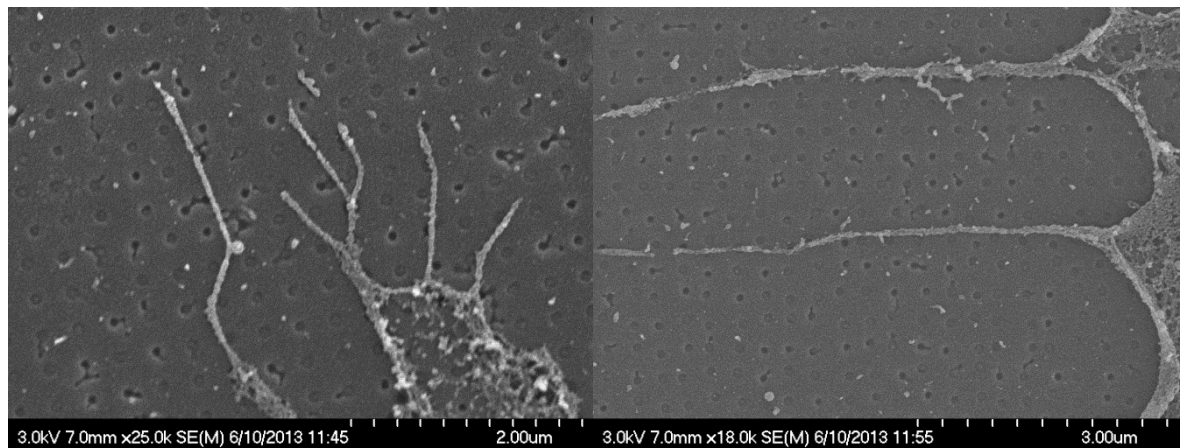


**Figure 6.9 High magnification SEM images of filopodial extensions on nanopit arrays. Here, it is evident that cellular protrusions ‘navigate’ between nanopits, extending through the flat region between features.**

Although the navigation of cellular processes inbetween nanopit structures has been shown previously by SEM imaging [167], [168] the orientation of cellular focal adhesions in relation to nanopit arrays has not been visualised. Super-resolution imaging of the protein structures which interface with the nanostructured substrate offer the first opportunity to observe the cell-nanopit interaction rather than simply the guidance of protrusions by the topography as seen above. This has profound impact on our potential understanding of how the nanotopography induced changes in adhesion structure affect cellular mechanosensing and so drive cell behaviour.

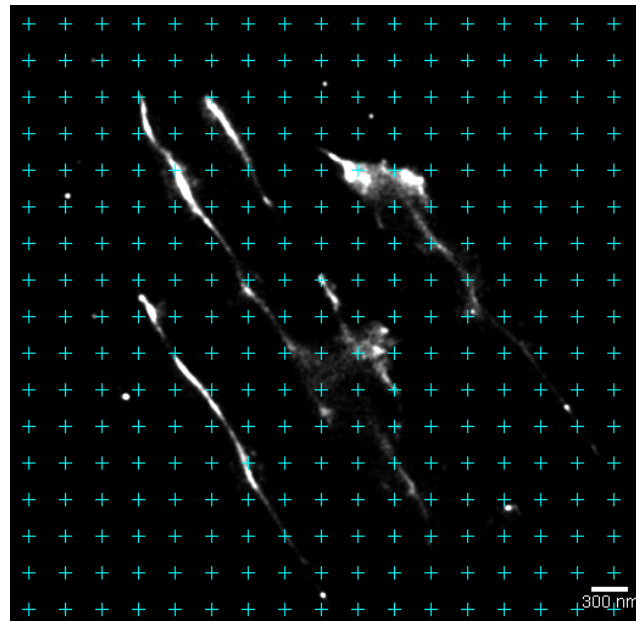


**Figure 6.10 Focal adhesion orientation on nanopit arrays. Adhesions extend in between nanopits at approximately  $45^\circ$ . Here, a regular array with pitch of 300 nm has been overlaid onto a super-resolution reconstruction of paxillin labelled focal adhesion complex. As the nanostructures cannot be observed in brightfield or fluorescence, there is no means of aligning the grid to the true underlying structure.**

Alignment of focal adhesions at the nanoscale is clear, as can be seen in Figure 6.10. This was surprising as previous work looking at adhesion orientation with respect to nanopatterned surfaces found no apparent guidance in FA angle. Investigation with super-resolution microscopy, however, reveals that adhesions are constructed from narrow subunits, and indeed appear to conform to the underlying topography.

## 6.4 Quantification of adhesion geometry on nanopatterns

Clear morphological differences in nanoscale adhesion geometry on nanopitted substrates can be seen in the correlative microscopy study presented earlier in this chapter. The outstanding question is how best to interpret this data, and discover what it might tell us about the manner in which cells sense, understand, and react to their environment. Nanopatterned surfaces are a relatively new technology, but papers have demonstrated their use as a system for indirect control or guidance of cell behaviour in studies of biochemical processes. Tsimbouri et al described a ‘plasticity’ system whereby ordered

and disordered surfaces were used to guide cell behaviour, followed by the investigation of cell-ECM interactions such as the role of  $\beta 1$  integrins in MSC differentiation[79].

The body of work produced on these surfaces, looking at cell response when cultured on nanopatterns with different levels of disorder, has found a marked difference in functional response. This is accompanied by clear differences in cell morphology such as spreading profiles and focal adhesion distribution. The differentiation profile of MSCs on nanopatterned polymer substrates matches that which one might expect if they were grown in induction media to force differentiation, or on a substrate whose mechanical properties were matched to that of the *in vivo* environment - i.e. on soft substrates with a similar Young's modulus to brain tissue drive neuronal differentiation [169].

This raises an interesting question: *are these surfaces and materials synonymous?*

Nanopitted arrays provide a physical cue which, through super-resolution microscopy, this thesis has shown causes a distinct change in focal adhesion geometry. It is not known how this difference in structural organisation of the focal adhesion affects the function of the macromolecular complex. Due to the complexity of focal adhesion protein plaques – which have over 100 proteins associated with them – classical microscopy techniques have fallen short of better defining the interplay of proteins in these highly heterogeneous structures. Super-resolution microscopy of focal adhesions on ordered and disordered nanopit arrays has revealed a stark contrast in the sub-diffraction morphology of these adhesions. Classification by length clearly misrepresents the true mechanical ‘foothold’ of a cell on its culture substrate. Adhesions which appear to be equal in length at standard epifluorescent magnifications may be distinctly unequal in strength.



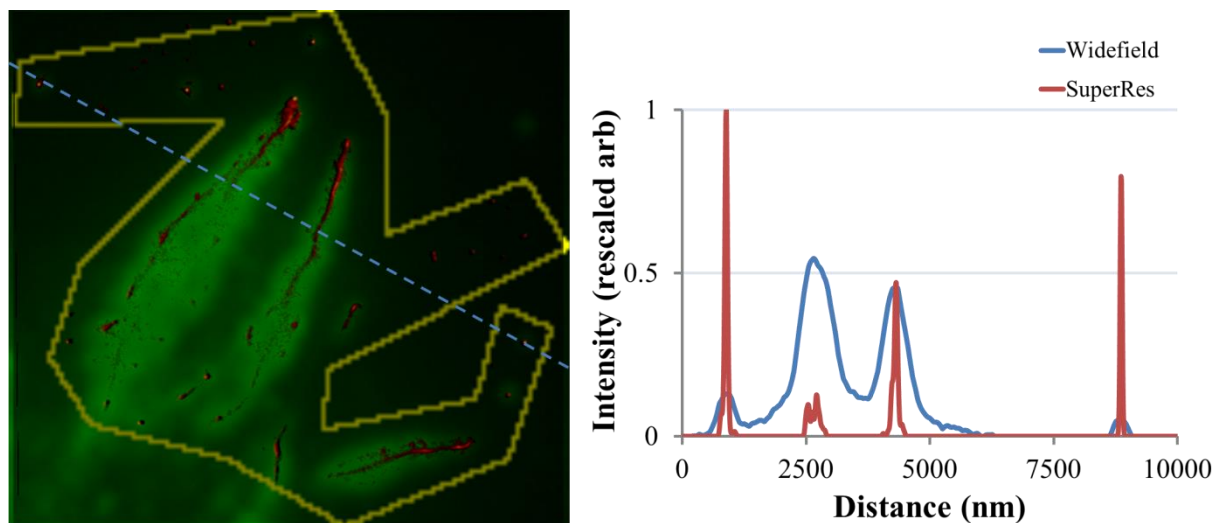


**Figure 6.11** Line scan across super-resolution reconstruction of focal adhesions on disordered nanopit array. Adhesion formation is quantised spatially into the regions between nanopits. What appears to be a single adhesion (A) is revealed to be two separate structures with a pitch of approximately 300 nm

Correlative microscopy of FAs on nanopit arrays answers a question that could not be addressed by conventional microscopy techniques – that of how the cell actually interacts with the nanostructured surface. Do proteins accumulate within the nanopits, providing nucleation points for FA formation and growth, or do the pits present obstacles which ‘guide’ FA growth by limiting the degrees of freedom for extension. With no discernible alignment of FAs when cells are cultured on these patterns which have only two or three degrees of symmetry, it is clear that the effect is not as simple or broadly global as aligning FAs to the array axis. Studies of focal adhesion orientation show minimal correlation in angular alignment.

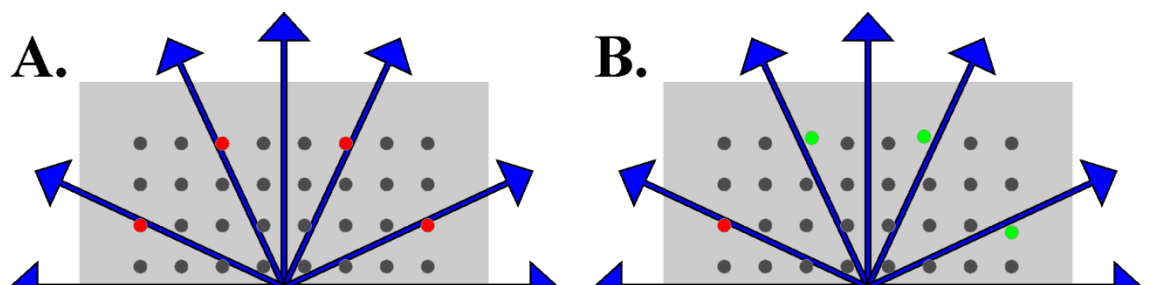


**Figure 6.12** Possible avenues of FA propagation from a central point in a square nanopit array (100 nm diameter pits, 300 nm pitch). Blue arrows represent propagation routes. Red dots represent pits which block/interfere with those routes. Green dots in (B) are randomly displaced in such a manner as to allow the route of propagation to continue whilst red dots

are displaced but still block the FA path. Here, we can see how displacements in the pattern may allow for larger FAs versus on highly ordered patterns.

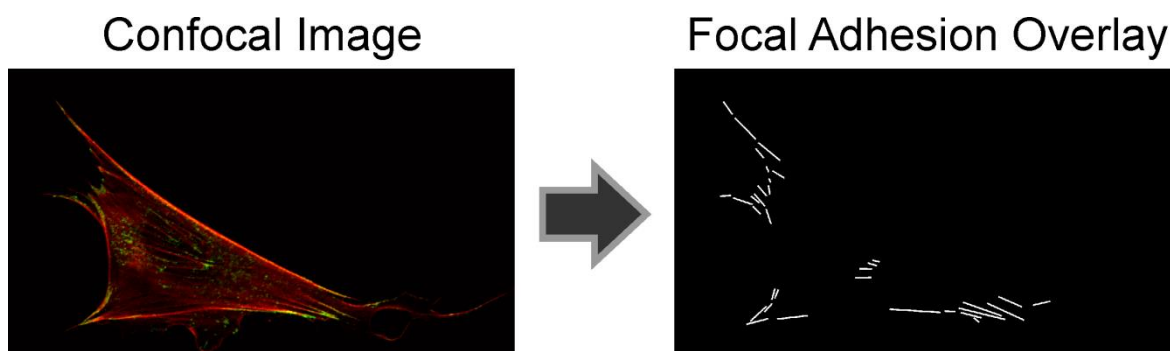


**Figure 6.13** Focal adhesions were quantified by generating a manual overlay on fluorescent micrographs captured at 40x. Original images (left) were loaded in ImageJ and an overlay created (right) which was then analysed.

Both ordered or disordered square arrays offer two clear axes of propagation perpendicular to one another, Figure 6.12. Linear propagation in any axis other than horizontal or vertical is only possible for approximately 1  $\mu\text{m}$  in either direction before a nanopit (red) interrupts the path. If, as shown in Figure 6.8, mature FAs must circumvent nanopits, then this places an intrinsic limit on the distribution and size of focal adhesions on highly ordered nanopattern arrays. This may go some way to explaining the well documented non-adhesive properties of regular nanopattern arrays for certain cell types[170].

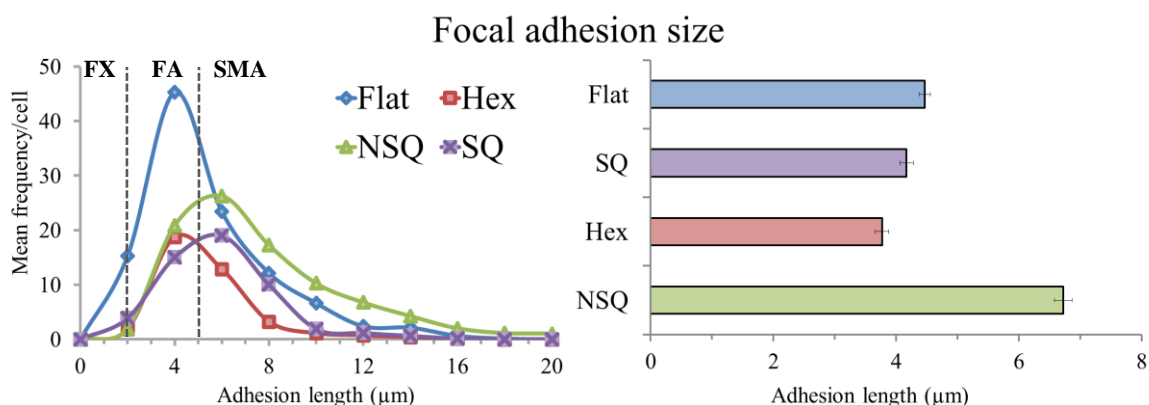


**Figure 6.14** The geometrical arrangement of nanopit arrays directly influences the size of focal adhesions. Differences in adhesion length are statistically significant between surfaces ( $p < 0.001$  by One Way ANOVA). Bars show SEM.

Cells cultured on four different injection moulded surfaces were fixed 24h after plating and immunolabelled for paxillin and actin. The FAs were classified as described by *Biggs et al* in 2007 into three categories of focal complexes (FX)  $< 2 \mu\text{m}$ , focal adhesions (FA) of  $2 - 5 \mu\text{m}$  in length, and super-mature adhesions (SMA) which were  $> 5 \mu\text{m}$ [168][167]. Classification was carried out in ImageJ by tracing over adhesions in a series of blind images. Differences in focal adhesion size were statistically significant across all four surfaces employed ( $P < 0.001$ ). This is apparent from the distribution of focal adhesions presented in Figure 6.14, showing a reduction in adhesion number per cell on ordered arrays (HEX and SQ) whilst showing a shift towards longer adhesions on the disordered nanopit arrays (NSQ). All three nanopit arrays supported a higher number of FA and SMA as a proportion of the total adhesions per cell. In the case of NSQ surfaces, few FX were identified, with almost 50% of adhesions being classified as SMAs.

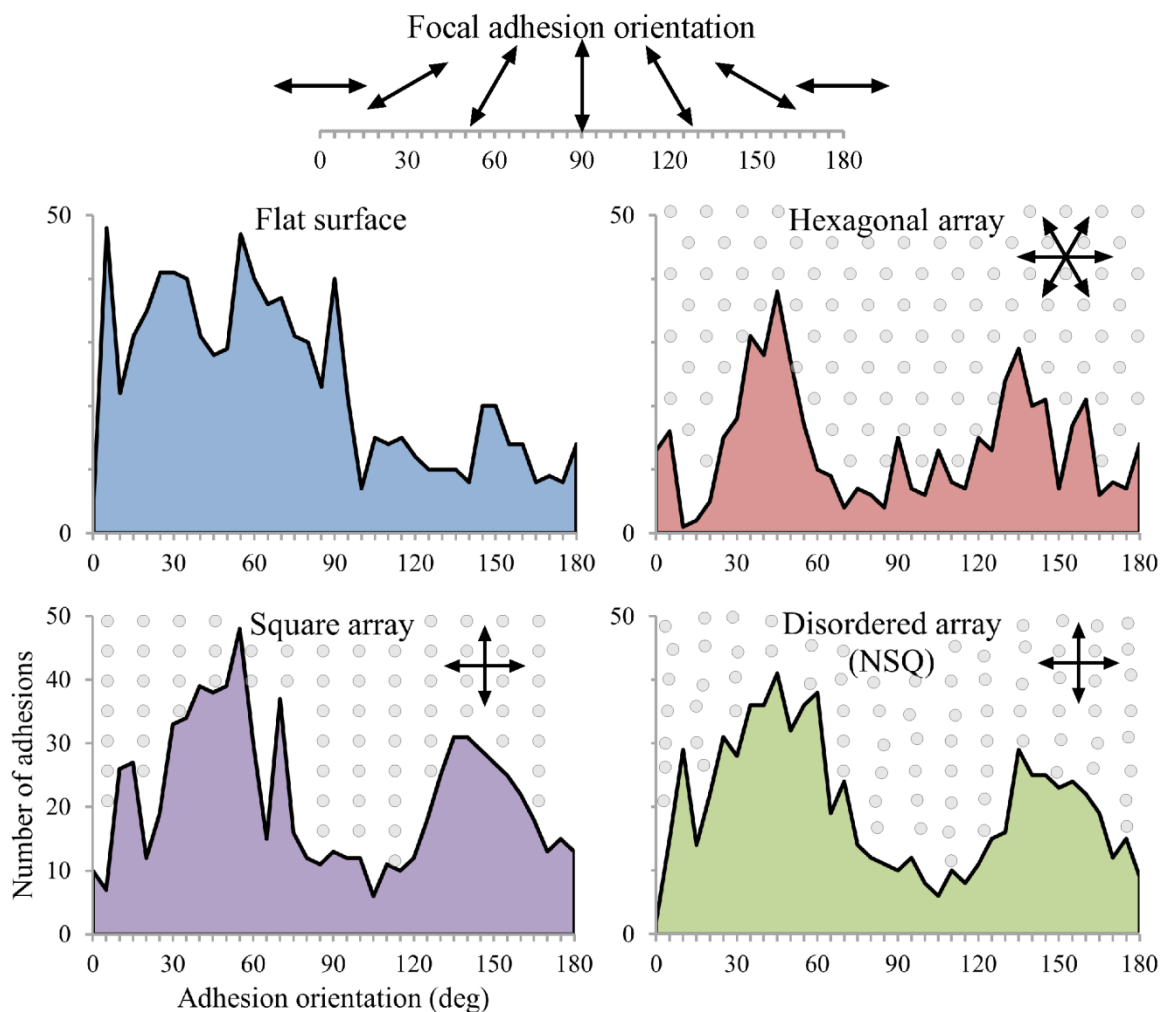


**Figure 6.15 Focal adhesions orientate to the underlying nanotopography. Orientation to the horizontal axis was measured for at least 500 MEF adhesions on each surface type stained**

**for paxillin. These were classified into 5° bins from 0° to 180°. Differences in adhesion orientation are statistically significant between surfaces ( $p < 0.001$  by One Way ANOVA).**

Orientation of MF cells to the underlying nanotopography is not immediately apparent on inspection of immunofluorescent image datasets, which one might attribute to the variety and heterogeneity of cell morphology. In the case of microscale topographies such as grooves cellular alignment is clear even at low magnifications, as in Figure 3.12. Focal adhesions do not immediately appear aligned to any axes of the underlying nanotopography either. A simple hypothesis as to why there is no alignment may be that 100 nm diameter nanopits are relatively small compared to focal adhesion plaques, and therefore a microscale influence may not manifest itself. There are, however, statistically significant patterns which emerge in adhesion alignment upon closer inspection.

Cells growing on a flat surface would be expected to show no alignment of cell body, focal adhesions, or any other subcellular structure – with orientation being random as the sample size increases. Figure 6.15 shows two regions of FA orientation – up to 90° alignment is high, and from 90° to 180° alignment is low. The low sample size ( $n = 10$  per surface) may contribute to the weighting in favour of angles between 0° and 90°. Patterned surfaces, however, show a level of alignment which can be related back to the actual nanopit array geometry. Hexagonally packed patterns have three orders of symmetry, whereas square and near-square patterns only have two. This appears to correlate with the number of peaks in FA alignment shown in Figure 6.15. For the hexagonally packed array, we see two clear peaks, and another spanning from 180° back to 0°. This may show a tendency to align to the clear path in between pits, however the peaks themselves do not fall at 0°, 60°, and 120°.

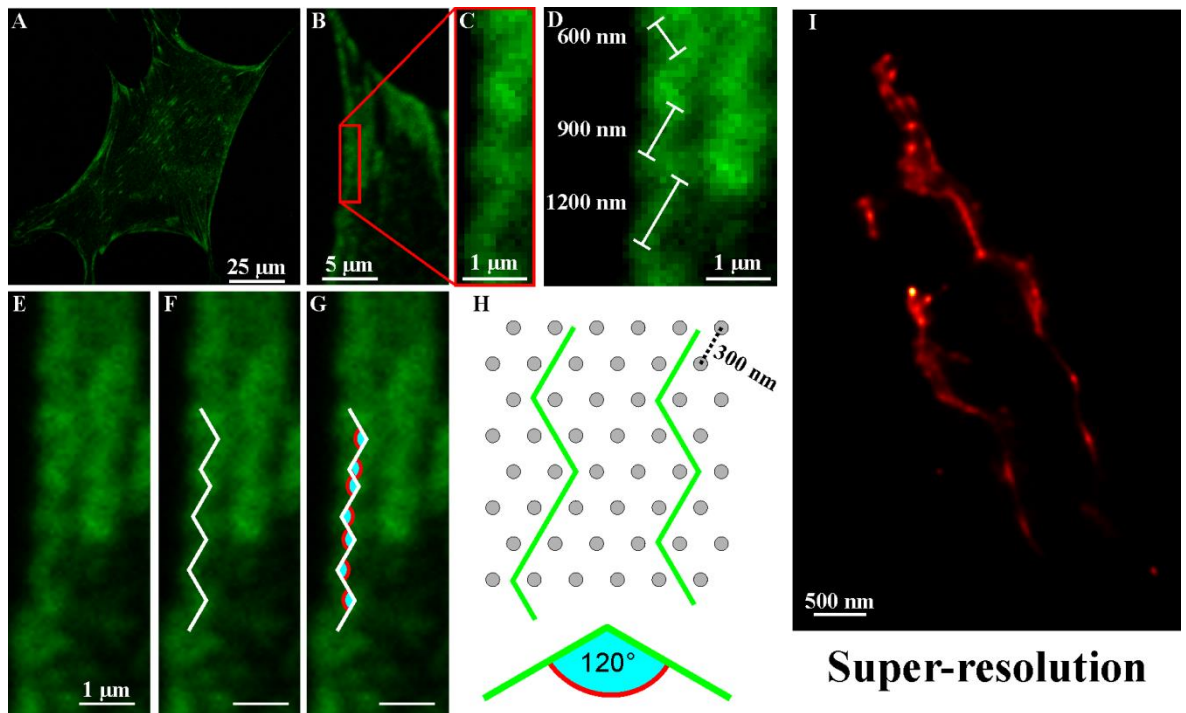


**Figure 6.16** Classification of FA orientation at standard magnifications (A) is prone to error. Upon closer inspection (B-D) what appears to be a vertical adhesion is composed of short sub-micron sections which intersect at  $60^\circ$  angles (E&F). This fits the proposed model of adhesions propagating between pillars/pits (G&H). Super-resolution imaging confirms the nanoscopic structure – again reinforcing that adhesions are built in the free space between pits.

Classification of adhesion phenotype has been shown via a multitude of methods in the literature, across a variety of magnifications and levels of detail. Figure 6.16 raises the question of whether the nature of an adhesion can truly be determined at standard magnifications. Kinking of the FA highlighted in Figure 6.16E gives rise to a disparity in both length and orientation when observed at different magnifications. Firstly, this adhesion was classified as being orientated near-vertical at an angle of  $87^\circ$  when in fact, it appears to be composed of sub-micron sections creating a ‘zig-zag’ pattern. This FA complex has a nanoscale orientation of both  $60^\circ$  and  $120^\circ$ , however its microscale orientation averages to approximately  $90^\circ$ . Secondly, the adhesion length and area which are commonly used as metrics of a cells FA profile differ at the nanoscale. The zig-zag geometry means that the true length of the adhesion is nearly 15% greater than would be measured from tip to tip. Finally, the contribution of diffraction blur to the perceived adhesion area may inflate measurements by as much as 200%. In this instance, the adhesion is confined to the area between nanopits arranged in a hexagonal array. The

nanopit spacing from edge to edge is approximately 200 nm – and correlative microscopy images suggest that adhesions are confined to this space. Imaging adhesions on a widefield system lacks the resolution to distinguish the true width of adhesions, and often makes parallel adhesions appear as a single entity and single adhesions appear to be a micron wide or more. This argument is reinforced by the comparison in Figure 6.11 of FA intensity profiles in widefield and super-resolution microscopy.

## 6.5 Conclusions

At the nanoscale, focal adhesions appear to be continuous within the resolution confinements of the techniques used here. Of course, the adhesions themselves are composed of a family of proteins and are therefore expected to be partially quantised at the molecular level. Further investigation with improved spatial resolution looking at multiple adhesion components is required to determine if there is any spatial heterogeneity or defined reorganisation of macromolecular protein complexes by the nanotopography.

This work has revealed and reinforced the importance of understanding the limitations of experimental methods. Previous work at standard resolutions found no correlation between the nanopatterns orientation and adhesion orientation – however on inspection with super-resolved microscopy it is clear that what appears to be a randomly orientated adhesion at standard resolution is actually a series of short, sub-micron adhesions which are highly ordered to the topography.

Numerous studies in the literature have investigated the impact of protein patterning on focal adhesion architecture – and as more super-resolved microscopy techniques become available, the level of detail being observed is increasing. The results in this chapter demonstrate that the architecture of focal adhesions can be modulated by simple arrays of nanopits on a polymer surface. Correlation in the distribution of focal adhesions on these nanopit arrays across multiple materials (PCL[36] and PC[44] as described in **Chapter 4**) and cell types (MSC[38], [79] and MEF as shown in this chapter) indicate that the modulation of FA structure by nanopatterned substrates is well conserved – possibly working through the fundamental building blocks of cellular mechanosensing. The use of a new cell type to investigate changes in the focal adhesion population within a cell reinforces that this is a topographically driven effect and may have applications across

a variety of cell types and materials – providing a versatile new tool in the design of a host of biomedical interfaces. With others having demonstrated the use of such surfaces to create a ‘plasticity system’ for studies of osteogenesis in hMSCs, there is surely scope to develop further defined stimulus to a host of relevant biological systems for more detailed studies in cancer, developmental biology and biomaterials.

Due to the differences in fabrication methods of nanopit and nanopillars substrates, it was not possible to use a consistent polarity of nanostructures throughout the features. Due to the demanding requirements of super resolution microscopy, substrates with nanopits were used to investigate the nanoscale geometry of focal adhesions – the fabrication process yields substrates which are flatter and therefore easier to use with high power, short working distance objectives. Moving forward, a comparison of the impact of nanopits and nanopillars is essential to define whether these are two different stimuli, or similar in their effect on cellular substructures.

## 7 Conclusion & discussion

New fabrication processes for creating gradients of feature height/depth have been developed which are applicable to both nanoscale and microscale ranges. These are realised by etching through plasma polymer gradient films, and the behaviour of such films as sacrificial etch masks has been characterised against both silicon and quartz substrates. A single deposition and etch step is capable of producing gradients up to 1  $\mu\text{m}$  in depth, whereas a tandem etch through an intermediate oxide layer offers the potential of height/depth gradients spanning tens of microns. These new gradient topographies, exhibiting exquisite resolution in all dimensions, have been demonstrated as effective screening platforms to elucidate the drivers and nature of cell response to micro- and nanostructured surfaces. High volume, high fidelity replication of gradient topographies was realised by injection moulding in biocompatible polymers such as polycarbonate and polystyrene.

Cell response to these high-content screening platforms was investigated. Fibroblast and endothelial cells displayed unique modes of response on a gradient of microgroove depth and width – allowing the identification of the minimal effective groove depth to drive fibroblast alignment. Alignment dropped below 30% for groove depths under 500 nm, and was at its most pronounced as groove pitch was reduced to 5  $\mu\text{m}$ . In contrast, endothelial cells showed little or no alignment to the groove axis, but did proliferate more rapidly towards forming a characteristic cobblestone layer at groove depths below 500 nm and with groove pitches above 70  $\mu\text{m}$ . The response of these cell types was also investigated on a gradient of nanopillar height, in a geometrical configuration which had been shown to deplete fibroblast populations and enhance endothelial cell proliferation. A new method was developed for the label free segmentation of a co-culture of these two cell types with an accuracy of 84%, allowing investigation of the simultaneous behaviour of these cell types on the nanostructured substrate. In this more relevant culture model, the response was found to be similar in nature to the earlier work – in that fibroblast populations are depleted on nanopillars whilst endothelial cells are enriched. The gradient of height also showed that at pillar heights over 150 nm, endothelial cells were also inhibited, suggesting an optimal pillar height of 75 nm to combine the two effects.



A device was devised, designed, fabricated and patented to allow for the uniform seeding of cells across the gradient screening platforms being developed. This device reduces the standard deviation of local cell density by an order of magnitude – ensuring that gradient surfaces can be seeded uniformly and the cell response more reliably analysed. The device also has broader applications in cell culture studies. It offers the chance to homogenise cell seeding between experiments, users and laboratories – going some way to tackling the problems introduced by the currently varied seeding methods. Alongside collaborators, the effect of homogeneous seeding on stem cell differentiation was assessed.

Finally, the true ability of a cell to sense nanotopographical structures was investigated using super-resolution microscopy. Array substrates were fabricated with subtle variations in nanopatterns geometry. It was found that focal adhesions exhibit nanoscale architecture in response to their underlying surface – and that heterogeneity in the surface patterning and geometry is reflected in adhesions which have modified structure at the nanoscale. Observation using super-resolution microscopy also revealed the geometry of focal adhesions with respect to the underlying nanotopography. Adhesion proteins do not co-localise or aggregate within nanopits, but rather the adhesions appear to navigate their way between pits, and are composed of many small adhesive units. This presents a stark contrast with the adhesion morphology perceived at standard resolutions – meaning that comparisons of focal contact area, length and size are unsuitable at standard resolution. In fact, adhesions were constrained and could be no wider than the 200 nm space between nanopit features used in this thesis.

Taken as a whole this thesis represents a stepwise analysis of cell response to engineered surfaces environments, developing new methods for fabrication, use, and analysis of high-content screening platforms. This has revealed the nanoscale sensitivity of cells to engineered culture substrates. Broad analysis across millimetre scale gradients showed re-organisation of cell populations in accordance with the underlying topography, whilst super-resolution imaging revealed that nanopatterned substrates affect the very shape of subcellular components with differences in architecture within single focal adhesion complexes.

## **Appendix A: immunohistochemistry protocol**

- Remove media from substrate
- Rinse substrate in 1x PBS
- Fix cells in 10% formaldehyde/PBS at 37°C for 10 min
- Rinse twice in 1x PBS
- Permeabilise cell membrane in 0.1% Triton-X/PBS at 4°C for 10 min
- Incubate substrate in 1% BSA/PBS (blocking buffer) 4°C for 1 hour
- Incubate with primary antibody at 1:500 dilution in PBS at 4°C overnight
- Wash three times with 1% Tween-20/PBS on shaker set to slow swirl for 5 min
- Incubate with secondary antibody (1:500 concentration in PBS) 4°C for 1 hour
- Wash three times with 1% Tween-20/PBS on shaker set to slow swirl for 5 min
- Store in PBS or mount sample on microscope slide using mounting medium

## Appendix B: plasma chamber operation protocol

1. Turn on the support PC.
2. Turn on the LAF cupboard (two switches at the top middle of the cupboard)
3. Vent chamber using filtered vent valve. Close valve again after chamber is fully vented
4. Check precursor liquid level. Change if necessary.
5. Turn on thickness monitor and verify correct settings and operation.
6. Open chamber and place sample on the plastic support. Close chamber and cage door.
7. Turn on pump.
8. Open isolation valve, and pump down chamber.
  1. Chamber usually pumps to at least 0.04 mbar.
  2. While pumping, open the plasmachamber log spreadsheet and the labview control system. Begin filling out the required information.
9. Close isolation valve and vent chamber. Pump down again.
10. When chamber pressure reaches below 0.05 mbar, begin filling the nitrogen trap with LN2
11. Pressure should further decrease, usually to at least 0.01 mbar.
12. Open the monomer valve - pressure in the chamber will rise.
13. Use the isolation valve to control chamber pressure to around 0.2 mbar.
14. Refill LN2 in trap and wait for five minutes.
15. Turn on RF power unit. Adjust power setting to required value (dial reads in 1/1000 of max power (300 W). If using pulsed deposition, set function generator. Reset QCM.
  1. Pressure in the chamber will likely rise. Adjust isolation valve again to stabilize at desired operating pressure.
  2. Adjust Load/Tune dials on the matching unit to minimize reflected power, if possible.
  3. Verify that plasma is ignited properly (you may wish to turn off the room lights if plasma is dim)
  4. Under NO CIRCUMSTANCES can the cage doors be open while the RF power is on.
  5. Remember to fill out logsheet.
16. Wait for the desired process time, or until the thickness monitor displays the desired value.
17. Stop Labview logging. Turn off RF power and the unit. Close monomer valve. Fully open isolation valve. Turn off thickness monitor
18. Perform two pump/vent cycles as during pumpdown.
19. After the second pumpdown, close isolation valve fully and turn off pump. Vent chamber and close vent valve. Open chamber and remove sample. Close door.
20. Remove the LN2 trap and place in LAF cabinet. Check nitrogen trap o-ring for any particulates and clean with IPA if necessary.
  1. NOTE: Hexane is relatively harmless, and it is sufficient to remove the insert and take it directly to the LAF cabinet. For more hazardous precursors, the entire nitrogen trap should be removed from the pump line and the insert removed once inside the LAF cabinet.
21. Turn off support PC
22. After at least 4 hours, and no later than the day after deposition, return to the chamber and replace the LN2 trap.
23. Perform a single pumpdown, close isolation valve and turn off pump.
24. Turn off LAF cabinet.

## Appendix C: PCA code

A basic outline of code that one may use to setup and begin to process a multivariate microscopy dataset obtained using CellProfiler in MATLAB®.

```

%load in data - don't bother if it already exists (saves a few seconds)
if exist('a','var')
    disp('variable called input already exists, using existing variable')
else
    [a,id]=xlsread('nanogradclas_double.csv');
end

%only keep top row of id column and from 10 onwards
id = id(1,10:end);
%exclude meaningless columns
data=a(:,10:end);
%extract gradient position from each cell measurement
pos=a(:,5);
%how many unique positions on the gradient are there? This unfortunately
%assumes that there will be a cell in every possible sub division...
scans = length(unique(a(:,7)));
positions = length(unique(pos));

%extract cell type (1 =end, 2 = fib), then generate positions of each
cell
%class in dataset
cellid=a(:,9);
idfib=find(cellid==2);
idend=find(cellid==1);

%isolate data for each individual cell type
datafib=data(idfib,:);
dataend=data(idend,:);

posend=a(idend,5);
posfib=a(idfib,5);

%Counting cells%
numfib=zeros(1,positions);

for n=1:positions
    numfib(n)=length(find(posfib==n));
end

numend=zeros(1,positions);

for n=1:positions
    numend(n) = length(find(posend==n));
end

%Measuring cell area%
areafib=zeros(1,positions);

```

```

for n=1:positions
    areafib(n)=mean(datafib(posfib==n,1));
end

areaend= zeros(1,positions);
for n=1:positions
    areaend(n)=mean(dataend(posend==n,1));
end
close

%PCA analysis%

%setup figure
h=figure;
set(h,'name','fibroblast biplot')
%find standard deviation of each column of fibroblast data
stdrfib = std(datafib);
%divide through data by stdev of each column. repmat just arrays the
stdev
%data into a big matrix that matches data
srfib = datafib./repmat(stdrfib,length(datafib),1);

%perform actual PCA - generating the loadings(coefficients), scores and
variances
[coefsfib,scoresfib,variancesfib] = princomp(srfib);
biplot(coefsfib(:,1:2), 'scores',scoresfib(:,1:2))

%=====

%setup figure
h=figure;
set(h,'name','endothelial biplot')
stdrend = std(dataend);
srend = dataend./repmat(stdrend,length(dataend),1);
[coefsrend,scoresrend,variancesrend] = princomp(srend);
biplot(coefsrend(:,1:2), 'scores',scoresrend(:,1:2))

%chuck these figures out
close all

%Fibroblast analysis%
h=figure;
set(h,'name','fibroblast')

subplot(2,2,1)
biplot(coefsfib(:,1:2), 'scores',scoresfib(:,1:2))

subplot(2,2,2)
plotyy(1:positions,areafib,1:positions,numfib);legend('Area','number');

subplot(2,2,3)
plot(scoresfib(:,1),scoresfib(:,2),'.',scoresfib(posfib==3,1),scoresfib(p
osfib==3,2),'r.')
title('pos 3')

subplot(2,2,4)

```

```

plot(scoresfib(:,1),scoresfib(:,2),'.',scoresfib(posfib==11,1),scoresfib(
posfib==11,2),'r.')
title('pos 11')

%Endothelial analysis%
h=figure;
set(h,'name','endothelial')

subplot(2,2,1)
biplot(coefsend(:,1:2), 'scores',scoresend(:,1:2))

subplot(2,2,2)
plotyy(1:positions,areaend,1:positions,numend);legend('Area','number');

subplot(2,2,3)
plot(scoresend(:,1),scoresend(:,2),'.',scoresend(posend==3,1),scoresend(p
osend==3,2),'r.')
title('pos 3')

subplot(2,2,4)
plot(scoresend(:,1),scoresend(:,2),'.',scoresend(posend==11,1),scoresend(
posend==11,2),'r.')
title('pos 11')

%%
%load feature labels

h=figure;
set(h,'name','fibroblast and features')
biplot(coefsfib(:,1:2), 'scores',scoresfib(:,1:2),'varlabels',id)

h=figure;
set(h,'name','endothelial and features')
biplot(coefsend(:,1:2), 'scores',scoresend(:,1:2),'varlabels',id)

idimg=a(:,1);

%% Averaging the data per image%%

dataavgfib=mean(data(idimg==1&cellid==2,:));

for n=2:(scans*positions)

    %when there is only one cell, it averages the row and makes array
size
    %mismatch
    next = mean(data(idimg==n&cellid==2,:));
    if (length(next)==1)
        next = data(idimg==n&cellid==2,:);
    end;
    dataavgfib=[dataavgfib; next];
end

dataavgend=mean(data(idimg==1&cellid==1,:));
if (length(dataavgend)==1)

```

```

        dataavgend=data(idimg==1&cellid==1,:);
    end;

for n=2:(scans*positions)

    next = mean(data(idimg==n&cellid==1,:));
    if (length(next)==1)
        next = data(idimg==n&cellid==1,:);
    end;

    dataavgend=[dataavgend; next];
end

%% Analysis %%
h=figure;
set(h,'name','all features')
plot(scoresfib(:,1),scoresfib(:,2),'.',scoresfib(1:24:396,1),scoresfib(1:
24:396,2),'ro')
plot(scoresfib(:,1),scoresfib(:,2),'.',scoresfib(23:36:396,1),scoresfib(2
3:36:396,2),'ro',scoresfib(3:36:396,1),scoresfib(3:36:396,2),'ks')
biplot(coefsfib(:,1:2), 'scores',scoresfib(:,1:2),'varlabels',id)

%% Averaging the data per position%%

dataavgfib=mean(data(pos==1&cellid==2,:));
for n=2:positions
    dataavgfib=[dataavgfib; mean(data(pos==n&cellid==2,:))];
end

dataavgend=mean(data(pos==1&cellid==1,:));
for n=2:positions
    dataavgend=[dataavgend; mean(data(pos==n&cellid==1,:))];
end

%PCA analysis%
stdravgfib = std(dataavgfib);
savgfib = dataavgfib./repmat(stdravgfib,positions,1);
[coefsavgfib,scoresavgfib,variancesavgfib,t2] = princomp(savgfib);
biplot(coefsavgfib(:,1:2), 'scores',scoresavgfib(:,1:2),'varlabels',id)

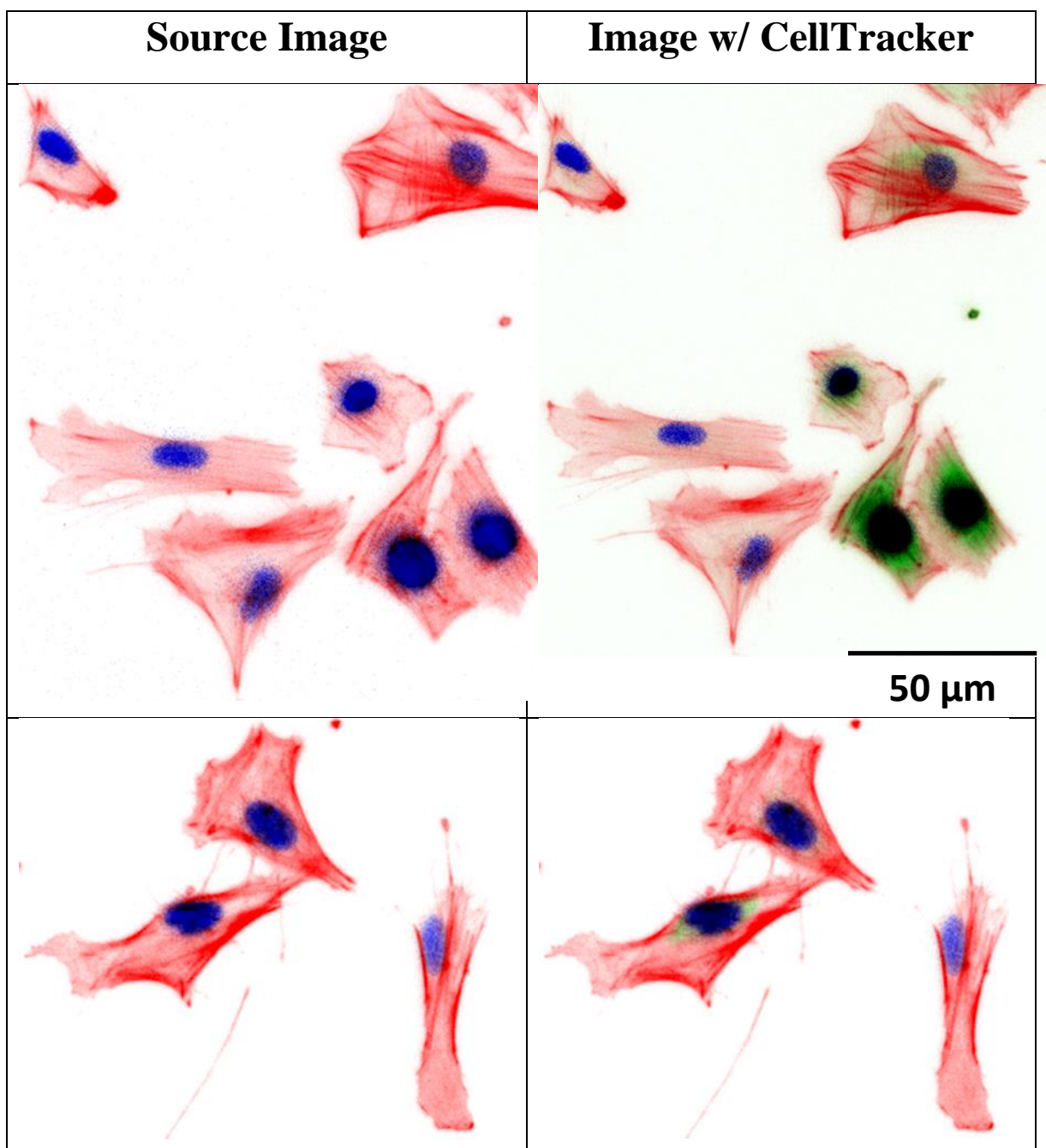
h=figure;
set(h,'name','avg per position')
stdravgend = std(dataavgend);
savgend = dataavgend./repmat(stdravgend,positions,1);
[coefsavgend,scoresavgend,variancesavgend,t2] = princomp(savgend);
biplot(coefsavgend(:,1:2), 'scores',scoresavgend(:,1:2),'varlabels',id)

spanFigures

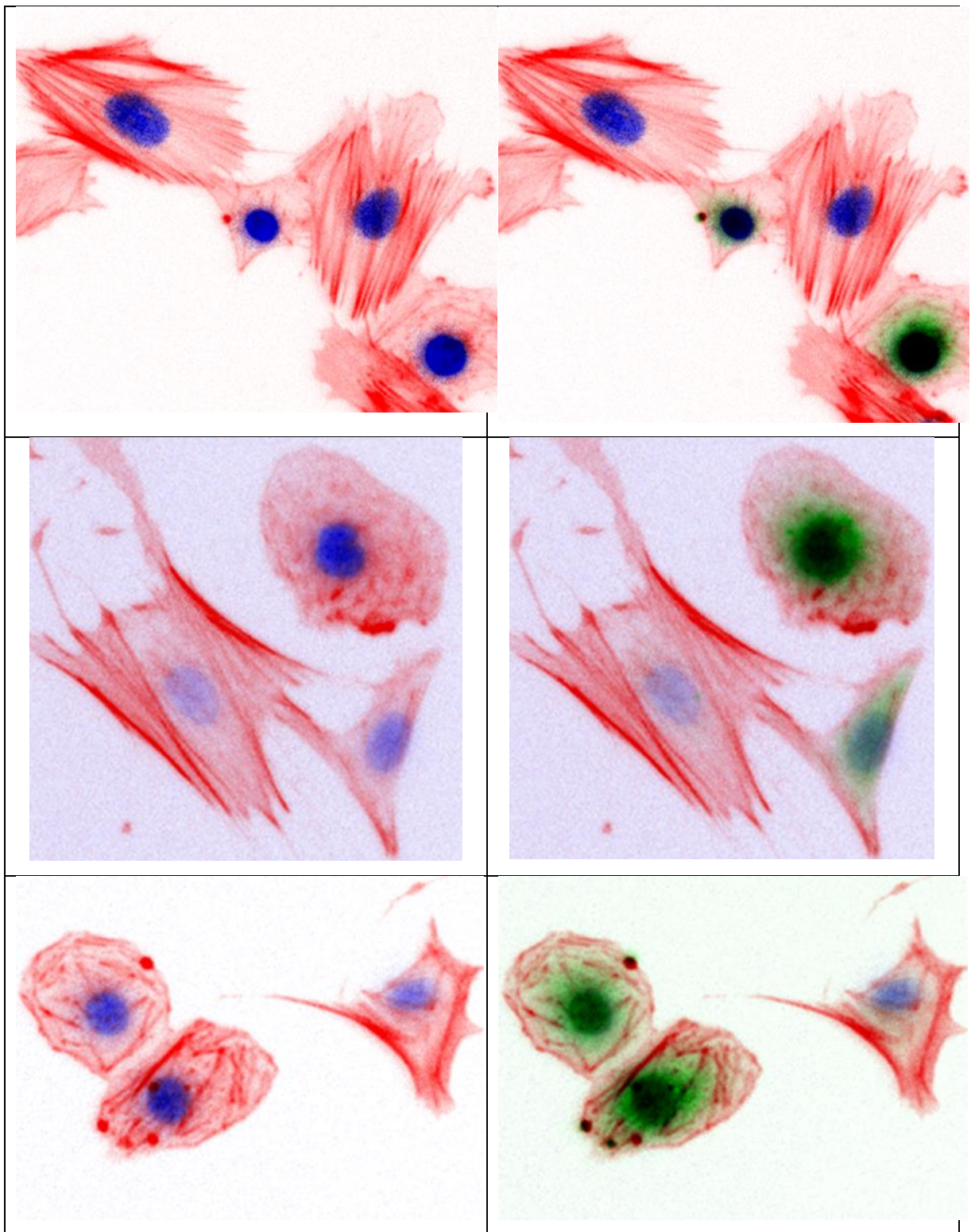
```

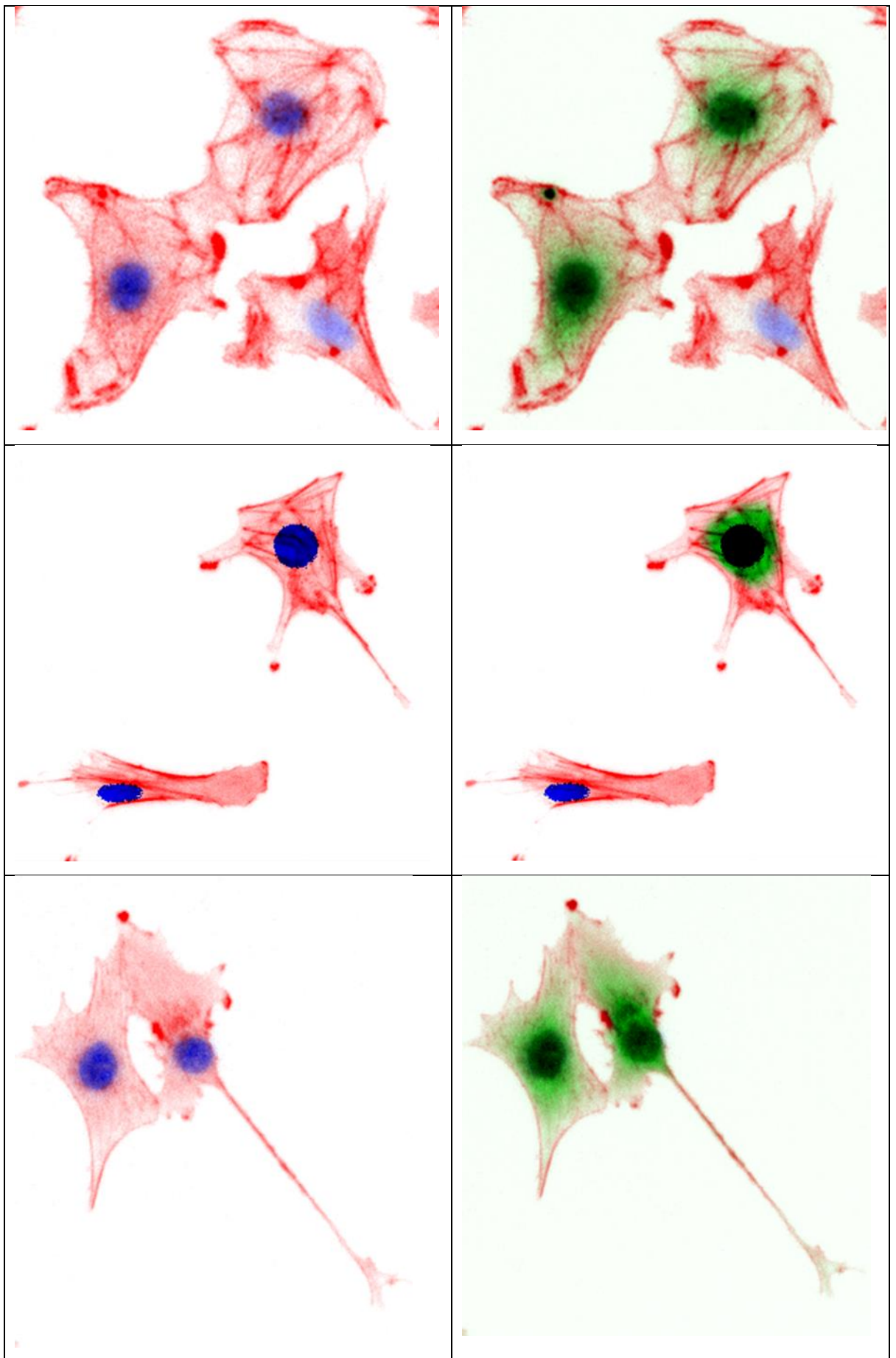
## Appendix D: manual classification exercise

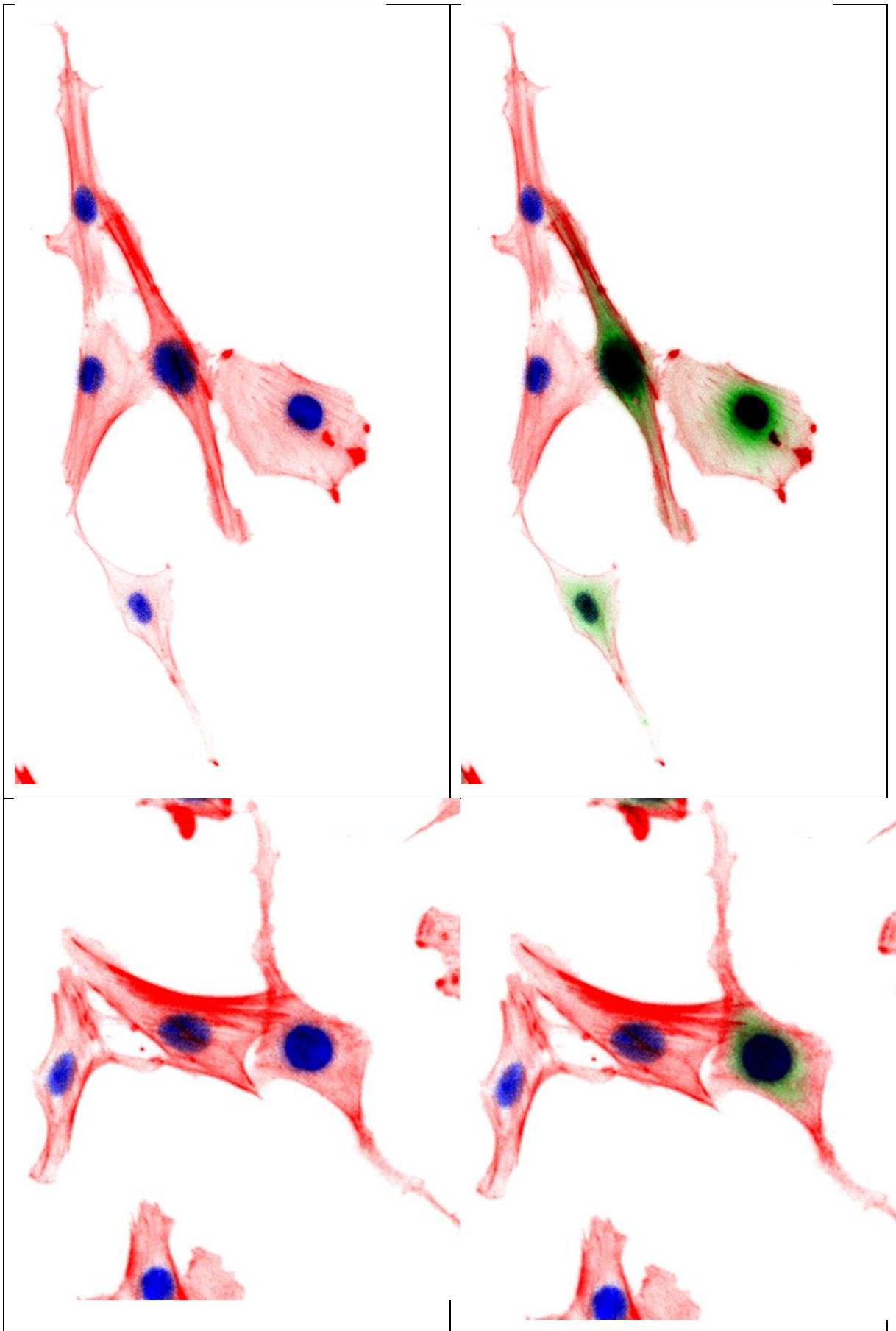
Classification exercise which was conducted with a group of researchers. Source images of fibroblast and endothelial cells in co-culture were shown, with participants asked to classify them by cell type. Sample size was 50 cells, obtained from randomly selected images. The following table shows the blind test images (red: actin, blue: DAPI) and also the overlay of CellTracker intensity (green) which was pre-loaded into only endothelial cells.



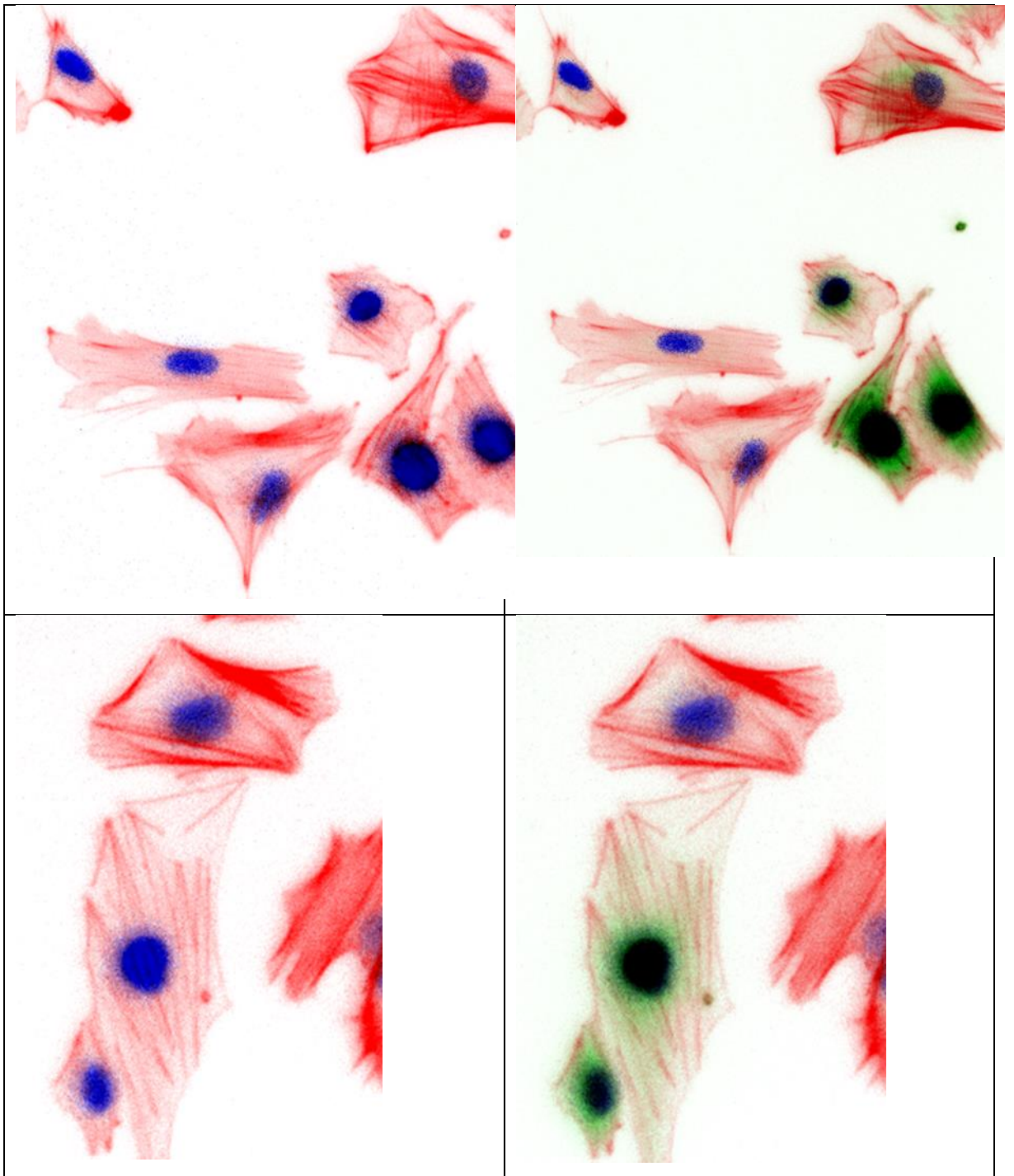












## Appendix D: reagents

<u>1X staining buffer</u>	<u>ThreeB ‘blinking’ buffer</u>
1% BSA 20mM Tris-base 155mM NaCl 2mM EGTA 2mM MgCl <sub>2</sub>  <i>i.e. to make 1L</i>  2.4228g Tris Base 9.0582g NaCl 0.4060g MgCl <sub>2</sub> 0.7607g EGTA  Correct pH to 7.5	– 100mM 2-mercaptoethanol (BME)  <i>i.e. to make 1.41 ml</i>  1.4 ml 1X PBS 10 µl 14.3M BME  <b>NB:</b> Modern dyes are too stable, blinking and bleaching too slowly or sparsely. The 3B super-resolution technique requires that Alexa family dyes are mounted in a reducing agent to induce bleaching and blinking – yielding the information necessary for reconstruction of a super-resolved image. Fluorescent proteins such as GFP fluoresce in a different manner, which produces a blinking effect meaning they can be used as is.
<u>DMEM</u>	
71% Dulbecco’s modified Eagles medium (DMEM) (Sigma, UK) 17.5% Medium 199 (Sigma, UK) 9% foetal calf serum (FCS) (Life Technologies, UK) 1.6% 200mM L-glutamine (Life Technologies, UK) 0.9% 100mM sodium pyruvate (Life Technologies, UK)	
<u>HAMS</u>	
92.4% HAMS F10 medium (Sigma Aldrich, UK) 3% foetal bovine serum (FBS) 2.9% antibiotic mixture 0.8% ITS liquid media supplement (Sigma Aldrich, UK) 0.9% sodium bicarbonate (Sigma Aldrich, UK)	

## References

- [1] D. F. Williams, "On the nature of biomaterials.," *Biomaterials*, vol. 30, no. 30, pp. 5897–909, Oct. 2009.
- [2] L. L. Hench and J. M. Polak, "Third-generation biomedical materials.," *Science*, vol. 295, no. 5557, pp. 1014–7, Feb. 2002.
- [3] B. D. Ratner and S. J. Bryant, "Biomaterials: where we have been and where we are going.," *Annu. Rev. Biomed. Eng.*, vol. 6, no. 1, pp. 41–75, Jan. 2004.
- [4] K. Vasilev, J. Cook, and H. J. Griesser, "Antibacterial surfaces for biomedical devices.," *Expert Rev. Med. Devices*, vol. 6, no. 5, pp. 553–67, Sep. 2009.
- [5] J. Voldman, M. L. Gray, and M. a Schmidt, "Microfabrication in biology and medicine.," *Annu. Rev. Biomed. Eng.*, vol. 1, pp. 401–25, Jan. 1999.
- [6] M. M. Stevens and J. H. George, "Exploring and engineering the cell surface interface.," *Science*, vol. 310, no. 5751, pp. 1135–8, Nov. 2005.
- [7] H. M. Geysen, F. Schoenen, D. Wagner, and R. Wagner, "Combinatorial compound libraries for drug discovery: an ongoing challenge.," *Nat. Rev. Drug Discov.*, vol. 2, no. 3, pp. 222–30, Mar. 2003.
- [8] C. G. Simon and S. Lin-Gibson, "Combinatorial and high-throughput screening of biomaterials.," *Adv. Mater.*, vol. 23, no. 3, pp. 369–87, Jan. 2011.
- [9] J. Genzer and R. R. Bhat, "Surface-Bound Soft Matter Gradients," *Langmuir*, vol. 24, pp. 2294–2317, 2008.
- [10] A. L. Hook, D. G. Anderson, R. Langer, P. Williams, M. C. Davies, and M. R. Alexander, "High throughput methods applied in biomaterial development and discovery.," *Biomaterials*, vol. 31, no. 2, pp. 187–98, Jan. 2010.
- [11] S. Ankam, B. K. K. Teo, M. Kukumberg, and E. K. F. Yim, "High throughput screening to investigate the interaction of stem cells with their extracellular microenvironment.," *Organogenesis*, vol. 9, no. 3, pp. 128–42, 2013.
- [12] S. Morgenthaler, C. Zink, and N. D. Spencer, "Surface-chemical and -morphological gradients," *Soft Matter*, vol. 4, no. 3, p. 419, 2008.
- [13] M. Singh, C. Berkland, and M. S. Detamore, "Strategies and Applications for Incorporating Physical and Chemical Signal Gradients in Tissue Engineering," *Tissue Eng. Part B*, vol. 14, no. 4, 2008.
- [14] M. Suk, G. Khang, and H. Bang, "Gradient polymer surfaces for biomedical applications," *Prog. Polym. Sci.*, vol. 33, pp. 138–164, 2008.
- [15] F. E. Edalat, H. Bae, S. Manoucheri, J. Min Cha, and A. Khademhosseini, "Engineering Approaches Toward Deconstructing and Controlling the Stem Cell Environment," *Ann. Biomed. Eng.*, vol. 40, no. 6, pp. 1301–1315, 2012.
- [16] D. B. Weibel, W. R. Diluzio, and G. M. Whitesides, "Microfabrication meets microbiology.," *Nat. Rev. Microbiol.*, vol. 5, no. 3, pp. 209–18, Mar. 2007.
- [17] X. Wang and T. Ha, "Defining single molecular forces required to activate integrin and notch signaling.," *Science (80-. )*, vol. 340, no. 6135, pp. 991–4, May 2013.
- [18] J. Wu, Z. Mao, H. Tan, L. Han, T. Ren, and C. Gao, "Gradient biomaterials and their influences on cell migration.," *Interface Focus*, vol. 2, no. 3, pp. 337–55, Jun. 2012.
- [19] L. Altomare, N. Gadegaard, L. Visai, M. C. Tanzi, and S. Farè, "Biodegradable microgrooved polymeric surfaces obtained by photolithography for skeletal muscle cell orientation and myotube development.," *Acta Biomater.*, vol. 6, no. 6, pp. 1948–57, Jun. 2010.

- [20] D.-H. Kim, C.-H. Seo, K. Han, K. W. Kwon, A. Levchenko, and K.-Y. Suh, "Guided Cell Migration on Microtextured Substrates with Variable Local Density and Anisotropy," *Adv. Funct. Mater.*, vol. 19, no. 10, pp. 1579–1586, May 2009.
- [21] J. Yang, F. R. a. J. Rose, N. Gadegaard, and M. R. Alexander, "A High-Throughput Assay of Cell-Surface Interactions using Topographical and Chemical Gradients," *Adv. Mater.*, vol. 21, no. 3, pp. 300–304, Jan. 2009.
- [22] K. Kolind, A. Dolatshahi-Pirouz, J. Lovmand, F. S. Pedersen, M. Foss, and F. Besenbacher, "A combinatorial screening of human fibroblast responses on micro-structured surfaces.," *Biomaterials*, vol. 31, no. 35, pp. 9182–91, Dec. 2010.
- [23] D.-H. Kim, K. Han, K. Gupta, K. W. Kwon, K.-Y. Suh, and A. Levchenko, "Mechanosensitivity of fibroblast cell shape and movement to anisotropic substratum topography gradients.," *Biomaterials*, vol. 30, no. 29, pp. 5433–44, Oct. 2009.
- [24] M. T. Lam, S. Sim, X. Zhu, and S. Takayama, "The effect of continuous wavy micropatterns on silicone substrates on the alignment of skeletal muscle myoblasts and myotubes.," *Biomaterials*, vol. 27, no. 24, pp. 4340–7, Aug. 2006.
- [25] M. J. Dalby, M. O. Riehle, S. J. Yarwood, C. D. . Wilkinson, and A. S. G. Curtis, "Nucleus alignment and cell signaling in fibroblasts: response to a micro-grooved topography," *Exp. Cell Res.*, vol. 284, no. 2, pp. 272–280, Apr. 2003.
- [26] J. Meyle, H. Wolburg, and a. F. Von Recum, "Surface Micromorphology and Cellular Interactions," *J. Biomater. Appl.*, vol. 7, no. 4, pp. 362–374, Jan. 1993.
- [27] A. I. Teixeira, G. a Abrams, P. J. Bertics, C. J. Murphy, and P. F. Nealey, "Epithelial contact guidance on well-defined micro- and nanostructured substrates.," *J. Cell Sci.*, vol. 116, no. Pt 10, pp. 1881–92, May 2003.
- [28] M. C. Lensen, V. a. Schulte, J. Salber, M. Diez, F. Menges, and M. Möller, "Cellular responses to novel, micropatterned biomaterials," *Pure Appl. Chem.*, vol. 80, no. 11, pp. 2479–2487, 2008.
- [29] C. Miller, S. Jeftinija, and S. Mallapragada, "Micropatterned Schwann cell-seeded biodegradable polymer substrates significantly enhance neurite alignment and outgrowth.," *Tissue Eng.*, vol. 7, no. 6, pp. 705–15, Dec. 2001.
- [30] B. Wójciak-Stothard, A. S. G. Curtis, W. Monaghan, M. McGrath, I. Sommer, and C. D. Wilkinson, "Role of the cytoskeleton in the reaction of fibroblasts to multiple grooved substrata.," *Cell Motil. Cytoskeleton*, vol. 31, no. 2, pp. 147–58, Jan. 1995.
- [31] P. Clark, P. Connolly, A. S. G. Curtis, J. a Dow, and C. D. Wilkinson, "Topographical control of cell behaviour. I. Simple step cues.," *Development*, vol. 99, no. 3, pp. 439–48, Mar. 1987.
- [32] B. Wójciak-Stothard, A. S. G. Curtis, W. Monaghan, K. MacDonald, and C. Wilkinson, "Guidance and activation of murine macrophages by nanometric scale topography.," *Exp. Cell Res.*, vol. 223, no. 2, pp. 426–35, Mar. 1996.
- [33] P. Clark, P. Connolly, A. S. G. Curtis, J. a Dow, and C. D. Wilkinson, "Cell guidance by ultrafine topography in vitro.," *J. Cell Sci.*, vol. 99 ( Pt 1), pp. 73–7, May 1991.
- [34] N. F. Huang, S. Patel, R. G. Thakar, J. Wu, B. S. Hsiao, B. Chu, R. J. Lee, and S. Li, "Myotube assembly on nanofibrous and micropatterned polymers.," *Nano Lett.*, vol. 6, no. 3, pp. 537–42, Mar. 2006.
- [35] M. J. Dalby, N. Gadegaard, R. Tare, A. Andar, M. O. Riehle, P. Herzyk, C. D. W. Wilkinson, and R. O. C. Oreffo, "The control of human mesenchymal cell differentiation using nanoscale symmetry and disorder.," *Nat. Mater.*, vol. 6, no. 12, pp. 997–1003, Dec. 2007.

- [36] L. Csaderova, E. Martines, K. Seunarine, N. Gadegaard, C. D. W. Wilkinson, and M. O. Riehle, "A Biodegradable and Biocompatible Regular Nanopattern for Large-Scale Selective Cell Growth," *Small*, vol. 6, no. 23, pp. 2755–2761, 2010.
- [37] E. K. F. Yim, E. M. Darling, K. Kulangara, F. Guilak, and W. Leong, "Nanotopography-induced changes in focal adhesions, cytoskeletal organization, and mechanical properties of human mesenchymal stem cells," *Biomaterials*, vol. 31, no. 6, pp. 1–16, 2011.
- [38] R. J. McMurray, N. Gadegaard, P. M. Tsimbouri, K. V Burgess, L. E. Mcnamara, R. Tare, K. Murawski, E. Kingham, R. O. C. Oreffo, and M. J. Dalby, "Nanoscale surfaces for the long-term maintenance of mesenchymal stem cell phenotype and multipotency," *Nat. Mater.*, no. July, pp. 1–8, 2011.
- [39] E. K. F. Yim, R. M. Reano, S. W. Pang, A. F. Yee, C. S. Chen, and K. W. Leong, "Nanopattern-induced changes in morphology and motility of smooth muscle cells," *Biomaterials*, vol. 26, no. 26, pp. 5405–13, Sep. 2005.
- [40] E. K. F. Yim, S. W. Pang, and K. W. Leong, "Synthetic nanostructures inducing differentiation of human mesenchymal stem cells into neuronal lineage," *Exp. Cell Res.*, vol. 313, no. 9, pp. 1820–9, May 2007.
- [41] S. Gerecht, C. J. Bettinger, Z. Zhang, J. T. Borenstein, G. Vunjak-Novakovic, and R. Langer, "The effect of actin disrupting agents on contact guidance of human embryonic stem cells," *Biomaterials*, vol. 28, no. 28, pp. 4068–77, Oct. 2007.
- [42] E. Rebollar, I. Frischauf, M. Olbrich, T. Peterbauer, S. Hering, J. Preiner, P. Hinterdorfer, C. Romanin, and J. Heitz, "Proliferation of aligned mammalian cells on laser-nanostructured polystyrene," *Biomaterials*, vol. 29, no. 12, pp. 1796–806, Apr. 2008.
- [43] T. Tzvetkova-Chevolleau, A. Stéphanou, D. Fuard, J. Ohayon, P. Schiavone, and P. Tracqui, "The motility of normal and cancer cells in response to the combined influence of the substrate rigidity and anisotropic microstructure," *Biomaterials*, vol. 29, no. 10, pp. 1541–51, Apr. 2008.
- [44] P. Reynolds, R. H. Pedersen, J. Stormonth-Darling, M. J. Dalby, M. O. Riehle, and N. Gadegaard, "Label-free segmentation of Co-cultured cells on a nanotopographical gradient," *Nano Lett.*, vol. 13, no. 2, pp. 570–6, Feb. 2013.
- [45] P. M. Reynolds, R. H. Pedersen, M. O. Riehle, and N. Gadegaard, "A Dual Gradient Assay for the Parametric Analysis of Cell-Surface Interactions," *Small*, vol. 8, no. 16, pp. 2541–2547, Jun. 2012.
- [46] H. V Unadkat, M. Hulsman, K. Cornelissen, B. J. Papenburg, R. K. Truckenmüller, G. F. Post, M. Uetz, M. J. T. Reinders, D. Stamatialis, C. a van Blitterswijk, and J. de Boer, "An algorithm-based topographical biomaterials library to instruct cell fate," *Proc. Natl. Acad. Sci. U. S. A.*, Sep. 2011.
- [47] N. D. Gallant, K. a. Lavery, E. J. Amis, and M. L. Becker, "Universal Gradient Substrates for 'Click' Biofunctionalization," *Adv. Mater.*, vol. 19, no. 7, pp. 965–969, Apr. 2007.
- [48] J. Genzer and R. R. Bhat, "Classification of Key Attributes of Soft Material Gradients," in *Soft Matter Gradient Surfaces: Methods and Applications, First Edition*, 2012.
- [49] J. Genzer, "Surface-Bound Gradients for Studies of Soft Materials Behavior," *Annu. Rev. Mater. Res.*, vol. 42, pp. 435–68, 2012.
- [50] M. R. Alexander, J. D. Whittle, D. Barton, and R. D. Short, "Plasma polymer chemical gradients for evaluation of surface reactivity: epoxide reaction with carboxylic acid surface groups," *J. Mater. Chem.*, vol. 14, no. 3, p. 408, 2004.



- [51] D. J. Menzies, B. Cowie, C. Fong, J. S. Forsythe, T. R. Gengenbach, K. M. Mclean, L. Puskar, M. Textor, L. Thomsen, M. Tobin, B. W. Muir, R. May, R. Manuscript, and R. July, "One-Step Method for Generating PEG-Like Plasma Polymer Gradients : Chemical Characterization and Analysis of Protein Interactions," *Langmuir*, vol. 252, no. 23, pp. 13987–13994, 2010.
- [52] J. H. Lee, J. O. I. W. Pazk, and H. B. Lee, "Cell adhesion and growth on polymer surfaces with hydroxyl groups prepared by water vapour plasma treatment," vol. 12, no. Figure 1, pp. 443–448, 1991.
- [53] H. S. Seo, Y. M. Ko, J. W. Shim, Y. K. Lim, J.-K. Kook, D.-L. Cho, and B. H. Kim, "Characterization of bioactive RGD peptide immobilized onto poly(acrylic acid) thin films by plasma polymerization," *Appl. Surf. Sci.*, vol. 257, no. 2, pp. 596–602, Nov. 2010.
- [54] S. Roy, N. Bhandaru, R. Das, G. Harikrishnan, and R. Mukherjee, "Thermally Tailored Gradient Topography Surface on Elastomeric Thin Films," *ACS Appl. Mater. Interfaces*, 2014.
- [55] N. R. Washburn, K. M. Yamada, C. G. Simon, S. B. Kennedy, and E. J. Amis, "High-throughput investigation of osteoblast response to polymer crystallinity : influence of nanometer-scale roughness on," *Biomaterials*, vol. 25, pp. 1215–1224, 2004.
- [56] J. Zhang, L. Xue, and Y. Han, "Fabrication Gradient Surfaces by Changing Polystyrene Microsphere Topography," *Langmuir*, no. 15, pp. 5–8, 2005.
- [57] A. M. Bowen, J. A. Ritchey, J. S. Moore, and R. G. Nuzzo, "Programmable Chemical Gradient Patterns by Soft Grayscale Lithography," *Small*, no. 23, pp. 3350–3362, 2011.
- [58] J. Almodóvar, T. Crouzier, Š. Selimović, T. Boudou, A. Khademhosseini, and C. Picart, "Gradients of physical and biochemical cues on polyelectrolyte multilayer films generated via microfluidics.," *Lab Chip*, vol. 13, no. 8, pp. 1562–70, Apr. 2013.
- [59] R. C. Gunawan, J. Silvestre, H. R. Gaskins, P. J. A. Kenis, and D. E. Leckband, "Cell Migration and Polarity on Microfabricated Gradients of Extracellular Matrix Proteins," *Langmuir*, vol. 22, no. 7, pp. 4250–4258, 2006.
- [60] J. A. Burdick, A. Khademhosseini, and R. Langer, "Fabrication of Gradient Hydrogels Using a Microfluidics/ Photopolymerization Process," *Langmuir*, vol. 20, no. 13, pp. 8–11, 2004.
- [61] D. Julthongpiput, M. J. Fasolka, W. Zhang, T. Nguyen, and E. J. Amis, "Gradient Chemical Micropatterns : A Reference Substrate for Surface," *Nano Lett.*, vol. 5, no. 8, pp. 1535–1540, 2005.
- [62] K. Kreppenhof, J. Li, R. Segura, L. Popp, M. Rossi, P. Tzvetkova, B. Luy, C. J. Ka, A. E. Guber, and P. A. Levkin, "Formation of a Polymer Surface with a Gradient of Pore Size Using a Microfluidic Chip," *Langmuir*, vol. 29, pp. 3797–3804, 2013.
- [63] F. J. Harding, L. R. Clements, R. D. Short, H. Thissen, and N. H. Voelcker, "Assessing embryonic stem cell response to surface chemistry using plasma polymer gradients.," *Acta Biomater.*, vol. 8, no. 5, pp. 1739–48, May 2012.
- [64] M. Zelzer, R. Majani, J. W. Bradley, F. R. a J. Rose, M. C. Davies, and M. R. Alexander, "Investigation of cell-surface interactions using chemical gradients formed from plasma polymers.," *Biomaterials*, vol. 29, no. 2, pp. 172–84, Jan. 2008.
- [65] N. Wells, M. a Baxter, J. E. Turnbull, P. Murray, D. Edgar, K. L. Parry, D. a Steele, and R. D. Short, "The geometric control of E14 and R1 mouse embryonic stem cell

- pluripotency by plasma polymer surface chemical gradients.," *Biomaterials*, vol. 30, no. 6, pp. 1066–70, Feb. 2009.
- [66] W. Pitt, "Fabrication of a continuous wettability gradient by radio frequency plasma discharge," *J. Colloid Interface Sci.*, vol. 133, no. 1, pp. 223–227, Nov. 1989.
- [67] J. Kim and R. G. Carbonell, "Deposition of poly[2-(perfluorooctyl)ethyl acrylate] from liquid CO<sub>2</sub> high-pressure free meniscus coating—Uniformity and morphology," *J. Supercrit. Fluids*, vol. 42, no. 1, pp. 129–141, Aug. 2007.
- [68] T. Ueda-yukoshi and T. Matsuda, "Cellular Responses on a Wettability Gradient Surface with Continuous Variations in Surface Compositions of Carbonate and Hydroxyl Groups," no. 8, pp. 4135–4140, 1995.
- [69] C. Xu, T. Wu, Y. Mei, C. M. Drain, J. D. Batteas, and K. L. Beers, "Synthesis and Characterization of Tapered Copolymer Brushes via Surface-Initiated Atom Transfer Radical Copolymerization," no. 18, pp. 11136–11140, 2005.
- [70] S. B. Kennedy, N. R. Washburn, C. G. Simon, and E. J. Amis, "Combinatorial screen of the effect of surface energy on fibronectin-mediated osteoblast adhesion, spreading and proliferation.," *Biomaterials*, vol. 27, no. 20, pp. 3817–24, Jul. 2006.
- [71] B. C. Isenberg, P. a Dimilla, M. Walker, S. Kim, and J. Y. Wong, "Vascular smooth muscle cell durotaxis depends on substrate stiffness gradient strength.," *Biophys. J.*, vol. 97, no. 5, pp. 1313–22, Sep. 2009.
- [72] C.-H. R. Kuo, J. Xian, J. D. Brenton, K. Franze, and E. Sivaniah, "Complex stiffness gradient substrates for studying mechanotactic cell migration.," *Adv. Mater.*, vol. 24, no. 45, pp. 6059–64, Nov. 2012.
- [73] L. Xie, L. Shen, and B. Jiang, "Modelling and Simulation for Micro Injection Molding Process," 2002.
- [74] J. M. Stormonth-Darling and N. Gadegaard, "Injection moulding difficult nanopatterns with hybrid polymer inlays," *Macromol. Mater. Eng.*, 2012.
- [75] J. M. Stormonth-Darling and N. Gadegaard, "Injection Moulding Difficult Nanopatterns with Hybrid Polymer Inlays," *Macromol. Mater. Eng.*, vol. 297, no. 11, pp. 1075–1080, Nov. 2012.
- [76] X. Zhang, G. Jiang, Y. Cai, S. J. Monkley, D. R. Critchley, and M. P. Sheetz, "Talin depletion reveals independence of initial cell spreading from integrin activation and traction.," *Nat. Cell Biol.*, vol. 10, no. 9, pp. 1062–8, Sep. 2008.
- [77] I. Patla, T. Volberg, N. Elad, V. Hirschfeld-Warneken, C. Grashoff, R. Fässler, J. P. Spatz, B. Geiger, and O. Medalia, "Dissecting the molecular architecture of integrin adhesion sites by cryo-electron tomography.," *Nat. Cell Biol.*, vol. 12, no. 9, pp. 909–15, Sep. 2010.
- [78] T. Cao, C. Zach, S. Modla, and D. Powell, "Registration for Correlative Microscopy using Image Analogies," pp. 1–10.
- [79] P. M. Tsimbouri, R. J. McMurray, K. V Burgess, E. V Alakpa, P. Reynolds, K. Murawski, E. Kingham, R. O. C. Oreffo, N. Gadegaard, and M. J. Dalby, "Using nanotopography and metabolomics to identify biochemical effectors of multipotency.," *ACS Nano*, vol. 6, no. 11, pp. 10239–49, Nov. 2012.
- [80] P.-Y. Wang, H.-T. Yu, and W.-B. Tsai, "Modulation of alignment and differentiation of skeletal myoblasts by submicron ridges/grooves surface structure.," *Biotechnol. Bioeng.*, vol. 106, no. 2, pp. 285–94, Jun. 2010.
- [81] J. L. Charest, A. J. García, and W. P. King, "Myoblast alignment and differentiation on cell culture substrates with microscale topography and model chemistries.," *Biomaterials*, vol. 28, no. 13, pp. 2202–10, Apr. 2007.

- [82] M. a Bucaro, Y. Vasquez, B. D. Hatton, and J. Aizenberg, "Fine-tuning the degree of stem cell polarization and alignment on ordered arrays of high-aspect-ratio nanopillars.," *ACS Nano*, vol. 6, no. 7, pp. 6222–30, Jul. 2012.
- [83] Y. Ding, J. Sun, H. W. Ro, Z. Wang, J. Zhou, N. J. Lin, M. T. Cicerone, C. L. Soles, and S. Lin-Gibson, "Thermodynamic underpinnings of cell alignment on controlled topographies.," *Adv. Mater.*, vol. 23, no. 3, pp. 421–5, Jan. 2011.
- [84] T. P. Kunzler, T. Drobek, M. Schuler, and N. D. Spencer, "Systematic study of osteoblast and fibroblast response to roughness by means of surface-morphology gradients.," *Biomaterials*, vol. 28, no. 13, pp. 2175–82, Apr. 2007.
- [85] S. Morgenthaler, S. Lee, S. Zu, and N. D. Spencer, "Letters A Simple , Reproducible Approach to the Preparation of Surface-Chemical Gradients," vol. 19, no. 25, pp. 988–989, 2003.
- [86] B. C. Berry, C. M. Stafford, M. Pandya, L. a Lucas, A. Karim, and M. J. Fasolka, "Versatile platform for creating gradient combinatorial libraries via modulated light exposure.," *Rev. Sci. Instrum.*, vol. 78, no. 7, p. 072202, Jul. 2007.
- [87] S. a Fraser, Y.-H. Ting, K. S. Mallon, A. E. Wendt, C. J. Murphy, and P. F. Nealey, "Sub-micron and nanoscale feature depth modulates alignment of stromal fibroblasts and corneal epithelial cells in serum-rich and serum-free media.," *J. Biomed. Mater. Res. Part A*, vol. 86, no. 3, pp. 725–35, Sep. 2008.
- [88] M. J. Dalby, D. McCloy, M. Robertson, C. D. W. Wilkinson, and R. O. C. Oreffo, "Osteoprogenitor response to defined topographies with nanoscale depths.," *Biomaterials*, vol. 27, no. 8, pp. 1306–15, Mar. 2006.
- [89] H. Yasuda, M. O. Bumgarner, and J. J. Hillman, "Polymerization of Organic Compounds in an Hydrocarbons i n a Closed System," *J. Appl. Polym. Sci.*, vol. 19, pp. 531–543, 1975.
- [90] P. Bajaj, B. Reddy, L. Millet, C. Wei, P. Zorlutuna, G. Bao, and R. Bashir, "Patterning the differentiation of C2C12 skeletal myoblasts.," *Integr. Biol. (Camb).*, vol. 3, no. 9, pp. 897–909, Sep. 2011.
- [91] R. B. Vernon, M. D. Gooden, S. L. Lara, and T. N. Wight, "Microgrooved fibrillar collagen membranes as scaffolds for cell support and alignment.," *Biomaterials*, vol. 26, no. 16, pp. 3131–40, Jun. 2005.
- [92] Y. Zhao, H. Zeng, J. Nam, and S. Agarwal, "Fabrication of skeletal muscle constructs by topographic activation of cell alignment.," *Biotechnol. Bioeng.*, vol. 102, no. 2, pp. 624–31, Feb. 2009.
- [93] X. Wang, A. Albrecht, H. H. Mai, C. Woidt, T. Meinl, M. Hornung, M. Bartels, and H. Hillmer, "High resolution 3D NanoImprint technology: Template fabrication, application in Fabry–Pérot-filter-array-based optical nanospectrometers," *Microelectron. Eng.*, vol. 110, pp. 44–51, Oct. 2013.
- [94] A. E. Carpenter, T. R. Jones, M. R. Lamprecht, C. Clarke, I. H. Kang, O. Friman, D. a Guertin, J. H. Chang, R. a Lindquist, J. Moffat, P. Golland, and D. M. Sabatini, "CellProfiler: image analysis software for identifying and quantifying cell phenotypes.," *Genome Biol.*, vol. 7, no. 10, p. R100, Jan. 2006.
- [95] H. Yasuda and T. Hirotsu, "Critical evaluation of conditions of plasma polymerization," *J. Polym. Sci. Polym. Chem. Ed.*, vol. 16, no. 4, pp. 743–759, Apr. 1978.
- [96] P. Reynolds, N. Gadegaard, and M. Riehle, "Plasmapolymerisation for high throughput screening of cell- substrate interactions," University of Glasgow, UK, 2011.

- [97] S. a Voronin, M. Zelzer, C. Fotea, M. R. Alexander, and J. W. Bradley, "Pulsed and continuous wave acrylic acid radio frequency plasma deposits: plasma and surface chemistry.," *J. Phys. Chem. B*, vol. 111, no. 13, pp. 3419–29, Apr. 2007.
- [98] R. G. Pierce, G. Padron-Wells, and M. J. Goeckner, "Gas-Phase Chemistry of Pulsed n-Hexane Discharge," *Plasma Chem. Plasma Process.*, vol. 29, no. 1, pp. 1–11, Nov. 2008.
- [99] R. H. Pedersen, Q. Xu, J. M. Stormonth-Darling, and N. Gadegaard, "Strategies for High Quality Injection Moulding of Polymer Nanopillars," *Macromol. Mater. Eng.*, p. n/a–n/a, Aug. 2014.
- [100] D. I. M. Zelzer, "Plasma Polymer Gradients," University of Nottingham, 2009.
- [101] R. H. Pedersen, M. Hamzah, S. Thoms, P. Roach, M. R. Alexander, and N. Gadegaard, "Electron beam lithography using plasma polymerized hexane as resist," *Microelectron. Eng.*, vol. 87, no. 5–8, pp. 1112–1114, May 2010.
- [102] T. R. Gengenbach, Z. R. Vasic, R. C. Chatelier, and H. J. Griesser, "A multi-technique study of the spontaneous oxidation of N-hexane plasma polymers," *J. Polym. Sci. Part A Polym. Chem.*, vol. 32, no. 8, pp. 1399–1414, Jun. 1994.
- [103] R. H. Pedersen, D. J. Scurr, P. Roach, M. R. Alexander, and N. Gadegaard, "Full-Thickness Characterization of Plasma Polymerized Hexane Films Irradiated by an Electron Beam," *Plasma Process. Polym.*, vol. 9, pp. 22–27, Oct. 2012.
- [104] J. E. Meredith, B. Fazeli, and M. a Schwartz, "The extracellular matrix as a cell survival factor.," *Mol. Biol. Cell*, vol. 4, no. 9, pp. 953–61, Sep. 1993.
- [105] C. S. Izzard and L. R. Lochner, "Cell-to-substrate contacts in living fibroblasts: an interference reflexion study with an evaluation of the technique.," *J. Cell Sci.*, vol. 21, no. 1, pp. 129–59, Jun. 1976.
- [106] J. Y. Lim and H. J. Donahue, "Cell sensing and response to micro- and nanostructured surfaces produced by chemical and topographic patterning.," *Tissue Eng.*, vol. 13, no. 8, pp. 1879–91, Aug. 2007.
- [107] J. Sun, Y. Ding, N. J. Lin, J. Zhou, H. Ro, C. L. Soles, M. T. Cicerone, and S. Lingibson, "Exploring Cellular Contact Guidance Using Gradient Nanogratings Jirun," *Biomacromolecules*, pp. 3067–3072, 2010.
- [108] B. Alberts, A. Johnson, J. Lewis, M. Raff, K. Roberts, and P. Walter, *Molecular Biology of the Cell*. 2008, p. 1725.
- [109] M. K. Vickaryous and B. K. Hall, "Human cell type diversity, evolution, development, and classification with special reference to cells derived from the neural crest.," *Biol. Rev. Camb. Philos. Soc.*, vol. 81, no. 3, pp. 425–55, Aug. 2006.
- [110] D. G. Anderson, S. Levenberg, and R. Langer, "Nanoliter-scale synthesis of arrayed biomaterials and application to human embryonic stem cells.," *Nat. Biotechnol.*, vol. 22, no. 7, pp. 863–6, Jul. 2004.
- [111] C. J. Kirkpatrick, S. Fuchs, and R. E. Unger, "Co-culture systems for vascularization--learning from nature.," *Adv. Drug Deliv. Rev.*, vol. 63, no. 4–5, pp. 291–9, Apr. 2011.
- [112] S. R. Khetani and S. N. Bhatia, "Microscale culture of human liver cells for drug development.," *Nat. Biotechnol.*, vol. 26, no. 1, pp. 120–6, Jan. 2008.
- [113] J. T. Ngo, J. a Champion, A. Mahdavi, I. C. Tanrikulu, K. E. Beatty, R. E. Connor, T. H. Yoo, D. C. Dieterich, E. M. Schuman, and D. a Tirrell, "Cell-selective metabolic labeling of proteins.," *Nat. Chem. Biol.*, vol. 5, no. 10, pp. 715–7, Oct. 2009.
- [114] P. Rivera Gil, F. Yang, H. Thomas, L. Li, A. Terfort, and W. J. Parak, "Development of an assay based on cell counting with quantum dot labels for

- comparing cell adhesion within cocultures,” *Nano Today*, vol. 6, no. 1, pp. 20–27, Feb. 2011.
- [115] L. Kametsky, T. R. Jones, A. Fraser, M.-A. Bray, D. J. Logan, K. L. Madden, V. Ljosa, C. Rueden, K. W. Eliceiri, and A. E. Carpenter, “Improved structure, function and compatibility for CellProfiler: modular high-throughput image analysis software,” *Bioinformatics*, vol. 27, no. 8, pp. 1179–80, May 2011.
- [116] T. R. Jones, A. E. Carpenter, M. R. Lamprecht, J. Moffat, S. J. Silver, J. K. Grenier, A. B. Castoreno, U. S. Eggert, D. E. Root, P. Golland, and D. M. Sabatini, “Scoring diverse cellular morphologies in image-based screens with iterative feedback and machine learning,” *Proc. Natl. Acad. Sci. U. S. A.*, vol. 106, no. 6, pp. 1826–31, Feb. 2009.
- [117] A. Cardona and P. Tomancak, “Current challenges in open-source bioimage informatics,” *Nat. Methods*, vol. 9, no. 7, pp. 661–5, Jul. 2012.
- [118] B. H. Cho, I. Cao-Berg, J. A. Bakal, and R. F. Murphy, “OMERO.searcher: content-based image search for microscope images,” *Nat. Methods*, vol. 9, no. 7, pp. 633–4, Jul. 2012.
- [119] T. R. Jones, A. E. Carpenter, M. R. Lamprecht, J. Moffat, S. J. Silver, J. K. Grenier, A. B. Castoreno, U. S. Eggert, D. E. Root, P. Golland, and D. M. Sabatini, “Scoring diverse cellular morphologies in image-based screens with iterative feedback and machine learning,” *Proc. Natl. Acad. Sci. U. S. A.*, vol. 106, no. 6, pp. 1826–31, Feb. 2009.
- [120] D. G. Anderson, D. Putnam, E. B. Lavik, T. a Mahmood, and R. Langer, “Biomaterial microarrays: rapid, microscale screening of polymer-cell interaction,” *Biomaterials*, vol. 26, no. 23, pp. 4892–7, Aug. 2005.
- [121] A. de Mel, G. Jell, M. M. Stevens, and A. M. Seifalian, “Biofunctionalization of biomaterials for accelerated in situ endothelialization: a review,” *Biomacromolecules*, vol. 9, no. 11, pp. 2969–79, Nov. 2008.
- [122] A. S. G. Curtis, “Small is beautiful but smaller is the aim: review of a life of research,” *Eur. Cells Mater.*, vol. 8, pp. 27–36, Jan. 2004.
- [123] M. J. Dalby, D. Giannaras, M. O. Riehle, N. Gadegaard, S. Affrossman, and A. S. G. Curtis, “Rapid fibroblast adhesion to 27nm high polymer demixed nanotopography,” *Biomaterials*, vol. 25, no. 1, pp. 77–83, Jan. 2004.
- [124] R. M. Bakker, A. Boltasseva, Z. Liu, R. H. Pedersen, S. Gresillon, A. V Kildishev, V. P. Drachev, and V. M. Shalaev, “Near-field excitation of nanoantenna resonance,” *Opt. Express*, vol. 15, no. 21, pp. 13682–13688, 2007.
- [125] N. Gadegaard, S. Mosler, and N. B. Larsen, “Biomimetic Polymer Nanostructures by Injection Molding,” *Macromol. Mater. Eng.*, vol. 288, no. 1, pp. 76–83, Jan. 2003.
- [126] H. Schiff, C. David, J. Gobrecht, a. D’ Amore, D. Simoneta, W. Kaiser, and M. Gabriel, “Quantitative analysis of the molding of nanostructures,” *J. Vac. Sci. Technol. B Microelectron. Nanom. Struct.*, vol. 18, no. 6, p. 3564, 2000.
- [127] J. Boss, “Mitosis in Cultures of Newt Tissues,” *Exp. Cell Res.*, vol. 7, pp. 215–231, 1954.
- [128] B. Everitt and T. Hothorn, “An Introduction to Applied Multivariate Analysis with R,” in *An Introduction to Applied Multivariate Analysis with R*, no. 1983, New York, NY: Springer New York, 2011.
- [129] M. Yliperttula, B. G. Chung, A. Navaladi, A. Manbachi, and A. Urtti, “High-throughput screening of cell responses to biomaterials,” *Eur. J. Pharm. Sci.*, vol. 35, no. 3, pp. 151–60, Oct. 2008.

- [130] M. P. Lutolf, P. M. Gilbert, and H. M. Blau, "Designing materials to direct stem-cell fate.," *Nature*, vol. 462, no. 7272, pp. 433–41, Nov. 2009.
- [131] T. G. Fernandes, M. M. Diogo, D. S. Clark, J. S. Dordick, and J. M. S. Cabral, "High-throughput cellular microarray platforms: applications in drug discovery, toxicology and stem cell research.," *Trends Biotechnol.*, vol. 27, no. 6, pp. 342–9, Jun. 2009.
- [132] J. van den Dolder, P. H. M. Spauwen, and J. a Jansen, "Evaluation of various seeding techniques for culturing osteogenic cells on titanium fiber mesh.," *Tissue Eng.*, vol. 9, no. 2, pp. 315–25, Apr. 2003.
- [133] F. Prinz, T. Schlange, and K. Asadullah, "Believe it or not: how much can we rely on published data on potential drug targets?," *Nat. Rev. Drug Discov.*, vol. 10, no. 9, p. 712, Sep. 2011.
- [134] Editorial, "Reducing our irreproducibility," *Nature*, p. 2013, 2013.
- [135] B. K. Lundholt, K. M. Scudder, and L. Pagliaro, "A simple technique for reducing edge effect in cell-based assays.," *J. Biomol. Screen.*, vol. 8, no. 5, pp. 566–70, Oct. 2003.
- [136] B. Mosadegh, M. Agarwal, H. Tavana, T. Bersano-Begey, Y. Torisawa, M. Morell, M. J. Wyatt, K. S. O'Shea, K. F. Barald, and S. Takayama, "Uniform cell seeding and generation of overlapping gradient profiles in a multiplexed microchamber device with normally-closed valves.," *Lab Chip*, vol. 10, no. 21, pp. 2959–64, Nov. 2010.
- [137] E. Horn, C. Zehetmeier, and R. Zantl, "Homogeneous distribution of cells in culture," no. March, pp. 4–6, 2006.
- [138] H. Lu, L. Guo, M. J. Wozniak, N. Kawazoe, T. Tateishi, X. Zhang, and G. Chen, "Effect of cell density on adipogenic differentiation of mesenchymal stem cells," *Biochem. Biophys. Res. Commun.*, vol. 381, no. 3, pp. 322–327, Apr. 2009.
- [139] R. Xue, J. Y.-S. Li, Y. Yeh, L. Yang, and S. Chien, "Effects of matrix elasticity and cell density on human mesenchymal stem cells differentiation.," *J. Orthop. Res.*, vol. 31, no. 9, pp. 1360–5, Sep. 2013.
- [140] C. M. Lee and J. Hu, "Cell density during differentiation can alter the phenotype of bone marrow-derived macrophages.," *Cell Biosci.*, vol. 3, p. 30, Jan. 2013.
- [141] M. Bitar, R. a Brown, V. Salih, A. G. Kidane, J. C. Knowles, and S. N. Nazhat, "Effect of cell density on osteoblastic differentiation and matrix degradation of biomimetic dense collagen scaffolds.," *Biomacromolecules*, vol. 9, no. 1, pp. 129–35, Jan. 2008.
- [142] B. K. Gage, T. D. Webber, and T. J. Kieffer, "Initial Cell Seeding Density Influences Pancreatic Endocrine Development During in vitro Differentiation of Human Embryonic Stem Cells.," *PLoS One*, vol. 8, no. 12, p. e82076, Jan. 2013.
- [143] A. J. Almarza and K. a. Athanasiou, "Effects of Initial Cell Seeding Density for the Tissue Engineering of the Temporomandibular Joint Disc," *Ann. Biomed. Eng.*, vol. 33, no. 7, pp. 943–950, Jul. 2005.
- [144] A. A. K. Moe, M. Suryana, G. Marcy, S. K. Lim, S. Ankam, J. Z. W. Goh, J. Jin, B. K. K. Teo, J. B. K. Law, H. Y. Low, E. L. K. Goh, M. P. Sheetz, and E. K. F. Yim, "Microarray with micro- and nano-topographies enables identification of the optimal topography for directing the differentiation of primary murine neural progenitor cells.," *Small*, vol. 8, no. 19, pp. 3050–61, Oct. 2012.
- [145] F. Rehfeldt, A. J. Engler, A. Eckhardt, F. Ahmed, and D. E. Discher, "Cell responses to the mechanochemical microenvironment--implications for regenerative medicine and drug delivery.," *Adv. Drug Deliv. Rev.*, vol. 59, no. 13, pp. 1329–39, Nov. 2007.

- [146] F. Luo, T.-Y. Hou, Z.-H. Zhang, Z. Xie, X.-H. Wu, and J.-Z. Xu, “Effects of initial cell density and hydrodynamic culture on osteogenic activity of tissue-engineered bone grafts.,” *PLoS One*, vol. 8, no. 1, p. e53697, Jan. 2013.
- [147] J. Cai, C. Yu, Y. Liu, S. Chen, Y. Guo, J. Yong, W. Lu, M. Ding, and H. Deng, “Generation of Homogeneous PDX 1  $\beta$  Pancreatic Progenitors from Human ES Cell-derived Endoderm Cells,” *J. Mol. Cell Biol.*, vol. 2, pp. 50–60, 2010.
- [148] C. P. Pennisi, A. Dolatshahi-Pirouz, M. Foss, J. Chevallier, T. Fink, V. Zachar, F. Besenbacher, and K. Yoshida, “Nanoscale topography reduces fibroblast growth, focal adhesion size and migration-related gene expression on platinum surfaces.,” *Colloids Surf. B. Biointerfaces*, vol. 85, no. 2, pp. 189–97, Jul. 2011.
- [149] D. W. Hamilton and D. M. Brunette, “The effect of substratum topography on osteoblast adhesion mediated signal transduction and phosphorylation.,” *Biomaterials*, vol. 28, no. 10, pp. 1806–19, Apr. 2007.
- [150] J. L. Charest, M. T. Eliason, A. J. García, and W. P. King, “Combined microscale mechanical topography and chemical patterns on polymer cell culture substrates.,” *Biomaterials*, vol. 27, no. 11, pp. 2487–94, Apr. 2006.
- [151] E. Abbe, “Beitrag zur Theorie des Mikroskops und der mikroskopischen Wahrnehmung,” *Arch. für mikroskopische Anat.*, vol. 9, no. 1, 1873.
- [152] Lord Rayleigh, “Investigations in Optics, with special reference to the Spectroscope. By,” vol. 8, 1879.
- [153] D. T. Burnette, P. Sengupta, Y. Dai, J. Lippincott-Schwartz, and B. Kachar, “Bleaching/blinking assisted localization microscopy for superresolution imaging using standard fluorescent molecules.,” *Proc. Natl. Acad. Sci. U. S. A.*, vol. 108, no. 52, pp. 21081–6, Dec. 2011.
- [154] S. Cho, J. Jang, C. Song, H. Lee, P. Ganesan, T.-Y. Yoon, M. W. Kim, M. C. Choi, H. Ihee, W. Do Heo, and Y. Park, “Simple super-resolution live-cell imaging based on diffusion-assisted Förster resonance energy transfer.,” *Sci. Rep.*, vol. 3, p. 1208, Jan. 2013.
- [155] S. Cox, E. Rosten, J. Monypenny, T. Jovanovic-talisman, D. T. Burnette, J. Lippincott-schwartz, G. E. Jones, and R. Heintzmann, “Bayesian localization microscopy reveals nanoscale podosome dynamics,” *Nat. Methods*, vol. 9, no. 2, 2012.
- [156] O. Rossier, V. Oceau, J.-B. Sibarita, C. Leduc, B. Tessier, D. Nair, V. Gatterdam, O. Destaing, C. Albigès-Rizo, R. Tampé, L. Cognet, D. Choquet, B. Lounis, and G. Giannone, “Integrins  $\beta 1$  and  $\beta 3$  exhibit distinct dynamic nanoscale organizations inside focal adhesions.,” *Nat. Cell Biol.*, vol. 14, no. 10, pp. 1057–67, Oct. 2012.
- [157] B.-C. Chen, W. R. Legant, K. Wang, L. Shao, D. E. Milkie, M. W. Davidson, C. Janetopoulos, X. S. Wu, J. a. Hammer, Z. Liu, B. P. English, Y. Mimori-Kiyosue, D. P. Romero, a. T. Ritter, J. Lippincott-Schwartz, L. Fritz-Laylin, R. D. Mullins, D. M. Mitchell, J. N. Bembenek, a.-C. Reymann, R. Bohme, S. W. Grill, J. T. Wang, G. Seydoux, U. S. Tulu, D. P. Kiehart, and E. Betzig, “Lattice light-sheet microscopy: Imaging molecules to embryos at high spatiotemporal resolution,” *Science (80-. )*, vol. 346, no. 6208, pp. 1257998–1257998, Oct. 2014.
- [158] H. Wolfenson, Y. I. Henis, B. Geiger, and A. D. Bershadsky, “The heel and toe of the cell’s foot: a multifaceted approach for understanding the structure and dynamics of focal adhesions.,” *Cell Motil. Cytoskeleton*, vol. 66, no. 11, pp. 1017–29, Nov. 2009.
- [159] F.-C. Chien, C. W. Kuo, Z.-H. Yang, D.-Y. Chueh, and P. Chen, “Exploring the formation of focal adhesions on patterned surfaces using super-resolution imaging.,” *Small*, vol. 7, no. 20, pp. 2906–13, Oct. 2011.

- [160] E. Rosten, G. E. Jones, and S. Cox, "ImageJ plug-in for Bayesian analysis of blinking and bleaching.," *Nat. Methods*, vol. 10, no. 2, pp. 97–8, Feb. 2013.
- [161] H. Shroff, H. White, and E. Betzig, "Photoactivated localization microscopy (PALM) of adhesion complexes.," *Curr. Protoc. Cell Biol.*, vol. Chapter 4, no. December, p. Unit 4.21, Dec. 2008.
- [162] B. Huang, H. Babcock, and X. Zhuang, "Breaking the diffraction barrier: super-resolution imaging of cells.," *Cell*, vol. 143, no. 7, pp. 1047–58, Dec. 2010.
- [163] Z.-L. Huang, H. Zhu, F. Long, H. Ma, L. Qin, Y. Liu, J. Ding, Z. Zhang, Q. Luo, and S. Zeng, "Localization-based super-resolution microscopy with an sCMOS camera.," *Opt. Express*, vol. 19, no. 20, pp. 19156–68, Sep. 2011.
- [164] S. Auinger and J. V. Small, "Correlated light and electron microscopy of the cytoskeleton.," *Methods Cell Biol.*, vol. 88, no. 08, pp. 257–72, Jan. 2008.
- [165] A. Sartori, R. Gatz, F. Beck, A. Rigort, W. Baumeister, and J. M. Plitzko, "Correlative microscopy: bridging the gap between fluorescence light microscopy and cryo-electron tomography.," *J. Struct. Biol.*, vol. 160, no. 2, pp. 135–45, Nov. 2007.
- [166] B. G. Kopek, G. Shtengel, C. S. Xu, D. A. Clayton, and H. F. Hess, "Correlative 3D superresolution fluorescence and electron microscopy reveal the relationship of mitochondrial nucleoids to membranes," 2012.
- [167] M. J. P. Biggs, R. G. Richards, N. Gadegaard, C. D. W. Wilkinson, and M. J. Dalby, "Regulation of Implant Surface Cell Adhesion : Characterization and Quantification of S-phase Primary Osteoblast Adhesions on Biomimetic Nanoscale Substrates," *J. Orthop. Res.*, no. February, pp. 273–282, 2007.
- [168] M. J. P. Biggs, R. G. Richards, and M. J. Dalby, "Nanotopographical modification: a regulator of cellular function through focal adhesions.," *Nanomedicine*, vol. 6, no. 5, pp. 619–33, Oct. 2010.
- [169] A. J. Engler, S. Sen, H. L. Sweeney, and D. E. Discher, "Matrix elasticity directs stem cell lineage specification.," *Cell*, vol. 126, no. 4, pp. 677–89, Aug. 2006.
- [170] C. C. Berry, G. Campbell, A. Spadicino, M. Robertson, and A. S. G. Curtis, "The influence of microscale topography on fibroblast attachment and motility.," *Biomaterials*, vol. 25, no. 26, pp. 5781–8, Nov. 2004.